10)

Formation of Magnesium Metal and Magnesium and Calcium Carbides by Metal Oxide Reduction with Methane

by

Alexander F. Diaz

B.S. Chemical Engineering
University of the Philippines, 1986

S.M. Chemical Engineering Practice
Massachusetts Institute of Technology, 1991

M.B.A.
MIT Sloan School of Management, 1997

Submitted to the Department of Chemical Engineering
in partial fulfillment of the requirements for the degree of

DOCTOR OF PHILOSOPHY

at the

MASSACHUSETTS INSTITUTE OF TECHNOLOGY

June 1997

Signature of Author _____
Department of Chemical Engineering
May 23, 1997

Certified by _____
Jack B. Howard
Hoyt C. Hottel Professor of Chemical Engineering
Thesis Supervisor

_____
William A. Peters
Associate Director, Energy Laboratory
Thesis Supervisor

Accepted by _____
Robert E. Cohen
St. Laurent Professor of Chemical Engineering
Chairman, Committee for Graduate Students

Formation of Magnesium Metal and Magnesium and Calcium Carbides by Metal Oxide Reduction with Methane

by

Alexander F. Diaz

Submitted to the Department of Chemical Engineering
on May 23, 1997 in partial fulfillment of the requirements for
the degree of Doctor of Philosophy in Chemical Engineering

Abstract

A novel method for magnesium metal formation by the reduction of magnesium oxide with methane in a thermal plasma has been developed. In this approach, magnesium oxide (44 to 104 μm) entrained in a stream of methane gas is introduced into the inter-electrode region of a magnetically rotated DC arc discharge (thermal plasma) reactor consisting of a graphite cathode rod located at the axis of a tubular graphite anode. Originally proposed as an alternative route for methane conversion to solid magnesium carbide intermediates to overcome transportation limitations associated with remote natural gas, the reaction of methane and magnesium oxide in a thermal plasma presents a new approach to magnesium metal extraction from its oxide. The industrial production of magnesium is of interest because it is the lightest structural metal, weighing a third less than an equivalent volume of aluminum and almost a fifth as much as an equivalent volume of iron. As such, magnesium finds extensive applications in the automotive industry in view of increasingly stricter fuel economy and emissions standards.

A systematic study of the MgO-CH_4-Ar system has been performed at methane flow rates of 10, 20 and 30 l/min, inlet MgO/CH_4 molar ratios of 0.26 to 1.15 and Argon dilution levels of 0, 10 and 15 l/min over an arc power input range of 17 to 47 kW. The objective is to identify ranges of plasma operating conditions that would provide desired product yields, selectivity and CH_4/MgO conversion to Mg_2C_3 and/or MgC_2 and/or Mg, as well as to H_2 and CO. In addition, exploratory experiments with the MgO-C-CH_4-Ar, Mg-CH_4-Ar, CaO-CH_4-Ar and MgO-CaO-CH_4-Ar systems were also performed.

The extents of CH_4 and MgO conversion to Mg_2C_3 and MgC_2 under the thermal plasma conditions investigated are not found to be appreciable. The highest MgO "Mg" molar conversion to Mg_2C_3 achieved is 9%. The reaction of CH_4 with Mg metal in the thermal plasma reactor likewise does not lead to appreciable yields of Mg_2C_3 and MgC_2, although CH_4 is converted to carbon and hydrogen. Rather, the reaction of CH_4 and MgO under the conditions studied results in the formation of elemental magnesium, which is recovered as agglomerated, hexagonal crystalline particles in the 0.1 to 1 μm size range. The molar conversion of the magnesium in MgO to Mg over the range of experimental conditions investigated has a mean of 64% and a standard deviation of 16%, with extents as high as 95% achieved. The mean molar conversion of the hydrogen in CH_4 to H_2 is

91% with a standard deviation of 16%. The yield of Mg can be enhanced by feeding CH_4 in stoichiometric excess, doping the MgO with solid carbon as an additional reducing agent and diluting the system with inert gas which has an effect analogous to reducing the system pressure. The yield of CO can be improved by lowering the CH_4 flow rate to increase plasma residence times. The formation of magnesium has also been found to be feasible even with a mixed feed of CaO and MgO, with the CaO being converted to CaC_2.

Magnesium metal formation in the reactive thermal plasma system is considered to occur according to a general overall process of rapid vaporization and decomposition of the reactants into their constituent atomic species followed by fast quenching to below the metal melting point. The rapid quenching of the plasma effluent in the vapor state gives rise to a high supersaturation, which, in turn, leads to homogeneous nucleation when a critical supersaturation ratio is exceeded. Nucleation then occurs like a burst over a very short period of time. When nucleating species are depleted by diffusion to newly formed particles, the nucleation terminates and the particles continue to grow by physical condensation and particle coagulation. Since nucleation rates increase very sharply with decreasing temperature, the particles produced solidify within a small temperature range. For the MgO-CH_4 system, the reactants can be completely vaporized to the atomic species in the plasma if the residence time were sufficiently long. However, calculations of the time scale needed for complete evaporation of a 100 μm MgO particle indicate that the estimated residence times are not long enough, suggesting that MgO is only partially vaporized. Thus, the formation of magnesium is postulated to occur mainly by the reaction of nascent carbon species with the MgO particles.

Thermodynamic calculations indicate that magnesium vapor and carbon monoxide exist above 2000 K in equilibrium but that Mg is reoxidized by CO back to MgO below 2000 K. Rapid quenching is postulated to freeze the equilibrium in the 2000 to 1800 K range, providing the magnesium vapor with enough driving force to nucleate and condense before consumption by the reverse reaction with CO to form MgO and C becomes dominant. Estimated reaction and condensation rates support the observed magnesium yields and suggest that the backward reaction can be sufficiently slow relative to the nucleation and condensation kinetics of supersaturated magnesium vapor.

The lowest energy consumption achieved in this study is 30.4 kWh/kg Mg. Operation at higher methane flow rates suggests that energy efficiency can be improved at higher throughputs. Compared to the conventional magnesium production methods, this approach offers a potentially chlorine-free, continuous and atmospheric pressure process using low-cost and abundant raw materials, such as natural gas and dolomite, at competitive energy, environmental and capital costs.

Thesis Supervisors: Jack B. Howard
Hoyt C. Hottel Professor of Chemical Engineering

William A. Peters
Associate Director, Energy Laboratory

To Mom and Dad

and

To the Memory of Corazon Manalili
(1940 - 1989)

Acknowledgments

It's been four and a half years since I started this project and almost seven since I first came to MIT. Looking back at all these years is overwhelming, for it has been a roller coaster ride with many ups and downs. But throughout the long journey, many people helped and supported me. First and foremost, I want to thank my advisors, Prof. Jack Howard and Dr. Bill Peters, without whom this thesis would not have been possible. Their ideas and inputs to this work are invaluable and their patience with me remarkable. Despite the difficulties I encountered in the early stages of this work, Jack and Bill kept their confidence in me. One unique experience I will always remember is when I tried to show Jack how to hydrolyze the highly pyrophoric solid products from my reactor under "controlled" conditions. One day in the summer of '95, I had managed to isolate some solids inside a glove box. I set a half-filled pint-size tin can on the bench top in 66-153 and was squirting water into it when a long luminous flame, about 7 feet long, shot out of the can all the way up to the 2nd floor ceiling, leaving us open-mouthed and in awe. That probably got me into an elite group of grad students who can claim to have almost blown up their advisor, literally. I still owe Jack his laundry bill for that 4th of July episode ☺. Jack and Bill showed not only enthusiasm in my work but also understanding of my needs and long term goals. They have been very supportive of me even in my simultaneous pursuit of an MBA, with Bill even writing my letter of recommendation to Sloan (hopefully, it was type-, not hand-written ☺). For that, I am most appreciative. I consider myself fortunate in having advisors who gave me a free hand in pursuing different avenues within (as well as outside) my research and who willingly offered their time and advice when I needed them. It was by letting me figure out things for myself that I gained the most from this learning experience. Even when my thesis took a radical turn from carbide synthesis to metal extraction, Bill and Jack gave me the latitude to explore that which I considered interesting and promising. I realize that it took them years to get funding for the work on natural gas conversion and that they took a chance on me when they gave me the opportunity to work on this project. While I never got to make enough carbides for them (well maybe, I did for Prof. Howard), I sincerely hope that this work on magnesium was worth their while. It has been my privilege to learn from such distinguished scholars as part of my professional and personal development.

One person who deserves special acknowledgment is my buddy, Tony Modestino, the experimental guru. The apparatus that took me three years to design, build and get to working status would have taken a lot longer without Tony's help. He has been a great mentor and an even greater friend. Amidst the fires, the burn-outs and the explosions, Tony was always there to guide and support me. Tony and I share a dream of some day building our first magnesium plant, maybe in the next century.

I want to thank the members of my thesis committee for providing different perspectives and insightful advice on my work: Prof. Klavs Jensen, who had the highest attendance in my committee meetings, Prof. Adel Sarofim, who gave me his AVCO plasma gun to play with but which eventually got vaporized, and Prof. Jeff Tester, who,

as my academic advisor during my first two years, encouraged me to pursue my Ph.D. I am also grateful to Howie Herzog, at the Energy Lab, for helping me make a transition to what turned out to be a fruitful, though experimentally hazardous, research project.

Many more people, both inside and outside the Institute, contributed to the final product. My heartfelt thanks to John Cremin, the Department's former machinist, Manny Cabral at RLE, and Mike Aloisi, Peter Morley and their crew of machinists at LNS for the three years' worth of machining work they did for me. Dr. Tao Sun at Prof. Ying's group and Joe Adario, Mike Frongillo and Tony Garratt-Reed at CMSE performed X-ray diffraction and a lot of microscopy analyses for me. Prof. Sam Allen, Dr. Joe Marr, Dr. Kevin Sparks and Dr. Gokhan Senel helped me with my thermodynamics calculations. Two UROP students who worked with me in the construction phase of this project also deserve special mention: Jason Pride and Mike Chung. Betty Kespyn at Specialty Minerals provided me with the high calcium quicklime for my experiments.

The financial support for this work from DOE/PETC-MIT Contract No. DE-AC22-92PC92111 under our Program Officers, Dr. Arun Bose and George Cinquegrane, is gratefully acknowledged.

Then, there are also my distinguished colleagues at the labs in 66-053 and 66-153 to thank: Bill Grieco, Scott Macadam, Carlo Procaccini, Guido Sacchi, Kentaro Saco, Angelo Kandas, Sergei Serbin, Hiroshi Saito, Jack Brouwer, Jon Allen, Yanping Zhang, Tim Benish, Dave Kronholm, Matt DiPippo, Brian Phenix, Joanna Dinaro, Randy Weinstein, Josh Taylor, Henning Richter, Rich Shandross, Chris Pope and Wei Lu.

I also wish to express my gratitude to all the administrative people for the little things that made a big difference: Kathy Brownell, Emmi Snyder, Craig Abernathy and Greg Sands at Jack's office; Bonnie Caputo, Anne Carbone, Alice Colby, Mary Elliff, Peter Flynn, Barbara Johnson, Caroline Johnston, Rosemary McDonnell and Frank Tilley at the Energy Lab; Carol Phillips, Arline Benford, Linda Mousseau, Steve Wetzel and, of course, Janet Fischer and Elaine Aufiero-Peters at Chem. E.

Over the course of this work, my friends, who have always been behind me, contributed to my education and made life at MIT more bearable. For their friendship, I am thankful: my friends in the Filipino community, especially Leah and David, Dante, Gerald, Joel, Chris, Numer, Marvin, Marcel and Jimmy (thanks for the coveralls that I used in my experiments); my host families, the Batys, the Fotises and the Navatos; and my friends at TCC, Fr. Bernard Campbell, Fr. Jac Campbell, Sr. Mary Karen, Mary Ann, Ri, Bill and Dianne and their daughters, my church buddies, Ashlynn, Tess and Bridget.

Saving the best for last, all this would not have been possible without the unwavering love and support of my family. My parents, Fred and Tita; my brothers, Fred Jr. and Albert; my sisters-in-law, Nong and Loi, and the rest of my family have always stood by me, in good times and in bad. They believed in me and, despite the distance, were always there to lean on, especially when the going got tough. I particularly thank my brother Fred for all his encouragement; his words kept the fire burning. To my Mom and Dad and to Azon, who made me what I am today, I dedicate this work.

Contents

1 Introduction **16**

1.1 Motivation 17
1.1.1 Natural Gas Upgrading 17
1.1.1.1 Methane Conversion to Metal Carbides 18
1.1.1.2 Description of Proposed Methane Upgrading Approach 20
1.1.2 Magnesium Metal Production 21
1.2 Thesis Objectives 22
1.3 Literature Review 23
1.3.1 Alternative Approaches to Methane Upgrading 23
1.3.2 Acetylene and Methylacetylene 25
1.3.3 Alkaline Earth Metals, Metal Oxides and Carbides 28
1.3.4 Chemical Processing in Thermal Plasmas 33
1.3.5 Methane Pyrolysis 36
1.3.6 Carbide Formation 37
1.3.7 Metal Formation with Methane as Reductant 42

2 Experimental Apparatus and Procedure **45**

2.1 Rationale for Selection of Apparatus 45
2.2 Description of Apparatus 47
2.2.1 Thermal Plasma Generator System 49
2.2.1.1 DC Arc Discharge (Plasma) Reactor 49
2.2.1.2 Magnetic Solenoid 52
2.2.1.3 High Frequency Oscillator 55
2.2.1.4 DC Power Supply Unit 56
2.2.1.5 Control Console 59
2.2.2 Powder Feeder 59
2.2.3 Post-Plasma Cooling Chamber and Gas Discharge System 61

2.2.4 Sample Collection System 63
2.2.5 Cooling Water System 67
2.2.6 Data Acquisition and Process Control System 68
2.2.7 Equipment Safety Considerations 69
2.3 Experimental Procedure 71
2.3.1 Preparation of Reactor 71
2.3.2 Reactor Operation 73
2.3.3 Post-Operation Procedures 76
2.4 Analysis of Products 77
2.4.1 Analysis of Solid Product 79
2.4.2 Analysis of Gaseous Product 81
2.4.3 Reactant-to-Product Conversion and Uncertainty of Analysis 81

3 Experimental Results 90

3.1 Reactants 90
3.2 MgO-CH_4-Ar System 99
3.2.1 Reaction Products of MgO-CH_4-Ar System 103
3.2.2 Effect of Arc Power Input 112
3.2.3 Effect of Methane Flow Rate 116
3.2.4 Effect of Inlet MgO:CH_4 Molar Ratio 124
3.2.5 Effect of Argon Dilution 128
3.2.6 Effect of Secondary CH_4 Quench 130
3.2.7 Effect of Quench Distance 131
3.2.8 Product Morphology and Elemental Distribution 133
3.3 MgO-Ar System 143
3.4 MgO-CH_4-C-Ar System 145
3.4.1 Reaction Products of MgO-CH_4-C-Ar System 145
3.4.2 Effect of Carbon Addition 147
3.4.3 Product Morphology and Elemental Distribution 150
3.5 Mg-CH_4-Ar System 154
3.6 CaO-CH_4-Ar System 159
3.7 MgO-CaO-CH_4-Ar System 164
3.8 Operational Characteristics 170

4 Thermodynamic Analysis 174

4.1 Mg-C-H-O-Ar System 176
4.2 Mg-C-H-Ar System 185

4.3 Ca-C-H-O-Ar System 187
4.4 Mg-Ca-C-H-O-Ar System 191
4.5 Accuracy and Sensitivity Analysis of Thermodynamic Calculations 195

5 Mechanistic Interpretation and Practical Implications 199

5.1 Reactant Evaporation and Decomposition 201
5.2 Nucleation and Growth of Magnesium Particles 205
5.3 Backward Reaction of Mg Vapor with CO 210
5.4 Process Economics 217
5.5 Process Design and Development 221

6 Conclusions 225

7 Recommendations 228

A Propagation of Errors Analysis Sample Calculation 230

Bibliography 232

List of Figures

1-1 Schematic View of Electric Arc Discharge (Thermal Plasma) Generator .. 34
1-2 CaO Conversion as a Function of Power Input at Various Methane Flow Rates 38
1-3 Conversion of Carbon in Methane as a Function of CaO Feed Rate..... 39
2-1 Process Engineering Flow Scheme 48
2-2 Schematic Representation of DC Arc Discharge (Plasma) Reactor 51
2-3 Volt-Ampere Curve of DC Power Supply Unit 58
2-4 Schematic Representation of Post-Plasma Cooling Chamber Assembly.... 62
2-5 Schematic Representation of Top Section of Sample Collection Probe 65
2-6 Schematic Representation of Solid Sampler 66
2-7 Control Sequence of Reactor Operation 74
3-1A SEM of MgO Powder, x125(1) 92
3-1B SEM of MgO Powder, x125(2) 92
3-1C SEM of MgO Powder, x500 92
3-1D SEM of MgO Powder, x745 92
3-1E SEM of MgO Powder, x2000 92
3-1F SEM of MgO Powder, x5000 92
3-2 X-Ray Spectrum of MgO Powder 93
3-3A SEM of CaO Powder, x125 94
3-3B SEM of CaO Powder, x505 94
3-3C SEM of CaO Powder, x2000(1) 94
3-3D SEM of CaO Powder, x2000(2) 94
3-4 X-Ray Spectrum of CaO Powder 95
3-5A SEM of Graphite Powder, x125(1) 96
3-5B SEM of Graphite Powder, x125(2) 96
3-5C SEM of Graphite Powder, x500 96
3-5D SEM of Graphite Powder, x2000 96
3-6 X-Ray Spectrum of Graphite Powder 97
3-7A SEM of Mg Powder, x125 98
3-7B SEM of Mg Powder, x250 98
3-7C SEM of Mg Powder, x1000 98
3-7D SEM of Mg Powder, x2500 98

3-8 X-Ray Spectrum of Mg Powder 99
3-9 Log K_p Values for Metal and Metal Carbide Formation and Metal Carbide Decomposition 103
3-10 X-Ray Diffraction Pattern of Run M27 Sample from Chamber Bottom..... 105
3-11 MgO "Mg" Conversion to Mg vs. Power Input at Various CH_4 Flow Rates..... 113
3-12 MgO "Mg" Conversion to Mg_2C_3 vs. Power Input at Various CH_4 Flow Rates 113
3-13 CH_4 "H" Conversion to H_2 vs. Power Input at Various CH_4 Flow Rates 115
3-14 CH_4 "C" Conversion to CO vs. Power Input at Various CH_4 Flow Rates and Inlet MgO:CH_4 Ratios 115
3-15 MgO "Mg" Conversion to Mg vs. Specific Gas Energy 118
3-16 CH_4 "H" Conversion to H_2 vs. Specific Gas Energy 118
3-17 CH_4 "C" Conversion to CO vs. Specific Gas Energy at Various CH_4 Flow Rates and Inlet MgO:CH_4 Ratios 120
3-18 H_2/CO Ratio vs. Specific Gas Energy at Various Methane Flow Rates and Inlet MgO:CH_4 Ratios..... 121
3-19 CH_4 "C" Conversion to Non-Carbide C vs. Specific Gas Energy 123
3-20 CH_4 "C" Conversion vs. Inlet MgO:CH_4 Molar Ratio 128
3-21A Stem Images and Elemental Mapping of Run M27 Sample 136
3-21B SEM of Run M27 Sample, x3,500 137
3-21C SEM of Run M27 Sample, x35,000 137
3-21D SEM of Run M27 Sample, x100,000 137
3-22A Stem Images and Elemental Mapping of Sample from Run M33 138
3-22B SEM of Run M33 Sample, x10,000 139
3-22C SEM of Run M33 Sample, x35,000 139
3-22D SEM of Run M33 Sample, x100,000 139
3-23A Stem Images and Elemental Mapping of Sample from Run M7 140
3-23B SEM of Run M7 Sample, x3,500 141
3-23C SEM of Run M7 Sample, x35,000 141
3-23D SEM of Run M7 Sample, x100,000 141
3-24A TEM of Run M13 Sample, x120,000..... 142
3-24B TEM of Run M13 Sample, x590,000..... 142
3-25 SEM of Run LM Sample, x320 144
3-26 SEM of Run LMM Sample, x750 144
3-27 SEM of Run HM Sample, x320 144
3-28 SEM of Run HMM Sample, x320 144
3-29 MgO "Mg" Conversion to Mg vs. Power Input at 10 l/min CH_4 and 1.15:1 MgO:CH_4 with and without Carbon Addition 148
3-30 CH_4 "H" Conversion to H_2 vs. Power Input at 10 l/min CH_4 and 1.15:1 MgO:CH_4 with and without Carbon Addition 149
3-31 (CH_4 + Graphite) "C" Conversion to CO vs. Power Input at 10 l/min CH_4 and 1.15:1 MgO:CH_4 with and without Carbon Addition 150
3-32A Stem Images and Elemental Mapping of Sample from Run MC5 152
3-32B SEM of Run MC5 Sample, x3,500 153

3-32C SEM of Run MC5 Sample, x35,000 153
3-32D SEM of Run MC5 Sample, x100,000 153
3-33A Stem Images and Elemental Mapping of Sample from Run MG1 157
3-33B SEM of Run MG1 Sample, x3,500 158
3-33C SEM of Run MG1 Sample, x35,000 158
3-33D SEM of Run MG1 Sample, x100,000 158
3-34A Stem Images and Elemental Mapping of Sample from Run C3 162
3-34B SEM of Run C3 Sample, x3,500 163
3-34C SEM of Run C3 Sample, x35,000 163
3-34D SEM of Run C3 Sample, x100,000 163
3-35A Stem Images and Elemental Mapping of Sample from Run CM1 168
3-35B SEM of Run CM1 Sample, x3,500 169
3-35C SEM of Run CM1 Sample, x35,000 169
3-35D SEM of Run CM1 Sample, x100,000 169
3-36 Voltage-Current Curves of CH_4 Arc with MgO Feeding 170
4-1 Maximum Reaction Temperature as a Function of Specific Gas Energy ... 176
4-2 Thermodynamic Equilibrium Diagram for 1.15 MgO + 1 CH_4 + 0.42 Ar ... 177
4-3 Thermodynamic Equilibrium Diagram for 1.15 MgO + 1 CH_4 + 1.92 Ar ... 180
4-4 Thermodynamic Equilibrium Diagram for 1.15 MgO + 1 CH_4 (0.34 Atm).. 180
4-5 Thermodynamic Equilibrium Diagram for 1.15 MgO + 1 CH_4 + 0.42 Ar + 2 H_2 182
4-6 Thermodynamic Equilibrium Diagram for 0.46 MgO + 1 CH_4 + 0.42 Ar ... 184
4-7 Thermodynamic Equilibrium Diagram for 1.15 MgO + 1 CH_4 + 0.4 C + 0.42 Ar 185
4-8 Thermodynamic Equilibrium Diagram for 0.7 Mg + 1 CH_4 + 0.42 Ar 186
4-9 Thermodynamic Equilibrium Diagram for 0.34 CaO + 1 CH_4 + 0.42 Ar 188
4-10 Thermodynamic Equilibrium Diagram for 0.34 CaO + 1 CH_4 + 0.42 Ar with Solid Carbon Formation Suppressed 190
4-11 Thermodynamic Equilibrium Diagram for 0.2 MgO + 0.2 CaO + 1 CH_4 + 0.42 Ar 192
4-12 Thermodynamic Equilibrium Diagram for 0.2 MgO + 0.2 CaO + 1 CH_4 + 0.42 Ar with Solid Carbon Formation Suppressed..... 194
4-13 Thermodynamic Equilibrium Diagram for 2 $CH_4 \rightarrow C_2H_2 + 3\ H_2$ 195
4-14 Thermodynamic Equilibrium Diagram for 2 $CH_4 \rightarrow C_2H_2 + 3\ H_2$ with Solid Carbon Formation Suppressed 196
4-15 Thermodynamic Equilibrium Diagram for 0.46 MgO + 1 CH_4 + 0.42 Ar with $\Delta H_{f,MgO}(298.15K) = 0.9\ \Delta H^{o}_{f,MgO}(298.15K)$ 197
4-16 Thermodynamic Equilibrium Diagram for 0.46 MgO + 1 CH_4 + 0.42 Ar with $\Delta H_{f,MgO}(298.15K) = 1.1\ \Delta H^{o}_{f,MgO}(298.15K)$ 198
5-1 Proposed Overall Mechanism for Mg Formation..... 200
5-2 ΔH, ΔG and $T\Delta S$ as a Function of Temperature for $CH_4 + MgO \rightarrow Mg + 2H_2 + CO$..... 218
5-3 Theoretical Energy Requirement, ΔH, as a Function of Temperature for Different Magnesium Production Processes 219

List of Tables

1-1 Estimated Process Thermal Efficiency of Methane Conversion in a Thermal Plasma 21
2-1 Typical Properties of Grade ECR Graphite 49
2-2 Specifications of 1500 Ampere C7 Model DC Power Supply Unit 56
2-3 Distribution of Cooling Water Flow 68
2-4 Composition of Standard Mixtures 78
2-5 Uncertainty of Analysis 89
3-1 Properties of MgO Powder 91
3-2 Typical Properties of High Calcium Metallurgical Grade Quicklime 93
3-3 Spectrographic Analysis of Mg Powder 97
3-4 Summary of Reactor Conditions for MgO-CH_4-Ar System 100
3-5 Percent Methane Molar Conversion to Products in MgO-CH_4-Ar System .. 106
3-6 Percent Magnesium Oxide Molar Conversion to Products in MgO-CH_4-Ar System 109
3-7 Summary Statistics of Reactant Conversion to Products for All Runs in MgO-CH_4-Ar System 114
3-8 Summary Statistics of Reactant Conversion to Mg and to H_2 at Different Methane Flow Rates 117
3-9 Summary Statistics of CH_4 "C" Conversion to CO at Different Methane Flow Rates and Inlet MgO:CH_4 Ratios 119
3-10 Summary Statistics of H_2/CO Ratio in Gas Product at Different Methane Flow Rates and Inlet MgO:CH_4 Ratios 122
3-11 Summary Statistics of CH_4 "C" Conversion to Non-Carbide Carbon at Different Methane Flow Rates and Inlet MgO:CH_4 Ratios 123
3-12 Summary Statistics of Reactant Conversion to Products at Different Inlet MgO:CH_4 Ratios and at 20 l/min CH_4 Flow 124
3-13 Summary Statistics of Reactant Conversion to Products at Different Inlet MgO:CH_4 Ratios and at 10 l/min CH_4 Flow 125
3-14 Summary Statistics of Reactant Conversion to Products at 15, 10 and 0 l/min Argon Dilution 129
3-15 Summary Statistics of MgO "Mg" Conversion to Mg_2C_3 and MgC_2 at 14, 10 and 5 in. Quench Distance 132
3-16 Summary of Reactor Conditions for MgO-Ar System 143

3-17 Summary of Reactor Conditions for MgO-CH_4-C-Ar System 145
3-18 Percent Methane and Graphite Molar Conversion to Products in MgO-CH_4-C-Ar System 146
3-19 Percent Magnesium Oxide Molar Conversion to Products in MgO-CH_4-C-Ar System 147
3-20 Summary Statistics of Reactant Conversion to Products and H_2/CO Ratio with and without Carbon Addition 147
3-21 Summary of Reactor Conditions for Mg-CH_4-Ar System..... 154
3-22 Percent Methane Molar Conversion to Products in Mg-CH_4-Ar System.... 155
3-23 Percent Magnesium Molar Conversion to Products in Mg-CH_4-Ar System 155
3-24 Summary Statistics of Reactant Conversion to Products for Mg-CH_4-Ar System 156
3-25 Summary of Reactor Conditions for CaO-CH_4-Ar System..... 159
3-26 Percent Methane Molar Conversion to Products in CaO-CH_4-Ar System... 160
3-27 Percent Calcium Oxide Molar Conversion to Products in CaO-CH_4-Ar System 160
3-28 Summary Statistics of Reactant Conversion to Products and H_2/CO Ratio for CaO-CH_4-Ar System..... 161
3-29 Summary of Reactor Conditions for MgO-CaO-CH_4-Ar System..... 164
3-30 Percent Methane Molar Conversion to Products in MgO-CaO-CH_4-Ar System 165
3-31 Percent Magnesium Oxide and Calcium Oxide Molar Conversion to Products in MgO-CaO-CH_4-C-Ar System 165
3-32 Summary Statistics of Reactant Conversion to Products and H_2/CO Ratio for MgO-CaO-CH_4-Ar System..... 166
5-1 Comparison of Theoretical and Actual Energy Requirement for Magnesium Production by Various Processes 220

Chapter 1

Introduction

The original overall objective of the present thesis is to develop new scientific and engineering knowledge bases for assessing the technical feasibility of converting methane to alkaline earth metal carbides using calcium oxide and magnesium oxide in a thermal plasma reactor according to the global reactions:

$$3\,CH_4 + CaO \rightarrow CaC_2 + 6\,H_2 + CO \qquad \Delta H_{298\,K} = 689.8\ kJ \quad \text{Reaction (1-1)}$$

$$5\,CH_4 + 2\,MgO \rightarrow Mg_2C_3 + 10\,H_2 + 2\,CO \qquad \Delta H_{298\,K} = 1435.3\ kJ \quad \text{Reaction (1-2)}$$

$$3\,CH_4 + MgO \rightarrow MgC_2 + 6\,H_2 + CO \qquad \Delta H_{298\,K} = 803.2\ kJ \quad \text{Reaction (1-3)}$$

If technically and economically viable, the above chemistry could be the basis for an alternative process technology for the commercial conversion of natural gas to premium liquid hydrocarbon fuels and chemicals via metal carbide intermediates.

Over the course of this research project, the investigation of CH_4/MgO reactions in a thermal plasma led, unexpectedly, to the observations of high yields of elemental magnesium, rather than of magnesium carbides (Mg_2C_3 and MgC_2). Such observations suggest an alternative method for the manufacture of magnesium metal by direct reduction of MgO with methane according to the global reaction:

$$CH_4 + MgO \rightarrow Mg + 2\,H_2 + CO \qquad \Delta H_{298\,K} = 565.6\ kJ \quad \text{Reaction (1-4)}$$

The production of magnesium metal is of interest because magnesium is the lightest structural metal (Cameron *et al.*, 1987), weighing a third less than an equivalent volume of aluminum and almost a fifth as much as an equivalent volume of iron. As such, magnesium finds extensive applications in the automotive industry, particularly at a time of increasingly stricter fuel economy and emissions standards.

The discovery of this potential approach to magnesium metal production, though fortuitous, has therefore led to a shift in the primary focus of this research to the study of the formation of magnesium metal by the reduction of magnesium oxide with methane.

1.1 Motivation

The motivation for the present thesis is twofold. Originally undertaken to investigate an alternative approach to methane upgrading which could overcome transportation limitations associated with abundant but remote natural gas, this study has also uncovered a novel and potentially continuous process for the manufacture of magnesium metal.

1.1.1 Natural Gas Upgrading

Diversification of the raw materials base for manufacturing premium fuels and chemicals offers U.S. and international consumers economic and strategic benefits (Longwell, 1993). Extensive reserves of natural gas in the world provide a valuable source of clean gaseous fuel and chemical feedstock. Assuming the availability of suitable conversion processes, natural gas offers the prospect of improving flexibility in liquid fuels and chemicals manufacture, and thus, the opportunity to complement, supplement, or displace petroleum-based production as economic and strategic considerations require. Many attractive deposits of natural gas are remotely located from key market sites. In order to utilize this remote resource commercially, natural gas must be transported to the market from the production site either via extensive pipeline distribution networks under pressure or in specially designed ocean-going tankers as liquefied natural gas at low temperatures. Due to the state in which it exists at normal conditions, natural gas has a low energy content per unit volume compared to petroleum or coal. This relatively low energy

density entails high transportation costs which exclude significant quantities of the resource from large-scale commercial utilization. Thus, there is considerable interest in developing new approaches to the volumetric energy densification of natural gas to enhance its marketability.

The composition of natural gas varies widely from reservoir to reservoir but the principal hydrocarbon constituent is always methane (CH_4). With its high hydrogen-to-carbon ratio, methane has the potential to produce hydrogen or hydrogen-rich products. However, methane is a very chemically stable molecule and thus, is not readily transformed to other molecules or easily reformed to its elements (hydrogen and carbon). With the interest in upgrading natural gas to value-added products, several technologies for methane conversion to liquid fuel and chemical precursors currently exist at various stages of scientific and technological development. In many cases, further research is needed to augment selectivity to desired product(s), increase single-pass conversions, or improve economics before the full potential of these methodologies can be realized on a commercial scale. With the trade-off between gas conversion and product selectivity, a major challenge common to many of these technologies is to simultaneously achieve high methane single-pass conversions and high product selectivity.

1.1.1.1 Methane Conversion to Metal Carbides

Prior work at MIT (Kim, 1977; Kim *et al.*, 1979) has demonstrated that, by reacting methane with calcium oxide (CaO) in a laboratory-scale rotating direct current (DC) arc discharge reactor, high (>95%) methane single-pass conversions to molecular hydrogen (H_2) and calcium carbide (CaC_2) can be obtained, according to Reaction (1-1).

Hydrogen can be used as a fuel in thermal processes and in fuel cells to generate electricity at efficiencies which may approach 60%. It finds wide applications in petroleum refining and coal liquefaction where it is used to improve fuel quality, e.g. by increasing hydrogen-to-carbon ratio and lowering the fuel content of pollutant precursors such as sulfur, nitrogen and heavy metals. Mixed with carbon monoxide (CO), hydrogen forms synthesis gas which is also valuable as a fuel and which, by various catalytic processes, can be upgraded to a wide range of petroleum-like fuels, methanol, waxes, and

other premium products. Calcium carbide, which exists as a solid at dry ambient conditions, is a particularly attractive product with significant commercial benefits in the present context: (a) being a solid, it can be separated from the gaseous products of Reaction (1-1) relatively easily; (b) it has an equivalent heating value (based on acetylene - see Reaction (1-5)) of about 20,200 kJ/kg (8700 BTU/lb) and thus, like low-rank coal, can be stored and transported over long distances at reasonable cost; and (c) by well-established hydrolysis processes, it can be converted to acetylene (C_2H_2) by the reaction:

$$CaC_2 + 2\ H_2O \rightarrow Ca(OH)_2 + C_2H_2 \qquad \text{Reaction (1-5)}$$

Acetylene is a reactive raw material that can be converted to a diverse array of organic chemicals and to high-grade liquid fuels.

In the light of the success of the previous work by Kim (1977) *et al.* (1979), there is incentive to investigate comparable reactions of methane with other alkaline earth metal oxides. In particular, an analogous reaction with magnesium oxide (MgO) to produce hydrogen, carbon monoxide and magnesium sesquicarbide (Mg_2C_3) and/or magnesium dicarbide (MgC_2) is of interest. Thermodynamic calculations imply that the sesquicarbide is strongly favored over the dicarbide above 1700 K. Noteworthy is the fact that magnesium is the only alkaline earth metal that forms a sesquicarbide, which, upon hydrolysis, yields methylacetylene (C_3H_4), providing a route for C_1-to-C_3 conversion. Furthermore, methylacetylene offers a potential route to benzene by condensation/dehydrocyclization. Concepts for synthesizing magnesium sesquicarbide from magnesium oxide and methane, with further upgrading of the sesquicarbide to C_3 hydrocarbons by hydrolysis, are described by Peters and Howard (1990; 1993). The earlier experimental work by Kim (1977) *et al.* (1979), together with preliminary cost estimates (Peters and Howard, 1989), indicate that the metal carbide route offers sufficient potential for good thermal efficiency and for favorable economics to warrant further systematic study for methane upgrading.

1.1.1.2 Description of Proposed Methane Upgrading Approach

In the proposed approach, methane would be reacted, essentially stoichiometrically (rather than catalytically), with relatively low-cost and recyclable alkaline earth metal oxides such as calcium oxide (quicklime), magnesium oxide (magnesia) or mixtures of the two (calcined dolomite) to achieve very high (approaching 100%) conversion to hydrogen, carbon monoxide and the corresponding alkaline earth metal carbide, according to Reactions (1-1) and (1-2):

$$3\,CH_4 + CaO \rightarrow CaC_2 + 6\,H_2 + CO \qquad \Delta H_{298\,K} = 689.8\ \text{kJ} \quad \text{Reaction (1-1)}$$

$$5\,CH_4 + 2\,MgO \rightarrow Mg_2C_3 + 10\,H_2 + 2\,CO \qquad \Delta H_{298\,K} = 1435.3\ \text{kJ} \quad \text{Reaction (1-2)}$$

In order to carry out these reactions, the extreme chemical stability of methane would be overcome under high severity conditions, i.e. high temperature (>2000 K), in an electrical arc discharge (thermal plasma) reactor or in a purely thermal (i.e. non-plasma) reactor.

The carbides thus produced are solids at dry ambient conditions which can be more readily separated, stored and transported. Their value as fuel precursors and chemical intermediates is further enhanced when, upon reaction with water, they yield the valuable hydrocarbon gases acetylene and methylacetylene:

$$CaC_2 + 2\,H_2O \rightarrow Ca(OH)_2 + C_2H_2 \qquad \Delta H_{298\,K} = -128.3\ \text{kJ} \quad \text{Reaction (1-5)}$$

$$Mg_2C_3 + 4\,H_2O \rightarrow 2\,Mg(OH)_2 + C_3H_4 \qquad \Delta H_{298\,K} = -599.2\ \text{kJ} \quad \text{Reaction (1-6)}$$

Reactions (1-5) and (1-6) are expected to produce acetylene and methylacetylene in high purity. Thus, the carbide approach may exhibit simpler and lower cost separation and purification steps than those needed in alternative processes for acetylene manufacture. Acetylenes can be upgraded to a wide range of chemicals or to premium-value liquid hydrocarbon fuels.

CaO and MgO for re-use in Reactions (1-1) and (1-2) can be regenerated from $Ca(OH)_2$ and $Mg(OH)_2$ according to:

$Ca(OH)_2 \rightarrow CaO + H_2O$ $\Delta H_{298\,K} = 65.2$ kJ Reaction (1-7)

$Mg(OH)_2 \rightarrow MgO + H_2O$ $\Delta H_{298\,K} = 37.6$ kJ Reaction (1-8)

and subsequently recycled back to the process.

A conceptual process wherein Reaction (1-1) [or (1-2)] is carried out under thermal plasma conditions followed by low temperature Reaction (1-5) [or (1-6)] to produce CO, H_2 and C_2H_2 (or C_3H_4) is estimated to have a reasonably high thermal efficiency. In the ideal case of perfect heat integration where the plasma provides only the endothermicity of Reaction (1-1) or (1-2) and where CH_4 is used to generate electricity for driving the plasma reactor at 33% efficiency, Table 1-1 shows that the process thermal efficiencies are comparable to the 60% thermal efficiency of hydrogen manufacture by steam reforming of methane (Gary and Handwerk, 1984).

Table 1-1. Estimated Process Thermal Efficiency of Methane Conversion in a Thermal Plasma[a]

Product LHV as a Percentage of Total Input CH_4, i.e. CH_4 Converted to Products or Used to Produce Electricity to Run Plasma[b]

Reaction[c]	H_2	CO	C_2H_2	C_3H_4	Total
(1-1) and (1-5)	32	6	28		66
(1-2) and (1-6)	29	7		22	58

[a] Assumes perfect heat integration so the plasma supplies only the endothermicity of Reaction (1-1) or (1-2).
[b] Methane is assumed to be converted to electricity at 33% efficiency.
[c] All chemical reactions are assumed to proceed to 100% completion.

1.1.2 Magnesium Metal Production

The worldwide consumption of magnesium is expected to increase from 315,000 tons in 1994 to 495,000 tons in 2005 (Ridgeway, 1995). This growth will be largely driven by the penetration of magnesium in automotive manufacture to reduce total vehicle weight. Its light weight, high strength-to-weight ratio and good machinability account for magnesium's extensive usage in alloying with other metals, mainly aluminum, in structural, die-cast applications. Ridgeway (1995) projects that magnesium usage per

Japanese car will grow from 5 kg in 1995 to 40 kg in 2000. The three largest applications of magnesium metal are aluminum alloying, lightweight die-castings and desulfurization of iron and steel.

Although an energy-saving structural material, magnesium is also an energy intensive product. The major conventional technologies for magnesium production are the electrolysis of molten magnesium chloride ($MgCl_2$) to magnesium metal and chlorine gas (Cl_2) and the thermal reduction of magnesium oxide with ferrosilicon (metallothermic reduction). Thermal reduction with carbon (carbothermic reduction) has been demonstrated but is not currently in commercial usage. The electrolytic method suffers from high costs of cell feed preparation and low metal production rate. The metallothermic reduction method requires expensive reductants and has drawbacks from operation at reduced pressure and in batch mode. The energy inefficiency of rapid quenching to inhibit loss of Mg from reoxidation with CO and the formation and recovery of finely divided pyrophoric Mg dust are among the technical difficulties associated with the carbothermic process. Compared to the conventional processes, a technology based on Reaction (1-4) potentially offers a chlorine-free, continuous and atmospheric pressure process for Mg production from low-cost and abundant raw materials such as natural gas and dolomite.

1.2 Thesis Objectives

The specific objectives of this thesis are:

1. To determine the technical feasibility of converting CH_4 and MgO to Mg, H_2 and CO in a thermal plasma, according to Reaction (1-4);
2. To determine the technical viability of converting CH_4 and MgO to Mg_2C_3, H_2 and CO in a thermal plasma, according to Reaction (1-2);
3. To define preferred ranges of plasma operating conditions that provide desired yields, selectivities and CH_4/metal oxide conversion to CaC_2 and/or Mg_2C_3 and/or MgC_2 and/or Mg, as well as to H_2 and CO according to Reactions (1-1), (1-2), (1-3) and (1-4);

4. To develop a better understanding of the underlying chemical and physical mechanisms by which this approach gives desired reactant conversion, product selectivity and kinetics behavior.

1.3 Literature Review

This section provides a brief review of pertinent literature on alternative approaches to methane upgrading; properties of acetylene, methylacetylene, and calcium and magnesium metals, oxides and carbides; chemical processing in thermal plasmas; methane pyrolysis; carbide formation; and metal formation with methane as reductant.

1.3.1 Alternative Approaches to Methane Upgrading

Considerable efforts and resources have been placed on research, development and even commercialization of various approaches to methane upgrading by the U.S. Department of Energy (Malone and Komar, 1989; Malone *et al.*, 1990), academia (Driscoll *et al.*, 1985; Gesser *et al.*, 1985; Yarlagadda *et al.*, 1987) and industry (Huff and Eastman, 1991; Fox, Chen *et al.*, 1988; Fox, Geosits *et al.*, 1988). Guthrie *et al.* (1995), Malone *et al.* (1990), and Malone and Komar (1989) at the U.S. DOE/Morgantown Energy Technology Center, Fox *et al.* (1988) at Bechtel, and Kuo and Ketkar (1987) at Mobil R&D give development status reviews as well as process and economic evaluations of the many technologies currently under investigation.

Methodologies for methane conversion can be broadly classified into two categories: direct and indirect. Indirect conversion methods require methane conversion to CO and H_2, or synthesis gas, followed by catalytic conversion of the synthesis gas to methanol or Fischer-Tropsch hydrocarbon liquids. Synthesis gas formation is commercially practiced by steam reforming and, to a lesser extent, by non-catalytic partial oxidation. The energy- and capital-intensive nature of steam reforming has stimulated research to devise a more direct pathway for methane conversion without the costly methane-reforming step to synthesis gas. Among the direct methods, research efforts have focused on: (1) Partial Oxidation, with or without a catalyst, to methanol and

formaldehyde; (2) Oxidative Coupling to light olefins by alkali metal-promoted alkaline earth metal oxide catalyst (MgO, CaO); (3) Oxyhydrochlorination to chloromethanes; (4) Electric Arc Discharge/Plasma Processing to acetylene; (5) Thermal Pyrolysis to acetylene; (6) Alkylation with unsaturated hydrocarbons, e.g. toluene, to produce styrene monomer; (7) Activation using metals, metal oxides or metal complexes; (8) Hydrogen Sulfide-Methane reaction to carbon disulfide (Erekson and Miao, 1995) and (9) Biomimetic approaches that seek to mimic the catalytic structures in methanotropic bacteria or that directly utilize biological systems for partial oxidation of hydrocarbons.

Currently, partial oxidation, oxidative coupling and oxyhydrochlorination are considered to be the most advanced direct conversion technologies. Under partial oxidation, methane is oxidized with oxygen, nitrous oxide or halogens to produce methanol and formaldehyde, which are then converted to gasoline and by-product water over zeolite catalyst. With oxidative coupling, alkali metal oxide-activated methane undergoes oxidative dehydrogenation to form methyl radicals and hydroxide ions. The radicals combine to form ethylene which is oligomerized to gasoline over ZSM-5 catalyst. Oxyhydrochlorination entails methane reaction with oxygen and hydrogen chloride to form chlorinated hydrocarbons, e.g. chloromethane, which can be made to undergo oligomerization to gasoline and HCl.

Despite the wide range of possible approaches, direct methane upgrading technology has yet to be demonstrated on full commercial scale. Economic evaluations (Fox, Chen *et al.*, 1988) suggest that premium-value fuels from the most promising direct approaches still entail high production costs ($40-$70/bbl of liquid in 1988 U.S.$). These high costs can be attributed to the fundamental trade-off between conversion and selectivity. Most of the methodologies exhibit poor single-pass conversions or poor selectivity to the desired product. Methane is considerably less reactive than the resulting products, making simultaneous achievement of high gas conversion and high product selectivity extremely difficult.

1.3.2 Acetylene and Methylacetylene

***Acetylene (Ethyne)*:** Berthelot was the first to study acetylene extensively and to realize that it was the first member of the alkyne series (Miller, 1965). As early as 1863, he was forming acetylene by passing methane through an electric arc (Spitz, 1988). In 1892, Moissan, a French researcher, obtained acetylene by the hydrolysis of calcium carbide, produced from lime and coal in an electric furnace. The discovery of the carbide process for acetylene production led to the birth of the acetylene industry. Early uses of acetylene were as an illuminant and later, for oxygen welding and metal cutting. However, it soon became evident that acetylene is valuable not only as a fuel but as an ideal chemical feedstock for a wide variety of products including solvents, plastics, synthetic rubber, dyes and pharmaceuticals, among others.

Due to its triple bond and its high positive free energy of formation, acetylene is highly reactive. The important acetylene reactions are hydrogen replacements, additions to the triple bond, additions by acetylene to other unsaturated systems, polymerization and cyclization. For example, the formation of a metal acetylide is a hydrogen replacement reaction while hydrogenation, halogenation, hydrohalogenation, hydration and vinylation are addition reactions. Thus, acetylene is a key precursor to a diverse array of industrially important chemicals such as vinyl chloride, acetaldehyde, acrylonitrile, vinyl acetate, tetrahydrofuran and chloroprene (Miller, 1965; Detz *et al.*, 1980; Tedeschi, 1982). However, over the last three decades, the acetylene industry suffered a decline despite growth in acetylene-derived chemicals. Acetylene has been displaced by olefin-based chemistries in chemical manufacturing processes which use more economically competitive raw materials. For example, besides the utilization of ethylene as feedstock for the manufacture of vinyl chloride and vinyl acetate (which are used as monomers in the preparation of a wide variety of polymeric materials), acetylene has also been replaced by propylene as preferred feedstock for acrylonitrile manufacture and by butadiene for chloroprene manufacture.

Acetylene is commercially derived from two principal sources: calcium carbide and hydrocarbons. The industry started and grew with carbide acetylene but the relative

economics of acetylene for chemical usage has now shifted in favor of hydrocarbon-based, or petrochemical, acetylene. The processes for the production of petrochemical acetylene can be broadly classified into: (1) Electric Arc (Hüls, Germany; Du Pont; AVCO); (2) Regenerative Pyrolysis (Union Carbide, Wulff); and (3) Partial Combustion (BASF, Dow, Monsanto, SBA, M.W. Kellogg, Montecatini). The common principle characterizing these methodologies is the use of an intense energy source that heats a hydrocarbon feedstock above 1500 K within short residence times of 0.01-0.001 s, followed by the rapid (in the order of a few milliseconds) cooling of the acetylene product to prevent decomposition into its elements (Tedeschi, 1982).

By providing energy at a very high flux density, electrical discharge processes have the advantage of keeping reaction time to a minimum. Furthermore, they give a higher acetylene yield than regenerative or partial combustion processes (Duncan, 1980; Tedeschi, 1982). The primary role of the electrical energy is to raise the temperature of the reactants to the reaction temperature and to supply the endothermic heat of reaction. In several modifications to the process, preheating of the feedstock with cheaper fuel energy provides the enthalpy of the reacting gas stream, thus reducing the electrical energy requirements. Miller (1965) calculates a theoretical energy requirement of 6.45 kWh to produce a kilogram of acetylene from methane according to:

$$2\,CH_4 \rightleftarrows C_2H_2 + 3\,H_2 \qquad \text{Reaction (1-9)}$$

at a reaction temperature of 1743 K. However, in addition to this, the enthalpy of unreacted feedstock, energy requirements of side-reactions, heat losses and energy for separating acetylene from the gas product entail a much higher total energy requirement.

Arc processes in general consume more electrical energy (average of about 11 kWh/kg of acetylene (Tedeschi, 1982)) than the 9.5-10.5 kWh/kg needed for carbide-derived acetylene (Miller, 1965). As an example, the Hüls Arc Process had a total power consumption of 13.2 kWh/kg of acetylene, inclusive of 2.9 kWh/kg required for separation processes from the cracked gas. The acetylene concentration in the cracked gas was 14.5 vol %. Total natural gas (92.3% CH_4) conversion was about 78 wt % with

an acetylene yield of about 36 wt % (Miller, 1965). For comparison, in the AVCO Arc-Coal Process based on the gasification of coal in a hydrogen plasma, Gannon and Krukonis (1972) and Krukonis *et al.* (1974) reported an energy requirement as low as 9.5 kWh/kg of acetylene at an acetylene yield of up to 35 wt %. Acetylene concentration in the gas product was 15.7 vol %.

The formation of acetylene from carbon and hydrogen is highly endothermic. With a high positive free energy of formation, the acetylene molecule is thermodynamically unstable with respect to its constituent elements. Acetylene can polymerize exothermically and explode even in the absence of oxygen when compressed above 2 atm, making transport of compressed acetylene very dangerous. However, the use of a solvent such as acetone and a porous mass inhibits explosive decomposition. Thus, acetylene can be transported as a solution in acetone under pressure in a cylinder completely filled with porous mass (Miller, 1965).

Acetylene is unlike other hydrocarbons in having a decreasing free energy of formation with increasing temperature. In contrast, lower paraffinic hydrocarbons, which are thermodynamically stable below 500 K, become progressively unstable upon heating. Acetylene thus becomes more stable than most hydrocarbons including methane above 1500 K (Clarke, 1967), although it is nonetheless still unstable relative to its elements. Under thermodynamic equilibrium conditions, it will not exist appreciably until the temperature is above 2500 K. Therefore, formation of acetylene from hydrocarbon pyrolysis entails rapid heating to cracking temperatures, followed by immediate cooling or quenching to avoid reaching the true thermodynamic equilibrium of C and H_2. Furthermore, acetylene decomposition can be reduced by lowering its partial pressure, which can be achieved by operating at reduced total pressures and/or by adding a diluent (Miller, 1965).

***Methylacetylene (Propyne)*:** Methylacetylene also has a positive free energy of formation and is thus unstable with respect to its elements. Its value lies not only in its high volumetric heating value as a fuel but also in its reactivity as a chemical feedstock. Calculations indicate that dimerization of methylacetylene to form benzene and molecular hydrogen:

$$2\,C_3H_4 \rightarrow C_6H_6 + H_2 \qquad \text{Reaction (1-10)}$$

is strongly favored thermodynamically at temperatures of practical interest. $Log_{10}\ K_p$ values range from over 30 at 373 K to about 10 at 973 K. Thus, the metal carbide approach effectively offers a convenient pathway for C_1-to-C_6 chemistry. Benzene, though presenting environmental concerns, is widely used as starting material for the synthesis of other industrial chemicals such as styrene.

1.3.3 Alkaline Earth Metals, Metal Oxides and Carbides

***Calcium*:** Calcium, atomic number 20, atomic mass 40.08, is a Group IIA metal between magnesium and strontium. In pure form, it is a bright silvery white metal which is extremely soft and ductile with melting and boiling points of 1115 ± 2 K and 1773.658 K, respectively (Chase *et al.* (JANAF Tables), 1985). The calcium crystal structure is face-centered cubic at room temperature but transforms to a body-centered cubic at 716 ± 2 K (Chase *et al.*, 1985). Being an excellent reducing agent, calcium quickly becomes covered with an oxide coating under normal atmospheric conditions. Thus, it does not occur freely in nature but is abundant in oxide form.

Magnesium: Magnesium, atomic number 12, atomic mass 24.305, is a Group IIA element between beryllium and calcium. Magnesium is a silvery white metal with a melting point of 923 K (Chase *et al.*, 1985) and a boiling point of 1383 K (Perry, 1984). Its crystal structure is closed-packed hexagonal, with unit cell parameters: a_o=3.20936 Å and c_o=5.2112 Å (NBS, 1984). It is the lightest structural metal, with a specific gravity of 1.74. Its alloys with one or more elements including aluminum, manganese, rare earth metals, lithium, silver, thorium, zinc and zirconium have the highest strength-to-weight ratios of the ultralight metals at elevated temperatures (Lockwood *et al.*, 1981).

The high position of magnesium in the electromotive series indicates its strong chemical activity. However, because of its affinity for oxygen, the formation of a protective oxide layer makes magnesium fairly resistant to atmospheric attack. Finely divided magnesium powder is relatively easy to ignite, resulting in a bright, strongly

actinic light. Magnesium reacts with water to produce hydrogen but the reaction is retarded by the formation of an insoluble hydroxide film:

$$Mg + 2\,H_2O \rightarrow Mg(OH)_2 + H_2 \qquad \text{Reaction (1-11)}$$

It also reacts with hydrochloric acid to form hydrogen according to:

$$Mg + 2\,HCl \rightarrow MgCl_2 + H_2 \qquad \text{Reaction (1-12)}$$

The predominant commercial process for magnesium production is the electrolysis of magnesium chloride:

$$MgCl_{2\,(l)} \rightarrow Mg_{(l)} + Cl_{2\,(g)} \qquad \text{Reaction (1-13)}$$

The two major steps of the process are feed preparation for the electrolytic cell and electrolysis. The cell feed material is prepared from an aqueous solution of magnesium chloride derived from seawater, brine, or industrial waste. Because the water is chemically bound, the dehydration is non-trivial. In order to operate at high current efficiencies and reduce cell maintenance costs, large quantities of energy are consumed to produce anhydrous cell feed. Alternatively, costly final dehydration steps can be avoided by electrolysis of the partially hydrated compound $MgCl_2 \cdot 1.7H_2O$ at the expense of higher anode consumption and maintenance (Flemings *et al.*, 1981).

Magnesium is also produced by metallothermic reduction of its oxide derived from abundant minerals such as periclase (MgO), brucite ($Mg(OH)_2$), magnesite ($MgCO_3$) and dolomite ($CaCO_3 \cdot xMgCO_3$). The oxide is reacted with ferrosilicon at a reduced pressure in a resistively heated furnace:

$$Si(Fe)_{(s)} + 2\,(CaO \cdot MgO)_{(s)} \rightarrow 2\,Mg_{(g)} + (CaO)_2SiO_{2\,(s)} + Fe(Si)_{(s)} \qquad \text{Reaction (1-14)}$$

Magnesium is collected by condensing the resulting vapor in an adjoining vessel.

Though not currently practiced commercially, thermal reduction with carbon has been demonstrated on an industrial scale (Byrns, 1947). Also known as the carbothermic process, magnesium vapor is produced according to the reaction:

$$MgO_{(s)} + C_{(s)} \rightleftarrows Mg_{(g)} + CO_{(g)} \qquad \text{Reaction (1-15)}$$

which is in equilibrium at 1 atm pressure and 2123 K and above. However, below 2123 K, CO acts as an oxidizing agent due to the high chemical activity of magnesium. Shock cooling which forms fine magnesium dust, dilution with an inert gas and absorption into another molten metal are the principal methods for inhibiting the reverse reaction (Flemings *et al.*, 1981).

***Calcium Oxide*:** Calcium oxide (CaO) is a white solid which exists in cubic crystalline form with a molecular weight of 56.08 g/mol. Widely divergent values for its melting point are reported in literature ranging from 2843 K (Perry, 1984) to 2888 K (Barin *et al.*, 1973) to 3200 ± 50 K (Chase *et al.*, 1985). Reported values for its boiling point also vary widely from 3123 K (Perry, 1984; CRC, 1982) to 3773 K (Barin *et al.*, 1973).

Calcium oxide, commercially known as quicklime, can be produced by subjecting limestone, which is primarily composed of calcium carbonate ($CaCO_3$), to high temperatures (>900 K). The process, known as calcination, results in the decomposition of $CaCO_3$ into CaO with decarbonation, i.e. release of carbon dioxide (CO_2), taking place through the reaction:

$$CaCO_3 \rightleftarrows CaO + CO_2 \qquad \text{Reaction (1-16)}$$

Commercial calcining operations are carried out between 1473 and 1573 K (Shreve snd Brink, 1977).

***Magnesium Oxide*:** Magnesium oxide (magnesia), MgO, is a white cubic crystalline solid with a molecular weight of 40.3 g/mol. It occurs in nature as the mineral periclase. The principal sources of MgO are magnesite ($MgCO_3$), dolomite ($CaCO_3 \cdot xMgCO_3$), and

magnesium hydroxide ($Mg(OH)_2$) (Copp *et al.*, 1980). MgO is commercially produced by calcining the mineral magnesite or magnesium hydroxide obtained from seawater:

$$MgCO_3 \rightleftarrows MgO + CO_2 \qquad \text{Reaction (1-17)}$$

$$Mg(OH)_2 \rightleftarrows MgO + H_2O \qquad \Delta H_{298\,K} = 81.6\ \text{kJ} \qquad \text{Reaction (1-18)}$$

Various sources report slightly different values for the melting point of MgO and widely discordant values for its boiling point. Reported melting point values are as follows: 3073 K (Perry, 1984), 3098 K (Barin *et al.*, 1973), 3105K (Chase *et al.*, 1985), and 3125 (Copp *et al.*, 1980; CRC, 1982). Boiling point values range from 3533 K (Barin *et al.*, 1973) to 3873 K (Perry, 1984; CRC, 1982).

***Calcium Carbide*:** Calcium carbide is a colorless solid with a density in its pure form of 2.22 g/cm^3 (Kosolapova, 1971) and a molecular weight of 64.1 g/mol. The crystal structure of CaC_2 is known to exist in four modifications. CaC_2-I, which is stable up to 720 K, crystallizes in a face-centered tetragonal lattice containing four CaC_2 molecules per unit cell. CaC_2-II has a triclinic structure and is stable above 720 K. CaC_2-III is metastable and has a monoclinic structure while CaC_2-IV exists as a face-centered cubic and is stable above 723 K (Shine, 1980). Of these, CaC_2-I and CaC_2-II are the most widely studied forms. Commercial calcium carbide consists of the tetragonal modification of CaC_2-I (Kosolapova, 1971). The melting point of calcium carbide is 2573 K (Kosolapova, 1971; Barin *et al.*, 1973; Shine, 1980).

The most extensively used method for the commercial production of calcium carbide is by reduction of high-purity quicklime (CaO) with carbon in an electric furnace at 2273-2473 K:

$$CaO + 3\,C \rightleftarrows CaC_2 + CO \qquad \Delta H_{298\,K} = -466\ \text{kJ} \qquad \text{Reaction (1-19)}$$

The process yields a molten product, which contains about 80% CaC_2, with the remainder consisting of CaO and 2-5% impurities (Shine, 1980). The carbide is drained or tapped intermittently from the furnace and allowed to cool in molds before shipping for the

subsequent generation of acetylene by hydrolysis. Despite the additional weight of the calcium component, the solid carbide is of interest for economical storage and transport of energy since its energy content based on the acetylene it can produce is 19,600 kJ/kg (8,400 Btu/lb), which is comparable to those of lignites and sub-bituminous coal. The highly exothermic hydrolysis reaction represented by Reaction (1-5) to produce acetylene represents the most important industrial use of calcium carbide.

***Magnesium Carbide*:** Two forms of carbide exist in the Mg-C system: magnesium dicarbide (MgC_2) and magnesium sesquicarbide (Mg_2C_3). The dicarbide form, with a molecular weight of 48.3 g/mol, has a tetragonal structure whereas the sesquicarbide, with a molecular weight of 84.6 g/mol, exists in hexagonal form (Kosolapova, 1971). Mg_2C_3 is apparently anionic and is believed to contain the $(C=C=C=)^{4-}$ anion (Keiffer *et al.*, 1980). It yields methylacetylene upon hydrolysis, according to Reaction (1-6), while MgC_2 yields acetylene according to:

$$MgC_2 + 2\,H_2O \rightarrow Mg(OH)_2 + C_2H_2 \qquad \Delta H_{298\,K} = -214.1\ kJ \quad \text{Reaction (1-20)}$$

Based on the potential acetylene/methylacetylene yield, Mg_2C_3 and MgC_2 have energy contents of 21,900 kJ/kg (9,400 Btu/lb) and 26,000 kJ/kg (11,200 Btu/lb), respectively. In spite of the additional weight of the magnesium component, they are attractive not only as intermediates but also as economical forms of energy storage and transport.

Magnesium dicarbide can be prepared by heating magnesium powder in an acetylene or other hydrocarbon stream at 773 K (Kosolapova, 1971). Magnesium sesquicarbide can be obtained as a porous sintered rod of gray color by the reaction of n-pentane vapor with pulverized magnesium at 953 K (Fjellvåg and Karen, 1992). It can also be formed, without co-production of the dicarbide, by the reaction of methane with magnesium metal at 973 K (Durrant and Durrant, 1971):

$$3\,CH_4 + 2\,Mg \rightarrow Mg_2C_3 + 6\,H_2 \qquad \text{Reaction (1-21)}$$

Materials, safety and economic difficulties are expected to be encountered in

commercialization of Reaction (1-21) due to the need to handle very large quantities of nascent reactive magnesium metal.

Both types of magnesium carbide have positive Gibbs free energy of formation (Chase *et al.*, 1985) but the formation of Mg_2C_3 from methane is more thermodynamically favored than the formation of MgC_2 above 1700 K. This is consistent with actual observations of the relative stability of the two carbide forms at high temperatures. In reacting carbon and MgO, MgC_2 is formed at about 773 K. It undergoes thermal decomposition to form Mg_2C_3 with separation of graphite at 773-973 K while Mg_2C_3 breaks down to its elements upon further heating to 1013-1033 K (Kosolapova, 1971; Cotton and Wilkinson, 1962):

$$2\,MgC_2 \rightleftarrows Mg_2C_3 + C_{(gr)} \qquad \text{Reaction (1-22)}$$

$$Mg_2C_3 \rightleftarrows 2\,Mg_{(g)} + 3\,C_{(gr)} \qquad \text{Reaction (1-23)}$$

Apparently, kinetic limitations prevent spontaneous decomposition of Mg_2C_3 back to its elements for temperatures up to 1013 K. Thus, rapid product quenching to below 1013 K, similar to that practiced in acetylene synthesis from hydrocarbons, may be necessary in the implementation of Reaction (1-2).

1.3.4 Chemical Processing in Thermal Plasmas

The term *plasma* is generally used to describe a gaseous system that is sufficiently ionized to be electrically conducting but still electrically neutral (Baddour and Timmins, 1967). Such a system may be completely ionized, in which state it exists as a mixture of ions and electrons, or it may be partially ionized, with only a fraction of the molecules ionized and the remainder electrically neutral species (Venugopalan, 1971). A plasma can be created by exposing a gas to an electric field. Electrical breakdown of an originally non-conducting gas can be brought about by a number of ways, a common example of which is by an electrical discharge between a pair of electrodes. Other methods of producing a plasma include electrodeless radio frequency (RF) discharges,

shock waves, and laser or high-energy particle beams (Flemings, 1985). Figure 1-1 is a simplified sketch of a plasma generator in which a gaseous discharge is created by the passage of an electrical current through the gap between a negative electrode (cathode) and a positive electrode (anode).

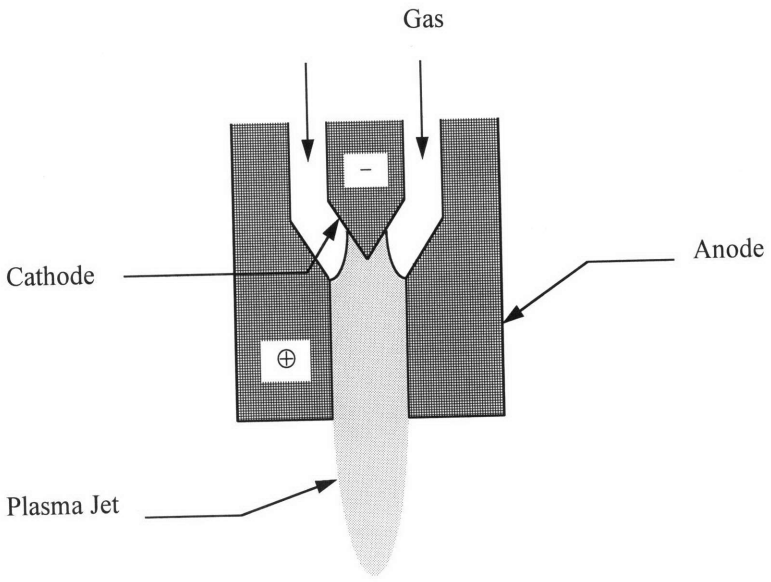

Figure 1-1. Schematic View of Electric Arc Discharge (Thermal Plasma) Generator

Plasmas may be classified either as "hot", that is, thermal, characterized by approximate equality between the gas and ion temperature and the electron temperature, i.e. $T_{gas} \approx T_{ion} \approx T_{electron}$, or "cold", meaning non-thermal, with the electrons at considerably higher temperatures than the gas and ion particles, i.e. $T_{electron} > T_{gas} \approx T_{ion}$ (Baddour and Timmins, 1967; Venugopalan, 1971; Flemings, 1985). Under thermal plasma conditions, the state of the discharged gas approaches complete thermodynamic equilibrium (CTE) under certain conditions and often leads to the establishment of local thermodynamic equilibrium (LTE). Thermal plasmas occur typically in high-intensity arcs and RF high-pressure discharges whereas cold plasmas are produced in glow and corona discharges and in RF low-pressure discharges. Cold plasmas usually require operation at low pressures (probably below 50 mm Hg) making their usage in bulk chemical processing less economically appealing.

The use of plasmas in high-temperature synthesis of chemicals constitutes an important application of plasmas to chemical processing. Plasmas offer a source of extremely concentrated specific energy, resulting in system temperatures in the range of 5000-50,000 K, well beyond the maximum temperatures attainable in chemical combustion flames (Stokes, 1971). Furthermore, plasmas are a source of positive and negative ions that are potential precursors for ion and ion-molecule reactions. These characteristics make plasma processing especially suitable to chemical reactions in which (1) the equilibrium is shifted to high temperatures; (2) reaction rates are sharply increased with temperature; and (3) high yields are obtained under substantially non-equilibrium conditions. Among the advantages of plasma chemical processing are high processing rates (reaction time ~ 10^{-5} to 10^{-3} s), applicability to single-stage processes, insensitivity to reactant impurities (e.g. natural gas, metallic ores) and suitability to processing stable but widely available raw materials such as natural gas and minerals (Vursel and Polak, 1971).

Chemical synthesis in a high-temperature plasma jet may be considered as occurring in a number of steps. First, the decomposition of the molecules, either of the reactive plasma gas or of the molecules fed into the plasma "flame" is brought about by thermal excitation leading to free radicals, atoms, ions and other reactive species. These species then react with one another to form free radical intermediates, which subsequently undergo rapid recombination reactions. Finally, the desired products are formed by freezing out the chemical equilibrium attained under the high plasma temperatures using fast quenching techniques (Stokes, 1971; Venugopalan, 1971). The purpose of the quenching is to cool the reaction products rapidly so that they do not have the time to decompose within the intermediate range of temperatures.

According to these steps, two types of chemical reactions may be carried out, depending on whether the end products are intermediate or final from an equilibrium point of view. The first type includes mostly gaseous reactions, the decomposition of methane into acetylene being the most notable example. For processes of this type, both the quenching rate and the time at which quenching is applied are important. The second type includes mostly gas-solid metallurgical reactions although it may include homogeneous reactions such as nitrogen fixation from air. Magnesium sesquicarbide

synthesis from CH_4 and MgO, Reaction (1-2), apparently falls under the first type as rapid quenching to below 1013 K would seem to be required so that the carbide does not decompose to its constituent elements. In contrast, calcium carbide synthesis from CH_4 and CaO, Reaction (1-1), is of the second type, as CaC_2 is likely to be thermodynamically stable with respect to its elements up to very high gas temperatures in the thermal plasma. Similarly, Reaction (1-4) belongs to the second type, with magnesium metal as the end product, provided that the Mg vapor can separated from CO before reoxidation occurs.

1.3.5 Methane Pyrolysis

The overall methane decomposition is postulated to occur as a first order reaction leading to acetylene formation and ultimately to carbon and hydrogen according to the path:

$$2\,CH_4 \rightarrow \underset{+\,H_2}{C_2H_6} \rightarrow \underset{+\,H_2}{C_2H_4} \rightarrow \underset{+\,H_2}{C_2H_2} \rightarrow 2\,C + H_2 \qquad \text{Reaction (1-24)}$$

Reported values for the activation energy for methane decomposition vary from about 356 to 431 kJ/mol, with shock tube studies generally giving higher activation energy values than non-shock tube studies (Chen *et al.*, 1975).

The initiation stage is the splitting of methane into radicals but the identity of these radicals which form the C_2 unit in acetylene is uncertain. Two possible mechanisms have been proposed for the initial dissociation (Chen *et al.*, 1975):

$$CH_4 \rightarrow CH_3 + H \qquad \Delta H_{298\,K} = 435\ \text{kJ} \qquad \text{Reaction (1-25)}$$

$$CH_4 \rightarrow CH_2 + H_2 \qquad \Delta H_{298\,K} = 464\ \text{kJ} \qquad \text{Reaction (1-26)}$$

Although the thermodynamic stability of the CH_3 and CH_2 radicals with respect to their constituent elements increases with temperature, they are highly reactive species and, according to thermodynamic equilibrium, exist only in low concentrations even at substantially high temperatures, e.g. >2000 K. They are considered to react further with

each other as well as with methane molecules to form C_2H_6 which undergoes dehydrogenation reactions leading to acetylene and ultimately to C and H_2, if the reaction mixture is not quenched rapidly enough.

1.3.6 Carbide Formation

A review of the mechanism and kinetics of calcium carbide formation from carbon and CaO is provided by Miller (1965). The carbide synthesis reaction is believed to occur in two elementary reversible steps:

$$CaO + C \rightleftarrows Ca + CO \qquad \Delta H_{298\,K} = -542.6\ kJ \quad \text{Reaction (1-27)}$$

$$Ca + 2C \rightleftarrows CaC_2 \qquad \Delta H_{298\,K} = 59.0\ kJ \quad \text{Reaction (1-28)}$$

The first reaction step involves the production of metallic calcium vapor. The forward reaction is inhibited by high CO pressure and goes faster as the area of contact between the lime and carbon is increased. The activation energy for the forward reaction is 615.5 kJ/mol at 1673 K. In the second step, the forward reaction is brisk at 1873 K but slow at 1573 K. The reaction velocity is controlled by the diffusion of the calcium vapor through the CaC_2 layers formed on the carbon surface. The rate of the reverse reaction, whereby CaC_2 decomposes into its elements, increases with temperature and is rapid at 2473 K.

Studies on the overall kinetics of calcium carbide synthesis from compressed cylindrical pellets of lime and carbon as a solid-state reaction were performed by Tagawa and Sugarawa (1962) at temperatures between 1873 and 2073 K and at CO pressures of 50, 100, and 200 mm Hg. The rate has a strong dependence on CO pressure with an activation energy of 598.7 kJ/mol at 50 mm Hg CO pressure and over 837 kJ/mol above 100 mm Hg. The formation reaction is controlled by the diffusion rate of gas through the product layer, as well as by the diffusion of solids. The decomposition of CaC_2, which occurs from the surface, is a zero-order reaction, approximately linear with time.

Kim (1977) *et al.* (1979) demonstrated high methane carbon conversions (> 95 mole %) to CaC_2 and CO at CaO "Ca" molar conversions of 70 ± 15% by passing

premixed suspensions of fine lime powder in a stream of methane gas through the arc zone of a magnetically-rotated electric arc discharge plasma reactor. Figures 1-2 and 1-3 show conversion data for the range of experimental parameters examined by Kim. The global chemistry of the reaction is attributed to Reaction (1-1).

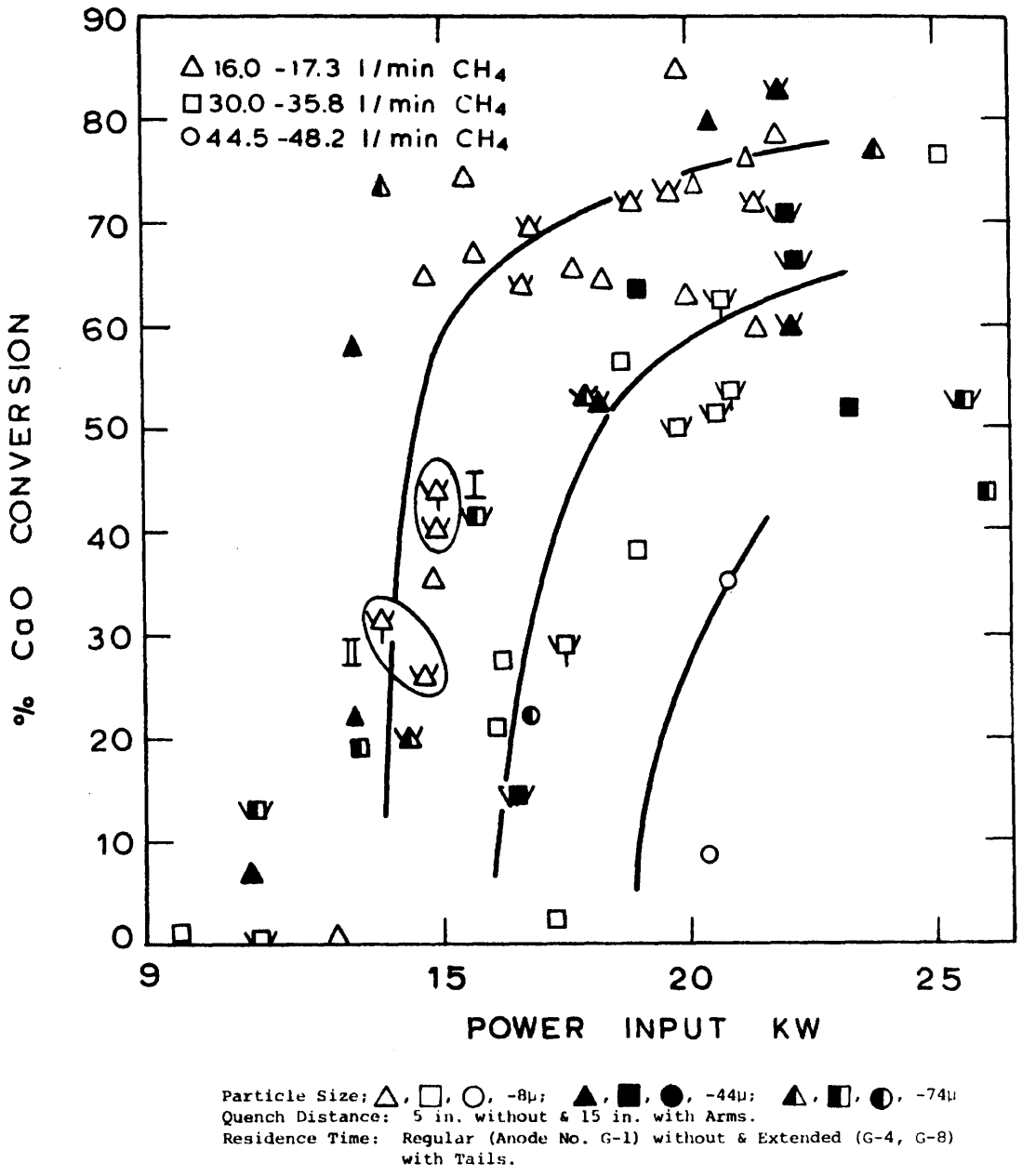

Figure 1-2. CaO Conversion as a Function of Power Input at Various Methane Flow Rates (Kim, 1977)

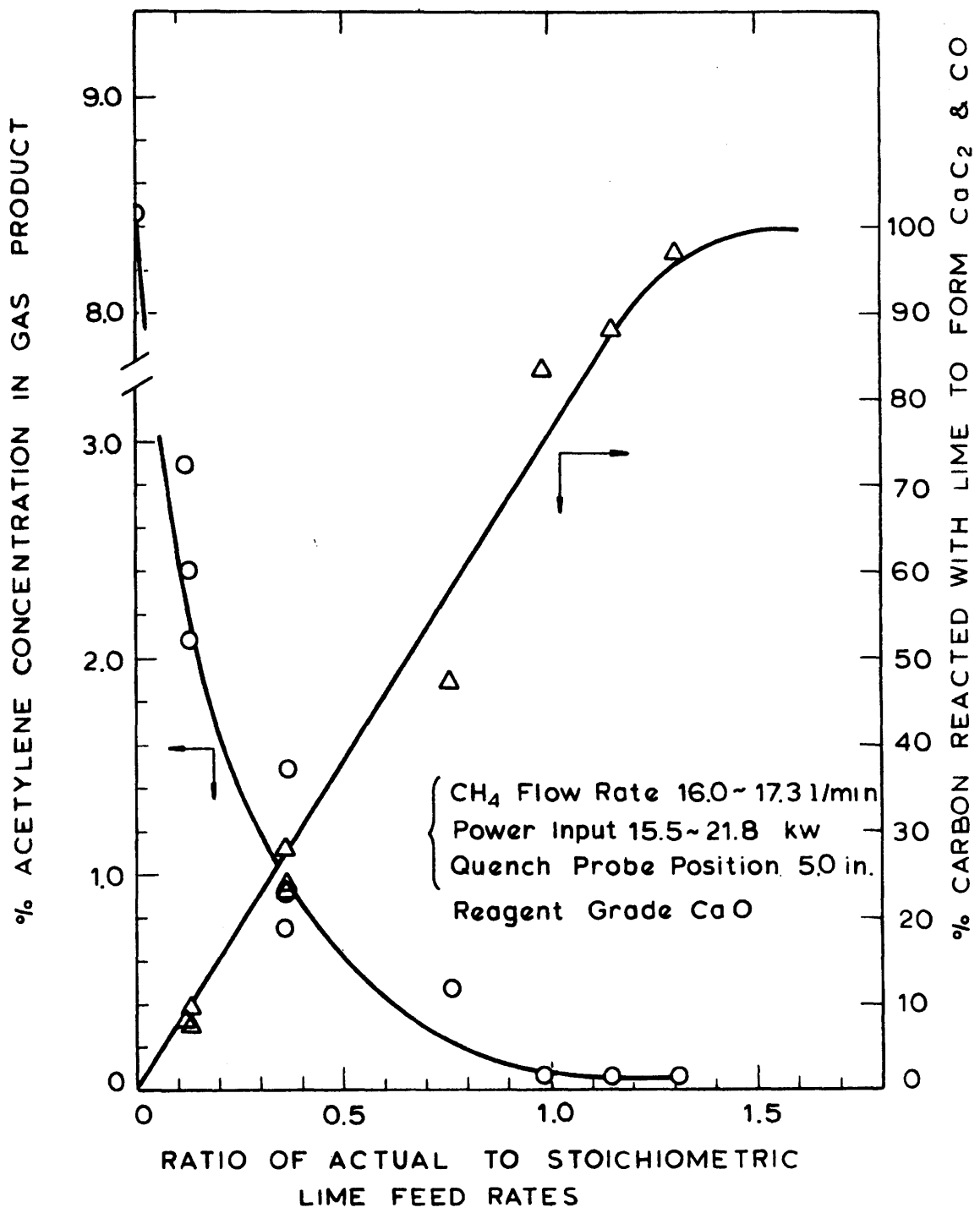

Figure 1-3. Conversion of Carbon in Methane as a Function of CaO Feed Rate (Kim, 1977)

Kim postulated that the formation of CaC_2 in this reaction scheme required an energy on the order of the activation energy for methane decomposition. On this basis, he surmised a gas temperature at or above 3000 K. Furthermore, residence times based on gas flow rates and geometry of the anode were estimated to be typically 0.5-1.0 ms.

Kim's work was primarily concerned with producing CaC_2 from rapid heating of a high-volatile coal in hydrogen. Although extensive studies were conducted with methane as source of nascent carbon species to help delineate the overall reaction mechanism, these studies did not have as their major objective the optimization of experimental parameters to identify the range of conditions of interest for commercial operation. He did however observe the following:

a) For each methane flowrate, there existed a critical power input range in which CaO "Ca" conversion to CaC_2 increased rapidly with only slight increases in the power input. Below this critical range, no carbide was detected, and above it, CaO conversion attained a more or less constant value. This critical power level is on the order of the overall activation energy of methane decomposition;
b) The conversion of the calcium in CaO to CaC_2 was essentially unaffected by the initial CaO particle size, CaO feed rate and the global residence time of CaO within (controlled by the length of the anode nozzle) or downstream (controlled by the distance of the quench probe to the nozzle exit) the arc;
c) The solid product particles were always less than 0.3 μm regardless of the initial CaO particle size;
d) The formation of acetylene decreased at an accelerated rate from over 80% at low carbide yield to essentially zero at high yield (approaching 100% CH_4 "C" conversion to CaC_2 and CO) while CaC_2 and CO formation increased only linearly with lime feed rate;
e) The energy efficiency of the process was far from that currently needed for economic viability at commercial scale operation. The lowest energy consumption achieved in this study with methane is 35.9 kWh/kg of acetylene.

Based on the existence of a critical power level on the order of the overall activation energy of methane decomposition and the absence of residence time effects, Kim postulated the conversion of methane to very reactive but short-lived nascent carbon species such as free radicals, which are abundant only in and immediately beyond the arc zone. CaO is viewed as a chemical quenching agent that reacts with the methane-derived intermediates to form CaC_2, which is stable up to the gas temperatures in the reactor. Thus, increasing the quench distance did not affect the carbide yield. Without CaO, methane would simply pyrolyze to acetylene, soot and tars. Kim further postulated that CaO conversion is a localized phenomenon around individual CaO particles and that the rate controlling step shifts from the gas phase to and around the individual CaO particles as the input power is increased above the critical level. Thermodynamic considerations indicated that CaO conversion can be enhanced by H atoms which may directly reduce CaO to Ca and H_2O. The reverse reaction is inhibited by the reaction of the methane-derived carbon species with H_2O to produce CO and H_2.

Saito (1991) performed some investigations on the use of the thermal approach to carbide synthesis. He heated a thin layer of CaO between two tungsten strips in a screen heater reactor to temperatures ranging from 1473 to 2573 K in a methane atmosphere at a pressure of 2 psig but obtained only minute quantities of calcium carbide (maximum CaO conversion of ~0.1%). The insignificant carbide yield was attributed to the methane undergoing competing pyrolytic reactions to form soot before coming into contact with the CaO particles. To overcome the mass transfer limitations inherent in this study, Saito reduced the methane pressure to as low as 50 mm Hg. He found a higher CaO conversion of 0.79% at 100 mm Hg and 0.22% at 50 mm Hg over a temperature range of 2073-2273 K. He also observed less soot formation under these conditions.

El-Naas *et al.* (1995) formed CaC_2 by reacting CaO powder with a mean particle size of 170 μm and graphite powder with a mean particle size of 150 μm in a laboratory-scale fluidized bed reactor heated with a DC plasma torch. A 1 kg mix of 3:1 CaO:C was charged into a batch reactor and Argon was used to fluidize the bed at 1.1 times the minimum fluidization velocity. A mixture of Argon and hydrogen was used as plasma-forming gas. The reaction was observed to take place at about 2150 K mainly in the jet

zone and conversion to CaC_2 was found to increase linearly with reaction time. They concluded that the reaction occurs through gaseous intermediates, calcium vapor and CO, and that the overall rate is controlled by chemical kinetics.

1.3.7 Metal Formation with Methane as Reductant

Merriam (1944) in U.S. Patent 2,364,742 describes a cyclic process for the reduction of solid MgO and ZnO with methane. At high temperatures, methane decomposes into hydrogen and carbon, which are relatively ineffective for reducing the metal oxide. To avoid decomposition prior to reduction, methane gas is applied to preheated charges of the solid in an abrupt manner. Specifically, a charge of solid MgO and solid carbonaceous material such as coke is introduced into a reaction zone. A blast of preheated air is passed through the mixture until sufficient coke is burned to raise the temperature above the reduction temperature of the oxide (2273 K for MgO). The air blast is then discontinued and methane or natural gas is introduced into the hot solid mixture as a blast, thereby reacting with the oxide and carrying away metal vapor. The resulting magnesium or zinc vapor is condensed and separated from the gases. Because the reduction is endothermic, the temperature of the solid mixture will drop gradually until further reaction substantially ceases. At this point, the methane blast is discontinued and the mixture is heated again by introduction of a hot air blast and burning of more carbonaceous material. Thus, the process described operates cyclically or intermittently.

Stokes (1971) investigated the reduction of various metal oxides with hydrogen and methane by pneumatic injection of gas-entrained powder into helium and argon plasma jets. Aluminum oxide (Al_2O_3) powder, 200-mesh, entrained in 8.5 and 8.7 l/min of methane, was injected at rates of 1.5 and 3 g/min into the flame jet of an 11.9 l/min Argon plasma at 8.9 and 9.6 kW, respectively. Particle residence time in the plasma flame was calculated to be between 5 and 20 ms. Solid products were collected on a copper cold finger attached to the reaction chamber after fast quenching with a water-cooled funnel located 1.5 inches below the anode. Aluminum metal was definitely formed but the conversion to Al was only 0.20%. Based on the similarity of the particle

size of starting material and end products, the limited decomposition of the alumina was attributed to either too short a residence time or injection into a relatively cold region of the flame.

The feasibility of iron oxide reduction in an arc-heated mixture of hydrogen and natural gas at 100 kW and 1 MW was investigated by Gold *et al.* (1975) at Bethlehem Steel. Compared to a thermodynamic energy requirement of about 2.2 kWh/kg Fe (1.0 kWh/lb Fe), pure molten iron was produced in the single-stage process at a net energy consumption as low as 2.6 kWh/kg Fe (1.2 kWh/lb Fe).

Detering *et al.* (1987) used atomic emission spectroscopy to determine and quantify thermal decomposition and reduction products and concentration upon injection of metal oxide particles into a non-transferred arc plasma. Metal oxide powder was injected through a hollow cathode tube into an Argon plasma operating at 16.5 kW (750 A, 22 V). Al_2O_3 and Co_3O_4 powder (<10 μm) were used as reactants for reduction with methane which was injected tangentially at 1 mm from the exit of the plasma torch. The inlet plasma gas flow was 15 l/min while the powder carrier gas flow was 1.7 l/min. Aluminum was produced by thermal decomposition of the oxide and its concentration determined by spectroscopic measurement made at 10 mm axial distance from the torch exit. Several emission spectra were obtained from the cobalt oxide experiment in the arc region and downstream the injection point of methane. These spectra indicated elemental cobalt, elemental carbon, elemental oxygen, elemental hydrogen, molecular carbon (C_2) and also cyanogen (CN) from nitrogen entrainment. Emission lines for cobalt oxide (CoO), molecular oxygen (O_2) and CO were not observed. X-ray diffraction analysis of collected particle products revealed the material to be almost entirely metallic cobalt, with small contaminant amounts of cobalt oxide and carbon.

Steinfeld *et al.* (1995) studied the combined thermal reduction of ZnO and reforming of CH_4 according to:

$$CH_4 + ZnO \rightarrow Zn + 2\,H_2 + CO \qquad \text{Reaction (1-29)}$$

in an electrically heated Al_2O_3 tube and in a solar furnace. The equilibrium composition of the ZnO-CH_4 system at 1200 K and 1 atm consists of a gas phase of Zn vapor and a 2:1 mixture of H_2 and CO. ZnO powder with a mean particle size of 1.2 μm was heated to different predetermined temperatures in a 3-cm diameter Al_2O_3 tube under an Argon flow and then isothermally reduced to Zn under various CH_4-Ar flow rates at slightly above atmospheric pressure. Powder X-ray diffraction analysis of the solid products revealed complete conversion to Zn in all cases. Methane conversion was found to increase with temperature: 51% at 1373 K, 84% at 1473 K, and almost 100% at 1573 K. H_2 yield also increased with temperature and reached about 65 mole % at 1573 K. From thermogravimetric measurements on ZnO at various temperatures and CH_4 concentrations, the apparent activation energy was found to be 146 kJ/mol. Based on a shrinking particle model, Steinfeld *et al.* concluded that the reaction mechanism is controlled by gas film diffusion in the Stokes regime.

Chapter 2

Experimental Apparatus and Procedure

A laboratory-scale rotating DC arc discharge (plasma) reactor is used to investigate the technical feasibility of Reactions (1-2) and (1-4) and to systematically investigate the effects of variations in thermal plasma operating conditions on the yields, selectivity and CH_4/metal oxide conversion to CaC_2 and/or Mg_2C_3 and/or MgC_2 and/or Mg, as well as to H_2 and CO according to Reactions (1-1), (1-2), (1-3) and (1-4).

2.1 Rationale for Selection of Apparatus

In implementing gas-solid reactions such as (1-1) and (1-4) whose end products are final at high temperatures and thermodynamically allowed under equilibrium conditions, complete conversion can be attained with sufficient residence time in a suitable plasma device, as in a plasma jet directed to a stationary bed of solids or upwards to a fluidized bed of solid reactants. Kim (1977) contemplated that, if hydrocarbon or high-volatile coal were mixed with lime and injected into a hydrogen plasma jet, the formation of extremely reactive "nascent" carbon species can reduce the equipment size significantly and possibly eliminate the need for a fluidized bed provided that the reaction is rapid enough. However, the energy efficiencies of plasma-heated stationary and fluidized beds are relatively poor. High-quality electrical energy is used to provide sensible heat to the solids and to the off-gas, from which there can be significant energy losses through the

reactor walls per unit mass resulting from a long retention time and a high gas-to-solid ratio.

Alternatively, high extents of conversion can be attained in a high-intensity arc using consumable anodes of the reactant materials. Vursel and Polak (1971) cite the work of Kusch (1963) in the reduction of Fe_2O_3, SiO_2, Al_2O_3, MgO and B_2O_3 to their parent metal using a laboratory-scale high-intensity arc with anodes of oxide pressed with carbon powder. High yields of products up to 83% Fe, 73% Si and 17% Mg, collected on a cooled metal surface, were reported. High-intensity arcs are, however, also relatively energy inefficient because of the need to vaporize the anode material at temperatures probably significantly higher than the threshold equilibrium reaction temperature. As with the plasma-heated stationary and fluidized beds, the throughput of high-intensity arcs can be rather limited.

The drawbacks of low energy efficiency and limited throughput can be overcome with the injection of a mixture of gas and solid reactants into a plasma jet, which may be inert or reacting, to implement single-stage reactions provided that such heterogeneous reactions can occur rapidly enough (reaction time ~ 10^{-5} to 10^{-3} s). Stokes' (1971) work on metal oxide reduction and carbide and nitride syntheses involved pneumatically conveying solid reactants to a plasma jet, which is the tail flame of an arc-heated auxiliary or reacting gas stream.

In order to increase plasma-solid contact and interaction, Gannon and Krukonis (1972) synthesized acetylene by introducing coal entrained in hydrogen directly into the inter-electrode region rather than into the plasma jet downstream of the electrodes. The gas-solid mixture was passed through the annulus of a cylindrical anode at the center of which is a cathode and thus, through the electrical discharge itself. The plasma was made relatively uniform throughout the annular region by rotating the arc at a radial velocity greater than the axial velocity of the coal and carrier gas with a magnetic field directed transversely to the current path. Kim (1977) used the same approach in reacting lime with methane to form calcium carbide.

This rotating arc design which allows passage of the reactants through the arc zone has rather well-established operational and mechanical features that include high

energy efficiency, mechanical simplicity, arc stability, relative ease of operation and a comparatively large cross-sectional inter-electrode annular area for high feed throughput through the arc zone. Thus, the rotating DC arc discharge reactor used in this study is of the type used by Gannon and Krukonis (1972) and Kim (1977). Such a reactor needs to be operated for only one to five minutes to achieve steady state operation with intrinsic reaction times in the range of 10^{-5} to 10^{-3} s.

2.2 Description of Apparatus

The experimental apparatus used in the present study consists of a thermal plasma generator, mechanical powder feeder, post-plasma cooling chamber and gas discharge system, sample collection system, cooling water system, and data acquisition and process control system. A process engineering flow scheme of the experimental apparatus is shown in Figure 2-1.

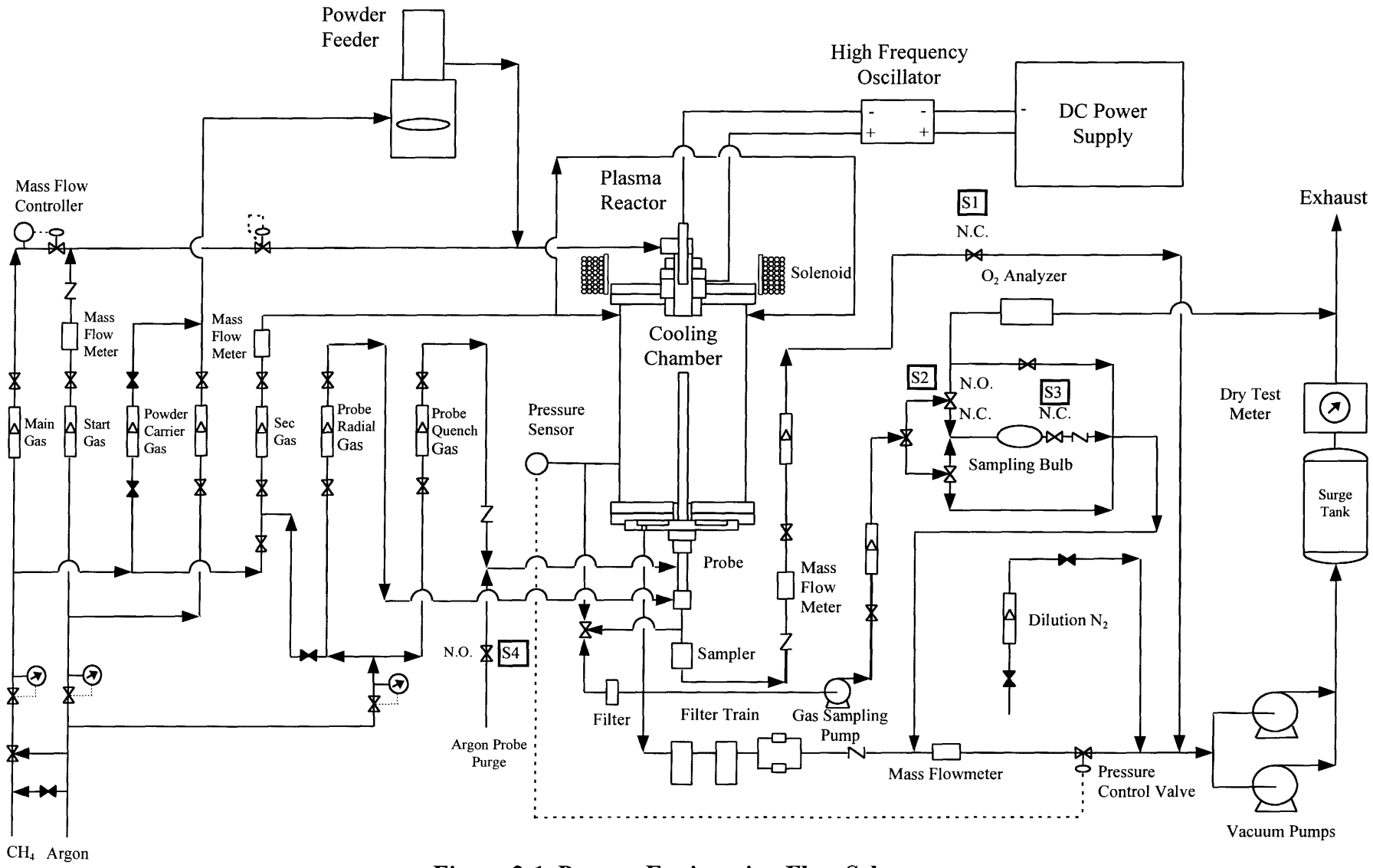

Figure 2-1. Process Engineering Flow Scheme

2.2.1 Thermal Plasma Generator System

The thermal plasma generator is composed of a DC arc discharge reactor, a magnetic solenoid, a high frequency oscillator, a DC power supply unit and a control console.

2.2.1.1 DC Arc Discharge (Plasma) Reactor

The primary components of the DC arc discharge (plasma) reactor are the anode and the cathode. Both electrodes are made of graphite and designed for convenient replacement of worn parts after every run. The electrodes are held in place by water-cooled holders to prevent overheating of other parts of the reactor. Initial attempts to use a ¼-in. O.D., 2% thoriated tungsten cathode with a conical tip proved inadequate as more than half the cathode tip was consumed by erosion/vaporization after a minute of sustaining a plasma with an Ar-CH_4 feed. Similarly, in attempting to switch from Argon to methane feed, the Ar-CH_4 plasma burned several small orifices through the walls of a water-cooled copper anode in a spiral pattern. Electrodes made of graphite were found to be robust enough to withstand the severe thermal and chemical environment imposed by the experimental conditions, provided that the current density is not high enough to erode the cathode. Graphite is electrically conducting, can sustain a thermionic cathode arc, is machinable and does not require intensive cooling (Knight *et al.*, 1990). The graphite material used as electrodes in this study is Grade ECR graphite manufactured by National Electrical Carbon with the typical properties shown in Table 2-1.

Table 2-1. Typical Properties of Grade ECR Graphite

Maximum Grain Size, inches	0.006
Density, g/ml	1.60
Specific Resistance, μΩ·m	6.0
Flexural Strength, psi	3000
Tensile Strength, psi	2000
Compressive Strength, psi	6000
Maximum Ash, %	0.1

The rate of consumption of the cathode depends strongly on the current density at the tip. A one-inch long, ¼ in. O.D. graphite cathode is severely eroded in an Argon plasma operating at the minimum starting current of 600 A because the current density of 1,895 A/cm^2 is too high. The typical cathode length consumption rate for Kim's (1977) ¼ in. O.D. graphite cathode under a methane flow rate of 16.0-17.3 l/min over a 90 s run time is: 3/16-½ in. for a current density of 950-1100 A/cm^2, 1/16-¼ in. for 790-950 A/cm^2, and 0-1/16 in. for 470-790 A/cm^2. Below 470 A/cm^2, Kim did not observe any cathode erosion. Gannon and Krukonis (1972) give a much more conservative upper limit of 200 A/cm^2 (1,250 A/in^2) to avoid excessive cathode erosion. Based on these design considerations, a ¾ in. O.D. cathode is used in the present study. Such a cathode would have a current density of 350 A/cm^2 at the maximum current of 1000 A.

Figure 2-2 shows a schematic representation (1:2 scale) of the plasma reactor, which is made up of a ¾ in. O.D. cylindrical graphite cathode in the center of a 1 in. I.D. annular graphite anode. The cathode assembly consists of a cylindrical nylon (Zytel 101) piece, which serves as mounting body for the water-cooled copper cathode holder. This nylon piece electrically insulates the anode from the cathode. Three inches tall with the top 2 in. having an O.D. of 4 in. and the bottom 1 in. an O.D. of 5½ in., it is secured to the brass anode holder and to the top steel flange with three screws. A silicone o-ring constitutes a face seal between the nylon piece and the brass anode holder. A low-density alumina ring (1¼ in. I.D. by 3 in. O.D. by ½ in. thick) thermally insulates the nylon body from the graphite anode. A high-density alumina tube (1 in. I.D. by 1¼ in. O.D. by 1½ in. long) further insulates the nylon from arc radiation. The cathode holder is made up of a ¾ in. O.D. by 8 in. long copper tube. The bottom end of the holder is soldered to a ¾ in. O.D. and 2 in. long copper rod, with the upper 1½ in. drilled to a 5/8 in. I.D. and the lower ½ in. externally tapped with a ½"-20 thread. A 3/8 in. O.D. stainless steel (SS) tube located concentrically inside the cathode holder serves as a cooling water flow divider. The cathode tip, which is replaced after every run, is a ¾ in. O.D. by 1½ in. long graphite rod, axially bored with a 5/8 in. deep ½"-20 internal thread so that it can be secured to the threaded bottom end of the copper cathode holder.

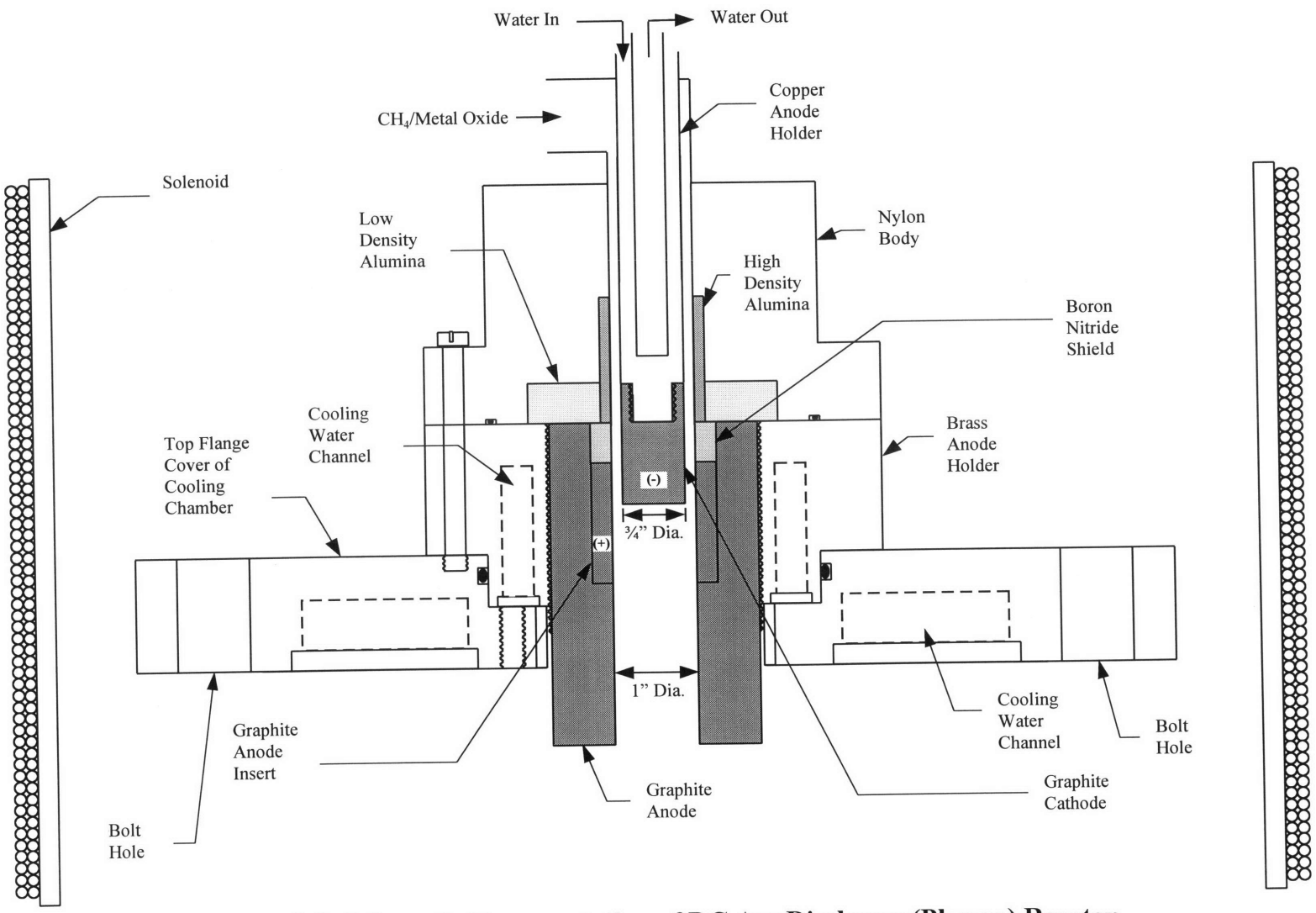

Figure 2-2. Schematic Representation of DC Arc Discharge (Plasma) Reactor

The anode assembly consists of a graphite anode insert which slides into the graphite anode. The anode is screwed into a water-cooled cylindrical brass anode holder, which fits into a 4 in. diameter, 5/8 in. deep counterbore on the top steel flange of the cooling chamber. The anode holder is 2¼ in. tall with the top 1-5/8 in. having an O.D. of 5½ in. and the bottom 5/8 in. an O.D. of 4 in. The steel flange is 12½ in. O.D. by 1-3/8 in. thick. A silicone o-ring forms a rod-seal between the brass anode holder and the steel flange. The graphite anode is a 2½ in. O.D. by 4 in. long cylinder with its outer top 2½ in. section tapped with 2.46"-12 thread to fit the brass holder. The top half of the anode is counterbored to 1½ in. I.D. to accommodate the anode insert and a boron nitride shield while the bottom half is drilled to a 1 in. I.D. to form the anode nozzle. The inner top ½ in. portion of the graphite anode is electrically insulated with a ring of grade HBT boron nitride shield (1 in I.D. by 1½ in. O.D. by ½ in. long). The anode insert, which is replaced after each run, is a 1 in I.D. by 1½ in. O.D. by 1½ in. long ring.

The cathode tip is positioned so that it penetrates the anode region to a depth of ½ in. below the top of the anode insert. The distance from the flat face of the cathode tip to the anode nozzle exit is 3 in. The anode nozzle protrudes 1 in. below the bottom face of the steel flange. Gas or gas plus entrained powder is introduced in the 1/8 in. wide annular slit (¾ in. I.D. by 1 in. O.D.) between the cathode and anode.

2.2.1.2 Magnetic Solenoid

With the use of a solenoid, a magnetic field is applied perpendicular to the arc current which induces in the charged particles a velocity component perpendicular to their original direction of travel. Consequently, the path of charged particles moving in a plane perpendicular to the magnetic field will curve. However, the mean free path of the particles remains practically unaltered. One effect is that the electric conductivity of the plasma becomes more anisotropic under these conditions (Gross *et al.*, 1969), resulting in a better confined plasma.

A solenoid placed coaxially with the plasma reactor works to rotate the arc column by imparting an axial magnetic field. This magnetic field interacts with the radial arc column to produce a force perpendicular to the plane of the arc and the field. The force, $\vec{F}$, which induces rotation is given by:

$$\vec{F} = \vec{I} \times \vec{B} \qquad \text{Equation (2-1)}$$

where $\vec{I}$ is the arc current and $\vec{B}$ is the axial magnetic field vector. Applying Newton's Second Law to equate the centrifugal force to the magnetically generated force, as given by Halliday and Resnick (1978),

$$\frac{m_e v^2}{R} = qvB \qquad \text{Equation (2-2)}$$

where m_e is the electron mass in kg, v is the speed of electrons in m/s, R is the inter-electrode gap in m, B is the required field strength in tesla and q is the elementary charge in coulomb. Solving for B gives

$$B = \frac{m_e v}{qR} \qquad \text{Equation (2-3)}$$

To determine the electron speed, v, Blanchet (1963) used the following relation equating the potential existing between the anode and the cathode to the kinetic energy of the electrons:

$$qV = \frac{m_e v^2}{2} \qquad \text{Equation (2-4)}$$

where V is the arc voltage. This equation gives the relation for v:

$$v = \sqrt{\frac{2qV}{m_e}} \qquad \text{Equation (2-5)}$$

Substituting Equation (2-5) in the expression for B gives:

$$B = \frac{\sqrt{2Vm_e/q}}{R} \qquad \text{Equation (2-6)}$$

or

$$B(\text{in gauss}) = \frac{1.33\sqrt{V}}{R(\text{in inches})} \qquad \text{Equation (2-7)}$$

For an arc operating at atmospheric pressure, the actual rpm is much lower than the value estimated from Equation 2-5 due to the aerodynamic drag of the arc column and collisions of electrons with gas molecules (Kim, 1977). Based on an inter-electrode gap of 1/8 in. and arc voltages of 60 to 120 V, B should be in the range of 80 to 120 gauss.

The field strength B for an infinite solenoid is given by

$$B = \mu_o i_o n \qquad \text{Equation (2-8)}$$

where μ_o is the permeability constant in Ampere's Law, i_o is the solenoid current and n is the number of turns per unit length. Kim (1977) used Equation (2-8) to approximate a solenoid of finite length:

$$B = \frac{1.26\, i_o N}{l} \qquad \text{Equation (2-9)}$$

where N is the total number of turns, l is the solenoid length in cm, i_o is in A and B is in gauss (G).

The solenoid design initially consisted of four layers of No. 15 enamel-coated copper wire windings over an 8 in. section of a 9 in. long bakelite tube, 14½ in. I.D. by 15½ in. O.D., which is wide enough to enclose the entire reactor. Power to the magnetic coils is provided by a 400 watt DC regulated power supply capable of delivering up to 25 A in the 0 to 20 V range. The number of turns per layer is approximately 130. The total resistance of the solenoid was measured as 0.7 Ω. Thus, with a current of 13 A, the solenoid can theoretically have a maximum magnetic field strength of 420 G. However, at a total current of 15 A, measurements made with a Bell 610 Gaussmeter varied from only 43 G at the base of the anode insert to 77 G at the top of the anode insert. The presence of the steel flange and cooling chamber significantly alters the field strength at the center of the reactor. In order to have a stronger magnetic field, four more coils have been installed on the solenoid for a total of eight. Every two coils are connected in series and the four two-coils-in-series segments are connected in parallel. This configuration gives a total solenoid resistance of 0.9 Ω, which is optimum for maximizing the magnetic field from the 20V/25A capacity of the solenoid power supply. At a total current of 20.6 A with an accompanying voltage drop of 19 V, the measured axial magnetic field varies from 118 G at the base of the anode insert to 195 G at the top of the insert.

2.2.1.3 High Frequency Oscillator

The arc is started with a high frequency oscillator, AIRCO model HF-20-1, which is placed in series with the DC power supply. A high frequency oscillator is a spark-gap-type self-contained unit which superimposes high frequency voltage on normal direct current. The unit has a power rating of 120 watts, with input voltage at 115 V and input current at 2.2 A for operation at 50/60 cycles AC. It is connected to the plasma reactor via a 16 ft. length of water-cooled power line made of extra strong (0.840 in. O.D. by 0.149 in. wall thickness) copper pipe alloy C12200 (99.9 wt% Cu, 0.02 wt% P) to minimize ohmic losses. When activated, the high frequency voltage is impressed across the output terminals of the power supply and hence across the inter-electrode gap until an

arc is initiated. As soon as this is accomplished, the high frequency voltage automatically shuts off.

2.2.1.4 DC Power Supply Unit

Power to the arc discharge reactor is provided by an AIRCO rectifier-type welding power supply, 1500 Ampere C7 Model, rated by the manufacturer at up to 83 kW and capable of providing open circuit output voltages of 82, 164 and 328 V. The specifications of the power supply unit are given in Table 2-2.

Table 2-2. Specifications of 1500 Ampere C7 Model DC Power Supply Unit

Primary		Secondary			
Voltage, V	460	Load Voltage, V	40	80	160
Current, A	145	DC Current Range, A	200 - 2000	100 - 1000	50 - 500
Frequency, cycles	60	Rated Output, A	1500	750	375
Power Input at Rated Load (Three Phase), kW	83.2	Open Circuit Voltage, V	82	164	328
Power Input at Rated Load (Three Phase), kVA	115	Duty Cycle, %	100	100	100

The electrical field strength which provides the main source of energy to ionize a gas is higher for molecular gases like methane than that for atomic gases such as Argon. Molecular gases require such a higher electrical field strength for sustaining an arc discharge because of the accompanying chemical processes of dissociation, ionization and recombination. In such a gas, the density of the molecules decreases and that of atoms increases with rising temperature. Density gradients arise, causing diffusion currents whereby pairs of atoms diffuse into cooler regions to recombine while molecules migrate into warm regions to dissociate (Gross *et al.*, 1969). Energy is liberated in the recombination process in the cool region while energy is absorbed in the dissociation process in the warm region. These combined processes of atomic diffusion and chemical recombination cause significant heat losses from the arc. Consequently, more energy is needed to sustain a plasma fed by molecular rather than by atomic gases. Thus, in the present case, methane, despite its lower ionization potential relative to Argon, requires a higher operating arc voltage.

In Kim's (1977) experiments, arc voltages for a methane plasma ranged from 60 to 110 V for flow rates of 16.0-17.3 l/min and from 65 to 115 V for flow rates of 30.0-35.8 l/min. He found the arc to be moderately stable at gas flow rates of 16.0-17.3 l/min and at arc voltages less than 75 V but mostly unstable at higher gas flow rates. The instability is presumably due to limitations on the output voltage of the power supply. The arc becomes unstable when the load voltage exceeds half the open circuit voltage (OCV). Instability at high gas flow rates is not unexpected because increasing the gas flow velocity requires a higher enthalpy input and a higher electric field strength in order to compensate for increased energy losses due to the higher convective cooling of the arc column. Furthermore, a higher gas flow rate results in elongation of the arc column which also requires an increased voltage to sustain the same field strength. This is consistent with Blanchet's (1963) ability to sustain a methane plasma between a continuously fed graphite anode and a water-cooled brass cathode at a much lower gas flow rate of 1.5 l/min at voltages of 40-80 V.

Operating a methane plasma at up to 30 l/min requires a voltage presumably higher than 80 V because an Argon arc discharge at that flow rate is extinguished upon introduction of methane. Thus, the power supply has been configured for the highest OCV of 328 V to enable stable operation of the arc at higher load voltage levels. Indeed, the arc voltage values in this study range from 15 to 115 V. However, at the minimum current setting under an OCV of 328 V, an Argon arc operates at a current of 600 A when the same setting gives only 200 A under the 160 V OCV configuration.

The falling voltage vs. amperage characteristic of the power supply, shown in Figure 2-3, in principle allows a reasonable variation in arc length or voltage with relatively minor changes in arc current.

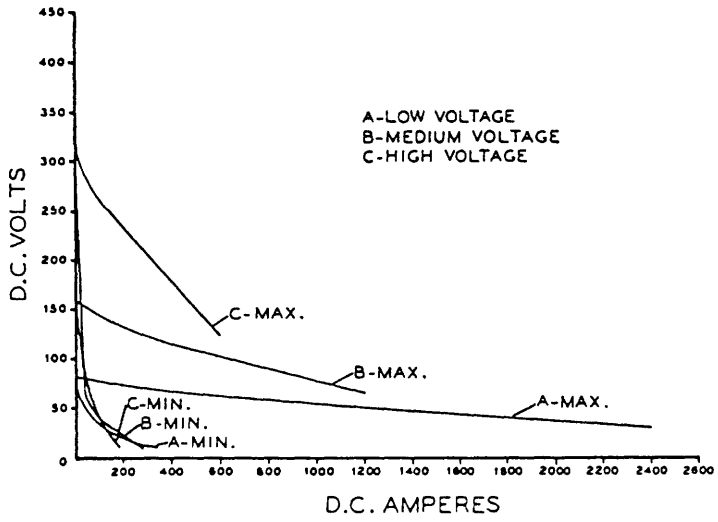

Figure 2-3. Volt-Ampere Curve of DC Power Supply Unit (AIRCO Manual)

The output of the power supply is controlled from a remote control panel. A contactor control switch allows the electrodes to be energized remotely. A start control is used to set the starting current and allows this preset current to flow for approximately 2/3 s before automatically changing to the setting of the current control. In this study, the start control is always set to zero. Current adjustment is accomplished with a current (weld) control, which essentially varies the slope of the volt-ampere curve pivoted around the OCV. This changes both the arc voltage and arc current by shifting the intersection of the power supply characteristic and the arc characteristic. The current control is at minimum setting at the beginning of every run. The remote control panel is equipped with a 0-500 V DC voltmeter and a 0-2 kA ammeter.

Power input to the reactor is determined as the product of voltage and current measurements. Voltage is measured with a Fluke 8050A bench digital multimeter via shrouded test leads connected to lines leading to the cathode and anode holders. Current is measured using a 1-1300 A DC Fluke 80i-kW Current/Power Probe, which is a clamp-on unit with two movable jaws, each containing half a magnetic core. The jaws are clamped around the water-cooled (-) power line leading to the cathode at a location overhead of the control console, allowing current measurement without breaking the circuit. The 80i-kW probe uses two Hall devices located in gaps of the magnetic core and generates an output of 1 mV per A, which is read by a handheld Fluke 87 True RMS

Multimeter. The voltage and current measurements are also recorded by the data acquisition system.

2.2.1.5 Control Console

Control and monitoring of the plasma reactor is done from the control console. The unit is provided with safety interlocks that prevent operation of the system until sufficient flows of cooling water and gas are attained or when overloading of the power supply occurs. A gas flow switch and indicator ensure adequate flows of main gas, start gas, or a combination of both to the plasma reactor while a water flow switch and indicator serve the same purpose for the cooling water flow to the power lines and the plasma reactor.

The start gas is the gas with which the arc discharge is initiated. The main gas is the gas with which the plasma reactor is operated. In the present study, Argon is the start gas and methane is the main gas. Secondary gas, which can be either Argon or methane, is gas introduced (in selected runs) into the top part of the cooling chamber downstream of the anode nozzle. The console has a mass flow controller for the main gas flow and mass flow meters for the start and secondary gas flows. In addition, flow indications of main, start, secondary and powder carrier gas flows are provided by rotameters. Pressure regulators enable adjustment of the delivery pressures of the start and main gases.

With adequate gas and cooling water flows, a power start switch energizes the electrodes, bringing the potential across them to the OCV. A plasma start switch activates the High Frequency Oscillator to initiate arcing. A power stop switch can be used to manually cut off power to the arc, although automatic shutdown is normally performed through the process control system.

2.2.2 Powder Feeder

A mechanical wheel-type powder feeder, Miller Thermal Model 1270 Computerized Powder Hopper, is used to deliver powder into the plasma reactor. It is an electronically controlled, pressurized unit that discharges powder based on volumetric feed. Slots in a rotating wheel at the base of the pressurized canister fill with powder. When a slot lines

up with the exit port, the powder is forced out of the slot and is transported by the carrier gas through a 3/16 in. I.D. hose to the plasma gas inlet line. The rate of powder delivery to the reactor is predominantly a function of the speed of wheel rotation. A built-in tamper assembly assists in feeding material with a tendency to bridge or clog by tamping powder into the wheel slots. Turning the hopper off actuates a pressure relief valve to release pressure from the canister. Rapid pressure release reduces residual powder flow to reduce accumulation in the line. An alpha-numeric display shows hopper conditions, including control mode, actual and set-point wheel rpm. The feeder is operated in console (semi-automatic) mode, which enables automated "feed-on" or "feed-off" in response to the presence or absence of a feed request from the process control system.

Although using methane as carrier gas would ensure good gas-solid mixing and avoid introducing additional components in the feed to the reactor, the powder is delivered with Argon as carrier gas because the feeder is not designed to handle combustible gases. Throughout this study, an Argon carrier gas flow rate of 4.2 l/min has been suitable in ensuring steady and consistent powder feeding. Furthermore, the feeder has been found to be adequate only for feeding materials greater than 10 μm in particle size. Attempts to feed finer size powder result in clogging of the wheel and exit port.

The cover of the powder canister has been retrofitted to accept a transfer vessel. Both the cover and the transfer vessel have isolating ball valves that are opened only during replenishing operations. Charging is done by first filling the transfer vessel with the desired powder in a moisture-free, continuously Argon-purged glove box, sealing the vessel, and then connecting the vessel outlet fittings to the canister cover inlet. The vessel inlet fittings are then connected to a low pressure nitrogen supply. The inlet and outlet ball valves of the transfer vessel and the inlet valve of the canister cover are opened to commence transfer of the powder. All the valves are closed upon completion, enabling transfer of the powder with virtually no exposure to the atmosphere.

Calibration of the powder feeder is done by setting the wheel speed, collecting the powder over a predetermined period of time (on the order of a minute) in a porous stainless steel (SS) 5 μm filter cup and weighing the collected powder. The feed rate in g/min for the materials used in this study is a linear function of the wheel speed in rpm.

2.2.3 Post-Plasma Cooling Chamber and Gas Discharge System

The plasma reactor is mounted on top of a post-plasma cooling chamber assembly, as illustrated in Figure 2-4. The chamber is made of carbon steel and is 20 in. long with an I.D. of 6.065 in. and an O.D. of 6-5/8 in. It has a water-cooled wall to help cool the plasma effluent and to facilitate rapid quenching of solid and gaseous reaction products. The chamber cooling coils consist of three different sections of ¼ in. copper tubing wrapped helically around the chamber in parallel. The individual coil loops are soft-soldered to one another as well as to the chamber wall. The chamber is equipped with two 1 in. NPT ports located just below the top flange and on diametrically opposite sides and with two ¾ in. NPT ports 90° from the 1 in. ports, also diametrically opposed to one another. The 1 in. ports are connected to a pressure relief system and also serve as inlet ports for secondary gas injection when desired. One ¾ in. port, located midway down the length of the chamber, is used for insertion of a Type K thermocouple while the other, just above the bottom flange, is connected to a pressure sensor and doubles as a gas sample collection port.

A steel flange with a water-cooled channel on which the plasma reactor is mounted forms the top cover of this chamber. This top steel flange cover is seated on a matching steel flange welded to the chamber. The chamber bottom consists of a similar steel flange welded to the chamber, a matching steel flange which rests on a supporting aluminum plate, a removable brass flange and a small brass flange fitting for supporting the sample collection probe (Figure 2-4). The small brass flange fitting allows variable insertion lengths of the sample collection probe into the cooling chamber. It has two inner o-rings that act as rod seals against the wall of the probe. The removable brass flange contains two open channels inside: a lower channel for water cooling and an upper one for pulling vacuum. The effluent gas from the reactor is diverted through a layer of porous 100 μm, 1/8 in. thick SS filter disk which forms the top cover of the vacuum channel. Solid products that are not collected through the probe are deposited on this sintered disk at the bottom of the cooling chamber.

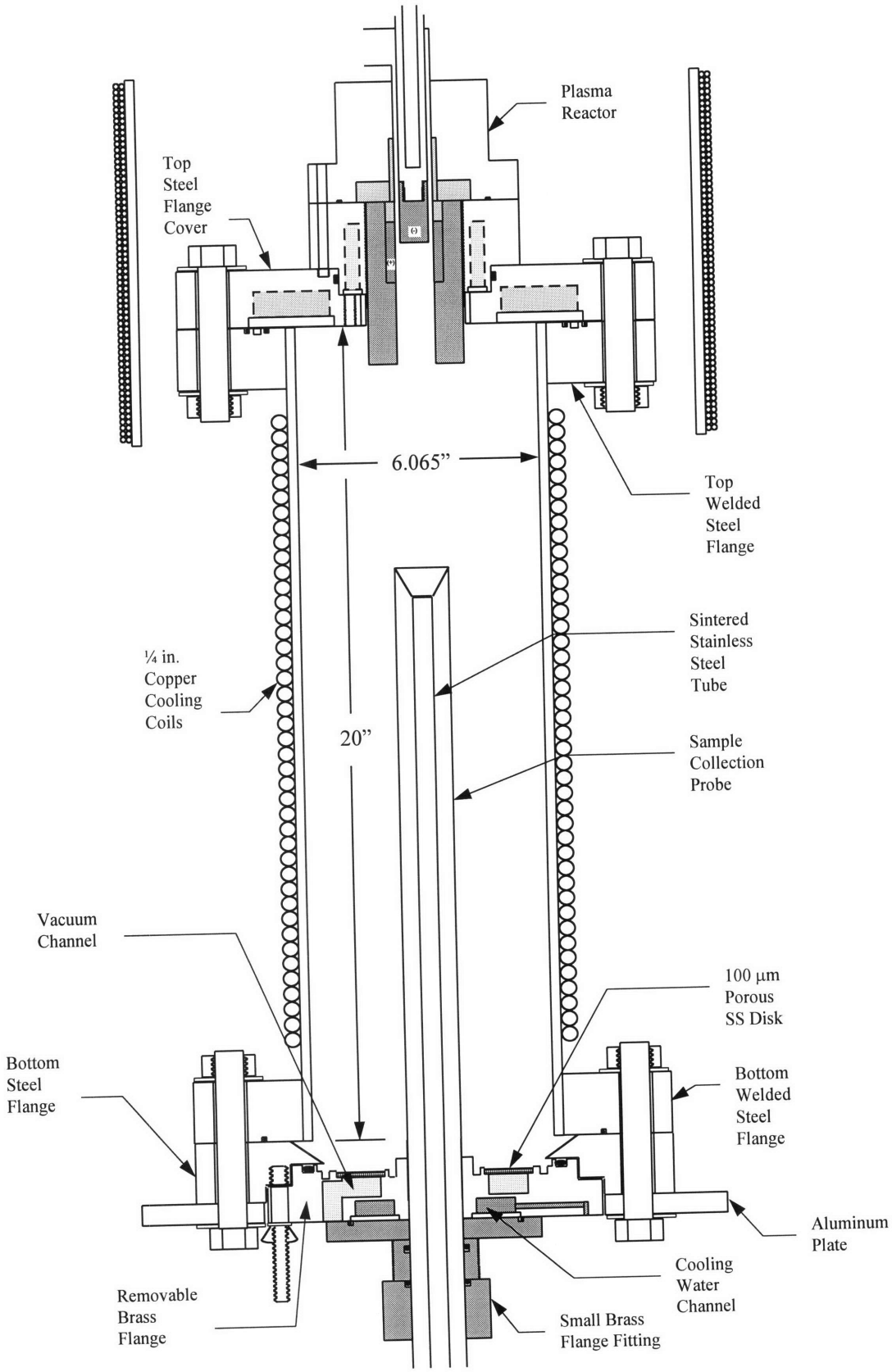

Figure 2-4. Schematic Representation of Post-Plasma Cooling Chamber Assembly

The gaseous products are aspirated from the chamber with two parallel-connected 500 l/min mechanical vane vacuum pumps through the porous disk, a filter train downstream of the chamber and a pressure control valve. Solids still entrained in the gaseous stream are retained in the filter train which consists of two separate filter units with stainless steel housing connected in series, followed by two smaller tee-type in-line filters connected in parallel. The filter immediately downstream of the chamber has a 10 in. long, 20 μm pleated cartridge-type element while the second one has a 10 in. long, 5 μm element. Both filter elements are discarded and replaced after every run. The in-line tee-type filters which act as final filters to remove residual solids have sintered SS elements which are cleaned after each run. The gases discharged from the vacuum pumps pass through a 12-gallon surge tank, which eliminates pressure pulsations and acts as a knock-out vessel for entrained pump oil, and then through a dry test meter before finally exiting to the ventilation stack.

The pressure inside the chamber is maintained at 1 atmosphere independent of inlet gas flow by controlling the exhaust rate of the effluent gases with a throttling valve. A stepper motor-powered butterfly valve, MKS Type 253A, with a 1.27 in. I.D. is mounted on a 1 in. line upstream of the intake of the vacuum pumps. An MKS Type 252 Exhaust Valve Controller takes a DC voltage signal from the pressure sensor, compares it to the set point and positions the butterfly valve to drive the actual pressure to the set pressure by modulating the gas flow from the chamber. The pressure sensor, connected to the chamber via the lower ¾ in. port, is an electronic manometer, MKS Baratron® Type 227A Pressure Transducer, operating on the variable capacitance technique, which converts a 0-1000 mm Hg pressure input to a 0-10 V DC output. Power to the transducer is supplied by an MKS Baratron® Type PDR-C-1B Power Supply which also serves as a readout unit.

2.2.4 Sample Collection System

The sample collection system consists of a movable, water-cooled and gas-quenched cylindrical probe that is inserted through and mounted at the center of the cooling

chamber bottom. The distance of separation between the exit of the anode nozzle of the plasma reactor and the entrance tip of the probe is adjustable. The nozzle exit-to-probe inlet distances used in the experimental runs are 14 in., 10 in., and 5 in. The tip of the probe is funnel-shaped to increase solids collection.

The probe, the top part of which is shown in Figure 2-5, consists of four concentric tubes: a 33.9 in. long, inner SS tube (¾ in. O.D. by 0.035 in. wall thickness) jacketed by an outer SS tube (1-3/8 in. O.D. by 0.035 in. thick) with a middle SS tube (1-1/8 in. by 0.020 in. thick) serving as water flow divider and an innermost 5 μm sintered SS tube (5/8 in. O.D. by ½ in. I.D.) inserted into the inner tube. Cooling water flows in from the bottom, up through the annular region between the outer and middle tubes, and down through the annular space between the middle and inner tubes. Through the innermost sintered tube, Argon is injected radially to the probe axis throughout its length. Argon quench gas is also delivered through a 0.6 in. long o-ring sealed section of the sintered tube at its probe tip end via two 1/8 in. O.D. by 0.010 in. thick SS tubes. The probe is designed to quench 6 l/min of hot gases at 1750 K to 750 K with 25 l/min of quench gas. The Argon quench gas flow in the experimental runs is typically 18 l/min while the Argon radial gas flow is 6 l/min. During a run, the probe is continuously purged with an additional 10-15 l/min Argon through the quench line, except during the sample collection period. The flows of quench and radial gases are continuous throughout the run.

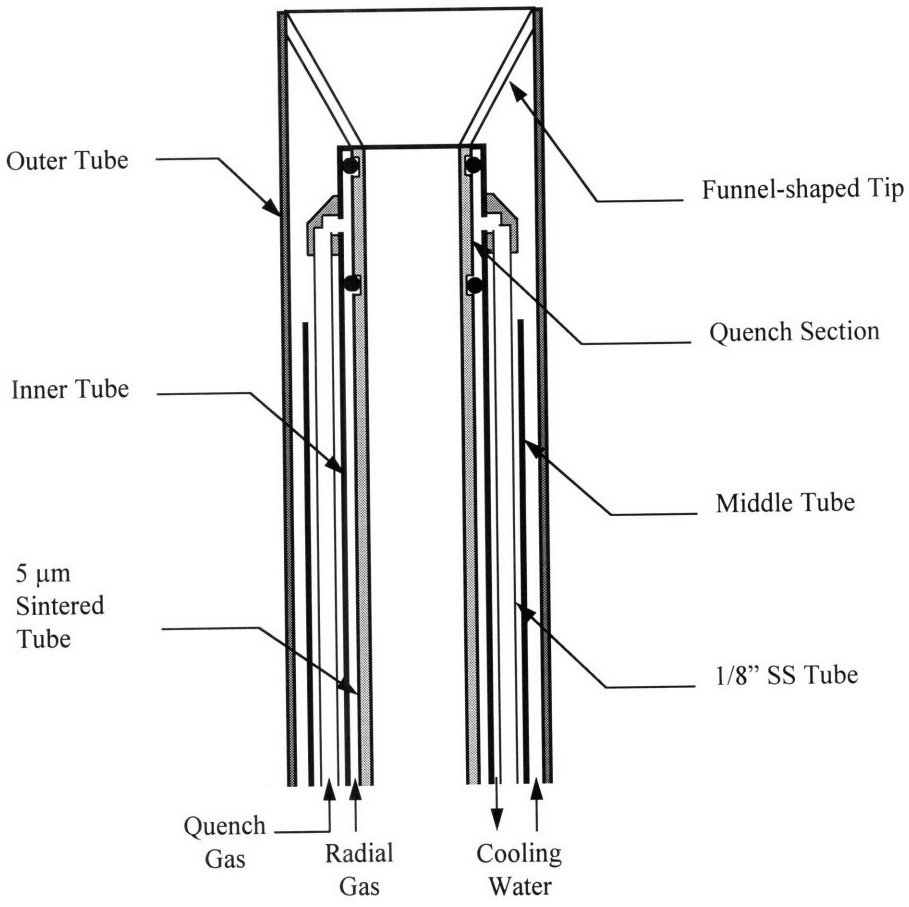

Figure 2-5. Schematic Representation of Top Section of Sample Collection Probe

Solid samples are collected in a cylindrical filter cup inside the solid sampler located downstream of the probe, as depicted in Figure 2-6. The filter cup is made of 5 μm sintered SS and is 1½ in. I.D. by 1¾ in. O.D. by 3½ in. long. It is held in place by a cylindrical fitting that slides into the top ¾ in. of the cup which is solid. Two o-rings act as rod seals between the outer wall of the fitting and the inner wall of the cup. The fitting is connected by a straight tube to the outlet of the probe. Gas flows through the porous cup and is contained by the solid sampler which is made of a 4 in. long, 2 in. nominal diameter stainless steel pipe nipple capped on both ends. The gas and solid product samples enter the sampler via the tube inserted through the removable top cap while the solid-free gas leaves through the fixed bottom cap. The inlet and outlet of the sampler are fitted with isolating ball valves which are open during the run and are closed right after

the run. The sampler is disconnected when the run is over and transferred to a glove box for sample preparation and analysis. The glove box is purged with Argon for 2 to 3 hours before the sampler is opened and the sample prepared for analysis.

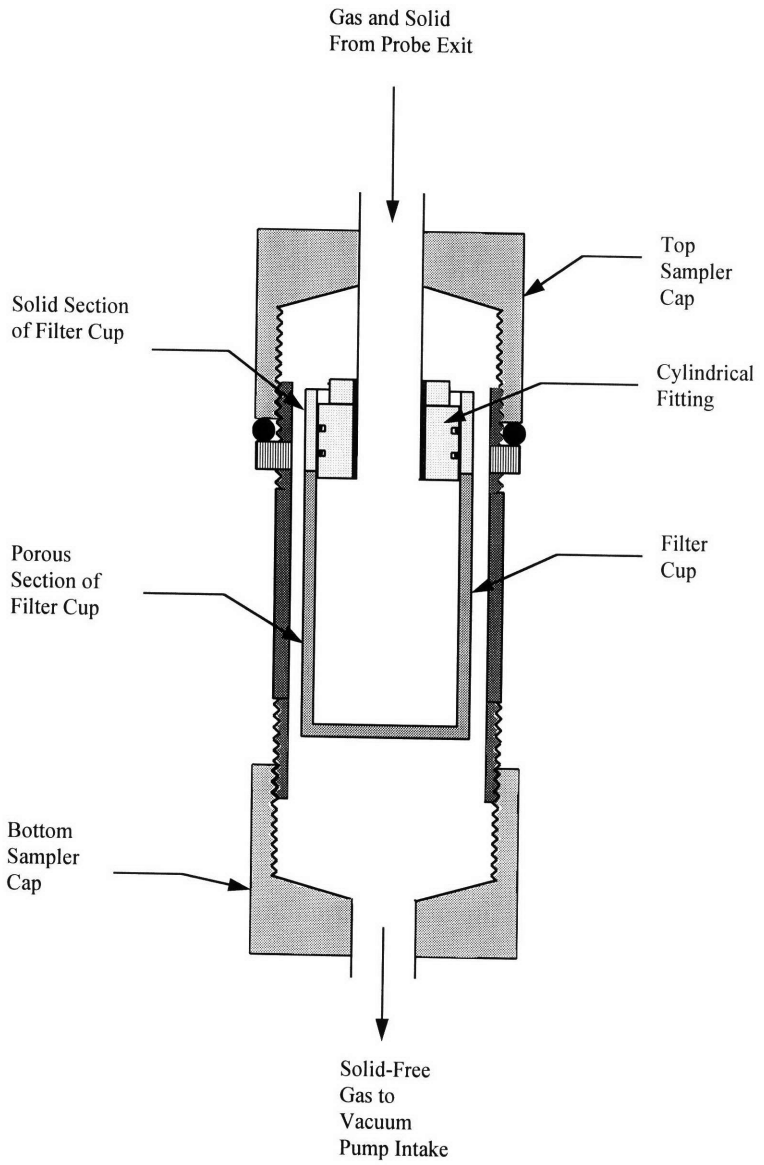

Figure 2-6. Schematic Representation of Solid Sampler

The gaseous products are withdrawn for sampling with a Parker MB-41 12 l/min vacuum pump from either of two sampling points: the bottom of the chamber through the same ¾ in. port connected to the pressure sensor or the exit of the probe at a tee

connection upstream of the solid sampler (Figure 2-1). The gas sample is typically withdrawn from the latter sampling point. An in-line gas purifier with a replaceable 5 μm sintered bronze cartridge filter removes solids from the gaseous stream at the sampling pump intake. The filter cartridge is cleaned after every run. The pump discharges the gas through a three-way solenoid valve S2 (Figure 2-1) normally open to a Teledyne Model 326AX Oxygen Analyzer, which vents the gas to the exhaust stack. The oxygen content of the gas product is monitored by the analyzer before, during and after the run, except during the sample collection period. When sample collection is initiated, solenoid valve S2 diverts the gas flow from the oxygen analyzer to a 250-ml gas sampling bulb, which is connected to the intake of the two 500 l/min vacuum pumps. This enables inclusion of the gas sample flow with the bulk gas flow in total gas flow measurements made with the dry test meter. The glass sampling bulb is equipped with teflon stopcocks and a septum port for withdrawal of a sample with a gas syringe through a plug-type septum for analysis by gas chromatography (GC). The upstream solenoid valve S2 redirects the gas flow to the oxygen analyzer at the end of the sample collection period while the normally open solenoid valve S3, located downstream of the bulb, closes. The inlet and outlet teflon stopcocks are closed at the end of the run before disconnecting the sample bulb for transport to the gas chromatographs.

2.2.5 Cooling Water System

Cooling water is supplied throughout the entire experimental system to remove excess heat from various parts of the system. There are two cooling water subsystems, each with its own water pump: a reactor subsystem for cooling the plasma generator, top steel flange cover, cooling chamber and removable brass flange, and a subsystem for cooling the sample collection probe. The typical cooling water flow rates are 15 gpm at a delivery pressure of about 90 psi for the reactor subsystem and 15 gpm at a delivery pressure of 120 psi for the probe subsystem. The total flow rate in each subsystem is measured with a 1 in. in-line turbine-type flow meter with a digital readout, GPI Model

A104GMA100NA1. Table 2-3 gives the distribution of the flow rates for the cooling water system.

Table 2-3. Distribution of Cooling Water Flow

Cooling Water Subsystem	Cooling Water Flow Rate, gpm
1. Plasma Generator	8
2. Top Steel Flange Cover	3
3. Cooling Chamber	3
4. Removable Brass Flange	1
A. Reactor Subsystem (= 1 to 4)	15
B. Sample Probe Subsystem	15

2.2.6 Data Acquisition and Process Control System

Measurements of arc voltage, arc current, start gas flow, main gas flow, secondary gas flow, chamber pressure and gas and water temperatures are recorded by the data acquisition system while the initiation and termination of probe purging, gas and solid sampling, and the termination of powder feeding and power input are controlled by the process control system. The data acquisition and process control system consists of a plug-in Keithley Metrabyte DAS-1602 data acquisition Analog/Digital (A/D) board installed on a 100 MHz 486 PC and a windows-based software package, LABTECH NOTEBOOKpro version 8.1. The 12-bit A/D board has 16 single-ended input channels, 32 digital input/output (I/O) channels, a maximum sample rate of 100 kHz per channel, and input voltage ranges of ±10, ±5, ±2.5, and ±1.25 V DC. Suitable analog input voltage signals are routed to the A/D board by way of a screw terminal accessory board (Metrabyte STA-MB), to which all input leads are connected. Because the 0-160 V arc voltage is too high for direct input to the A/D board, it is first converted to a 0-10 V signal using an ActionPak® AP4380-0000 isolating signal conditioner. Similarly, the 1 mV per A output of the 80i-kW current probe (0-1 V range for 1000 A maximum), which is too low and prone to interference by background noise, is amplified and scaled to a 0-

10 V signal by another signal conditioner, ActionPak® AP4380-2000. The 0-10 V output of the pressure transducer is proportional to the chamber pressure in mm Hg and is used as input to the A/D board. The 0-5 V output signals of the mass flow controller for the main gas flow and the mass flow meters of the start and secondary gas flows are also proportional to the gas flow rates in l/min and are used as direct inputs to the A/D board. A Keithley Metrabyte EXP-1600 expansion multiplexer/amplifier multiplexes 16 differential analog input channels into one analog input of the A/D board with signal amplification, filtering and conditioning. The output signals from Type K thermocouples at various inlet and outlet gas and water locations are conditioned by the EXP-1600 via a field wiring accessory, FWA-EXP, for input to the A/D board as temperature measurements. The system records measurements of the arc voltage, the arc current, the product of arc voltage and arc current, which is arc power, and the temperature at various points in the system at a 10 Hz sampling frequency for the duration of each run. Chamber pressure, and main, start, and secondary gas flow rates are recorded at a rate of 1 Hz for the run duration.

The process control system enables sampling only when fully developed flows of reactants have been established in the plasma, which is a prerequisite to steady-state operation. It also automatically terminates the run. Timed triggering of the plasma stop, powder feeder on/off and solenoid valves S1, S2, S3, and S4 (Figure 2-1) used for sampling and probe purging is accomplished by software control. Digital signals are sent to individual on/off solid state relay modules, type OAC5A, mounted on a Keithley Metrabyte SRA-01 solid state I/O accessory board, through the digital I/O channels of the A/D board, according to a run schedule.

2.2.7 Equipment Safety Considerations

In view of the explosion hazards associated with conducting experiments involving combustible gases such as CH_4, H_2 and CO, the plasma reactor and cooling chamber are housed inside a room designed and built to contain fragments in the event of an explosion. This fragmentation containment room is vented via a sheet metal duct into a

steel chimney with a combination ejector system and fan exhausting to the top of the building. The room is also designed with adequate air flow to dilute the effluent gases to 25% of the Lower Explosive Limit (LEL) at 1 atmosphere pressure. At a design maximum methane flow rate of 5 ft^3/min (cfm), the hydrogen production rate is twice this rate or 10 cfm. The LEL of H_2 is 4% and dilution to 25% of LEL requires the effluent gases to be diluted to 1%. This entails a total exhaust rate of 1000 cfm for safe emission. An opening at the bottom of the room allows for a 1000 cfm flow of ventilation air for this purpose. The exhaust of the vacuum pumps, after exiting the dry test meter, is directed to the duct leading to the steel chimney and diluted with the room ventilation air.

The containment room has nominal dimensions of 1½ ft. by 3 ft. by 11 ft. tall and is constructed with access from three sides. Both 3-ft. wide sides have 8-ft. high, 1/8 in. thick sliding aluminum doors. Access to the bottom part of the set-up is available from these two sides, with the bottom of the cooling chamber mounted 5 ft. from ground level. The topmost 3-ft. sections above the sliding doors have fixed aluminum panels. The 1½-ft. wide front side of the containment room has Dutch style 1/8 in. thick aluminum swinging doors consisting of a lower 7-ft. high section and an upper 3-ft. high section. The opening at the bottom of the lower swinging door for air inflow has an area of 0.785 ft^2. Rubber u-channel guides are installed along the perimeter of the doors to minimize air inflow through gaps along the length of the room and to force air inflow from the bottom instead. A fixed aluminum panel forms the back wall of the room against the plaster wall of the laboratory. A combustible gas monitor (1000 ppm CH_4 sensitivity) is installed inside the room to alert the operator of any gas leakage.

The cooling chamber is also equipped with a pressure relief system to minimize damage to equipment in case an explosion occurs inside the chamber. The maximum design pressure of the 6-5/8 in. O.D. by 0.280 in. thick wall by 20 in. long chamber is 40 psig at a shell temperature of 811 K (1000°F) and 140 psig at a shell temperature of 616 K (650°F). The worst case relief scenario occurs with a 4% H_2 / 96% air mixture, which has a relief requirement of 0.6 kg/s. This requires at least two 1 in. diameter rupture disks with a burst pressure of 35 psig. Since available 1 in. rupture disks have a minimum burst pressure of 60 psig, 1½ in. diameter disks are used instead to satisfy the 35 psig

burst pressure requirement. To avoid accidental damage to the disks during process upsets, two pressure relief valves, each with a flow coefficient, C_v, of 4.70 at full poppet opening and a cracking pressure of 20 psig, are installed in parallel with the rupture disks. Each rupture disk/relief valve combination is installed on one of the two 1 in. NPT ports on the upper section of the cooling chamber and is mounted to vent upwards.

In addition to the safety interlock on the control console of the plasma generator system, flow switches are installed on the cooling water outlet lines of the top steel flange, cooling chamber, removable brass flange and sample collection probe as part of an alarm system to warn the operator of cooling water failure. This alarm system is also provided with a safety interlock between the methane supply and a Dwyer Model 3002 Photohelic® Differential Pressure Switch/Gage installed on the exhaust chimney. In the event of inadequate draft due, for example, to a fan failure, a solenoid valve is actuated by the pressure switch, shutting off the supply of methane to the reactor and purging the system with Argon. A combustible gas monitor (1000 ppm CH_4 sensitivity) is also located just above the methane supply tank to detect leakage in the laboratory.

2.3 Experimental Procedure

The procedure for operation of the apparatus entails a preparation stage (typically lasting for about half an hour), the actual operation (lasting for only about 5 minutes) and a post-operation stage for disposing the excess reaction products and for resetting the reactor to its original configuration (lasting for 3-5 hours).

2.3.1 Preparation of Reactor

Cooling water is admitted into the system by opening the main inlet valves to the reactor and probe subsystems. Turning on the power to the control console activates the water flow switch to the plasma generator system and the cooling water alarm system. The audio alarm goes off when the two water pumps are turned on. The flow rate in each subsystem is typically 15 gpm at delivery pressures greater than 80 psi (Table 2-3). The system is then inspected for any signs of water leaks.

The data acquisition and control system is started up by switching on the power to the computer, voltage and current signal conditioners, mass flow meters and flow controller, and pressure controller and readout, which need about a 15 minute warm-up time. The bench multimeter for measuring voltage is turned on and switched to the ohmmeter function. The shrouded plugs of the leads to the anode and cathode are inserted into a pair of jacks connected to the voltage signal conditioner input and to the multimeter input to verify that the leads are connected to the electrodes. This effectively measures the resistance of the power supply, which, at the 328 OCV configuration, is typically ~360 Ω. The jacks are then unplugged to prevent potential damage to the signal conditioner when the arc is initiated with the high frequency oscillator. The handheld multimeter is also turned on and switched to the voltmeter function to accept the current probe output. The current probe leads are plugged into another pair of input jacks connected to the other signal conditioner and to the handheld multimeter. The current probe is adjusted to read zero and is not clamped onto the overhead power line until after the arc is struck to avoid potential damage from the high frequency discharge. An applications setup on the LABTECH NOTEBOOKpro software is initiated which activates the solid state relays connected to the plasma stop switch, powder feeder switch and the solenoid valve for probe purging.

The system is always purged of oxygen before introducing methane. The oxygen analyzer is turned on and, after a few minutes of warm-up, is calibrated with room air. A three-way valve on the inlet of the gas sampling pump is switched from downstream of the probe to a line open to the atmosphere. The gas sampling pump is actuated, drawing air into the oxygen analyzer, which is then calibrated to read 21%. After calibration, the three-way valve is switched back to the probe exit line. The main Argon supply is then opened. Toggle valves on the start gas, quench gas and radial gas inlets are then opened manually. Argon is admitted into the system as follows: about 20 l/min as plasma start gas, 18 l/min as quench gas, 6 l/min as probe radial gas and 10-15 l/min as probe purge gas. The Argon supply pressure is maintained at 30 psi by a pressure regulator. The vacuum pumps are switched on and the system is maintained at 1 atm and allowed to be purged of oxygen with Argon. When the oxygen analyzer reads 0% O_2, the methane tank

valve is opened and a tee-purge adapter connected to the Argon supply is closed. The methane toggle valve on the console is opened but the mass flow controller is set to zero.

Power to the powder feeder is then switched on. The wheel speed is set at a low value of ½ rpm by default. The software initiation procedure effectively has the feeder in the on position but the control has to be set to the console mode to initiate feeding. To prevent powder feeding before the run, the feeder is set to local control. The powder carrier gas flow meter valve is opened and set to a flow rate of 4.2 l/min Argon. The isolating ball valve at the inlet of the solid sampler downstream of the probe is initially closed to prevent solid particles from falling into the filter cup. Once the probe purging with Argon is initiated, this inlet valve is opened and the door to the reactor room closed.

The power switch on the remote control panel is turned on to activate the fans on the main power supply unit. The power supply to the solenoid is also switched on and the current should read 21 A. The weld and start controls of the main power supply are set to zero. The system is then ready for an experimental run.

2.3.2 Reactor Operation

To start an experimental run, the power start switch on the console is turned on to energize the electrodes. The OCV of 328 V will register on the voltmeter on the remote control panel. The arc is initiated with the plasma start switch on the console which activates the high frequency oscillator. If the discharge fails to initiate, the procedure is repeated after a few seconds. An Argon plasma is indicated by voltage and current readings on the analog voltmeter and ammeter on the remote control panel. The voltage is typically 20 V and the current 600 A. The current probe is then clamped onto the overhead power line and the electrode leads plugged into the jacks on the voltage signal conditioner box. This gives digital readings of the voltage and current on the bench and handheld multimeters, respectively.

The powder feeding is initiated by switching to console control. The gas to the plasma reactor is replaced with methane by gradually increasing the setting of the mass flow controller and slowly closing the start gas rotameter valve. As methane displaces

Argon in the plasma, the arc voltage will rise. To prevent the voltage from rising above the design load voltage of 160 V and the arc from being extinguished, the current is increased steadily to match the increase in methane input using the weld control on the remote control panel. During runs when a full methane flow to the plasma reactor is desired, the Argon start gas is shut off completely. At the same time that the plasma gas is switched over to methane, the wheel speed of the powder feeder is increased gradually. When the desired settings for the powder feed rate, methane flow rate and arc current are reached, the data acquisition and control sequence is initiated from the software application set-up. The entire switchover typically takes two to three minutes and the actual control sequence lasts for only one minute. Figure 2-7 shows the control sequence of reactor operation. The data acquisition and process control sequence is initiated at time zero.

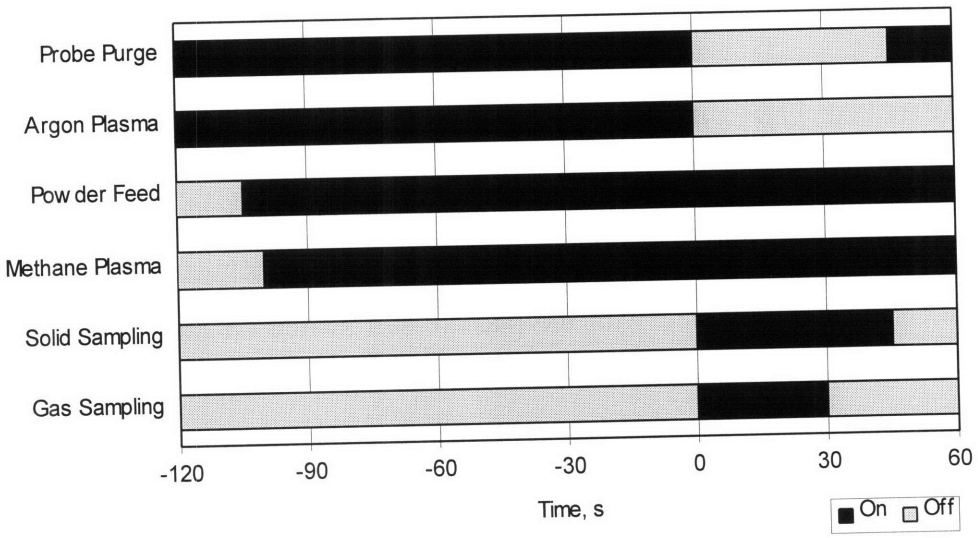

Figure 2-7. Control Sequence of Reactor Operation

The sampling protocol consists of a 45-second period of solid sampling and a 30-second period of gas sampling, simultaneously initiated after establishing the desired gas

flow and solid feed rates into the plasma. This is accomplished with timed triggering of solenoid valves using the solid state relays connected to the digital I/O channels of the A/D board. Solenoid valve S1 (Figure 2-1) is installed downstream of the sample collection probe and connected to the intake of the vacuum pumps. Normally closed, it opens at the start of sampling. To avoid a sudden change in chamber pressure when sampling starts, a regulating valve on the probe outlet line is kept closed and gradually opened when the control sequence is initiated. A three-way solenoid valve S2 allows normal gas sample flow to the oxygen analyzer but diverts the flow to the gas sampling bulb upon commencement of gas sampling. Solenoid valve S3, installed downstream of the gas sampling bulb, opens during gas sampling and closes two seconds before the end of the 30-second period. Solenoid valve S4, which is normally open, admits Argon purge gas through the quench line to the probe. This valve shuts off during the solid sampling period and reopens at the end of the 45-second period. The powder feeder and power to the plasma are turned off automatically at the end of the one-minute sequence. The total effluent gas flow is monitored and recorded by the operator at 15-second intervals by taking readings from the dry test meter.

When the power to the arc goes off, the Argon rotameter valve is opened to ensure a flow of about 20 l/min and the methane mass flow controller valve is closed. The solenoid power supply and gas sampling pump are turned off. The teflon stopcocks on the gas sampling bulb are closed, prior to disconnection. The inlet and outlet ball valves on the solid sampler are also closed in preparation for disassembly. The current probe is taken down and the arc voltage leads disconnected from the signal conditioner box. The probe purge valve S4 is shut off through the application set-up. The valve on the methane supply tank is closed and the tee-purge adapter is opened to purge the methane supply line with Argon. The mass flow controller valve is opened again to purge the reactor supply line. The system is allowed to cool down until the temperature reading on the chamber wall is below 100°C. All gas and cooling water flows are then turned off and the vacuum pumps shut down. The analyzer, signal conditioner, multimeters, pressure controller, and mass flow meters and controller are turned off, concluding the run.

2.3.3 Post-Operation Procedures

The solid products have been found to be highly reactive to air and moisture and to even exhibit pyrophoricity. For example, opening of the chamber and disassembly of the filter train in the open air have, on several occasions, led to spontaneous ignition of the solids. Thus, several precautions are observed not only in sample preparation but also in the disposal of the bulk solids produced.

The solid sampler is disconnected from the system and placed inside a 20¾ in. by 30½ in. by 36 in. plexiglass glove box for later sample preparation. The glove box is kept moisture-free with dessicants and is equipped with a Mettler analytical balance. The glove box is continuously purged with Argon for at least two hours before the sample is handled. The gas sampling bulb is disconnected and the gas analyzed by GC.

The filter train downstream of the probe is removed and placed inside a 21½ in. by 24½ in. by 33¾ in. glove box, which is purged continuously with nitrogen for at least an hour before the filter is disassembled. Virtually all the solids are collected on the 20 μm filter cartridge and hardly any solids are collected on the 5 μm filter. The solids are brushed from the filter cartridges and housing walls and retained on a piece of foil. When the glove box is opened, the collected solids are slowly disposed of in small amounts in an excess of water. The ignition of these solids upon contact with water gives off bright, dazzling lights, indicative of the presence of magnesium. The filter cartridges are washed with water prior to disposal. In the case of the in-line filters, the stainless steel cartridges are cleaned with water in a sonicator. New cartridges are installed and the filter train is then reassembled and leak-tested prior to reinstallation.

While purging the glove box, the probe is retracted from the chamber by loosening the small brass flange fitting. The probe is flushed and cleaned with nitrogen and Argon. The removable brass flange is lowered and supported by wing nuts on the three threaded rods connected to the bottom flange. Solids on the chamber walls and bottom are removed, collected and disposed of in the same manner as the solids from the filters. The sintered SS disk on the brass flange is cleaned with water in a sonicator.

The reactor cooling water subsystem is drained of cooling water and the cathode assembly of the plasma reactor is disconnected from the water-cooled power lines. The graphite anode is unscrewed from the anode holder from below. The anode insert is removed and the anode nozzle cleaned of solid deposits, which are hard and flaky in the case of MgO feed and soft but plentiful in the case of CaO feed. The anode insert and cathode tip are weighed and then replaced with brand new parts. The cathode assembly is reinstalled and the anode is screwed back into its holder until its top face touches the bottom face of the low density alumina in the cathode assembly. Because the nylon part of the cathode assembly can deform to some degree, the cathode tip is visually checked from below for concentricity with the anode nozzle and centered manually, if needed.

The o-ring and porous disk are then replaced on the removable brass flange and the chamber is sealed. The filter train is reinstalled and the probe is inserted into the chamber to the desired height. After solid sample preparation, the filter cup is sonicated in water to remove residual solids. The inlet to the sampler is flushed with nitrogen and a clean cup is installed before the sampler is reassembled and connected between the probe and vacuum pump intake. The inlet ball valve is closed to prevent solids from falling into the sampler and the outlet valve is left open. The gas sampling bulb is fitted with a new septum stopper and reinstalled. Finally, the system is tested for gas and water leaks.

2.4 Analysis of Products

The gas sample composition is determined by Gas Chromatography (GC) analysis. The solid sample is collected from the filter cup and prepared for analysis inside the Argon-purged glove box to prevent undesirable reactions with oxygen or moisture. The metal and metal carbide contents of the solid sample are determined indirectly by gas chromatographic measurement of the hydrogen and acetylenes evolved upon hydrolysis according to Reactions (1-11), (1-12), (1-5), (1-6) and (1-20). The standard gas mixtures used for quantification are provided by Scott Specialty Gases and have the following compositions:

Table 2-4. Composition of Standard Mixtures

Standard Mixture #1	Ne	99.996 %
	Accuracy of Analysis	± 2%
Standard Mixture #2	Ne	0.496%
	He	Balance
	Accuracy of Analysis	± 2%
Standard Mixture #3	Ar	0.503%
	He	Balance
	Accuracy of Analysis	± 2%
Standard Mixture #4	CO	0.514%
	CO_2	0.505%
	H_2	0.511%
	O_2	0.504%
	N_2	Balance
	Accuracy of Analysis	± 2%
Standard Mixture #5	CH_4	14.8 ppm
	C_2H_6	14.9 ppm
	C_2H_4	15.2 ppm
	C_2H_2	16.6 ppm
	C_3H_8	15.2 ppm
	C_3H_6	15.1 ppm
	C_3H_4	16.3 ppm
	n-C_4H_{10}	14.7 ppm
	N_2	Balance
	Accuracy of Analysis	± 10%
Standard Mixture #6	n-C_4H_{10}	15.0 ppm
	i-C_4H_{10}	14.9 ppm
	i-C_4H_8 (isobutylene)	15.0 ppm
	1-C_4H_8 (1-butene)	14.9 ppm
	cis-2-C_4H_8	15.0 ppm
	trans-2-C_4H_8	14.5 ppm
	1,3- C_4H_6	14.9 ppm
	Ethylacetylene	15.5 ppm
	N_2	Balance
	Accuracy of Analysis	± 10%

Total Mg and/or Ca content in the hydrolyzed sample is measured using Inductively Coupled Plasma - Atomic Emission Spectrometry (ICP-AES) and Mass Spectrometry (ICP-MS) analyses. Standard solutions of 1, 10 and 100 ppm Mg and 1, 10

and 100 ppm Ca are prepared from 1000 ppm Mg and 1000 ppm Ca plasma standard solutions in a matrix of 2% HNO_3.

Dilute hydrochloric acid (HCl) and dilute nitric acid (HNO_3) are used for hydrolysis and dissolution of unreacted oxides. The acid solutions are prepared by diluting 100 ml of concentrated acid to 2000 ml with distilled water to form approximately 0.6 M HCl and 0.8 M HNO_3.

2.4.1 Analysis of Solid Product

Due to fluctuations in the arc power input during the run, the composition of the solid product collected in the filter cup may have varied from layer to layer. Although the product distribution may not have been significantly different because the fluctuations were rapid, the solid sample is mixed to increase homogeneity before taking portions for subsequent analysis. Two separate 5-20 mg portions of the solid product are transferred from the filter cup to two 50-ml flasks and sealed with an S.T. 19/22 joint septum stopper. The remainder of the solid sample is retained in a vial and kept in a dessicator.

For each flask, 1 ml of standard mixture #1 (99.996% neon) is injected as internal standard through the septum port. The head space gas above the solids is analyzed by GC before and after hydrolysis. Hydrolysis is done by injecting 5 ml of dilute HCl into the flask; on some occasions, 1-2 ml of distilled water is first injected to avoid local hot spots and incandescence of the solids. The head space gas is quantitatively analyzed for H_2 and Ne content by withdrawing a 0.1 ml sample and injecting it into a Perkin Elmer Sigma-II gas chromatograph with a thermal conductivity detector (TCD) and with Helium as carrier gas. The H_2 and Ne are separated on a 1/8 in. O.D. by 10 ft. long SS, 60/80 mesh Molecular Sieve 5A column operated at -10°C with a He carrier gas flow of 30 ml/min (at 100°C). Retention times for H_2 and Ne are less than 2 minutes. Analytical quantification is done using standard mixtures #2 and #4.

Analysis for detection, identification and quantification of light hydrocarbon gases (C_1 to C_4 species) in the head space gas is performed by injecting a separate 0.1 ml sample into a Hewlett-Packard 5830A gas chromatograph fitted with a flame ionization

detector (FID) and using Argon as the carrier gas. The sample is injected on a 1/8 in. O.D. by 6 ft. long SS, 0.19% Picric Acid on 80/100 mesh Graphpac GC column connected in series, via an air-actuated six-port column switching valve, to a 1/8 in. O.D. by 6 ft. long SS, 80/100 mesh Porapak T column and then to the FID. The oven temperature is initially set at -5°C and the Argon carrier gas flow is 22 ml/min (at 100°C). CH_4 is carried by the Argon through the two columns into the FID within 6.7 minutes, when the valve is activated. Within the first 6.7 minutes before the valve is switched, the C_3 and C_4 species in the sample are separated on the Graphpac column while the C_2 species have eluted onto the Porapak T column. When the valve is actuated, the second column is bypassed, trapping the C_2 species. A restrictor valve provides a pressure drop equivalent to the second column to maintain the same carrier gas flow rate when the second column is bypassed. The oven temperature is raised to 50°C at a rate of 30°/min, 11.5 minutes after injection, and maintained at 50°C for another 24.5 minutes to complete the analysis. The C_3 and C_4 species then elute from the first column. The valve switch is again activated 23.5 minutes after injection, reconnecting the first and second columns in series to the FID, and the C_2 species elute. Standard mixtures #5 and #6 are used to quantify light hydrocarbon composition.

The pre-hydrolysis analysis always shows some small amounts of acetylene and C_3 species, which presumably result from decomposition of or desorption from the sample. No hydrogen is detected prior to hydrolysis. To correct for the additional hydrocarbons not directly evolved upon hydrolysis, the calculated pre-hydrolysis number of moles is subtracted from the post-hydrolysis number of moles.

After GC analysis of the head space gas, each flask is filled with dilute nitric acid solution and allowed to sit overnight in order to dissolve any unreacted metal oxides. The contents are subsequently filtered and the filtrate diluted to 100 ml with dilute nitric acid and analyzed by ICP-AES or ICP-MS for the total Mg and/or Ca content.

The solid samples are also analyzed for composition, particle size, particle morphology and elemental distribution by X-Ray Diffraction (XRD), Scanning Electron Microscopy (SEM), Transmission Electron Microscopy (TEM), Scanning Transmission Electron Microscopy (STEM) and Energy Dispersive Spectrometry (EDS).

2.4.2 Analysis of Gaseous Product

The gas sample is analyzed for fixed gases as well as for light hydrocarbons. The same Sigma-II gas chromatograph fitted with a TCD and Molecular Sieve 5A column is used to analyze separately for Argon and for H_2 and CO. A 0.05 ml sample is withdrawn from the gas sampling bulb through the septum stopper and injected onto the molecular sieve column at -55°C under a He carrier gas flow of 30 ml/min (at 100°C) to separate Argon from residual O_2 with retention times less than 7 minutes. Standard mixture #3 is used for quantification. Another 0.05 ml sample is subsequently withdrawn and injected into the same column at 50°C to separate H_2, Ar/O_2, CH_4, and CO with a run time of 6 minutes. Quantitative analysis is done with standard mixture #4. Although not done in every run, the gas sample was analyzed for CO_2 in the Sigma-II GC by injection onto a 1/8 in. O.D. by 6 ft. long SS, 80/100 mesh Porapak Q column. No CO_2 was detected in the sample analyzed.

Light hydrocarbon analysis is done utilizing the same method used for headspace gas analysis, described in Section 2.4.1. A third 0.05 ml sample is injected into the Graphpac GC and Porapak T columns of the HP 5830A gas chromatograph fitted with a FID and using Argon as carrier gas. Standard mixtures #5 and #6 are used for determination of light hydrocarbon composition.

2.4.3 Reactant-to-Product Conversion and Uncertainty of Analysis

The magnesium in the MgO feed is converted to Mg metal, Mg_2C_3 and MgC_2, according to Reactions (1-4), (1-2), and (1-3), respectively. The percentage molar conversion of the MgO "Mg" to magnesium metal in the product, $(Mg)\alpha_{MgO}^{Mg}$, is calculated as follows:

$$(Mg)\alpha_{MgO}^{Mg} = \frac{N_{Mg}}{N_{MgO}} \times 100\% \qquad \text{Equation (2-10)}$$

where N_{Mg} is the number of moles of magnesium metal in the sample and N_{MgO} is the total number of moles of magnesium in the sample equivalent to MgO before the reaction. N_{Mg} is equal to the number of moles of hydrogen, $N_{H_2}^{HS}$, in the headspace above the solid evolved upon hydrolysis, according to Reaction (1-12):

$$Mg + 2\,HCl \rightarrow Mg(Cl)_2 + H_2 \qquad \text{Reaction (1-12)}$$

$N_{H_2}^{HS}$ is given by:

$$N_{H_2}^{HS} = \frac{\frac{V_{H_2}^{HS}}{V_{Ne}^{HS}} \times V_{IS} \times f_{IS}}{22{,}412\ \text{ml/mol}} \qquad \text{Equation (2-11)}$$

where V_{IS} is the volume in ml of the internal standard injected into the headspace above the solid and f_{IS} is the purity of the internal standard. $V_{H_2}^{HS}$ and V_{Ne}^{HS}, the volume in ml of H_2 and Ne, respectively, in the headspace gas sample derived from GC analysis are calculated more generally according to:

$$V_i = \frac{A_i}{A_i^{std}} \times V_i^{std} \times f_i^{std} \qquad \text{Equation (2-12)}$$

where V_i = Volume of the species *i* contained in the sample, ml

A_i = Area under peak corresponding to species *i* in the sample

A_i^{std} = Area under peak corresponding to species *i* in the standard mixture

V_i^{std} = Injection volume of standard mixture containing species *i*, ml

f_i^{std} = Mole fraction of species *i* in the standard mixture

With all the magnesium in the product coming from the MgO feed, N_{MgO} is determined from the concentration of the Mg in the filtrate, $[Mg]_f$, given by ICP-AES or ICP-MS analysis as:

$$N_{MgO} = [Mg]_f \times V_f \qquad \text{Equation (2-13)}$$

where V_f is the volume of the filtrate. Thus, $(Mg)\alpha_{MgO}^{Mg}$ can be calculated by combining Equations (2-10) to (2-13) as:

$$(Mg)\alpha_{MgO}^{Mg} = \frac{\left[\frac{\frac{A_{H_2}^{HS}}{A_{H_2}^{std}} \times V_{H_2}^{std} \times f_{H_2}^{std}}{\frac{A_{Ne}^{HS}}{A_{Ne}^{std}} \times V_{Ne}^{std} \times f_{Ne}^{std}}\right] \times V_{IS} \times f_{IS}}{[Mg]_f \times V_f \times 22{,}412} \times 100\% \qquad \text{Equation (2-14)}$$

The percentage molar conversion of MgO "Mg" to Mg_2C_3 in the product, $(Mg)\alpha_{MgO}^{Mg_2C_3}$, is calculated according to:

$$(Mg)\alpha_{MgO}^{Mg_2C_3} = \frac{2N_{Mg_2C_3}}{N_{MgO}} \times 100\% \qquad \text{Equation (2-15)}$$

where the number of moles of Mg_2C_3, $N_{Mg_2C_3}$, in the sample is equal to the number of moles of C_3H_4, $N_{C_3H_4}^{HS}$, in the headspace above the solid evolved upon hydrolysis, according to Reaction (1-6):

$$Mg_2C_3 + 4\,H_2O \rightarrow 2\,Mg(OH)_2 + C_3H_4 \qquad \text{Reaction (1-6)}$$

Correcting $N_{C_3H_4}^{HS}$ for the methylacetylene desorbed from the sample prior to hydrolysis:

$$N_{C_3H_4}^{HS} = \frac{\left[\left(\frac{V_{C_3H_4}^{HS}}{V_{Ne}^{HS}}\right)_{Post-hyd} - \left(\frac{V_{C_3H_4}^{HS}}{V_{Ne}^{HS}}\right)_{Pre-hyd}\right] \times V_{IS} \times f_{IS}}{22{,}412 \text{ ml/mol}}$$

Equation (2-16)

where $\left(V_{C_3H_4}^{HS}\right)_{Post-hyd}$ is the volume of C_3H_4 in the headspace gas sample after hydrolysis and $\left(V_{C_3H_4}^{HS}\right)_{Pre-hyd}$ is the volume of C_3H_4 in the headspace gas sample before hydrolysis. Thus, following the same derivation for $(Mg)\alpha_{MgO}^{Mg_2C_3}$ as $(Mg)\alpha_{MgO}^{Mg}$ gives:

$$(Mg)\alpha_{MgO}^{Mg_2C_3} = \frac{\left\{2 \times \left[\left(\frac{\frac{A_{C_3H_3}^{HS}}{A_{C_3H_4}^{std}} \times V_{C_3H_4}^{std} \times f_{C_3H_4}^{std}}{\frac{A_{Ne}^{HS}}{A_{Ne}^{std}} \times V_{Ne}^{std} \times f_{Ne}^{std}}\right)_{Post-Hyd} - \left(\frac{\frac{A_{C_3H_3}^{HS}}{A_{C_3H_4}^{std}} \times V_{C_3H_4}^{std} \times f_{C_3H_4}^{std}}{\frac{A_{Ne}^{HS}}{A_{Ne}^{std}} \times V_{Ne}^{std} \times f_{Ne}^{std}}\right)_{Pre-Hyd}\right] \times V_{IS} \times f_{IS} \times 100\%\right\}}{[Mg]_f \times V_f \times 22{,}412}$$

Equation (2-17)

Similarly, the percentage molar conversion of MgO "Mg" to MgC_2 in the product, $(Mg)\alpha_{MgO}^{MgC_2}$, is given by:

$$(Mg)\alpha_{MgO}^{MgC_2} = \frac{\left\{\left[\left(\frac{\frac{A_{C_2H_2}^{HS}}{A_{C_2H_2}^{std}} \times V_{C_2H_2}^{std} \times f_{C_2H_2}^{std}}{\frac{A_{Ne}^{HS}}{A_{Ne}^{std}} \times V_{Ne}^{std} \times f_{Ne}^{std}}\right)_{Post-Hyd} - \left(\frac{\frac{A_{C_2H_2}^{HS}}{A_{C_2H_2}^{std}} \times V_{C_2H_2}^{std} \times f_{C_2H_2}^{std}}{\frac{A_{Ne}^{HS}}{A_{Ne}^{std}} \times V_{Ne}^{std} \times f_{Ne}^{std}}\right)_{Pre-Hyd}\right] \times V_{IS} \times f_{IS} \times 100\%\right\}}{[Mg]_f \times V_f \times 22{,}412}$$

Equation (2-18)

The percentage conversion of oxygen in the MgO feed to CO in the gas product, $(O)\alpha_{MgO}^{CO}$, is:

$$(O)\alpha_{MgO}^{CO} = \frac{n_{CO}}{n_{MgO}} \times 100\% \qquad \text{Equation (2-19)}$$

where n_{MgO} is the molar feed rate of MgO to the reactor and n_{CO} is the molar flow rate of CO from the reactor. n_{CO} is given by:

$$n_{CO} = n_{Gas} \times f_{CO}^{Gas} \qquad \text{Equation (2-20)}$$

where n_{Gas} is the total molar flow rate of (Argon-free) gas product from the reactor and f_{CO}^{Gas} is the mole fraction of CO in the Argon-free gas. The gas sample differs in composition from the total gas effluent stream because of the quench and radial gas flows through the probe that introduce more Argon into the gas sample. Therefore, n_{Gas} is taken on an Argon-free basis. This is calculated by subtracting the Argon main gas (in the case of CH_4-Ar plasma), probe quench gas, probe radial gas and powder carrier gas flows from the dry test meter measurement. From GC analysis:

$$f_i = \frac{A_i}{A_i^{std}} \times \frac{V_i^{std}}{V^{sample}} \times f_i^{std} \qquad \text{Equation (2-21)}$$

where f_i = Mole fraction of species *i* in the sample

f_i^{std} = Mole fraction of species *i* in the standard mixture

A_i = Area under peak corresponding to species *i* in the sample

A_i^{std} = Area under peak corresponding to species *i* in the standard mixture

V^{sample} = Volume of the sample, ml

V_i^{std} = Injection volume of standard mixture containing species *i*, ml

The sum of the volumes of all species in the sample excluding Argon is used to determine the mole fraction of CO on an Argon-free basis. Combining Equations (2-12) and (2-21), f_{CO}^{Gas} is given by:

$$f_{CO}^{Gas} = \frac{A_{CO}}{A_{CO}^{std}} \times \frac{V_{CO}^{std}}{\sum_{i \neq Ar}^{i} \left(\frac{A_i}{A_i^{std}} \times V_i^{std} \times f_i^{std} \right)} \times f_{CO}^{std} \qquad \text{Equation (2-22)}$$

Thus,

$$(O)\alpha_{MgO}^{CO} = \frac{n_{Gas} \times \left[\frac{A_{CO}}{A_{CO}^{std}} \times \frac{V_{CO}^{std}}{\sum_{i \neq Ar}^{i} \left(\frac{A_i}{A_i^{std}} \times V_i^{std} \times f_i^{std} \right)} \times f_{CO}^{std} \right]}{n_{MgO}} \times 100\% \qquad \text{Equation (2-23)}$$

The carbon in methane is converted to Mg_2C_3, MgC_2, CO, other hydrocarbons and solid carbon. Since the ratio of MgO molar feed rate, n_{MgO}, to CH_4 molar flow rate, n_{CH_4}, is constant, the molar conversion of CH_4 "C" to product i, $(C)\alpha_{CH_4}^{i}$, can be directly calculated as follows:

$$(C)\alpha_{CH_4}^{Mg_2C_3} = (Mg)\alpha_{MgO}^{Mg_2C_3} \times \frac{3}{2} \times \frac{n_{MgO}}{n_{CH_4}} \qquad \text{Equation (2-24)}$$

$$(C)\alpha_{CH_4}^{MgC_2} = (Mg)\alpha_{MgO}^{MgC_2} \times 2 \times \frac{n_{MgO}}{n_{CH_4}} \qquad \text{Equation (2-25)}$$

$$(C)\alpha_{CH_4}^{CO} = (O)\alpha_{MgO}^{CO} \times \frac{n_{MgO}}{n_{CH_4}} \qquad \text{Equation (2-26)}$$

The percentage molar conversion of CH_4 "C" to solid carbon is determined as the aggregate amount of "non-carbide C", referring to carbon that may be present in the residue from hydrolysis of the solid products, also designated "unhydrolyzable C". The exact composition of this material is not known, but it may consist of carbon-rich tar and various forms of solid carbon such as soot. To determine the contributions of this "non-carbide C" to the overall carbon balance, samples of solid residues from hydrolysis are sent to a commercial laboratory (Galbraith Laboratories) for elemental carbon assays.

The hydrogen in methane is converted to molecular H_2 and, to much smaller extents, to other hydrocarbons. The percentage molar conversion of the CH_4 "H" to molecular H_2 in the gas product, $(H)\alpha_{CH_4}^{H_2}$, is given by:

$$(H)\alpha_{CH_4}^{H_2} = \frac{n_{H_2}}{2n_{CH_4}} \times 100\% \qquad \text{Equation (2-27)}$$

where n_{H_2} is the molar flow rate of H_2 from the reactor. Applying Equations (2-20) and (2-22) to the hydrogen component of the gas product:

$$(H)\alpha_{CH_4}^{H_2} = \frac{n_{Gas} \times \left[\frac{A_{H_2}}{A_{H_2}^{std}} \times \frac{V_{H_2}^{std}}{\sum_{i \neq Ar}^{i} \left(\frac{A_i}{A_i^{std}} \times V_i^{std} \times f_i^{std} \right)} \times f_{H_2}^{std} \right]}{2n_{CH_4}} \times 100\% \qquad \text{Equation (2-28)}$$

In the case of CaO feed, the calcium in CaO is converted to CaC_2 and the oxygen in CaO to CO according to Reaction (1-1). Most of the carbon in CH_4 is converted to CaC_2, CO, C_2H_2, non-carbide C and other hydrocarbons while the hydrogen in CH_4 leaves mostly as molecular H_2 and C_2H_2. Analogous elemental percentage molar conversions, $(h)\alpha_j^i$, of element h in reactant j to product i for CaO reactions with CH_4 are given by the following expressions:

$$(Ca)\alpha_{CaO}^{CaC_2} = \frac{\left\{\left[\left(\frac{\frac{A_{C_2H_2}^{HS}}{A_{C_2H_2}^{std}} \times V_{C_2H_2}^{std} \times f_{C_2H_2}^{std}}{\frac{A_{Ne}^{HS}}{A_{Ne}^{std}} \times V_{Ne}^{std} \times f_{Ne}^{std}}\right)_{Post-Hyd} - \left(\frac{\frac{A_{C_2H_2}^{HS}}{A_{C_2H_2}^{std}} \times V_{C_2H_2}^{std} \times f_{C_2H_2}^{std}}{\frac{A_{Ne}^{HS}}{A_{Ne}^{std}} \times V_{Ne}^{std} \times f_{Ne}^{std}}\right)_{Pre-Hyd}\right] \times V_{IS} \times f_{IS} \times 100\%\right\}}{[Ca]_f \times V_f \times 22{,}412}$$

Equation (2-29)

$$(O)\alpha_{CaO}^{CO} = \frac{n_{Gas} \times \left[\frac{A_{CO}}{A_{CO}^{std}} \times \frac{V_{CO}^{std}}{\sum_{i \neq Ar}^{i}\left(\frac{A_i}{A_i^{std}} \times V_i^{std} \times f_i^{std}\right)} \times f_{CO}^{std}\right]}{n_{CaO}} \times 100\%$$

Equation (2-30)

$$(C)\alpha_{CH_4}^{CaC_2} = (Ca)\alpha_{CaO}^{CaC_2} \times 2 \times \frac{n_{CaO}}{n_{CH_4}}$$

Equation (2-31)

$$(C)\alpha_{CH_4}^{CO} = (O)\alpha_{CaO}^{CO} \times \frac{n_{CaO}}{n_{CH_4}}$$

Equation (2-32)

$$(C)\alpha_{CH_4}^{C_2H_2} = \frac{2n_{Gas} \times \left[\frac{A_{C_2H_2}}{A_{C_2H_2}^{std}} \times \frac{V_{C_2H_2}^{std}}{\sum_{i \neq Ar}^{i}\left(\frac{A_i}{A_i^{std}} \times V_i^{std} \times f_i^{std}\right)} \times f_{C_2H_2}^{std}\right]}{n_{CH_4}} \times 100\%$$

Equation (2-33)

$$(H)\alpha_{CH_4}^{H_2} = \frac{n_{Gas} \times \left[\frac{A_{H_2}}{A_{H_2}^{std}} \times \frac{V_{H_2}^{std}}{\sum_{i \neq Ar}^{i}\left(\frac{A_i}{A_i^{std}} \times V_i^{std} \times f_i^{std}\right)} \times f_{H_2}^{std}\right]}{2n_{CH_4}} \times 100\%$$

Equation (2-34)

and

$$(H)\alpha_{CH_4}^{C_2H_2} = \frac{n_{Gas} \times \left[\frac{A_{C_2H_2}}{A_{C_2H_2}^{std}} \times \frac{V_{C_2H_2}^{std}}{\sum_{i}^{i \neq Ar} \left(\frac{A_i}{A_i^{std}} \times V_i^{std} \times f_i^{std} \right)} \times f_{C_2H_2}^{std} \right]}{2n_{CH_4}} \times 100\%$$

Equation (2-35)

Table 2-5 gives the uncertainty associated with each calculated number based on a propagation of errors analysis. The uncertainty is expressed as a percentage of conversion $(h)\alpha_j^i$. A sample calculation of the uncertainty of analysis is provided in Appendix A.

Table 2-5. Uncertainty of Analysis

Conversion	Uncertainty
$(Mg)\alpha_{MgO}^{Mg}$	±17.1%
$(Mg)\alpha_{MgO}^{Mg_2C_3}$	±26.8%
$(Mg)\alpha_{MgO}^{MgC_2}$	±26.8%
$(O)\alpha_{MgO}^{CO}$	±27.0%
$(Ca)\alpha_{CaO}^{CaC_2}$	±26.8%
$(O)\alpha_{CaO}^{CO}$	±27.0%
$(C)\alpha_{CH_4}^{Mg_2C_3}$	±29.8%
$(C)\alpha_{CH_4}^{MgC_2}$	±29.8%
$(C)\alpha_{CH_4}^{CaC_2}$	±29.8%
$(C)\alpha_{CH_4}^{CO}$	±26.0%
$(C)\alpha_{CH_4}^{C_2H_2}$	±34.0%
$(H)\alpha_{CH_4}^{H_2}$	±26.0%
$(H)\alpha_{CH_4}^{C_2H_2}$	±34.0%

Chapter 3

Experimental Results

A systematic study of the MgO-CH_4-Ar system in the thermal plasma reactor has been undertaken to investigate the formation of magnesium metal and magnesium carbides by the reduction of magnesium oxide with methane under a wide range of experimental conditions. In order to elucidate the mechanisms behind metal and metal carbide formation, the MgO-Ar, MgO-C-CH_4-Ar, and Mg-CH_4-Ar systems have also been studied. In addition, exploratory experiments have been conducted with the CaO-CH_4-Ar and MgO-CaO-CH_4-Ar systems.

3.1 Reactants

Two grades of methane were used in the present study. In all of the runs with the MgO-CH_4-Ar system and in the first four runs with the MgO-C-CH_4-Ar system, Purified Grade 2™ Methane (99% CH_4) was used. In the rest of the experimental runs, a higher grade, Ultra Pure Grade 4™ Methane (99.99% CH_4), was utilized.

The reactant magnesium oxide is fused, -150 +325 mesh (-44 +104 μm) MgO powder from Aldrich Chemical. The purity of the material is 97.3%. Table 3-1 shows its properties, as reported by the supplier.

Table 3-1. Properties of MgO Powder

Appearance	Fine off-white powder	
X-Ray Diffraction Pattern	Conforms to Standard Pattern	
Complexometric Titration	58.7% Mg	
Particle Size Distribution	>140 mesh (107 μm)	2.4%
	>200 mesh (73.7 μm)	64.2%
	>230 mesh (63 μm)	25.7%
	>325 mesh (43.2 μm)	6.9%
	<325 mesh (43.2 μm)	0.8%

Examination of the MgO powder feed under a scanning electron microscope shows that the material is angular. Figures 3-1A to 3-1F are SEM images of the MgO powder at increasing levels of magnification. The length scale is given by the gray bar embedded in each figure. Although only 2.4% of the material is greater than 107 μm according to the particle size measurements, Figures 3-1 and 3-2 show the length of the particles to be typically greater than 100 μm. At higher magnification levels (Figures 3-1C to 3-1F), the particles appear to have non-porous surfaces essentially free of intracrystalline voids and to have micro-particles on them.

The MgO powder has been analyzed for constituent elements by EDS. Aside from Mg and O, Si and Ca have been identified as impurities. The X-ray spectrum of the MgO powder is shown in Figure 3-2. The microparticles on the surface have been determined to be of the same composition as the larger MgO particles by EDS analysis.

The calcium oxide is high calcium metallurgical grade quicklime which has been obtained from Specialty Minerals. The material comes from a deposit of high quality calcium carbonate in Adams, MA and is produced in a fluo-solid type kiln, yielding a granular, free-flowing quicklime of high reactivity. The typical properties of the material are given in Table 3-2, as reported by the supplier. In order to have a material in the -150 +325 mesh size range, comparable to MgO, the granular material has been crushed and sieved prior to use in the experiments.

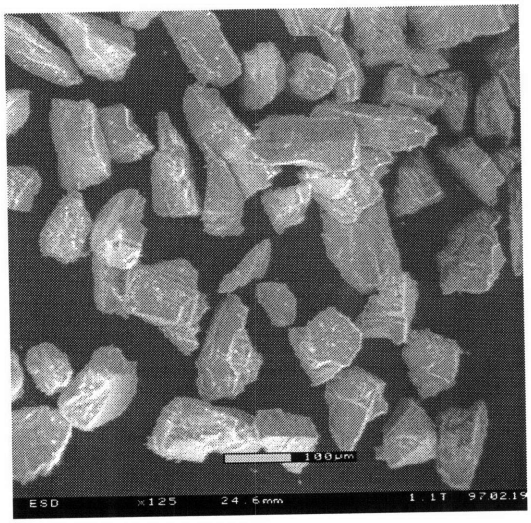

Figure 3-1A. SEM of MgO Powder, x125(1)

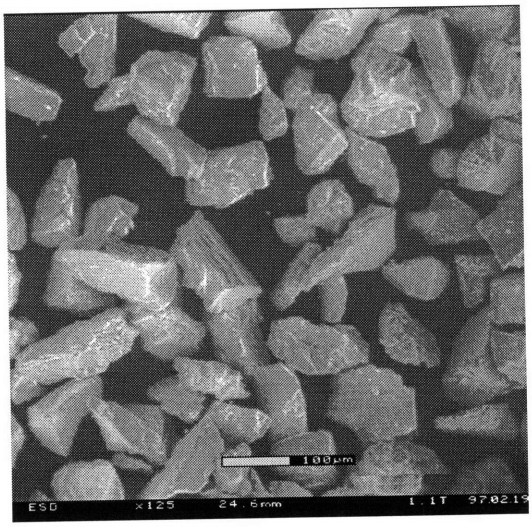

Figure 3-1B. SEM of MgO Powder, x125(2)

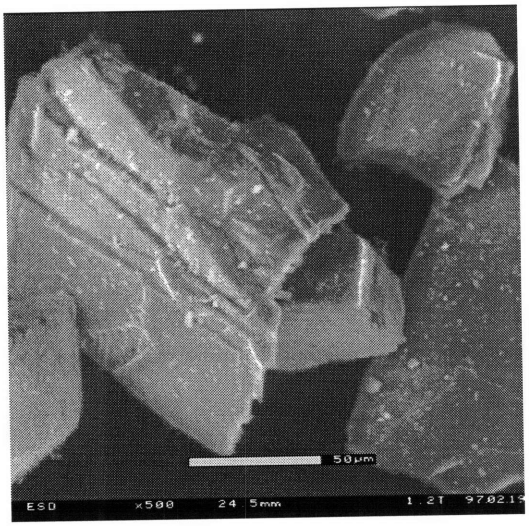

Figure 3-1C. SEM of MgO Powder, x500

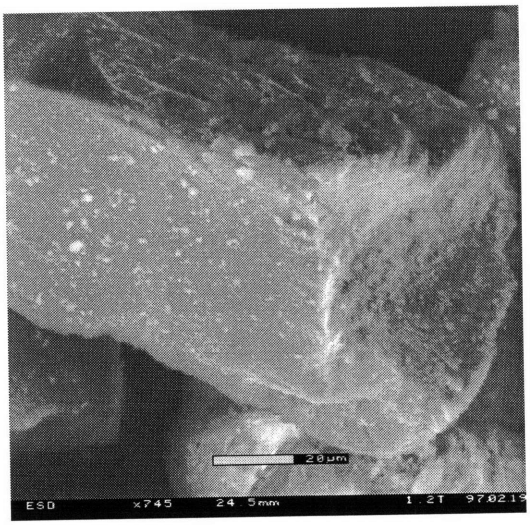

Figure 3-1D. SEM of MgO Powder, x745

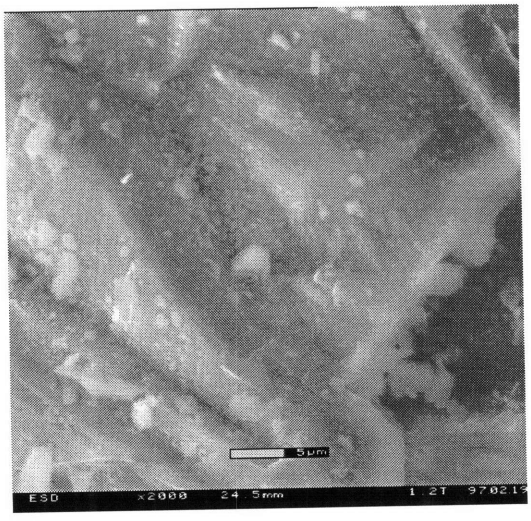

Figure 3-1E. SEM of MgO Powder, x2000

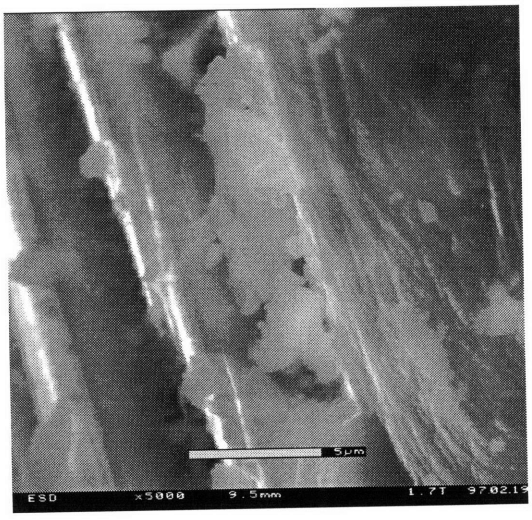

Figure 3-1F. SEM of MgO Powder, x5000

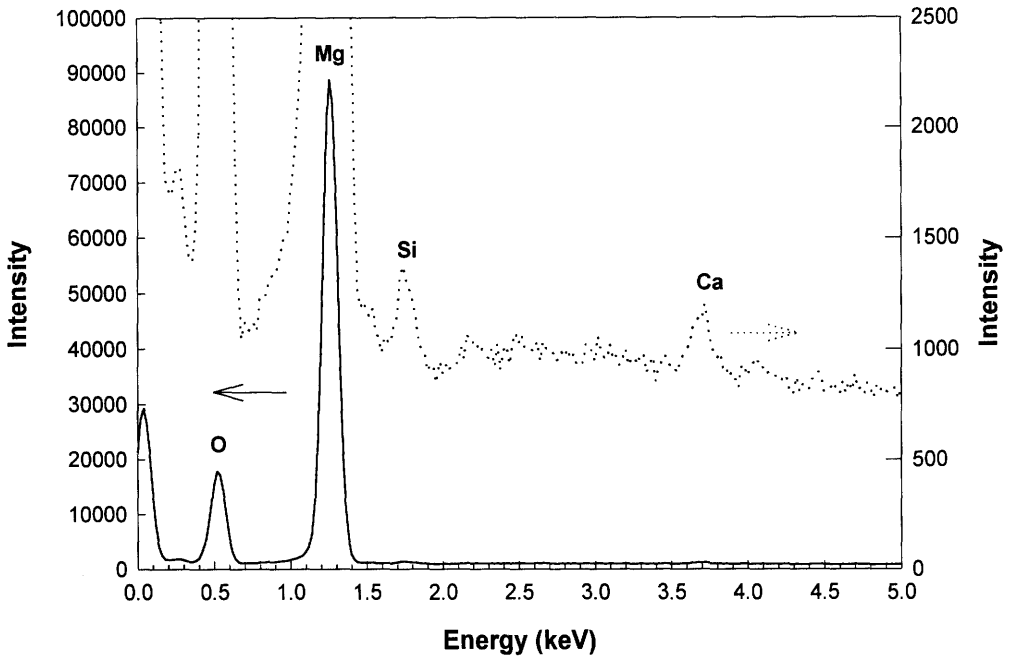

Figure 3-2. X-Ray Spectrum of MgO Powder

SEM images of the CaO powder at increasing magnification levels are shown in Figures 3-3A to 3-3D. Similar to MgO, the CaO particles are angular, non-porous and have microparticles on the surface. EDS analysis of the material, presented in Figure 3-4, shows the presence of Si and Mg as impurities in the powder.

Table 3-2. Typical Properties of High Calcium Metallurgical Grade Quicklime

Particle Size Distribution	>10 mesh (1.91 mm)	Trace
	>100 mesh (140 μm)	98%
Bulk Density		1.12 g/ml
Available Lime Index (ASTM C25)		95%
Water Reactivity (ASTM C110)		34°C
Chemical Composition	Total CaO	96%
	MgO	0.8%
	Fe_2O_3	0.10%
	C	<0.07%
	S	<0.05%
	Loss on Ignition	0.10%

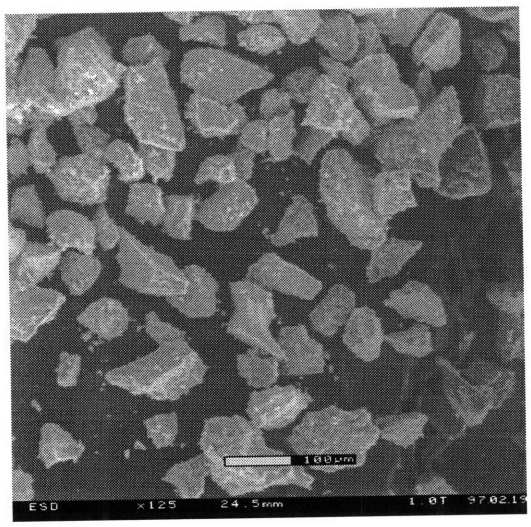

Figure 3-3A. SEM of CaO Powder, x125

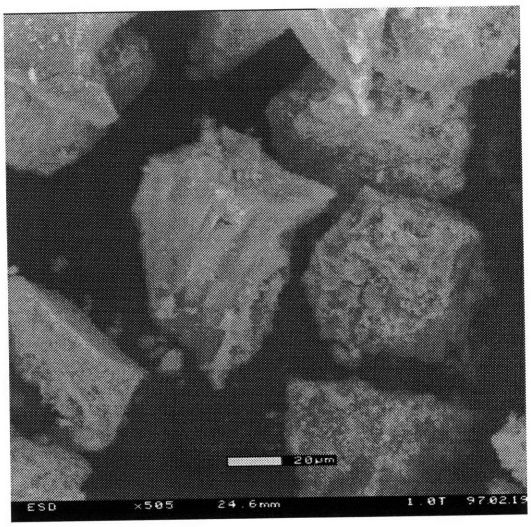

Figure 3-3B. SEM of CaO Powder, x505

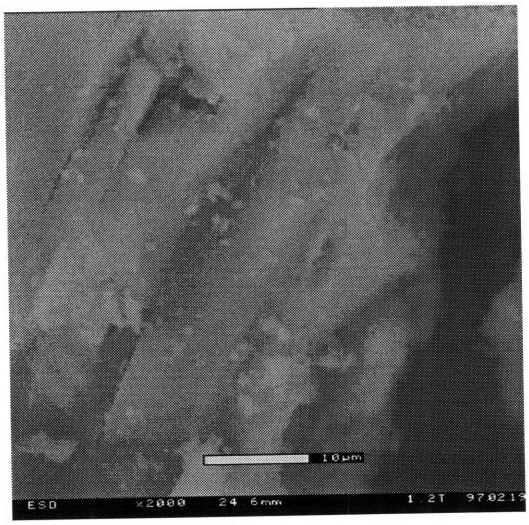

Figure 3-3C. SEM of CaO Powder, x2000(1)

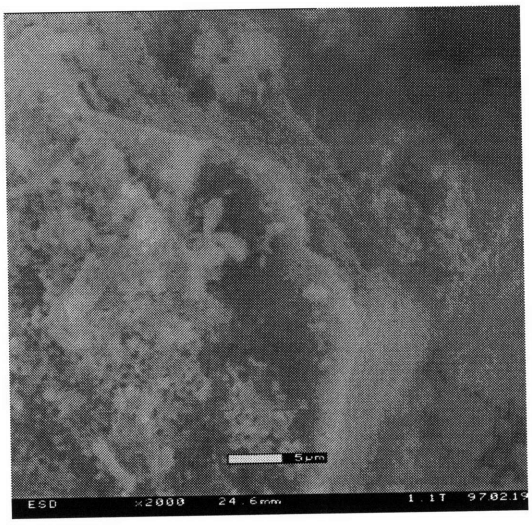

Figure 3-3D. SEM of CaO Powder, x2000(2)

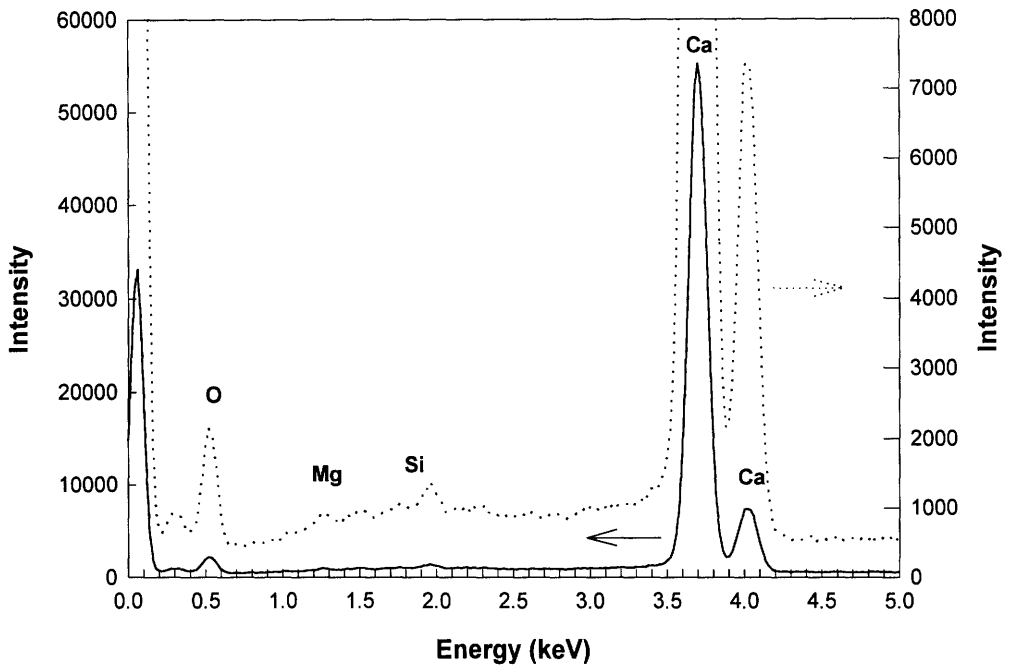

Figure 3-4. X-Ray Spectrum of CaO Powder

The graphite used in doping the MgO with carbon for the runs with the MgO-C-CH_4-Ar system is commercial lubricating graphite, Dixon Ticonderoga No. 2 Medium Powdered Flake Graphite. The graphite flakes are nominally above 100 μm, as can be seen from the SEM images at increasing levels of magnification in Figures 3-5A to 3-5D. Trace amounts of Si, Mg and O are present as impurities in the graphite powder, as shown by the EDS analysis in Figure 3-6.

The magnesium used in the experimental runs with the Mg-CH_4-Ar system is -100 +200 mesh (-140 +73.7 μm) Mg powder from Alfa Æsar, with a purity of 99.6% Mg + 0.1-1% Ca. The certified spectrographic analysis of the powder is given in Table 3-3. SEM images of the powder at increasing magnification levels (Figure 3-7A to 3-7D) show the Mg particles to be convoluted. The X-ray spectrum obtained by EDS analysis in Figure 3-8 reveals the presence of trace amounts of oxygen, suggesting slight oxidation or hydrolysis of the magnesium.

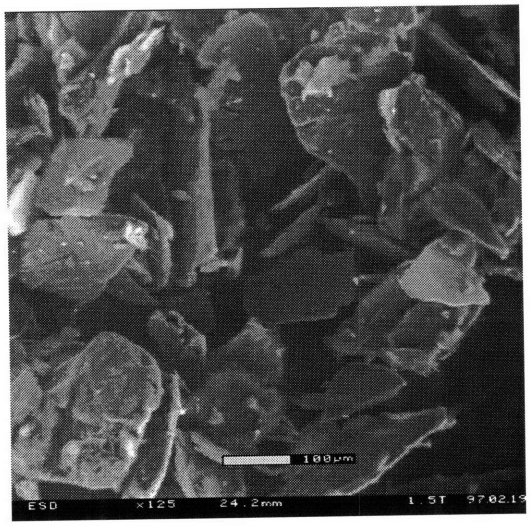

Figure 3-5A. SEM of Graphite Powder, x125(1)

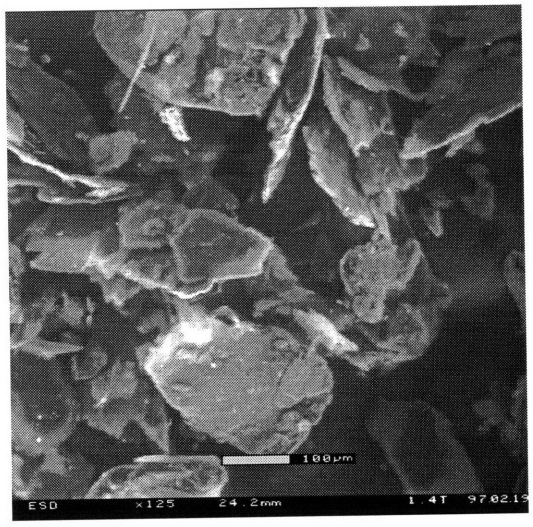

Figure 3-5B. SEM of Graphite Powder, x125(2)

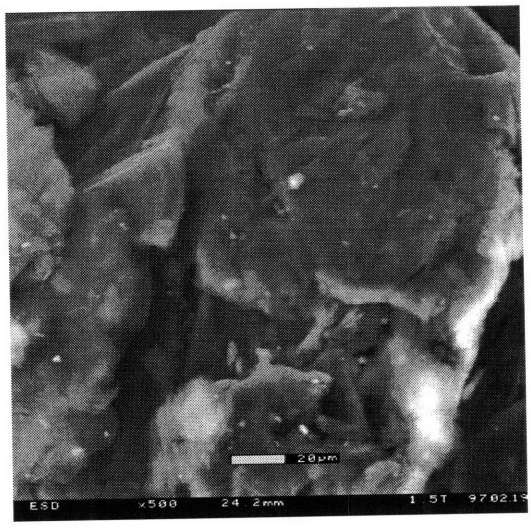

Figure 3-5C. SEM of Graphite Powder, x500

Figure 3-5D. SEM of Graphite Powder, x2000

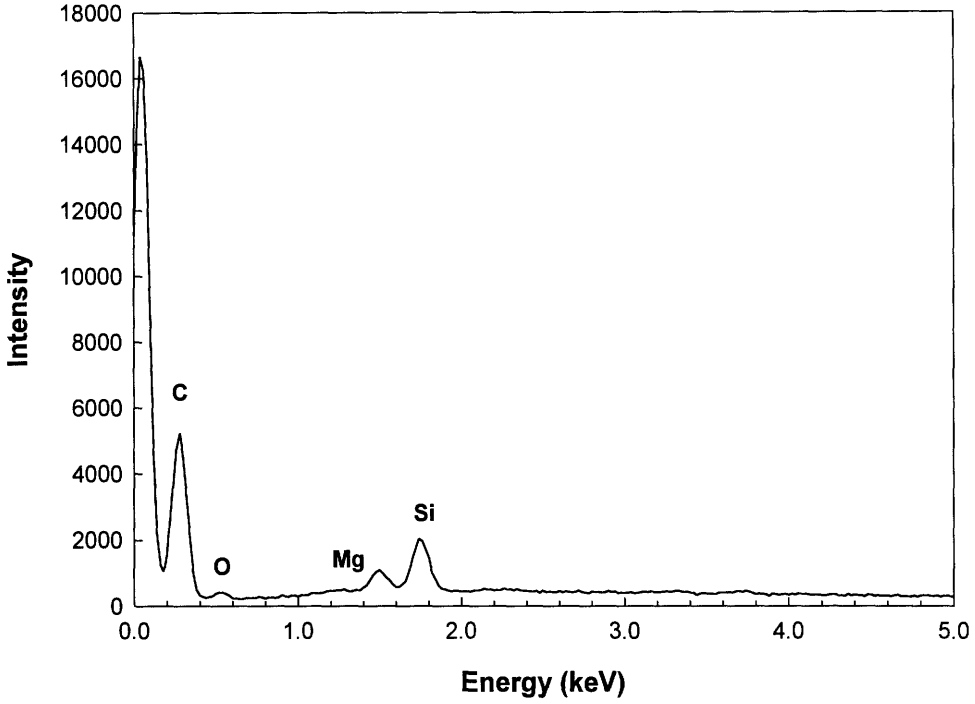

Figure 3-6. X-Ray Spectrum of Graphite Powder

Table 3-3. Spectrographic Analysis of Mg Powder

Al	0.01%
Ca	<0.001%
Cu	0.001%
Fe	0.06%
In	0.001%
Mn	0.08%
Si	0.06%
Zn	0.02%

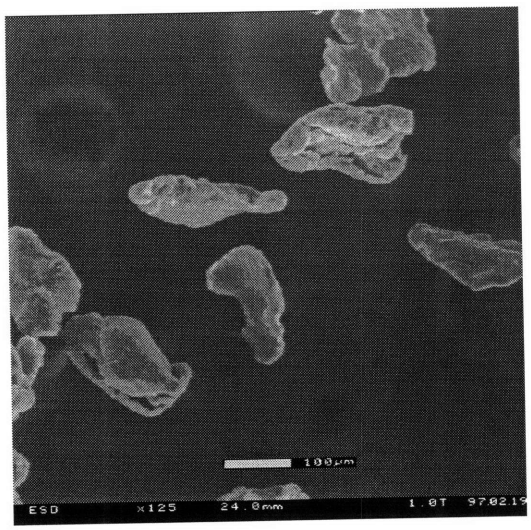

Figure 3-7A. SEM of Mg Powder, x125

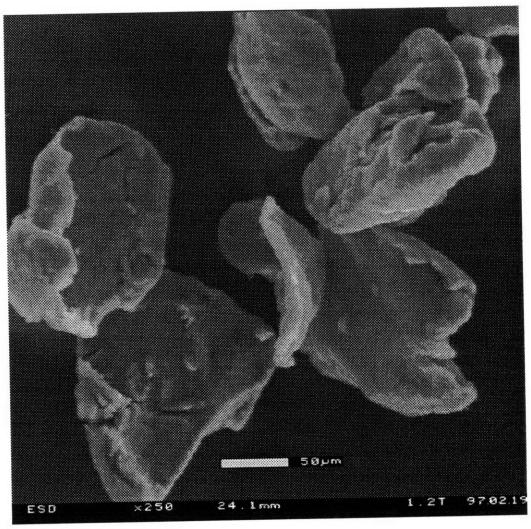

Figure 3-7B. SEM of Mg Powder, x250

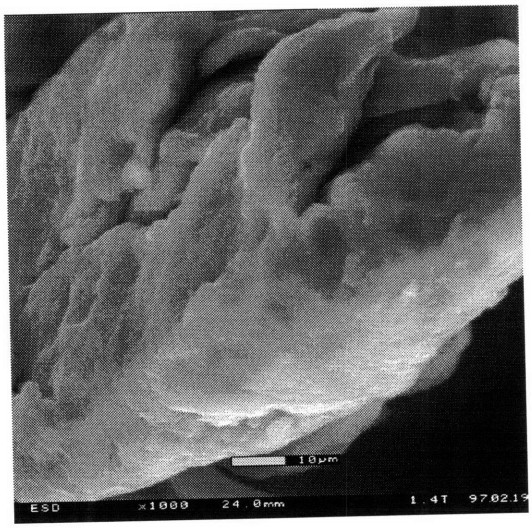

Figure 3-7C. SEM of Mg Powder, x1000

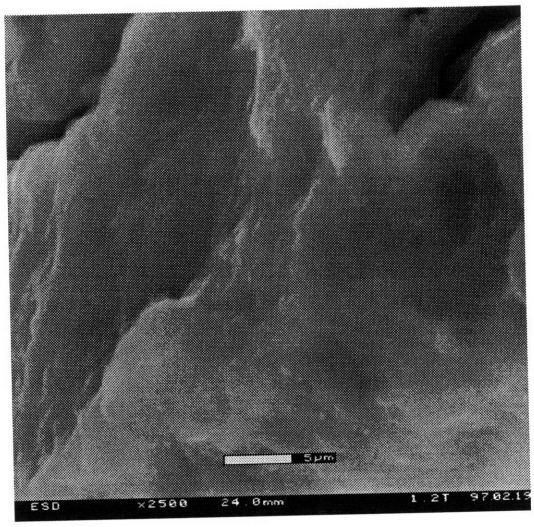

Figure 3-7D. SEM of Mg Powder, x2500

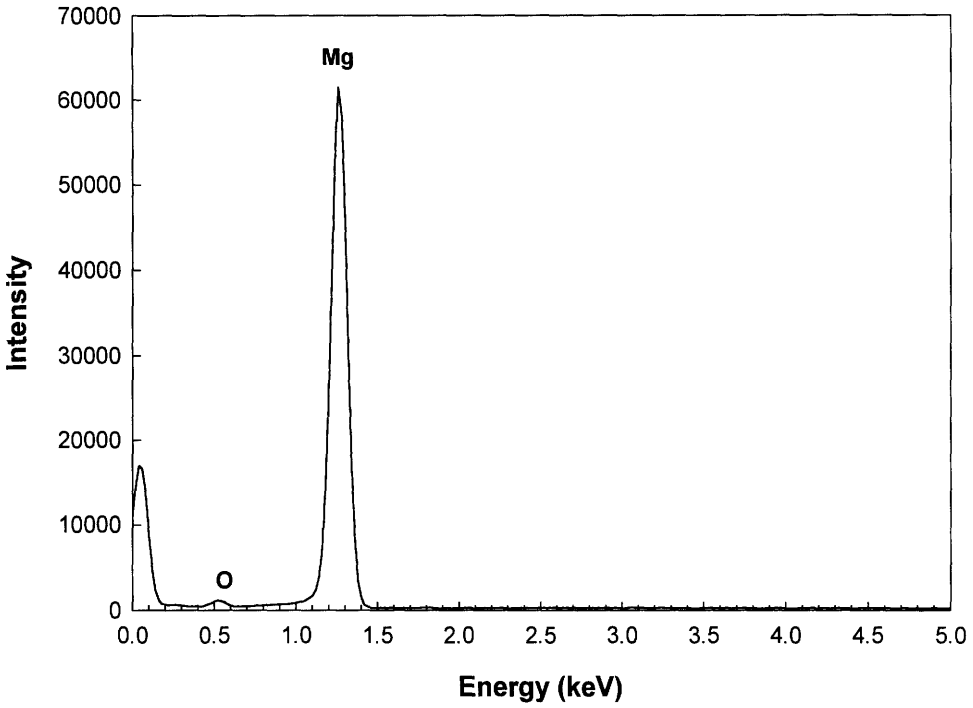

Figure 3-8. X-Ray Spectrum of Mg Powder

3.2 MgO-CH_4-Ar System

Fifty-six experimental runs, designated Runs M1 to M56, were conducted with the MgO-CH_4-Ar system to study how the conversion of reactants to various products is affected by arc power input (17-47 kW), CH_4 flow rate (10, 20 and 30 l/min), Argon dilution (0, 10 and 15 l/min), inlet MgO:CH_4 molar ratio (0.38-0.46:1, 0.8:1 and 1.15:1), secondary CH_4 quench (0 and 15 l/min) and anode-nozzle-exit-to-probe-tip quench distance (5, 10 and 14 in.). Because of safety issues in powder feeder operation, Argon was used as carrier gas at 4.2 l/min in all the runs and a study of the MgO-CH_4 system without Ar was not conducted. The reactor conditions for Runs M1 to M56 are summarized in Table 3-4. In Runs M1 to M20, the arc current was measured directly with the current probe without the signal conditioner. Because background noise interference caused wide fluctuations in the relatively low level output signals from the current probe, the 0-1000 mV signal was amplified to 0-10 V with the signal conditioner for the rest of the runs.

Table 3-4. Summary of Reactor Conditions for MgO-CH_4-Ar System [Ave (± 1 s.d.)]

Run	M1	M2	M3	M4	M5	M6	M7	M8	M9	M10
Main CH_4 Flow, l/min	30.0	30.0	30.0	30.0	30.0	30.0	30.0	30.0	30.0	30.0
Secondary CH_4 Flow, l/min										
Main Argon Flow, l/min										
Carrier Argon Flow, l/min	4.2	4.2	4.2	4.2	4.2	4.2	4.2	4.2	4.2	4.2
MgO Feed, g/min	25.5	19.1	22.3	22.3	12.7	12.7	22.3	22.3	22.3	22.3
Inlet MgO/CH_4 Molar Ratio	0.51	0.39	0.45	0.45	0.26	0.26	0.45	0.45	0.45	0.45
MgO Particle Size, μm	44 to 104	44 to 104	44 to 104	44 to 104	44 to 104	44 to 104	44 to 104	44 to 104	44 to 104	44 to 104
Chamber Pressure, mm Hg	741 ± 58	762 ± 13	763 ± 12	755 ± 13	759 ± 16	608 ± 90	754 ± 15	758 ± 14	783 ± 81	761 ± 14
Arc Voltage, V	95.4 ± 5.0	84.9 ± 4.5	97.6 ± 3.3	99.6 ± 3.4	98.3 ± 4.9	90.5±15.1	81.8±19.8	89.2 ± 9.7	80.0±14.5	85.8 ± 2.4
Arc Current, A	433 ± 80	519 ± 105	339 ± 72	328 ± 73	345 ± 58	250 ± 101	528 ± 164	419 ± 101	546 ± 149	542 ± 100
Arc Power Input, kW	41.1 ± 7.2	44.0 ± 8.5	33.1 ± 7.4	32.6 ± 7.1	33.9 ± 5.6	21.9 ± 8.2	41.5±12.8	37.0 ± 8.7	42.1 ± 8.6	46.6 ± 8.7
Quench Distance, in	14	14	14	10	10	10	10	10	5	5
Magnetic Field, G	118	118	118	118	118	118	118	118	118	0

Table 3-4. Summary of Reactor Conditions for MgO-CH_4-Ar System [Ave (± 1 s.d.)] (continued)

Run	M11	M12	M13	M14	M15	M16	M17[a]	M18[a]	M19[a]	M20
Main CH_4 Flow, l/min	15.0	15.0	10.0	10.0	10.0	10.0	10.0	9.9	10.0	10.0
Secondary CH_4 Flow, l/min			15.0	15.2	15.4					
Main Argon Flow, l/min	15.2	15.2	15.2	11.2	11.4	11.7	9.8	14.2	9.6	10.5
Carrier Argon Flow, l/min	4.2	4.2	0	4.2	4.2	4.2	4.2	4.2	4.2	4.2
MgO Feed, g/min	22.3	28.6	0	19.1	19.1	19.1	19.1	19.1	19.1	19.1
Inlet MgO/CH_4 Molar Ratio	0.90	1.15	0	0.46	0.46	1.15	1.15	1.15	1.15	1.15
MgO Particle Size, μm	44 to 104	44 to 104	44 to 104	44 to 104	44 to 104	44 to 104	44 to 104	44 to 104	44 to 104	44 to 104
Chamber Pressure, mm Hg	761 ± 10	760 ± 11	762 ± 6	759 ± 13	722 ± 53	753 ± 20	774 ± 82	693 ± 66	760 ± 7	698 ± 23
Arc Voltage, V	74.2±11.0	74.8 ± 2.8	42.7 ± 1.2	67.2±14.0	59.4 ± 2.0	48.2 ± 2.4	69.4±14.8	53.6 ±2.2	59.8 ± 0.5	46.9 ± 3.7
Arc Current, A	548 ± 94	444 ± 89	724 ± 122	461 ± 95	567 ± 89	670 ± 122	499 ± 131	529 ± 90	478 ± 95	750 ± 131
Arc Power Input, kW	40.7 ± 9.4	33.3 ± 6.9	30.9 ± 5.2	30.8 ± 7.7	33.7 ± 5.1	32.4 ± 6.6	33.2 ± 6.9	28.3 ± 4.8	28.6 ± 5.7	35.1 ± 6.1
Quench Distance, in	5	5	5	5	5	5	5	5	5	5
Magnetic Field, G	118	118	118	118	118	118	118	118	118	118

[a]Runs with electrodes lowered by 1"

Table 3-4. Summary of Reactor Conditions for MgO-CH_4-Ar System [Ave (± 1 s.d.)] (continued)

Run	M21	M22	M23	M24	M25	M26	M27	M28	M29	M30
Main CH_4 Flow, l/min	10.0	10.0	10.0	10.0	10.0	10.0	9.9	10.0	10.0	10.0
Secondary CH_4 Flow, l/min										
Main Argon Flow, l/min	14.6	15.9	15.1	15.1	10.2	15.1	10.1	8.5	10.0	9.9
Carrier Argon Flow, l/min	4.2	4.2	4.2	4.2	4.2	4.2	4.2	4.2	4.2	4.2
MgO Feed, g/min	19.1	19.1	19.1	19.1	19.1	19.1	19.1	19.1	19.1	19.1
Inlet MgO/CH_4 Molar Ratio	1.15	1.15	1.15	1.15	1.15	1.15	1.15	1.15	1.15	1.15
MgO Particle Size, μm	44 to 104	44 to 104	44 to 104	44 to 104	44 to 104	44 to 104	44 to 104	44 to 104	44 to 104	44 to 104
Chamber Pressure, mm Hg	760 ± 6	794 ± 90	743 ± 30	759 ± 8	752 ± 42	763 ± 4	749 ± 22	740 ± 35	745 ± 26	738 ± 52
Arc Voltage, V	62.3 ± 1.3	32.2±15.9	44.8 ± 0.7	49.4 ± 1.6	51.6 ± 6.0	52.5 ± 0.6	58.7 ± 9.0	60.9 ± 2.6	56.7 ± 1.1	57.7 ± 7.1
Arc Current, A	424 ± 10	626 ± 143	658 ± 5	666 ± 12	616 ± 40	722 ± 3	487 ± 65	446 ± 22	512 ± 10	411 ± 50
Arc Power Input, kW	26.4 ± 0.2	17.9 ± 2.3	29.5 ± 0.3	32.9 ± 0.5	31.5 ± 2.5	37.9 ± 0.3	28.1 ± 2.2	27.1 ± 0.2	29.0 ± 0.1	23.4 ± 1.6
Quench Distance, in	5	5	5	5	5	5	5	5	5	5
Magnetic Field, G	118	118	118	118	118	0	118	56	28	28

Table 3-4. Summary of Reactor Conditions for MgO-CH_4-Ar System [Ave (± 1 s.d.)] (continued)

Run	M31	M32	M33	M34	M35	M36	M37	M38	M39	M40
Main CH_4 Flow, l/min	10.0	10.0	10.0	10.0	10.0	10.0	9.9	10.0	19.8	10.0
Secondary CH_4 Flow, l/min										
Main Argon Flow, l/min	9.1	10.2		10.2						
Carrier Argon Flow, l/min	4.2	4.2	4.2	4.2	4.2	4.2	4.2	4.2	4.2	4.2
MgO Feed, g/min	19.1	19.1	19.1	19.1	19.1	19.1	19.1	19.1	38.2	7.6
Inlet MgO/CH_4 Molar Ratio	1.15	1.15	1.15	1.15	1.15	1.15	1.15	1.15	1.15	0.46
MgO Particle Size, μm	44 to 104	44 to 104	44 to 104	44 to 104	44 to 104	44 to 104	44 to 104	44 to 104	44 to 104	44 to 104
Chamber Pressure, mm Hg	726 ± 48	741 ± 56	757 ± 9	759 ± 7	760 ± 5	758 ± 10	647 ± 20	744 ± 16	757 ± 19	743 ± 10
Arc Voltage, V	66.8±11.2	50.3 ± 4.3	32.9 ± 3.7	58.3 ± 0.5	71.0 ± 0.9	68.4±14.9	45.4 ± 8.2	50.4 ± 8.7	93.1±17.6	70.1 ± 1.5
Arc Current, A	268 ± 62	699 ± 27	563 ± 88	464 ± 3	501 ± 5	407 ± 120	498 ± 70	639 ± 67	408 ± 119	417 ± 12
Arc Power Input, kW	17.3 ± 2.2	35.1 ± 2.1	32.9 ± 3.7	27.1 ± 0.1	35.6 ± 0.1	26.1 ± 2.2	22.0 ± 1.6	31.6 ± 1.8	35.9 ± 3.0	29.2 ± 0.3
Quench Distance, in	5	5	5	5	5	5	5	5	5	5
Magnetic Field, G	28	28	28	28	118	118	118	118	118	118

Table 3-4. Summary of Reactor Conditions for MgO-CH_4-Ar System [Ave (± 1 s.d.)] (continued)

Run	M41	M42	M43	M44	M45	M46	M47	M48	M49	M50
Main CH_4 Flow, l/min	10.0	19.8	19.8	19.8	19.8	19.8	19.8	19.8	19.8	19.8
Secondary CH_4 Flow, l/min										
Main Argon Flow, l/min										
Carrier Argon Flow, l/min	4.2	4.2	4.2	4.2	4.2	4.2	4.2	4.2	4.2	4.2
MgO Feed, g/min	7.6	38.2	38.2	38.2	38.2	38.2	15.3	26.7	12.7	12.7
Inlet MgO/CH_4 Molar Ratio	0.46	1.15	1.15	1.15	1.15	1.15	0.46	0.81	0.38	0.38
MgO Particle Size, μm	44 to 104	44 to 104	44 to 104	44 to 104	44 to 104	44 to 104	44 to 104	44 to 104	44 to 104	44 to 104
Chamber Pressure, mm Hg	698 ± 40	755 ± 11	758 ± 19	710 ± 55	755 ± 19	758 ± 15	752 ± 18	764 ± 103	758 ± 13	756 ± 15
Arc Voltage, V	56.8±10.7	82.2±15.1	70.5±21.8	86.9±12.9	73.7±19.4	78.3±13.2	69.5±15.1	88.9±17.4	67.6±16.8	86.0±16.1
Arc Current, A	438 ± 82	393 ± 111	395 ± 70	310 ± 89	414 ± 150	416 ± 89	468 ± 104	370 ± 118	442 ± 127	302 ± 104
Arc Power Input, kW	24.1 ± 2.4	30.7 ± 2.5	24.6 ± 3.7	25.8 ± 3.0	27.7 ± 2.7	31.4 ± 2.5	31.0 ± 3.1	30.9 ± 4.2	27.8 ± 2.9	24.4 ± 3.6
Quench Distance, in	5	5	5	5	5	5	5	5	5	5
Magnetic Field, G	118	118	118	118	118	118	118	118	118	118

Table 3-4. Summary of Reactor Conditions for MgO-CH_4-Ar System [Ave (± 1 s.d.)] (continued)

Run	M51	M52	M53	M54	M55	M56				
Main CH_4 Flow, l/min	19.8	9.9	10.0	10.0	10.0	10.0				
Secondary CH_4 Flow, l/min										
Main Argon Flow, l/min										
Carrier Argon Flow, l/min	4.2	4.2	4.2	4.2	4.2	4.2				
MgO Feed, g/min	26.7	7.6	7.6	7.6	13.4	13.4				
Inlet MgO/CH_4 Molar Ratio	0.81	0.46	0.46	0.46	0.80	0.80				
MgO Particle Size, μm	44 to 104	44 to 104	44 to 104	44 to 104	44 to 104	44 to 104				
Chamber Pressure, mm Hg	753 ± 20	728 ± 27	761 ± 4	761 ± 8	755 ± 10	750 ± 17				
Arc Voltage, V	96.4 ± 9.5	58.3 ± 9.6	44.4 ± 2.5	75.6±15.0	63.6±13.6	51.0±10.3				
Arc Current, A	284 ± 56	560 ± 73	668 ± 17	340 ± 125	436 ± 110	624 ± 75				
Arc Power Input, kW	26.9 ± 2.8	32.0 ± 1.9	29.6 ± 1.0	23.9 ± 2.8	26.3 ± 2.0	31.1 ± 2.2				
Quench Distance, in	5	5	5	5	5	5				
Magnetic Field, G	118	118	118	118	118	118				

3.2.1 Reaction Products of MgO-CH_4-Ar System

The major reaction products of the MgO-CH_4 system according to the global reactions

$$5\,CH_4 + 2\,MgO \rightarrow Mg_2C_3 + 10\,H_2 + 2\,CO \qquad \text{Reaction (1-2)}$$

$$3\,CH_4 + MgO \rightarrow MgC_2 + 6\,H_2 + CO \qquad \text{Reaction (1-3)}$$

$$CH_4 + MgO \rightarrow Mg + 2\,H_2 + CO \qquad \text{Reaction (1-4)}$$

are Mg_2C_3, MgC_2, Mg, H_2 and CO.

Figure 3-9 shows a plot of Log K_p vs. 1/T for Reactions (1-1), (1-2), (1-3), (1-4)

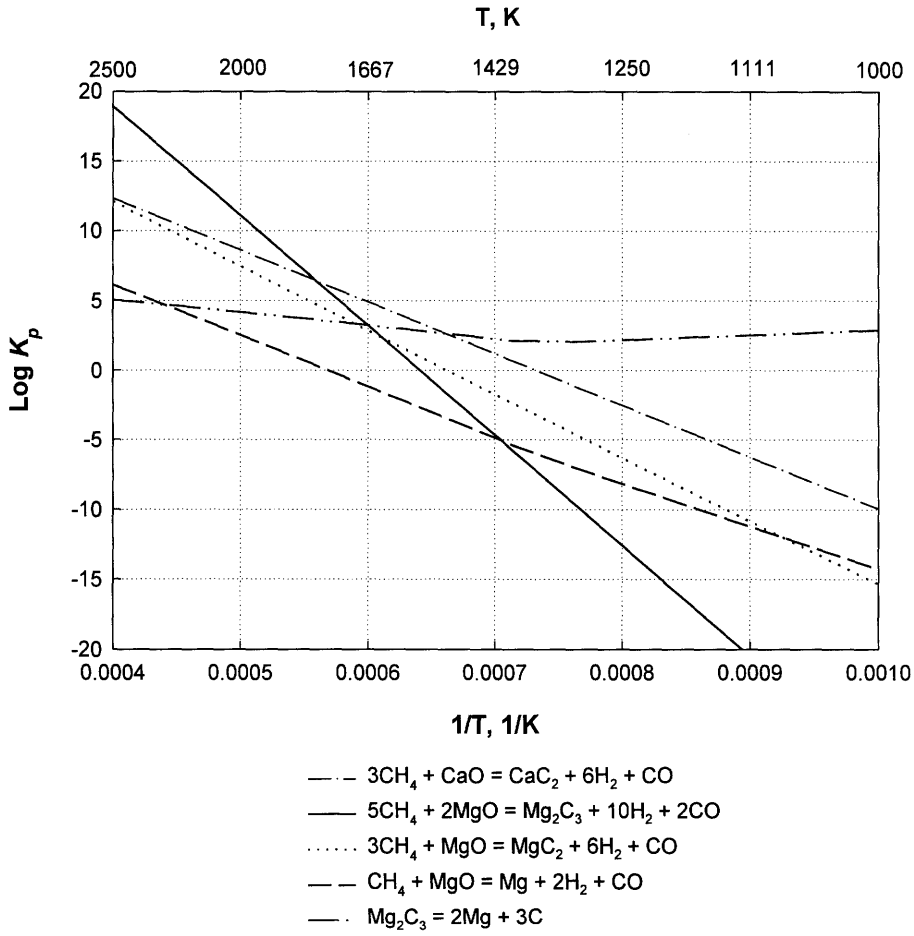

Figure 3-9. Log K_p Values for Metal and Metal Carbide Formation and Metal Carbide Decomposition

including the Mg_2C_3 decomposition reaction

$$Mg_2C_3 \rightarrow 2\,Mg + 3\,C \qquad \text{Reaction (3-1)}$$

Figure 3-9 suggests that the formation of Mg_2C_3 is thermodynamically favored above 1700 K. Assuming that equilibrium is attained within the relatively short residence time of the reactants in the plasma at greater than 2000 K and that the high quenching rate freezes the equilibrium, the product composition is expected to match the thermodynamic equilibrium at these high temperatures. Thus, in the first eight runs, Runs M1 to M8, the solids analysis was focused on quantification of the Mg_2C_3 yield and no attempt was made to analyze for Mg.

However, the extents of conversion of MgO and CH_4 to Mg_2C_3 or MgC_2 determined from GC analysis of the headspace above the hydrolyzed solids were observed to be well below those expected from Reactions (1-2) and (1-3). Solids analyses by Powder X-Ray Diffraction and STEM coupled with EDS revealed that the solid product is predominantly elemental magnesium. The XRD pattern of a sample from Run M27 presented in Figure 3-10 shows that the major constituent of the solid phase is crystalline magnesium. Silicon was used as an internal standard to obtain the crystal lattice parameters of the magnesium product. The XRD pattern of the magnesium in the sample was indexed on a hexagonal cell and the room temperature crystal lattice constants were determined to be a_o=3.209426 ± 0.000180 Å and c_o=5.211053 ± 0.000292Å, in good agreement with the reference unit cell parameters of a_o=3.20936 Å and c_o=5.2112 Å (NBS, 1984). Mg_2C_3 and MgC_2 were not identified by XRD, possibly due to decomposition during sample preparation. They are, however, postulated to be present in the solid products, as C_3H_4 and C_2H_2 are always detected in considerably small proportions in the headspace above the hydrolyzed solids. The hydrolyzed solid is also found to contain carbon (non-carbide C), generally in amounts less than 10% of the hydrolyzed sample, which probably existed as solid carbon before hydrolysis. In addition, other hydrocarbons typically corresponding to less than 1% of the input CH_4 have been detected by GC after hydrolysis. These hydrocarbons include C_2H_6, C_2H_4,

C_3H_8, C_3H_6, and various C_4 species. The solid products in all the runs consist of finely divided dark gray powder.

The gaseous product is composed mainly of H_2 and CO. By GC analysis, unreacted CH_4, small amounts (generally <1%) of C_2H_2 and C_3H_4, and trace amounts (<<1%) of C_2H_4, C_3H_6, C_2H_6, C_3H_8 and occasional C_4 species have also been detected. Although not performed on a routine basis, the presence of CO_2 in the gas sample was tested but CO_2 was not detected.

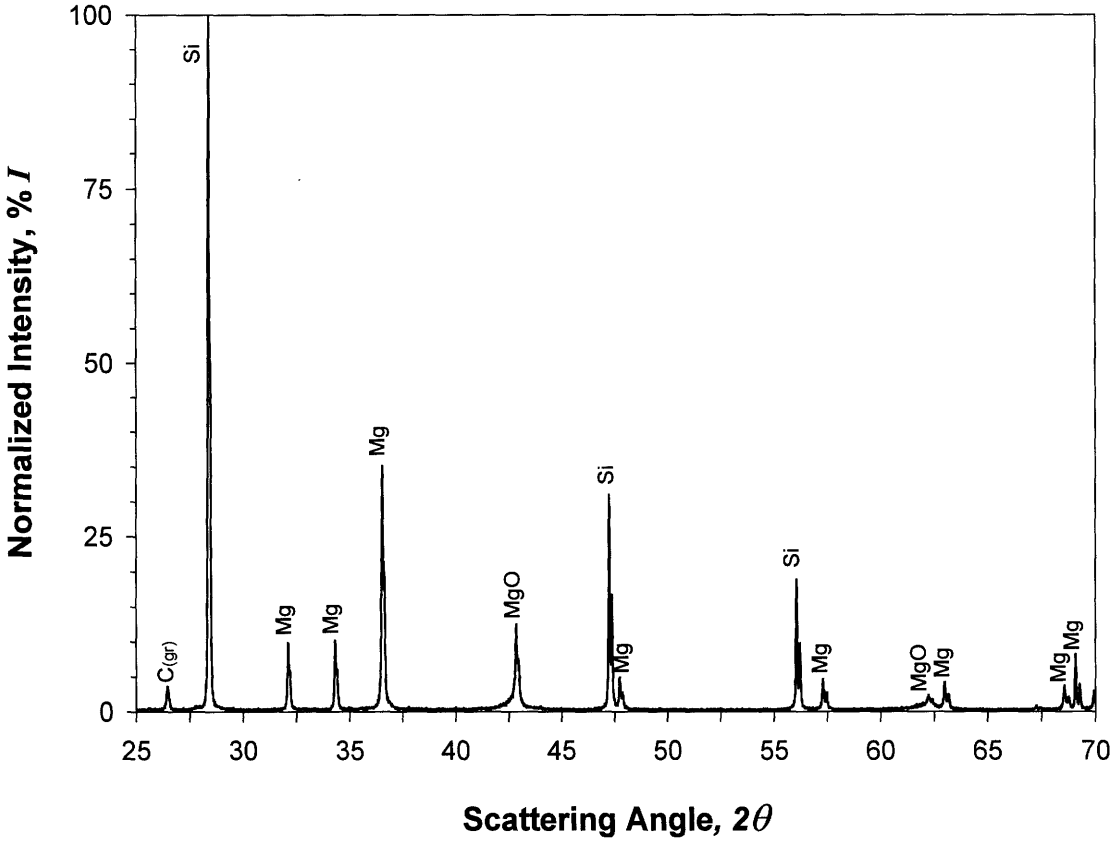

Figure 3-10. X-Ray Diffraction Pattern of Run M27 Sample From Chamber Bottom

Material balances on the constituent elements of the CH_4 and MgO reactants for Runs M1 to M56 are presented in Tables 3-5 and 3-6, respectively. The carbon in methane is converted to CO gas, non-carbide solid C, solid Mg_2C_3 and MgC_2, and other gaseous hydrocarbons (HCs) while the methane hydrogen is recovered as H_2 and other HCs in the gaseous products. The magnesium in MgO is converted to solid Mg, Mg_2C_3 and MgC_2 while the oxygen in MgO is transformed to CO gas.

Table 3-5. Percent Methane Molar Conversion to Products in MgO-CH_4-Ar System

Run	M1		M2		M3		M4		M5		M6		M7		M8		M9		M10	
Products	CH_4 "C"	CH_4 "H"	CH_4 "C"	CH_4 "H"	CH_4 "C"	CH_4 "H"	CH_4 "C"	CH_4 "H"	CH_4 "C"	CH_4 "H"	CH_4 "C"	CH_4 "H"	CH_4 "C"	CH_4 "H"	CH_4 "C"	CH_4 "H"	CH_4 "C"	CH_4 "H"	CH_4 "C"	CH_4 "H"
Mg_2C_3	1.8		1.0		1.5		1.5		a		0.2		3.0		1.3		1.1		0.4	
MgC_2	0.4		0.2		0.2		0.5		a		0.3		1.0		0.7		0.6		0.3	
Non-carbide C	27.9		49.9		48.1		52.4		a		a		17.2		67.2		23.3		18.9	
CO	49.8		31.6		28.4		40.9		22.2		29.9		55.1		30.5		a		41.6	
C_2H_2	1.4	0.4	1.5	0.4	0.5	0.1	1.4	0.4	2.6	0.6	56.8	14.2	2.2	0.6	1.9	0.5	a	a	4.7	1.2
C_3H_4	0.1	0.0	0.0	0.0	0.1	0.0	0.1	0.0	0.1	0.0	0.4	0.1	0.3	0.1	0.0	0.0	a	a	0.1	0.0
Other C_2, C_3, C_4	0.4	0.3	1.4	1.0	0.9	0.7	2.1	1.6	2.5	2.0	12.1	9.0	2.8	2.1	1.7	1.3	a	a	1.9	1.5
Unreacted CH_4	0.3	0.3	0.4	0.4	0.3	0.3	0.9	0.9	0.9	0.9	6.7	6.7	1.0	1.0	0.5	0.5	a	a	0.6	0.6
H_2		88.3		77.4		66.7		91.5		77.9		186.2		83.0		71.7		a		90.8
Total	82.1	89.3	86.0	79.2	80.0	67.8	99.7	94.4	a	81.4	a	216.2	82.6	86.8	103.8	74.0	a	a	68.5	94.0

[a] Not available

Table 3-5. Percent Methane Molar Conversion to Products in MgO-CH_4-Ar System (continued)

Run	M11		M12		M13[a,b]		M14[a]		M15[a]		M16		M17		M18		M19		M20	
Products	CH_4 "C"	CH_4 "H"	CH_4 "C"	CH_4 "H"	CH_4 "C"	CH_4 "H"	CH_4 "C"	CH_4 "H"	CH_4 "C"	CH_4 "H"	CH_4 "C"	CH_4 "H"	CH_4 "C"	CH_4 "H"	CH_4 "C"	CH_4 "H"	CH_4 "C"	CH_4 "H"	CH_4 "C"	CH_4 "H"
Mg_2C_3	4.8		4.9				5.8		3.7		3.0		0.1		5.8		3.8		0.0	
MgC_2	1.3		1.0				1.5		0.6		1.1		0.1		1.0		0.5		0.5	
Non-carbide C	33.7		28.4				25.9		13.4		66.3		17.4		16.1		5.7		42.3	
CO	116.6		66.1		0.0		34.3		49.0		79.8		40.0		83.8		78.6		58.9	
C_2H_2	0.7	0.2	0.3	0.1	83.3	20.8	1.0	0.3	0.5	0.1	6.5	1.6	4.0	1.0	0.4	0.1	0.2	0.1	0.7	0.2
C_3H_4	0.1	0.0	0.0	0.0	1.3	0.5	0.0	0.0	0.0	0.0	1.5	0.5	0.3	0.1	0.3	0.1	0.2	0.1	0.5	0.2
Other C_2, C_3, C_4	0.6	0.5	0.2	0.2	7.1	4.3	1.4	1.0	2.1	1.6	2.2	1.6	1.0	0.7	0.1	0.1	0.1	0.1	0.2	0.1
Unreacted CH_4	0.2	0.2	0.1	0.1	64.8	64.8	27.3	27.3	45.3	45.3	5.8	5.8	0.8	0.8	0.1	0.1	0.1	0.1	0.1	0.1
H_2		120.3		74.8		62.5		57.4		81.2		101.1		62.3		106.6		98.2		65.0
Total	158.0	121.2	101.0	75.1	156.5	152.9	97.2	86.0	114.6	128.5	166.2	110.7	63.7	64.9	107.6	107.0	89.2	98.6	103.2	65.6

[a] Primary and secondary (non-plasma) methane feed

[b] Pyrolysis run only; No MgO feeding

Table 3-5. Percent Methane Molar Conversion to Products in MgO-CH_4-Ar System (continued)

Run	M21		M22		M23		M24		M25		M26		M27		M28		M29		M30	
Products	CH_4 "C"	CH_4 "H"	CH_4 "C"	CH_4 "H"	CH_4 "C"	CH_4 "H"	CH_4 "C"	CH_4 "H"	CH_4 "C"	CH_4 "H"	CH_4 "C"	CH_4 "H"	CH_4 "C"	CH_4 "H"	CH_4 "C"	CH_4 "H"	CH_4 "C"	CH_4 "H"	CH_4 "C"	CH_4 "H"
Mg_2C_3	4.1		2.9		8.2		6.6		4.1		0.0		4.5		5.2		4.1		4.9	
MgC_2	0.6		0.5		1.7		1.1		1.0		0.0		0.8		1.1		0.7		1.0	
Non-carbide C	8.9		19.2		34.3		18.9		29.4		18.3		19.6		11.5		20.2		34.6	
CO	75.5		61.0		77.2		87.6		89.5		84.4		73.7		95.2		60.7		76.1	
C_2H_2	0.6	0.2	6.0	1.5	1.1	0.3	0.7	0.2	1.0	0.2	3.8	1.0	0.7	0.2	0.5	0.1	0.7	0.2	1.4	0.3
C_3H_4	0.9	0.3	4.2	1.4	0.9	0.3	0.8	0.3	0.6	0.2	1.0	0.3	0.5	0.2	0.4	0.1	0.3	0.1	0.5	0.2
Other C_2, C_3, C_4	0.0	0.0	2.3	1.7	0.2	0.2	0.3	0.2	0.3	0.2	0.5	0.4	0.2	0.1	0.1	0.1	0.2	0.1	0.4	0.3
Unreacted CH_4	0.1	0.1	4.9	4.9	0.2	0.2	0.2	0.2	0.2	0.2	0.4	0.4	0.1	0.1	0.2	0.2	0.1	0.1	0.2	0.2
H_2		102.5		112.2		103.1		93.7		117.5		108.9		93.4		123.3		87.1		111.6
Total	90.7	103.1	101.0	121.7	123.8	104.0	116.2	94.5	126.0	118.3	108.4	111.0	100.1	94.0	114.2	123.8	87.0	87.6	119.1	112.6

Table 3-5. Percent Methane Molar Conversion to Products in MgO-CH_4-Ar System (continued)

Run	M31		M32		M33		M34		M35		M36		M37		M38		M39		M40	
Products	CH_4 "C"	CH_4 "H"	CH_4 "C"	CH_4 "H"	CH_4 "C"	CH_4 "H"	CH_4 "C"	CH_4 "H"	CH_4 "C"	CH_4 "H"	CH_4 "C"	CH_4 "H"	CH_4 "C"	CH_4 "H"	CH_4 "C"	CH_4 "H"	CH_4 "C"	CH_4 "H"	CH_4 "C"	CH_4 "H"
Mg_2C_3	3.6		6.0		2.1		3.6		2.7		5.7		5.8		5.8		7.9		2.6	
MgC_2	1.0		1.4		0.4		0.6		0.5		0.7		0.8		0.8		1.4		0.7	
Non-carbide C	25.9		23.2		3.2		8.5		7.0		24.1		32.0		11.5		45.1		36.7	
CO	55.7		76.1		68.6		90.0		67.2		71.3		62.2		85.2		67.4		41.4	
C_2H_2	3.4	0.8	2.4	0.6	0.4	0.1	0.4	0.1	0.2	0.0	0.3	0.1	1.3	0.3	0.5	0.1	0.3	0.1	1.6	0.4
C_3H_4	0.7	0.3	0.4	0.1	0.1	0.0	0.2	0.1	0.0	0.0	0.2	0.1	0.2	0.1	0.3	0.1	0.1	0.0	0.2	0.1
Other C_2, C_3, C_4	0.9	0.6	0.8	0.6	0.0	0.0	0.0	0.0	0.2	0.0	0.1	0.1	0.4	0.3	0.1	0.1	0.1	0.1	1.0	0.7
Unreacted CH_4	0.4	0.4	0.3	0.3	0.4	0.4	0.1	0.1	0.1	0.1	0.1	0.1	0.2	0.2	0.2	0.2	0.1	0.1	0.3	0.3
H_2		96.2		123.9		79.8		117.4		80.7		85.7		73.6		99.7		91.5		92.7
Total	91.6	98.3	110.6	125.5	75.2	80.3	103.4	117.7	77.7	80.8	102.5	86.0	102.9	74.5	104.4	100.2	122.4	91.8	84.5	94.2

Table 3-5. Percent Methane Molar Conversion to Products in MgO-CH_4-Ar System (continued)

Run	M41		M42		M43		M44		M45		M46		M47		M48		M49		M50	
Products	CH_4 "C"	CH_4 "H"	CH_4 "C"	CH_4 "H"	CH_4 "C"	CH_4 "H"	CH_4 "C"	CH_4 "H"	CH_4 "C"	CH_4 "H"	CH_4 "C"	CH_4 "H"	CH_4 "C"	CH_4 "H"	CH_4 "C"	CH_4 "H"	CH_4 "C"	CH_4 "H"	CH_4 "C"	CH_4 "H"
Mg_2C_3	1.5		7.1		3.2		4.2		7.2		5.8		2.1		3.3		1.9		2.4	
MgC_2	0.4		0.9		0.6		0.8		0.9		0.8		0.8		0.5		0.7		1.0	
Non-carbide C	25.4		32.9		37.9		31.7		40.6		14.2		39.5		40.3		53.4		22.5	
CO	85.6		76.2		54.8		56.5		70.2		61.5		27.8		61.4		27.8		28.6	
C_2H_2	2.6	0.6	0.8	0.2	1.0	0.2	0.7	0.2	0.3	0.1	0.8	0.2	3.2	0.8	0.5	0.1	2.0	0.5	4.2	1.1
C_3H_4	0.5	0.2	0.3	0.1	0.2	0.1	0.0	0.0	0.2	0.1	0.2	0.1	0.0	0.0	0.1	0.0	0.1	0.0	0.2	0.1
Other C_2, C_3, C_4	1.2	0.9	0.4	0.3	0.5	0.4	0.3	0.2	0.2	0.2	0.3	0.2	0.7	0.5	0.1	0.1	0.6	0.4	1.5	1.1
Unreacted CH_4	7.2	7.2	0.2	0.2	0.4	0.4	0.4	0.4	0.1	0.1	0.2	0.2	0.3	0.3	0.2	0.2	0.2	0.2	0.4	0.4
H_2		66.9		111.8		100.8		93.1		100.8		97.7		63.8		83.7		85.6		84.4
Total	124.4	75.8	118.8	112.6	98.6	101.9	94.6	93.9	119.7	101.3	83.8	98.4	74.4	65.4	106.4	84.1	86.6	86.8	60.8	87.1

Table 3-5. Percent Methane Molar Conversion to Products in MgO-CH_4-Ar System (continued)

Run	M51		M52		M53		M54		M55		M56									
Products	CH_4 "C"	CH_4 "H"	CH_4 "C"	CH_4 "H"	CH_4 "C"	CH_4 "H"	CH_4 "C"	CH_4 "H"	CH_4 "C"	CH_4 "H"	CH_4 "C"	CH_4 "H"								
Mg_2C_3	4.9		2.7		2.1		2.0		4.1		4.4									
MgC_2	0.9		1.1		0.6		0.6		0.8		1.0									
Non-carbide C	43.7		32.2		19.0		11.8		28.7		22.9									
CO	58.7		45.6		46.5		35.6		58.6		62.4									
C_2H_2	1.5	0.4	2.8	0.7	3.0	0.8	1.6	0.4	0.8	0.2	1.3	0.3								
C_3H_4	0.2	0.1	0.3	0.1	0.5	0.2	0.4	0.2	0.2	0.1	0.3	0.1								
Other C_2, C_3, C_4	0.7	0.5	1.5	1.1	1.8	1.3	1.0	0.8	0.3	0.2	0.7	0.5								
Unreacted CH_4	0.3	0.3	0.5	0.5	0.6	0.6	0.3	0.3	0.1	0.1	0.3	0.3								
H_2		98.8		90.8		89.6		76.8		84.8		82.4								
Total	110.9	100.1	86.7	93.2	74.1	92.5	53.3	78.4	93.6	85.4	93.3	83.6								

Table 3-6. Percent Magnesium Oxide Molar Conversion to Products in MgO-CH_4-Ar System

Run	M1		M2		M3		M4		M5		M6		M7		M8		M9		M10	
Products	MgO "Mg"	MgO "O"	MgO "Mg"	MgO "O"	MgO "Mg"	MgO "O"	MgO "Mg"	MgO "O"	MgO "Mg"	MgO "O"	MgO "Mg"	MgO "O"	MgO "Mg"	MgO "O"	MgO "Mg"	MgO "O"	MgO "Mg"	MgO "O"	MgO "Mg"	MgO "O"
Mg_2C_3	2.7		2.0		2.5		2.4		a		0.1		4.9		2.2		1.7		0.7	
MgC_2	0.4		0.3		0.3		0.6		a		0.7		1.2		0.8		0.7		0.4	
Mg	a		a		a		a		a		a		a		a		77.8		35.3	
CO		106.9		90.3		69.7		100.4		95.4		128.1		135.1		74.8		a		101.9
Total	a	106.9	a	90.3	a	69.7	a	100.4	a	95.4	a	128.1	a	135.1	a	74.8	80.2	a	36.4	101.9

[a] Not available

Table 3-6. Percent Magnesium Oxide Molar Conversion to Products in MgO-CH_4-Ar System (continued)

Run	M11		M12		M13[a,b]		M14[a]		M15[a]		M16		M17		M18		M19		M20	
Products	MgO "Mg"	MgO "O"	MgO "Mg"	MgO "O"	MgO "Mg"	MgO "O"	MgO "Mg"	MgO "O"	MgO "Mg"	MgO "O"	MgO "Mg"	MgO "O"	MgO "Mg"	MgO "O"	MgO "Mg"	MgO "O"	MgO "Mg"	MgO "O"	MgO "Mg"	MgO "O"
Mg_2C_3	4.0		3.1				9.3		6.0		1.9		0.1		3.7		2.4		0.0	
MgC_2	0.9		0.5				1.8		0.7		0.5		0.0		0.5		0.2		0.2	
Mg	122.1		89.6				72.2		63.4		44.5		0.0		81.2		70.8		84.5	
CO		143.1		63.1				82.2		118.4		75.8		37.9		79.4		74.8		55.9
Total	126.8	143.1	93.1	63.1			83.3	82.2	70.1	118.4	46.9	75.8	0.1	37.9	85.4	79.4	73.4	74.8	84.7	55.9

[a] Primary and secondary (non-plasma) methane feed

[b] Pyrolysis run only; No MgO feeding

Table 3-6. Percent Magnesium Oxide Molar Conversion to Products in MgO-CH_4-Ar System (continued)

Run	M21		M22		M23		M24		M25		M26		M27		M28		M29		M30	
Products	MgO "Mg"	MgO "O"	MgO "Mg"	MgO "O"	MgO "Mg"	MgO "O"	MgO "Mg"	MgO "O"	MgO "Mg"	MgO "O"	MgO "Mg"	MgO "O"	MgO "Mg"	MgO "O"	MgO "Mg"	MgO "O"	MgO "Mg"	MgO "O"	MgO "Mg"	MgO "O"
Mg_2C_3	2.4		1.7		4.8		3.8		2.4		0.0		2.6		3.0		2.4		2.9	
MgC_2	0.3		0.2		0.7		0.5		0.4		0.0		0.4		0.5		0.3		0.5	
Mg	73.1		14.1		94.5		79.8		82.5		0.0		67.8		83.8		47.4		71.9	
CO		65.7		53.2		67.4		76.4		77.8		73.5		64.0		82.8		52.8		66.2
Total	75.8	65.7	16.0	53.2	100.0	67.4	84.1	76.4	85.3	77.8	0.0	73.5	70.8	64.0	87.3	82.8	50.1	52.8	75.3	66.2

Table 3-6. Percent Magnesium Oxide Molar Conversion to Products in MgO-CH_4-Ar System (continued)

Run	M31		M32		M33		M34		M35		M36		M37		M38		M39		M40	
Products	MgO "Mg"	MgO "O"	MgO "Mg"	MgO "O"	MgO "Mg"	MgO "O"	MgO "Mg"	MgO "O"	MgO "Mg"	MgO "O"	MgO "Mg"	MgO "O"	MgO "Mg"	MgO "O"	MgO "Mg"	MgO "O"	MgO "Mg"	MgO "O"	MgO "Mg"	MgO "O"
Mg_2C_3	2.1		3.5		1.2		2.1		1.6		3.3		3.3		3.4		4.6		3.7	
MgC_2	0.4		0.6		0.2		0.3		0.2		0.3		0.3		0.4		0.6		0.7	
Mg	47.7		48.4		39.1		61.5		46.4		60.2		54.3		57.6		78.5		94.7	
CO		48.4		66.2		59.7		78.4		58.5		62.0		54.0		74.3		58.4		90.2
Total	50.2	48.4	52.5	66.2	40.5	59.7	63.9	78.4	48.2	58.5	63.8	62.0	57.9	54.0	61.4	74.3	83.7	58.4	99.1	90.2

Table 3-6. Percent Magnesium Oxide Molar Conversion to Products in MgO-CH_4-Ar System (continued)

Run	M41		M42		M43		M44		M45		M46		M47		M48		M49		M50	
Products	MgO "Mg"	MgO "O"	MgO "Mg"	MgO "O"	MgO "Mg"	MgO "O"	MgO "Mg"	MgO "O"	MgO "Mg"	MgO "O"	MgO "Mg"	MgO "O"	MgO "Mg"	MgO "O"	MgO "Mg"	MgO "O"	MgO "Mg"	MgO "O"	MgO "Mg"	MgO "O"
Mg_2C_3	2.2		4.1		1.9		2.4		4.2		3.4		3.1		2.7		3.2		4.1	
MgC_2	0.5		0.4		0.3		0.3		0.4		0.4		0.9		0.3		0.9		1.3	
Mg	46.2		70.1		58.9		57.7		57.0		56.1		67.9		46.8		65.1		68.9	
CO		186.3		66.0		47.5		49.0		60.8		53.3		60.3		75.9		72.2		74.3
Total	48.9	186.3	74.6	66.0	61.1	47.5	60.4	49.0	61.6	60.8	59.9	53.3	71.9	60.3	49.8	75.9	69.2	72.2	74.3	74.3

Table 3-6. Percent Magnesium Oxide Molar Conversion to Products in MgO-CH_4-Ar System (continued)

Run	M51		M52		M53		M54		M55		M56									
Products	MgO "Mg"	MgO "O"	MgO "Mg"	MgO "O"	MgO "Mg"	MgO "O"	MgO "Mg"	MgO "O"	MgO "Mg"	MgO "O"	MgO "Mg"	MgO "O"								
Mg_2C_3	4.0		3.9		3.0		2.9		3.4		3.6									
MgC_2	0.5		1.2		0.7		0.6		0.5		0.6									
Mg	67.0		63.0		68.1		68.6		72.1		78.7									
CO		72.7		98.7		101.1		77.5		72.9		77.7								
Total	71.5	72.7	68.1	98.7	71.8	101.1	72.1	77.5	76.0	72.9	82.9	77.7								

3.2.2 Effect of Arc Power Input

The effect of power input on reactant conversion to the various products for the MgO-CH_4-Ar system was investigated over the arc power input range of 17 to 47 kW. The percentage molar conversion of the magnesium in MgO to Mg, $(Mg)\alpha_{MgO}^{Mg}$, and to Mg_2C_3, $(Mg)\alpha_{MgO}^{Mg_2C_3}$, for all the runs at various CH_4 flow rates are plotted as a function of the gross power input in Figures 3-11 and 3-12, respectively. The high degree of scatter can be attributed to differences in experimental conditions (Argon dilution level, inlet MgO:CH_4 ratio, CH_4 flow rate) at comparable power levels and to experimental uncertainty. Despite the scatter, these plots show that, over the range of experimental conditions studied, the majority of the magnesium in MgO is transformed to Mg and that a much lower percentage (<10%) is converted to Mg_2C_3. The average $(Mg)\alpha_{MgO}^{Mg}$ over all the runs is 64%, with the highest conversion at 95%. In contrast, the mean $(Mg)\alpha_{MgO}^{Mg_2C_3}$ is only 3%, with a maximum conversion of 9%. Although the average $(Mg)\alpha_{MgO}^{Mg}$ does not approach 100%, the high Mg yields and low Mg_2C_3 (and MgC_2) yields nonetheless suggest that the overall reaction of MgO with CH_4 can be attributed to Reaction (1-4), rather than to Reactions (1-2) and (1-3). Furthermore, unlike Kim's (1977) observation with the CaO-CH_4 system of a critical power input range for each methane flow rate on the order of the overall activation energy of methane decomposition, no such threshold power input range can readily be observed for MgO "Mg" conversion to either the carbide or the metal. However, because the minimum power of 17 kW in this study is above the 13-15 kW critical power input range observed by Kim for a CH_4 flow rate of 16.0-17.3 l/min, the existence of such a critical power range for the conversion of the magnesium in MgO to Mg cannot be ruled out. If there were such a critical power input range for the reaction of MgO and CH_4, it would probably be below the lower limit of the practical power input level for the thermal plasma apparatus used in the present study.

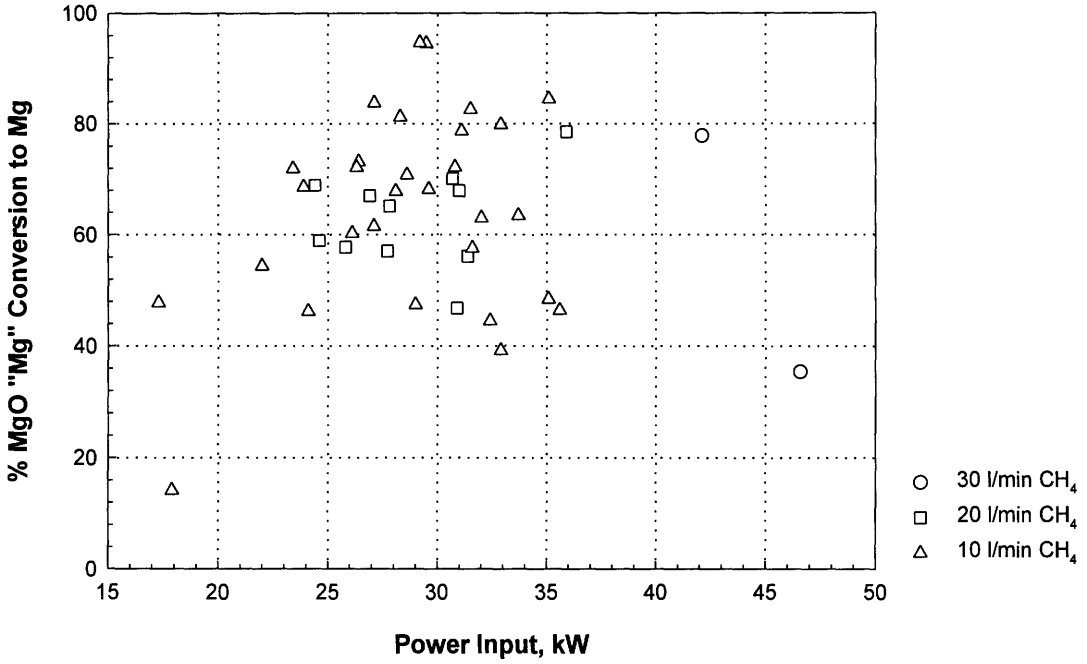

Figure 3-11. MgO "Mg" Conversion to Mg vs. Power Input at Various CH_4 Flow Rates

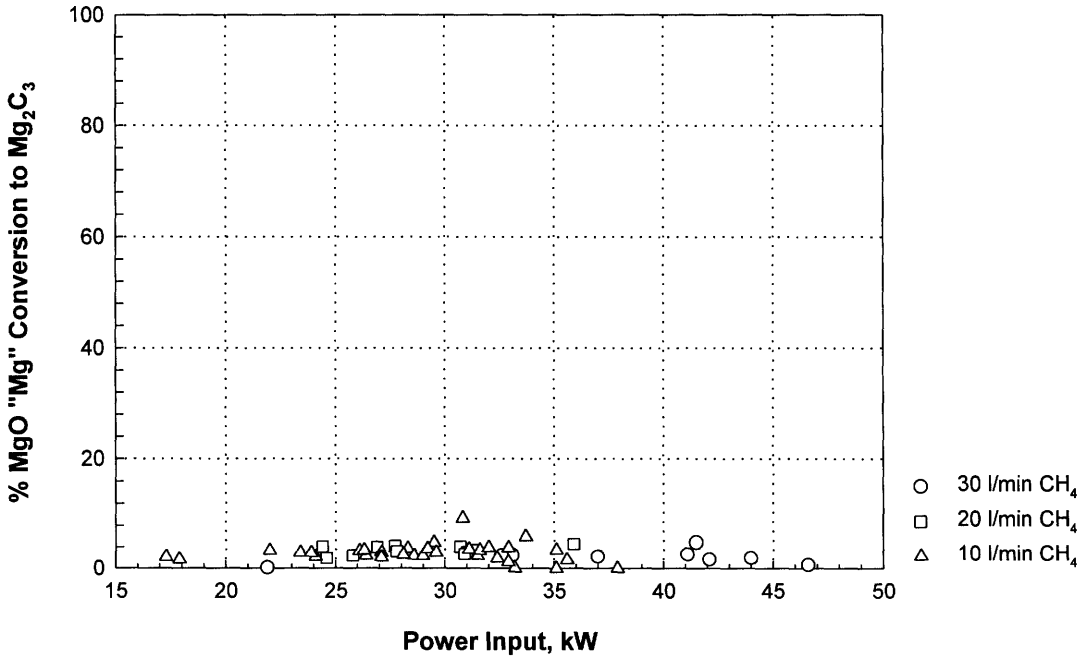

Figure 3-12. MgO "Mg"Conversion to Mg_2C_3 vs. Power Input at Various CH_4 Flow Rates

From a similar plot presented in Figure 3-13, CH_4 "H" conversion to H_2, $(H)\alpha_{CH_4}^{H_2}$, is seen to range from about 60% to virtual completion over the entire power input range. In some cases, the reported conversion is over 100%, which can be attributed to a relatively high degree of experimental uncertainty. Therefore, methane is almost completely decomposed to form H_2 and other carbon-containing products in most of the runs. Similar to MgO "Mg" conversion to Mg, $(H)\alpha_{CH_4}^{H_2}$ is found to be independent of the power input.

Figure 3-14 shows a plot of CH_4 "C" conversion to CO, $(C)\alpha_{CH_4}^{CO}$, vs. power input but with the data also classified according to the inlet MgO:CH_4 molar ratio at each CH_4 flow rate. The conversion to CO depends on the inlet MgO:CH_4 ratio, as the MgO becomes limiting at low ratios. For example, at an MgO:CH_4 molar ratio of 0.46, the MgO limits the maximum possible conversion to 46% whereas, at a 1.15:1 MgO:CH_4 ratio, all the carbon in CH_4 can be converted to CO, assuming that the reaction proceeds according to Reaction (1-4). CH_4 "C" conversion to CO at different MgO:CH_4 ratios does not depend on power input over the range of conditions investigated. The average $(C)\alpha_{CH_4}^{CO}$ over all the runs is 60%, in good agreement with the average $(Mg)\alpha_{MgO}^{Mg}$.

The sample mean, standard deviation, 95% confidence interval (C.I.) for the sample mean, minimum and maximum values for the percent molar conversion of the constituent elements of MgO and CH_4 to the various products are provided in Table 3-7.

Table 3-7. Summary Statistics of Reactant Conversion to Products for All Runs in MgO-CH_4-Ar System

% Conversion	Mean	Std. Dev.	95% C.I.	Minimum	Maximum
$(Mg)\alpha_{MgO}^{Mg}$	64.4	16.5	[59.4,69.4]	14.1	94.7
$(Mg)\alpha_{MgO}^{Mg_2C_3}$	3.0	1.5	[2.5,3.4]	0.0	9.3
$(Mg)\alpha_{MgO}^{MgC_2}$	0.5	0.3	[0.4,0.6]	0.0	1.8
$(H)\alpha_{CH_4}^{H_2}$	90.6	16.4	[86.1,95.1]	57.4	123.9
$(C)\alpha_{CH_4}^{CO}$	60.4	21.1	[54.6,66.1]	22.2	116.6
$(C)\alpha_{CH_4}^{C}$	28.0	14.7	[23.9,32.0]	3.2	67.2

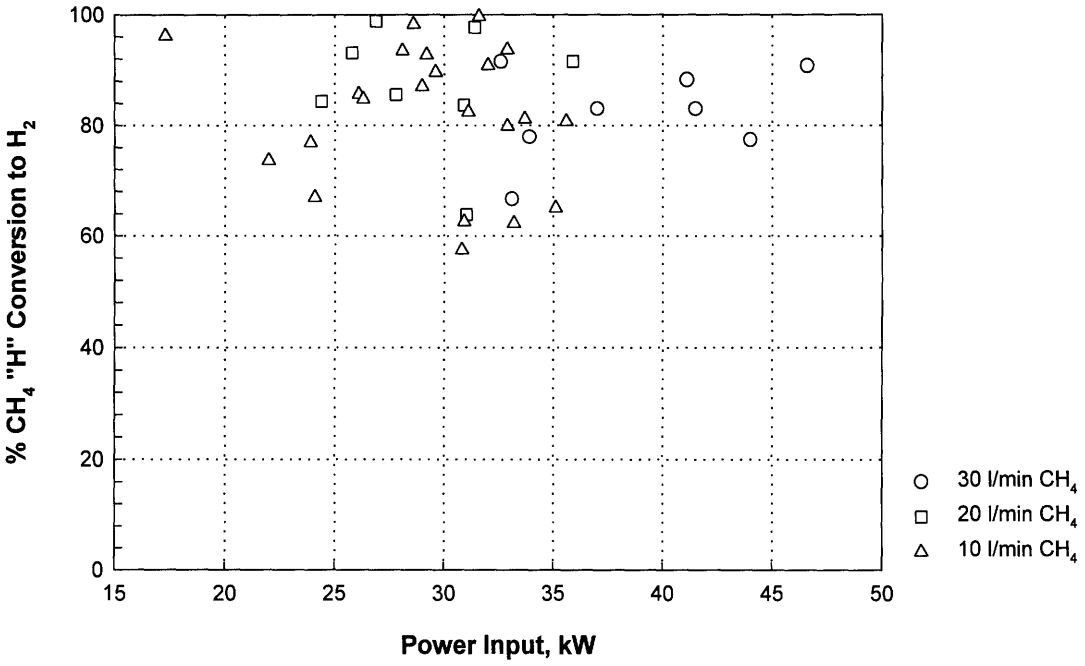

Figure 3-13. CH_4 "H" Conversion to H_2 vs. Power Input at Various CH_4 Flow Rates

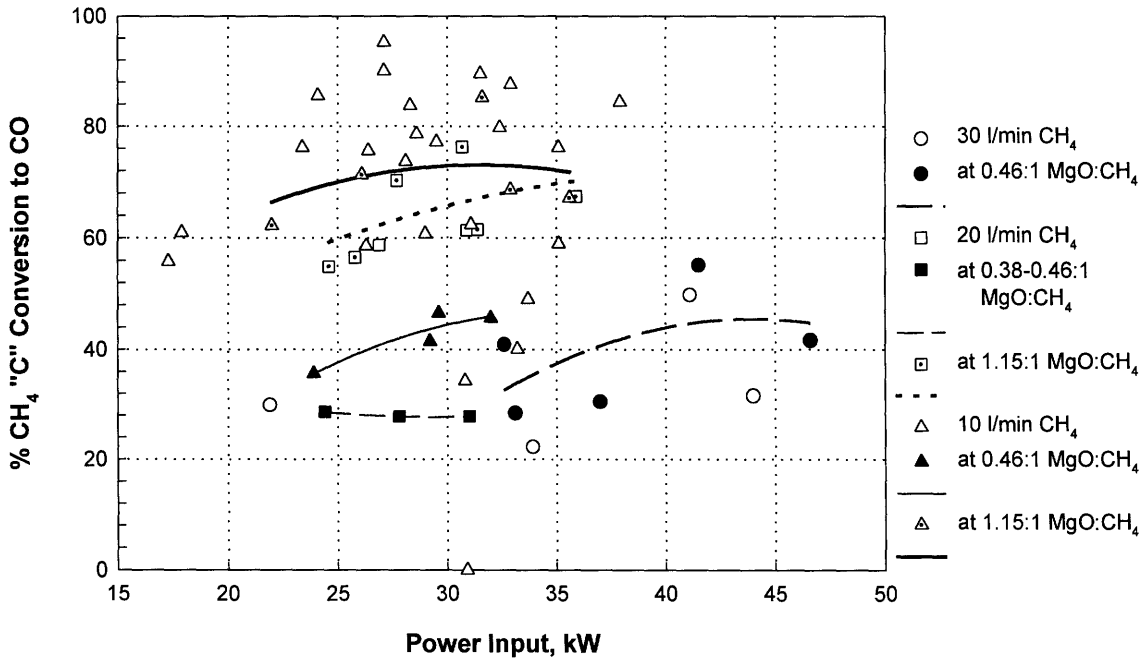

Figure 3-14. CH_4 "C" Conversion to CO vs. Power Input at Various CH_4 Flow Rates and Inlet MgO:CH_4 Ratios

3.2.3 Effect of Methane Flow Rate

The effect of methane flow rate on reactant conversion to products was studied over the power input range of 17 to 47 kW at three levels of methane flow rate: 30, 20 and 10 l/min. Statistical methods based on *t*-tests were used to determine the significance of the differences in the average $(Mg)\alpha_{MgO}^{Mg}$ and $(H)\alpha_{CH_4}^{H_2}$ observed under the three flow rates. The relevant statistics for $(Mg)\alpha_{MgO}^{Mg}$ and $(H)\alpha_{CH_4}^{H_2}$ are given in Table 3-8. The *p*-value is the probability of rejecting the null hypothesis when the null hypothesis is correct. In this case, the null hypothesis is that the mean $(Mg)\alpha_{MgO}^{Mg}$ and $(H)\alpha_{CH_4}^{H_2}$ at 30 and 20 l/min CH_4 flow rates are equal to the mean $(Mg)\alpha_{MgO}^{Mg}$ and $(H)\alpha_{CH_4}^{H_2}$ at 10 l/min CH_4 flow. Thus, the *p*-value of 0.66 given in Table 3-8 is the probability of making the error of rejecting the null hypothesis that the mean $(Mg)\alpha_{MgO}^{Mg}$ at 30 l/min CH_4 flow is equal to the mean at 10 l/min CH_4 flow when they are actually equal. At the 0.05 significance level, the *p*-value should therefore be less than or equal to 0.05 for the difference to be statistically meaningful.

The results of the *t*-tests at the 0.05 significance level show that the mean values of $(Mg)\alpha_{MgO}^{Mg}$ at 30 l/min and at 10 l/min are not statistically different, although the sample mean of $(Mg)\alpha_{MgO}^{Mg}$ of 62.4% at 10 l/min is greater than the sample mean of 56.6% at 30 l/min. Similarly, the difference between the mean values of $(Mg)\alpha_{MgO}^{Mg}$ at 20 l/min and at 10 l/min is not significant. The same is true of mean values of $(H)\alpha_{CH_4}^{H_2}$ at CH_4 flow rates of 30 and 10 l/min and of the mean values of $(H)\alpha_{CH_4}^{H_2}$ at 20 and 10 l/min. Therefore, $(Mg)\alpha_{MgO}^{Mg}$ and $(H)\alpha_{CH_4}^{H_2}$ are not strongly correlated with CH_4 flow rate.

Table 3-8. Summary Statistics of Reactant Conversion to Mg and to H_2 at Different Methane Flow Rates

% Conversion	CH_4 Flow, l/min	Mean	Standard Deviation	95% C.I.	Min.	Max.	*p*-value
$(Mg)\alpha_{MgO}^{Mg}$	30	56.6	30.1	-	35.3	77.8	0.66
	20	63.1	8.7	[57.2,69.0]	46.8	78.5	0.90
	10	62.4	15.5	[52.6,72.2]	39.1	94.7	
$(H)\alpha_{CH_4}^{H_2}$	30	82.3	8.3	[75.4,89.3]	66.7	91.5	0.75
	20	92.0	12.6	[83.5,100.5]	63.8	111.8	0.08
	10	83.6	9.0	[77.9,89.3]	66.9	99.7	

Despite the absence of a noticeable methane flow rate effect on conversion, increasing the methane flow rate, however, has the effect of raising the energy efficiency of the conversion process. This can be seen by examining plots of conversion as a function of specific gas energy. Specific gas energy (energy input per g-atom carbon) is a measure of the gas stream enthalpy and is the result of dividing the gross power input (energy per unit time) by the CH_4 molar flow rate (moles per unit time). When $(Mg)\alpha_{MgO}^{Mg}$ and $(H)\alpha_{CH_4}^{H_2}$ are plotted as a function of the specific gas energy, as shown in Figures 3-15 and 3-16, respectively, one finds that approximately the same extents of conversion at a high specific gas energy can also be achieved at a low specific gas energy.

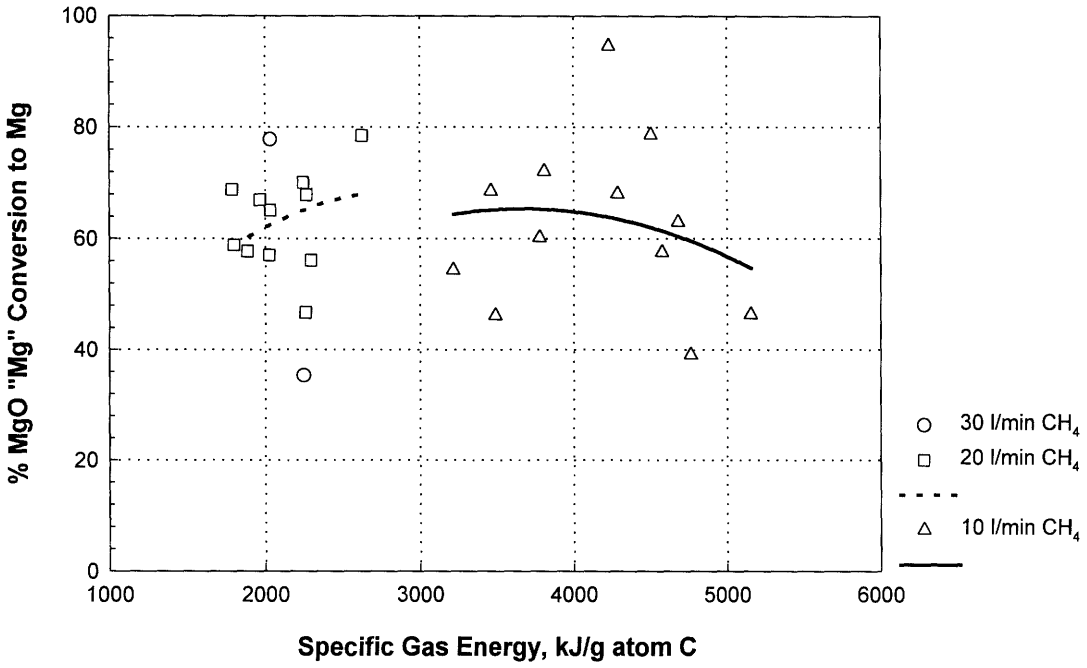

Figure 3-15. MgO "Mg" Conversion to Mg vs. Specific Gas Energy

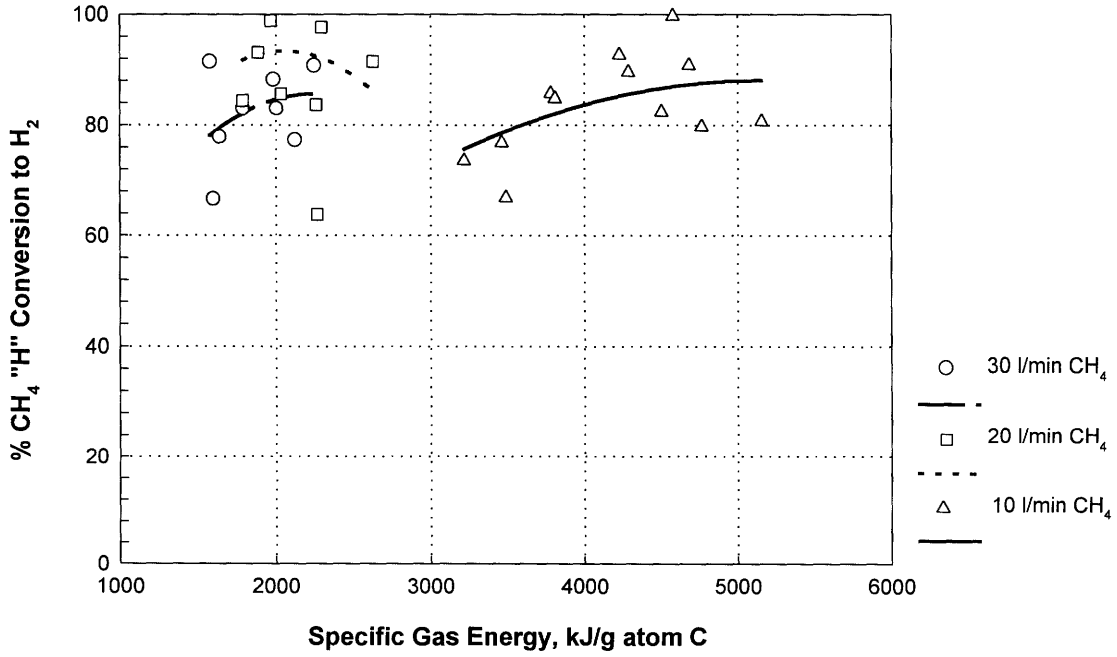

Figure 3-16. CH_4 "H" Conversion to H_2 vs. Specific Gas Energy

Thus, although the power input needed to effect the same extent of CH_4 "H" conversion to H_2 is higher at 30 l/min than at 10 l/min (Figure 3-13), Figure 3-16 shows that the specific gas energy for the same level of conversion is actually lower for 30 l/min than for 10 l/min CH_4 flow. Since the specific gas energy is inversely proportional to the CH_4 flow rate, this means that the additional power needed at the higher flow rate to achieve the same level of conversion as at the lower flow rate is less than proportional to the increase in gas flow. Therefore, increasing the CH_4 flow rate increases the energy efficiency of the conversion process. A similar enhancement in efficiency was observed by Kim (1977) with higher methane flow rates.

For CH_4 "C" conversion to CO, $(C)\alpha_{CH_4}^{CO}$, methane flow rate has a more pronounced effect. For the same inlet MgO:CH_4 ratio of 0.38-0.46:1, the difference between the $(C)\alpha_{CH_4}^{CO}$ sample mean of 42.3% at 10 l/min CH_4 flow and the sample mean of 28.1 at 20 l/min CH_4 flow is statistically significant at the 0.05 level. The null hypothesis here is that the mean $(C)\alpha_{CH_4}^{CO}$ at 20 l/min is greater than or equal to the mean $(C)\alpha_{CH_4}^{CO}$ at 10 l/min. Therefore, when CH_4 is in stoichiometric excess (MgO:CH_4<1), operation at a high CH_4 flow rate is likely to result in a lower $(C)\alpha_{CH_4}^{CO}$ than operation at a low CH_4 flow rate. At an MgO:CH_4 ratio of 1.15:1, although the mean conversion at 20 l/min is lower than that at 10 l/min, no such conclusion can be drawn because the *p*-value is 0.12. The summary statistics for CH_4 "C" conversion to CO are provided in Table 3-9.

Table 3-9. Summary Statistics of CH_4 "C" Conversion to CO at Different Methane Flow Rates and Inlet MgO:CH_4 Ratios

Inlet MgO:CH_4 Ratio	CH_4 Flow, l/min	Mean	Standard Deviation	95% C.I.	Min.	Max.	*p*-value
0.38-0.46:1	20	28.1	0.5	[26.9,29.2]	27.8	28.6	0.00
	10	42.3	5.0	[34.4,50.2]	35.6	46.5	
1.15:1	20	64.4	8.3	[55.7,73.1]	54.8	78.2	0.12
	10	70.9	8.7	[60.2,81.6]	62.2	85.2	

The effects of methane flow rate on CH_4 "C" conversion to CO can be explained in terms of residence time. The higher the CH_4 flow rate, the shorter the residence time of the CH_4 reactant or the nascent carbon derivative species in the plasma. Thus, there is less time for the carbon-bearing species to react with the MgO reactant (or the oxygen in the MgO). This effect is less pronounced when the CH_4 is stoichiometrically deficient relative to MgO ($MgO:CH_4>1$). The effect of inlet $MgO:CH_4$ ratio is discussed in more detail in the next section.

Figure 3-17 shows a plot of CH_4 "C" conversion to CO for different methane flow rates and inlet $MgO:CH_4$ ratios as a function of the specific gas energy. When comparing conversion at different methane flow rates at the same $MgO:CH_4$ ratio, a similar decrease in specific gas energy needed to effect roughly the same CH_4 "C" conversion to CO is observed with an increase in CH_4 flow rate. For example, given an inlet ratio of 1.15:1 $MgO:CH_4$, the same level of conversion is achieved at lower specific gas energies for 20 l/min than for 10 l/min CH_4 flow. This further supports the argument of enhanced efficiency at higher gas flow rates.

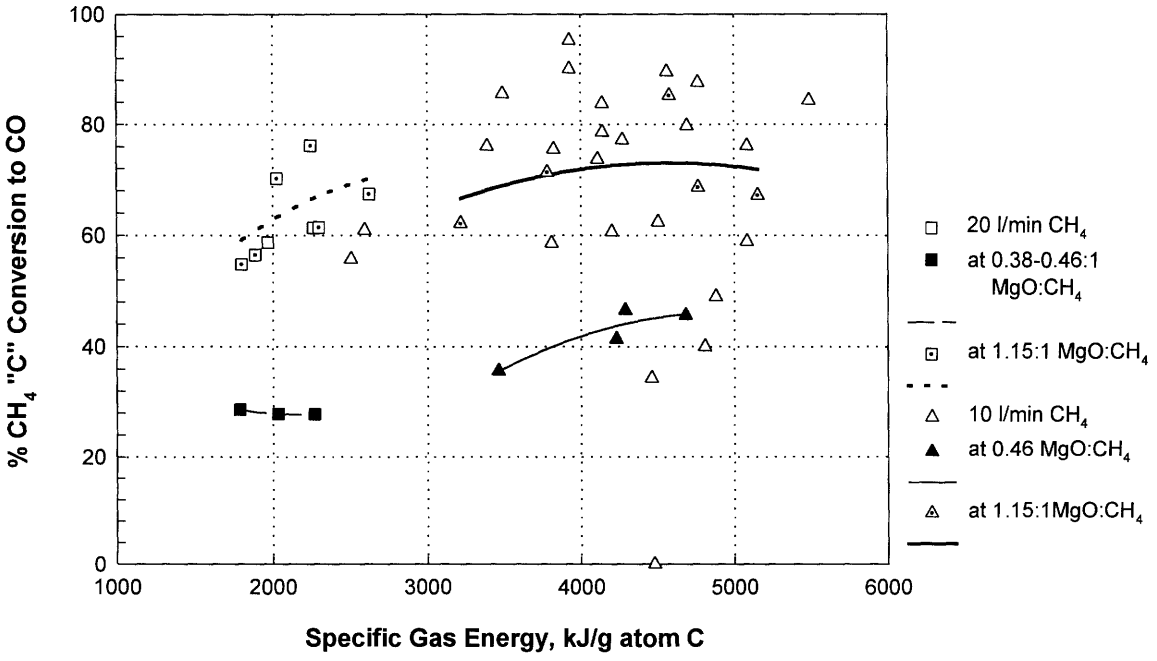

Figure 3-17. CH_4 "C" Conversion to CO vs. Specific Gas Energy at Various CH_4 Flow Rates and Inlet $MgO:CH_4$ Ratios

With CH_4 "H" conversion to H_2 independent of and CH_4 "C" conversion to CO inversely correlated with CH_4 flow rate, one should observe the H_2/CO ratio in the gas product to increase with CH_4 flow rate. Figure 3-18 is a plot of the H_2/CO ratio as a function of specific gas energy at specified MgO:CH_4 ratios for each methane flow rate. The range of H_2/CO ratios is found to be between 2 and 6, corresponding to the values expected from magnesium metal formation, Reaction (1-4), and magnesium carbide formation, Reactions (1-2) and (1-3). At the same inlet MgO:CH_4 ratio, higher H_2/CO ratios are indeed found to be associated with higher methane flow rates over the energy input range investigated. At an inlet MgO:CH_4 ratio of 1.15:1, the difference between the H_2/CO ratio sample mean of 3.1 at 20 l/min and the sample mean of 2.4 at 10 l/min is statistically significant at the 0.05 level. The same is true of the mean values at an inlet MgO:CH_4 ratio of 0.46:1. Table 3-10 summarizes the statistics for the H_2/CO ratio.

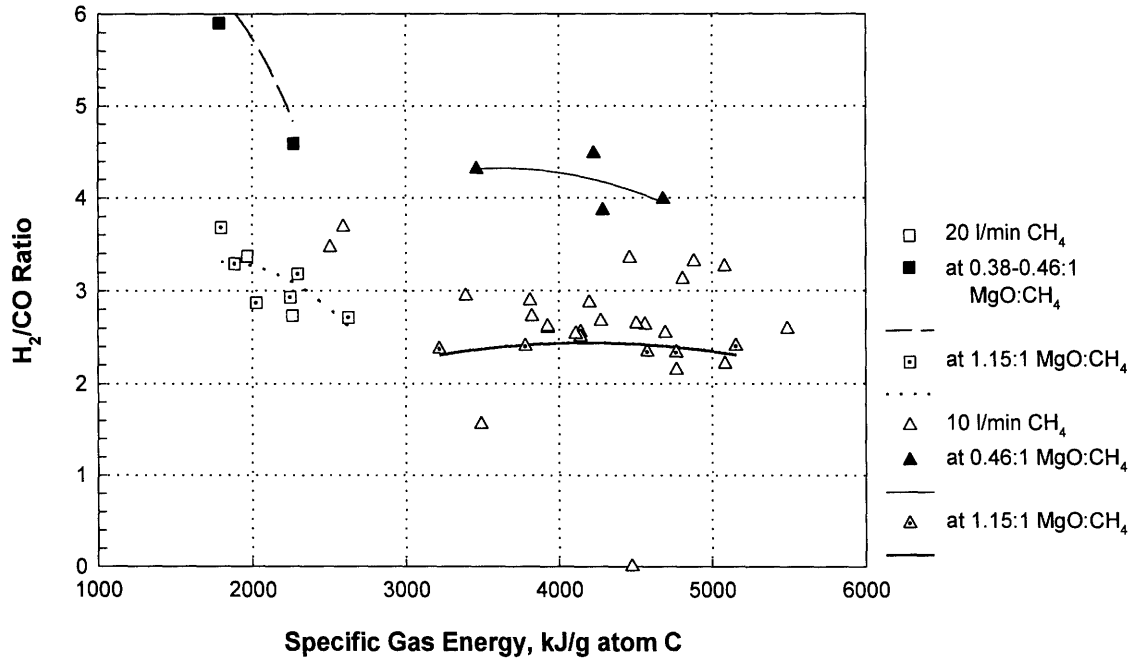

Figure 3-18. H_2/CO Ratio vs. Specific Gas Energy at Various Methane Flow Rates and Inlet MgO:CH_4 Ratios

Table 3-10. Summary Statistics of H_2/CO Ratio in Gas Product at Different Methane Flow Rates and Inlet MgO:CH_4 Ratios

Inlet MgO:CH_4 Ratio	CH_4 Flow, l/min	Mean	Standard Deviation	95% C.I.	Min.	Max.	*p*-value
0.46:1	20	5.6	0.8	[3.5,7.6]	4.6	6.2	0.01
	10	4.2	0.3	[3.7,4.6]	2.9	4.5	
1.15:1	20	3.1	0.3	[2.7,3.5]	2.7	3.7	0.00
	10	2.4	0.0	[2.3,2.4]	2.3	2.4	

Because no significant increase in CH_4 "C" conversion to Mg_2C_3 and MgC_2 has been observed at higher methane flow rates, the larger H_2/CO ratios suggest the formation of carbon or carbon-rich products at the higher gas flow rates. A plot of CH_4 "C" conversion to non-carbide C, $(C)\alpha_{CH_4}^{C}$, vs. specific gas energy, presented in Figure 3-19, illustrates similar trends as the H_2/CO ratio, thus providing support for the formation of solid carbon at higher methane flow rates. A *t*-test is performed based on the null hypothesis that, at a given inlet MgO:CH_4 ratio, the mean $(C)\alpha_{CH_4}^{C}$ at the 20 l/min CH_4 flow rate is less than or equal to the mean $(C)\alpha_{CH_4}^{C}$ at 10 l/min. The test results show that, at an inlet MgO:CH_4 ratio of 1.15:1, the mean of 33.7% at 20 l/min is statistically greater at the 0.05 significance level than the mean of 15.6% at 10 l/min. At 0.46:1 MgO:CH_4 ratio, the difference between the mean $(C)\alpha_{CH_4}^{C}$ at 20 l/min and at 10 l/min is only significant at the 0.09 level, although the conversion is higher at 20 l/min CH_4, on average, than at 10 l/min CH_4. The summary statistics for CH_4 carbon conversion to non-carbide C are presented in Table 3-11.

The absence of an apparent correlation between methane flow rate and CH_4 "H" conversion to H_2 suggests that the methane is always decomposed to hydrogen and carbon-bearing species, regardless of the flow rate. The carbon is likely to form nascent carbon that can either react with MgO to form CO or end up as solid carbon (non-carbide C). That one product is being formed at the expense of the other is substantiated by the reverse effect of gas flow rate on CH_4 "C" conversion to CO and to non-carbide C. When the CH_4 flow rate is high, the nascent carbon species may not have sufficient time to react

with MgO, so the conversion to non-carbide C is high and that to CO is low. But when the CH_4 flow rate is low, the longer residence time allows the nascent carbon to react with MgO to form more CO instead of non-carbide C. Since MgO is the only source of oxygen in the system and MgO "Mg" conversion to magnesium carbides does not change significantly when the methane flow rate is increased, an increase in the MgO "Mg" conversion to Mg is expected to follow from an increase in the CH_4 "C" conversion to CO.

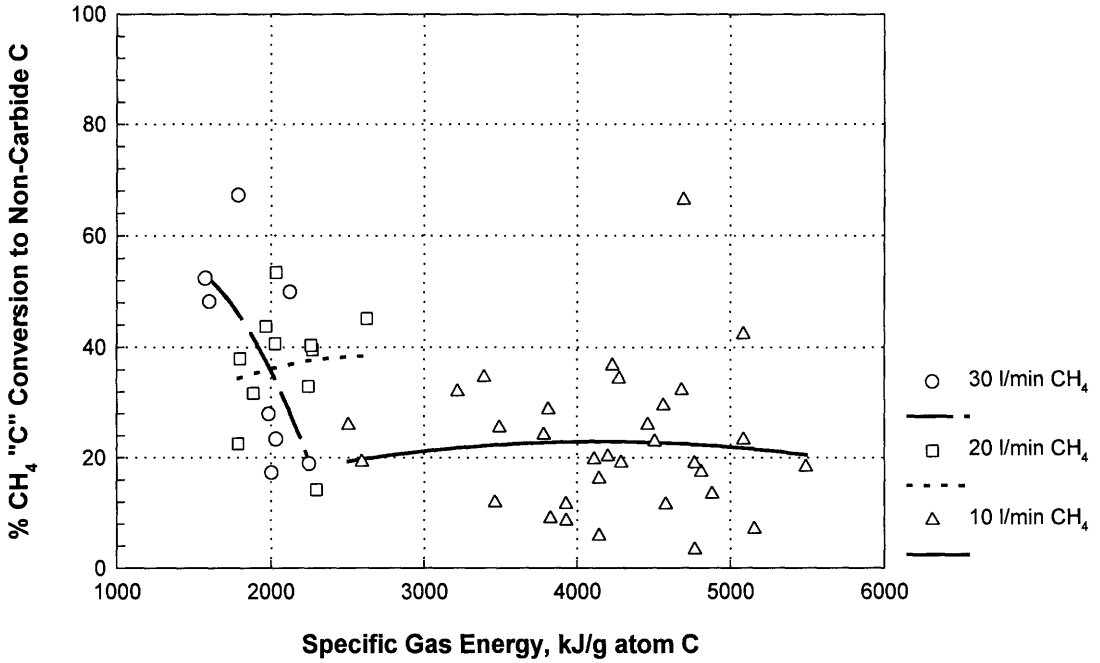

Figure 3-19. CH_4 "C" Conversion to Non-Carbide C vs. Specific Gas Energy

Table 3-11. Summary Statistics of CH_4 "C" Conversion to Non-Carbide Carbon at Different Methane Flow Rates and Inlet MgO:CH_4 Ratios

Inlet MgO:CH_4 Ratio	CH_4 Flow, l/min	Mean	Standard Deviation	95% C.I.	Min.	Max.	*p*-value
0.46:1	20	38.5	15.5	[0.1,76.8]	22.5	53.4	0.09
	10	25.0	10.0	[12.6,37.4]	11.8	36.7	
1.15:1	20	33.7	10.8	[22.4,45.0]	14.2	45.1	0.01
	10	15.6	12.1	[0.5,30.6]	3.2	32.0	

3.2.4 Effect of Inlet MgO:CH_4 Molar Ratio

The reactant conversion to products over a power input range of 22-38 kW at CH_4 flow rates of 20 l/min and 10 l/min was determined for inlet MgO:CH_4 molar ratios of 1.15:1 and 0.38-0.46:1. Statistical analysis was applied to the conversion data to assess the effect of inlet MgO:CH_4 molar ratio on extent of conversion. Table 3-12 gives the sample mean, standard deviation, 95% C.I. for the sample mean, minimum, maximum and *p*-values of reactant conversion to the various products for the two MgO:CH_4 ratios at 20 l/min CH_4. The *p*-values for $(H)\alpha_{CH_4}^{H_2}$ and $(C)\alpha_{CH_4}^{CO}$ correspond to the probability of rejecting the null hypothesis that the mean at the higher MgO:CH_4 ratio is less than or equal to the mean at the lower MgO:CH_4 when the null hypothesis is correct. The *p*-values for $(Mg)\alpha_{MgO}^{Mg}$, $(Mg)\alpha_{MgO}^{Mg_2C_3}$ and $(C)\alpha_{CH_4}^{C}$ correspond to the probability of rejecting the null hypothesis that the mean at the higher MgO:CH_4 ratio is greater than or equal to the mean at the lower MgO:CH_4 when the null hypothesis is correct.

Table 3-12. Summary Statistics of Reactant Conversion to Products at Different Inlet MgO:CH_4 Ratios and at 20 l/min CH_4 Flow

% Conversion	MgO:CH_4 Ratio	Mean	Standard Deviation	95% C.I.	Min.	Max.	*p*-value
$(Mg)\alpha_{MgO}^{Mg}$	1.15:1	63.1	9.2	[53.4,72.7]	56.1	78.5	0.23
	0.38-0.46:1	67.3	2.0	[62.4,72.2]	65.1	68.9	
$(Mg)\alpha_{MgO}^{Mg_2C_3}$	1.15:1	3.4	1.1	[2.3,4.6]	1.9	4.6	0.48
	0.38-0.46:1	3.5	0.6	[2.1,4.8]	3.1	4.1	
$(H)\alpha_{CH_4}^{H_2}$	1.15:1	99.3	7.2	[91.7,106.9]	91.5	111.8	
	0.38-0.46:1	77.9	12.3	[47.6,108.3]	63.8	85.6	0.01
$(C)\alpha_{CH_4}^{CO}$	1.15:1	64.4	8.3	[55.7,73.1]	54.8	76.2	
	0.38-0.46:1	28.1	0.5	[26.9,29.2]	27.8	26.8	0.00
$(C)\alpha_{CH_4}^{C}$	1.15:1	33.7	10.8	[22.4,45.0]	14.2	45.1	0.30
	0.38-0.46:1	38.5	15.5	[0.1,76.8]	22.5	53.4	

The p-values in Table 3-12 imply that, at a CH_4 flow rate of 20 l/min, $(H)\alpha_{CH_4}^{H_2}$ and $(C)\alpha_{CH_4}^{CO}$ are likely to be higher when methane is stoichiometrically deficient relative to MgO ($MgO:CH_4>1$) than when methane is in excess. On the other hand, although $(Mg)\alpha_{MgO}^{Mg}$, $(Mg)\alpha_{MgO}^{Mg_2C_3}$ and $(C)\alpha_{CH_4}^{C}$ at the lower $MgO:CH_4$ ratio are higher, on average, than at the higher $MgO:CH_4$ ratio, the difference is not significant at the 0.05 level.

A similar set of statistics for reactant conversion to the various products for the inlet $MgO:CH_4$ ratios of 0.46:1 and 1.15:1 at 10 l/min CH_4 is shown in Table 3-13. The p-values indicate that $(C)\alpha_{CH_4}^{CO}$ is likely to be greater at the higher $MgO:CH_4$ ratio than at the lower $MgO:CH_4$ ratio while $(H)\alpha_{CH_4}^{H_2}$ is not likely to vary with the $MgO:CH_4$ ratio. $(Mg)\alpha_{MgO}^{Mg}$ will also probably be higher, on average, when MgO is deficient relative to CH_4 than when it is in excess, supporting the trend observed under the 20 l/min condition. The mean $(Mg)\alpha_{MgO}^{Mg_2C_3}$ and $(C)\alpha_{CH_4}^{C}$ are also higher at the lower inlet $MgO:CH_4$ ratio than at the higher inlet $MgO:CH_4$ ratio but the differences are not significant.

Table 3-13. Summary Statistics of Reactant Conversion to Products at Different Inlet $MgO:CH_4$ Ratios and at 10 l/min CH_4 Flow

% Conversion	$MgO:CH_4$ Ratio	Mean	Standard Deviation	95% C.I.	Min.	Max.	p-value
$(Mg)\alpha_{MgO}^{Mg}$	1.15:1	51.5	8.7	[40.8,62.3]	39.1	60.2	0.05
	0.46:1	68.1	17.4	[46.5,89.7]	46.2	94.7	
$(Mg)\alpha_{MgO}^{Mg_2C_3}$	1.15:1	2.6	1.1	[1.2,3.9]	1.2	3.4	0.17
	0.46:1	3.1	0.7	[2.3,4.0]	2.2	3.9	
$(H)\alpha_{CH_4}^{H_2}$	1.15:1	83.9	9.8	[71.7,96.1]	73.6	99.7	
	0.46:1	83.4	11.1	[69.5,97.2]	66.9	92.7	0.47
$(C)\alpha_{CH_4}^{CO}$	1.15:1	70.9	8.7	[60.2,81.6]	62.2	85.2	
	0.46:1	42.3	5.0	[34.4,50.2]	35.6	46.5	0.00
$(C)\alpha_{CH_4}^{C}$	1.15:1	15.6	12.1	[0.5,30.6]	3.2	32.0	0.11
	0.46:1	25.0	10.0	[12.6,37.4]	11.8	36.7	

The comparison of the extents of conversion at the two inlet $MgO:CH_4$ ratios under CH_4 flow rates of 20 and 10 l/min suggests that CH_4 "C" conversion to CO can be enhanced by increasing the inlet $MgO:CH_4$ ratio, regardless of the CH_4 flow rate. The dependence of CH_4 "C" conversion to CO on the inlet $MgO:CH_4$ ratio is not unexpected because a sub-stoichiometric ratio will simply limit the maximum possible conversion level. At an inlet $MgO:CH_4$ ratio of 0.46:1, the maximum possible conversion is 46%, according to Reaction (1-4), while at 1.15:1 $MgO:CH_4$, all the carbon can react with the oxygen in MgO to form CO. Furthermore, the comparison also suggests that CH_4 "H" conversion to H_2 can be increased with a higher inlet $MgO:CH_4$ ratio, particularly when the methane flow rate is high. When the methane flow rate is low, the residence time is relatively long and the methane has sufficient time to decompose and react with MgO or its atomic constituents, regardless of the relative amounts of MgO. But with a high methane flow rate, the short residence time may limit the extent of reaction unless the MgO is in relative excess to promote the reaction.

With <1% unreacted CH_4 observed in the gas product, virtually all the methane is decomposed and/or converted in the plasma reactor. The low CH_4 "C" conversion to CO at $MgO:CH_4<1$ would suggest that the remaining carbon in the original CH_4 is converted to other hydrocarbons and/or solid carbon. The CH_4 "C" conversion to C_2H_2 ranges only from 0.5 to 4.2% at 20 l/min CH_4 and from 0.8 to 3.0% at 10 l/min CH_4 while the CH_4 "C" conversion to other HCs at both CH_4 flow rates is typically less than 2%. Hence, the carbon in CH_4 is most likely recovered as solid carbon in the non-carbide C. At both CH_4 flow rates, the mean CH_4 "C" conversion to non-carbide C is higher when $MgO:CH_4<1$ than when $MgO:CH_4>1$, whereas the average CH_4 "C" conversion to CO exhibits the reverse trend. This observation further provides support for the hypothesis that nascent carbon is formed from the methane which can either react with MgO to form CO or be condensed as solid carbon. The amount of solid carbon in the final product would then depend on the starting amount of MgO with which the nascent carbon can react and on the residence time in the reactor.

Under both CH_4 flow rates of 10 and 20 l/min, the average MgO "Mg" conversion to Mg is higher at the low inlet $MgO:CH_4$ ratio than at the inlet high $MgO:CH_4$ ratio,

although statistical analysis does not indicate the difference to be significant in the former case. Similarly, CH_4 "C" conversion to non-carbide carbon is also higher, on average, when the MgO is deficient relative to CH_4 than when it is in excess, but the difference is also not significant. Nonetheless, these observations are consistent with the trends observed in the data on CH_4 conversion to CO and H_2.

The conversion of a particular reactant to Mg, CO or H_2 is then postulated to increase when this reactant is stoichiometrically deficient relative to the other reactant based on Reaction (1-4). Specifically, the extent of MgO "Mg" conversion to Mg would be expected to increase when the CH_4 is in stoichiometric excess while the extents of CH_4 "H" conversion to H_2 and of CH_4 "C" conversion to CO would be enhanced when the MgO is in excess. Thus, the formation of Mg, CO and H_2 from its parent reactant can be promoted by feeding an excess of the other reactant.

Figure 3-20 shows the variation of CH_4 "C" conversion with the inlet MgO:CH_4 molar ratio over all the runs conducted. Analogous to Kim's (1977) observations shown in Figure 1-3, the conversion of the carbon in methane to gaseous hydrocarbons (C_2H_2, C_3H_4 and other C_2, C_3, and C_4 species) is observed to decrease abruptly from over 90% without MgO feeding to less than 10% with only a small addition of MgO. On the other hand, CH_4 "C" conversion to CO, Mg_2C_3 and MgC_2 is seen to increase steadily with increasing inlet MgO:CH_4 ratio. Therefore, the introduction of magnesium oxide (or calcium oxide) into a high-temperature methane reaction system significantly shifts the product chemistry of methane decomposition from pyrolysis end-products to CO and metal carbides.

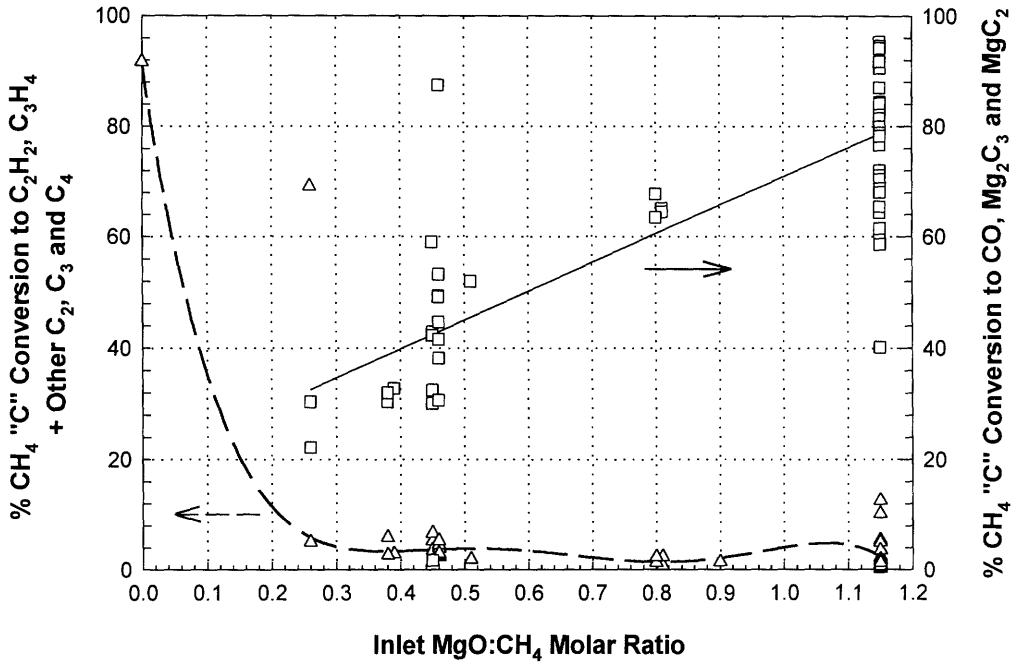

Figure 3-20. CH_4 "C" Conversion vs. Inlet MgO:CH_4 Molar Ratio

3.2.5 Effect of Argon Dilution

The effect of dilution of the plasma-forming gas with Argon on reactant conversion was investigated at three dilution levels: a) 15 l/min Argon; b) 10 l/min Argon; and c) no dilution, in addition to the 4.2 l/min Argon powder carrier gas. The experiments were performed with 10 l/min CH_4 flow and 1.15:1 inlet MgO:CH_4 molar ratio over a power input range of 22-38 kW. Statistical analysis was applied to the conversion data to determine whether Argon dilution has a significant effect on the extent of conversion. Table 3-14 gives the sample mean, standard deviation, 95% C.I. for the sample mean, minimum, maximum and *p*-values of reactant conversion to the various products at the three levels of Argon dilution. The *p*-value is the probability of rejecting the null hypothesis that the mean values at 15 and 10 l/min Argon dilution are less than or equal to the mean values without Argon dilution when the null hypothesis is correct.

Table 3-14. Summary Statistics of Reactant Conversion to Products at 15, 10 and 0 l/min Argon Dilution

% Conversion	Argon Dilution, l/min	Mean	Standard Deviation	95% C.I.	Min.	Max.	*p*-value
$(Mg)\alpha_{MgO}^{Mg}$	15	82.2	9.0	[67.9,96.4]	73.1	94.5	0.00
	10	66.3	15.4	[5.3,77.3]	44.5	84.5	0.04
	0	51.5	8.7	[40.8,62.3]	39.1	60.2	
$(Mg)\alpha_{MgO}^{Mg_2C_3}$	15	2.9	1.9	[0.6,5.2]	0.0	4.8	0.35
	10	2.1	1.1	[1.4,2.9]	0.0	3.5	0.23
	0	2.6	1.1	[1.2,3.9]	1.2	3.4	
$(H)\alpha_{CH_4}^{H_2}$	15	103.0	5.8	[95.8,110.2]	93.7	108.9	0.00
	10	100.1	21.7	[85.5,114.7]	62.3	123.9	0.07
	0	83.9	9.8	[71.7,96.1]	73.6	99.7	
$(C)\alpha_{CH_4}^{CO}$	15	81.7	5.1	[75.3,88.1]	75.5	87.6	0.02
	10	74.4	16.0	[63.7,85.2]	40.0	95.2	0.33
	0	70.9	8.7	[60.2,81.6]	62.2	85.2	
$(C)\alpha_{CH_4}^{C}$	15	19.3	9.3	[7.8,30.8]	8.9	34.4	0.30
	10	25.3	17.5	[13.6,37.1]	5.7	66.3	0.14
	0	15.0	12.1	[0.5,30.6]	3.2	32.0	

From the results of the *t*-tests, the addition of Argon is found to enhance the conversion of MgO "Mg" to Mg, despite the increase in residence time brought about by the higher total gas flow rate. The $(Mg)\alpha_{MgO}^{Mg}$ sample mean of 82.2% at 15 l/min Argon dilution is found to be significantly different from the mean of 51.5% without Argon dilution at the 0.05 level. On the other hand, this enhancement effect is not evident for $(Mg)\alpha_{MgO}^{Mg_2C_3}$, whose sample means at the different Argon dilution levels are not found to be significantly different.

The extents of conversion of CH_4 "H" to H_2 and of CH_4 "C" to CO exhibit similar improvements with higher Argon dilution levels. $(H)\alpha_{CH_4}^{H_2}$ is increased from an average of 83.9% without Argon dilution to virtually complete conversion with 15 l/min Argon

dilution. The mean $(C)\alpha_{CH_4}^{CO}$ of 81.7% at 15 l/min Argon dilution is likewise significantly different at the 0.05 level from the sample mean of 70.9% without Argon dilution.

The effect of inert gas addition on the extent of reaction can readily be explained by Le Chatelier's principle. With a net positive change in the number of moles in the system when going from reactants to products, as in Reactions (1-2), (1-3) and (1-4), the product yield can be increased by reducing the total system pressure. A similar effect is achieved with Argon dilution, which reduces the relative net increase in the number of moles from reactants to products. However, the effect of inert gas dilution differs from a mere system pressure reduction in the rate at which equilibrium is approached. Inert gas addition gives rise to different gas collision rates and mean free paths in the gas phase which change the transport rates. In addition, inert gas dilution reduces the temperature rise of the nascent clusters forming from the gas phase and the temperature at which condensed phases form, which can significantly enhance particle nucleation, condensation and growth rates (Stephens *et al.*, 1993).

3.2.6 Effect of Secondary CH_4 Quench

In the earlier part of this study, the effect of a secondary CH_4 gas quench directed immediately downstream of the plasma jet was investigated with a view to identifying conditions under which magnesium carbide can be synthesized more favorably. The following two-step mechanism has been proposed for magnesium carbide synthesis from CH_4 and MgO:

$$2\,CH_4 + 2\,MgO \rightarrow 2\,Mg + 4\,H_2 + 2\,CO \qquad \text{Reaction (1-4)}$$

$$3\,CH_4 + 2\,Mg \rightarrow Mg_2C_3 + 6\,H_2 \qquad \text{Reaction (1-21)}$$

$$5\,CH_4 + 2\,MgO \rightarrow Mg_2C_3 + 10\,H_2 + 2\,CO \qquad \text{Reaction (1-2)}$$

The above mechanism was tested in two experimental runs, M14 and M15, with secondary methane feeding. In Run M14, secondary methane feed was introduced into

the top portion of the cooling chamber through the two 1 in. ports just below the top flange. In Run M15, instead of feeding CH_4 through the entire cross-section of the 1 in. ports, CH_4 was introduced through two 1/8 in. SS tubes inserted through these ports to locations at the same radial distance from the arc axis as the outer diameter of the graphite anode. The first step of the proposed mechanism, Reaction (1-4), was simulated with a near-equimolar (1.15:1) flow of MgO and CH_4 into the plasma reactor. Thus, 10 l/min CH_4 diluted with 11 l/min Ar and 19 g/min MgO with 4.2 l/min of Ar carrier gas were fed into the plasma reactor. Secondary methane was then injected at 15 l/min downstream of the plasma jet to simulate the second step, Reaction (1-21). The inlet MgO:total CH_4 molar ratio was 0.46.

These two runs did not result in any drastic improvement in the yield of Mg_2C_3 (and MgC_2) but they did give the highest extents of MgO "Mg" conversion to Mg_2C_3, 9% and 6%, among all the runs. The major product was still Mg metal, with the extents of MgO "Mg" conversion at 72% and 63%. The nearly complete (>80%) MgO "O" conversion to CO indicates very high utilization of MgO but the 27% and 45% unreacted CH_4 for the two runs suggest that the secondary methane underwent little reaction, possibly due to too low a temperature and/or inadequate mixing.

3.2.7 Effect of Quench Distance

The speed of quenching the plasma effluent can greatly affect the product yield, especially if the product is thermally unstable. Such a product will simply decompose if the quenching is too slow. One hypothesis for the low carbide yields is that the carbides may be formed in the region immediately downstream of the arc but are decomposing into elemental carbon and magnesium as they are cooled down in the chamber. This is supported by the known thermal decomposition of Mg_2C_3 into its elements according to Reaction (1-23) at 1013-1033 K. Measurements taken halfway up the chamber with a type K thermocouple indicate temperatures greater than 1000 K. Therefore, the plasma effluent may not be quenched rapidly enough to temperatures below 1000 K and any carbides formed may plausibly be decomposing into the elements.

Ideally, a thorough study on the effect of quenching would entail knowing the temperature-time history of the product stream. However, given the nature of this experimental study, thermocouples could not be used effectively due to the electrical noise from the arc discharge, the carburizing effect of the product stream and the extremely high temperatures from which the gas is cooled. The 1/8 in. SS tubes for secondary CH_4 quench located about 1 in. from the anode nozzle exit eventually melted after several runs without any secondary gas flow. Similarly, a thermocouple inserted through the probe up to its tip did not last beyond several runs.

The rate of quenching can be increased by shortening the anode-nozzle-exit-to-probe-tip quench distance, which is achieved by inserting the sample collection probe farther up into the chamber. In an attempt to improve carbide yield, the nozzle-exit-to-probe-tip quench distance was progressively decreased from 14 in. to 10 in. and then to 5 in. under reactor feed conditions of 30 l/min CH_4 flow rate and 0.26-0.5 inlet MgO:CH_4 ratios in separate experimental runs over a 22-47 kW power input range. The summary statistics for data on MgO "Mg" conversion to Mg_2C_3 for these runs are presented in Table 3-15. The *p*-value is the probability of rejecting the null hypothesis that the mean values at 14 and 10 in. quench distance are equal to the mean at 5 in. quench distance when the null hypothesis is correct.

Table 3-15. Summary Statistics of MgO "Mg" Conversion to Mg_2C_3 and MgC_2 at 14, 10 and 5 in. Quench Distance

% Conversion	Quench Distance, in.	Mean	Standard Deviation	95% C.I.	Min.	Max.	*p*-value
$(Mg)\alpha_{MgO}^{Mg_2C_3}$	14	2.4	0.4	[1.5,3.3]	2.0	2.7	0.08
	10	2.4	2.0	[-0.7,5.5]	0.1	4.9	0.47
	5	1.2	0.7	[-4.8,7.2]	0.7	1.7	
$(Mg)\alpha_{MgO}^{MgC_2}$	14	0.3	0.1	[0.2,0.5]	0.3	0.4	0.17
	10	0.8	0.3	[0.4,1.2]	0.6	1.2	0.27
	5	0.6	0.2	[-1.3,2.4]	0.4	0.7	

The sample means of $(Mg)\alpha_{MgO}^{Mg_2C_3}$ and $(Mg)\alpha_{MgO}^{MgC_2}$ at different quench distances are not found to be statistically different at the 0.05 significance level. Regardless of quench distance, both $(Mg)\alpha_{MgO}^{Mg_2C_3}$ and $(Mg)\alpha_{MgO}^{MgC_2}$ are always less than 5%. Therefore, decreasing the quench distance is not likely to significantly improve Mg_2C_3 and MgC_2 yields under the conditions studied.

Although decreasing the nozzle-exit-to-probe-tip quench distance may not possibly increase the quench rate rapidly enough, magnesium carbide is more likely not the major product in this system. More rigorous thermodynamic calculations to be presented in Chapter 4 do not support the formation of Mg_2C_3 and MgC_2 over a temperature range of 298-6000 K. Both forms of magnesium carbide have a positive free energy of formation from 298 K to 2500 K and are thus thermodynamically unstable relative to their elements.

3.2.8 Product Morphology and Elemental Distribution

The solid products at different extents of conversion under various experimental conditions were subjected to SEM and STEM coupled with EDS analyses in order to shed light on the mechanisms behind the conversion process. The procedures for sample preparation and transfer to the microscopes in all these analyses entailed a certain amount of exposure of the sample to the atmosphere since there is no suitable transfer vessel for avoiding such. Thus, the sample could very well have undergone some degree of oxidation and/or hydrolysis by the time the analysis was conducted. Nevertheless, the analyses show some very interesting results.

The STEM/EDS analysis results are presented in Figures 3-21A and 3-22A for samples corresponding to MgO "Mg" conversion to Mg of 68% and 39%, respectively. Two STEM images, bright and dark normal, are on the top row of each figure and elemental mapping images comprise the bottom row. The leftmost image on the bottom row corresponds to the annular dark field (ADF) image. The bright spots on the succeeding images denote the presence of the element. The corresponding SEM images

of each sample at three levels of magnification are shown in Figures 3-21B to 3-21D and Figures 3-22B to 3-22D.

Figure 3-21A shows a hexagonal particle which is about 400 nm across with well-defined edges. Elemental mapping by EDS shows that this hexagonal particle is a magnesium crystal. From the elemental mapping, more intense oxygen signals are observed on the edges of the particles than throughout the particle, indicating that oxygen exists as an oxide layer on the magnesium. Thus, despite the fine particle size of the sample and its exposure to the atmosphere immediately before analysis, the magnesium did not oxidize completely and was possibly preserved by the oxide layer. The observation of well-defined hexagonal magnesium crystals in the final product is evidence that crystallization from the vapor phase occurred in reactor.

In some samples, relatively large micron-size shells of MgO are found such as the rightmost particle on Figure 3-22A. The lower intensity of the magnesium and oxygen signals in the middle of the particle relative to those on its perimeter indicates that the shell is probably hollow inside. Furthermore, its walls have the appearance of having collapsed inward. Unlike the oxide layer which may have been formed either inside the cooling chamber during the run or outside the system just before STEM analysis, this MgO shell is apparently a product of the reaction. Since the original MgO was injected as 100 μm solid particles, the existence of hollow MgO shells in the final product suggests that MgO is re-formed in the process, possibly from the reverse reaction of CO and magnesium in the vapor phase. If the surrounding temperature is below the oxide boiling point which is very likely, the re-oxidation of the magnesium vapor would result in a supersaturated magnesium oxide vapor that would immediately nucleate and condense.

The analyses of all the samples consistently show that the products are agglomerates of very fine particles in the 0.1 to 1 μm size range, independent of the degree of conversion. The particles have prominent hexagonal geometry as well as spherical shapes. Although both hexagonal and spherical particles exhibit smooth surfaces on some SEM images, most particles show rough surfaces which indicate small particles depositing on the surface of or possibly fusing with the larger particles. This is

particularly evident in the hexagonal particles in Figures 3-21D and 3-22D. This observation suggests that the products heterogeneously condense and grow on previously formed solid particles during quenching.

No Mg_2C_3 and MgC_2 particles were detected in any of the samples. Given their small yields, the fine particle size range of the products and the thermodynamic instability of these two carbides relative to the elements, any carbides present in the sample probably did not survive the exposure to the atmosphere prior to STEM and SEM analyses. The presence of the carbides would have been manifested by Mg and C signals of similar intensities on the same coordinates. Only a small amount of carbon was detected, mostly dispersed with MgO. In addition to MgO and Mg particles, the silicon impurities in the MgO reactant showed up mostly as the oxide in the product.

Figures 3-23A to 3-23D show the STEM and SEM images of a sample from a run with 30 l/min CH_4. Although the conversion of MgO "Mg" to Mg was not measured in this run, the carbon content of this sample is much higher than in the others. The solid sample is seen to be agglomerates of small particles with a wider size range, including much finer particles. From STEM/EDS analysis, the sample is determined to be mostly MgO with solid carbon dispersed throughout.

TEM images of a sample from the pyrolysis of CH_4 in the plasma reactor (no MgO feeding) are shown in Figures 3-24A and 3-24 B. The pyrolysis products are chain-like agglomerates of carbon particles which are a few hundred angstroms in size. Both graphitic carbon and sooty structures are evident in the TEM images. Since most of the samples from the runs with MgO feeding examined by electron microscopy did not show such agglomerates of fine particles, except possibly the 30 l/min CH_4 sample, the carbon particles that failed to react with the MgO in those runs did not seem to agglomerate together. Rather, they appear to have coagulated with the larger particles being formed. This suggests that methane is heterogeneously decomposed in the presence of MgO in the plasma reactor.

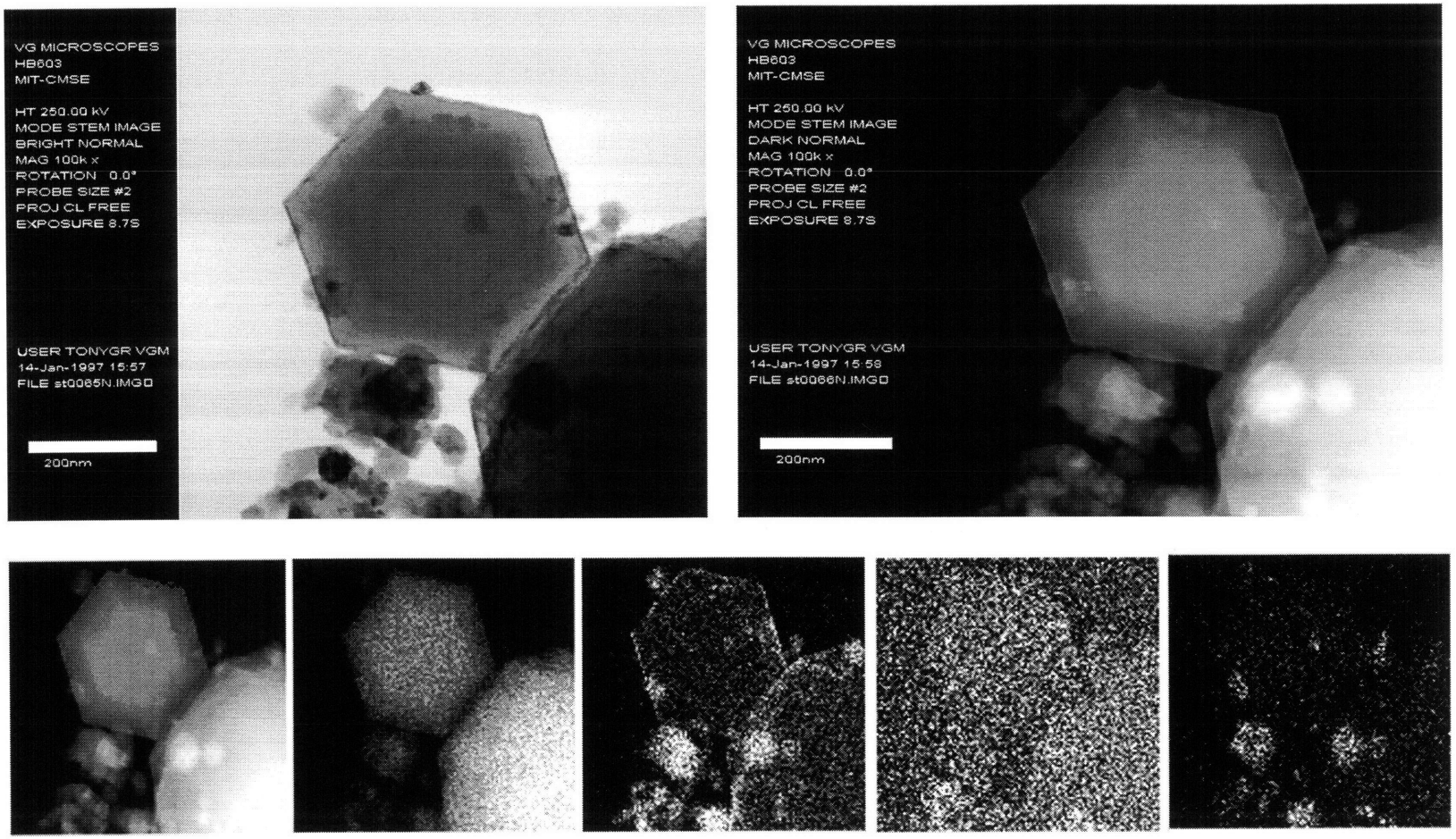

Figure 3-21A. STEM Images and Elemental Mapping of Run M27 Sample from Chamber (10 l/min CH_4 + 10 l/min Ar; 68% MgO "Mg" Conversion to Mg)

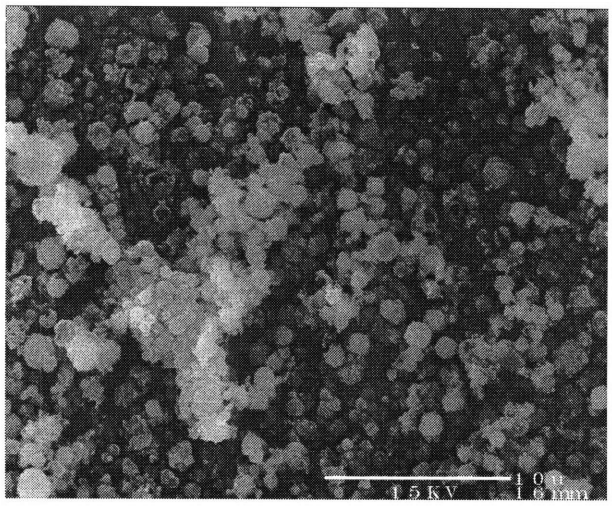

Figure 3-21B. SEM of Run M27 Sample, x3,500

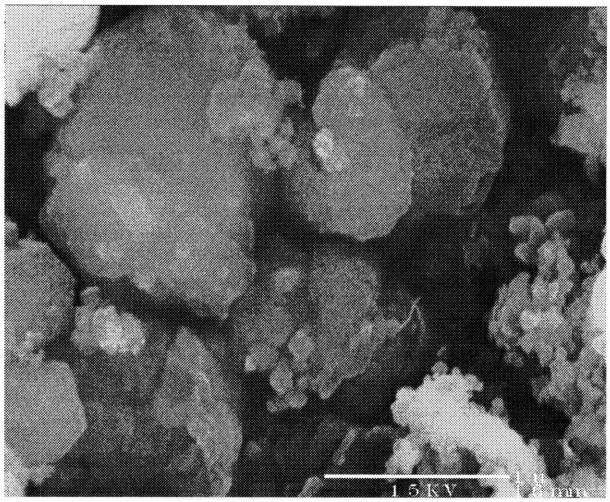

Figure 3-21C. SEM of Run M27 Sample, x35,000

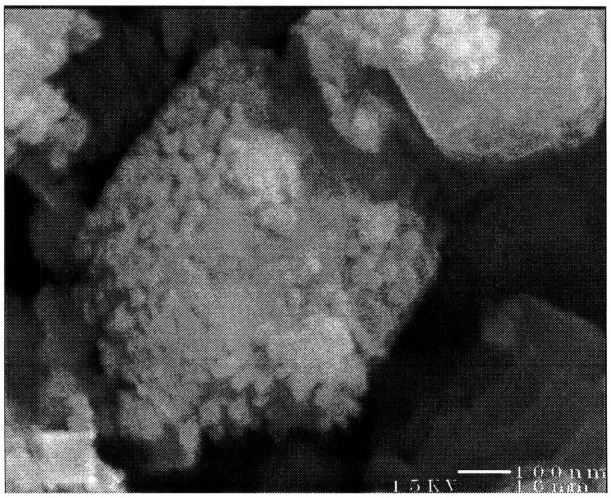

Figure 3-21D. SEM of Run M27 Sample, x100,000

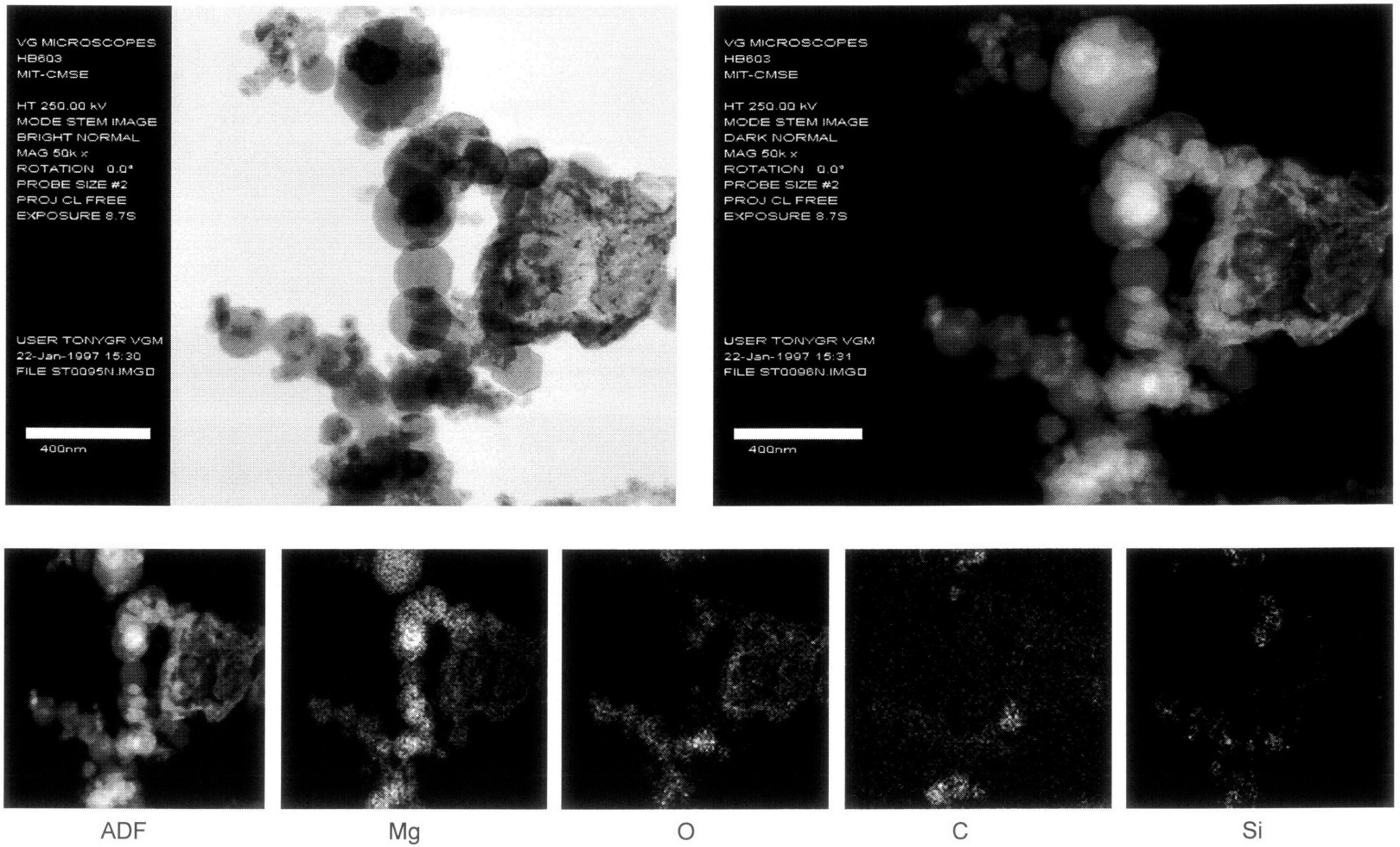

Figure 3-22A. STEM Images and Elemental Mapping of Sample from Run M33 (10 l/min CH_4; 39% MgO "Mg" Conversion to Mg)

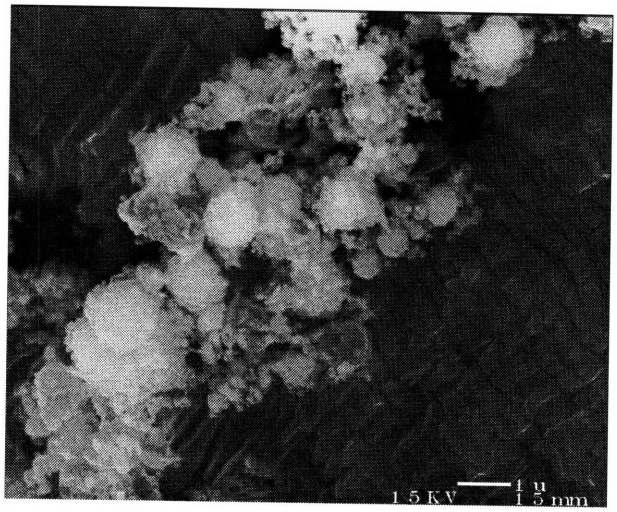

Figure 3-22B. SEM of Run M33 Sample, x10,000

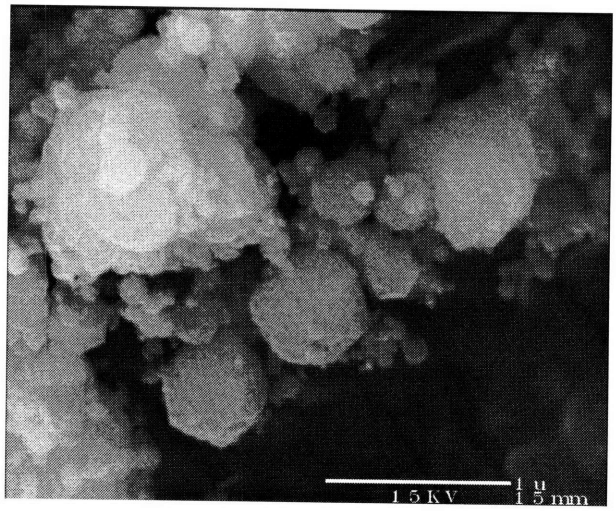

Figure 3-22C. SEM of Run M33 Sample, x35,000

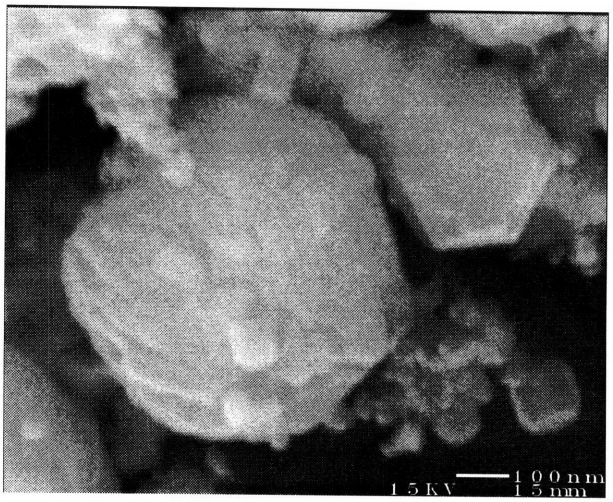

Figure 3-22D. SEM of Run M33 Sample, x100,000

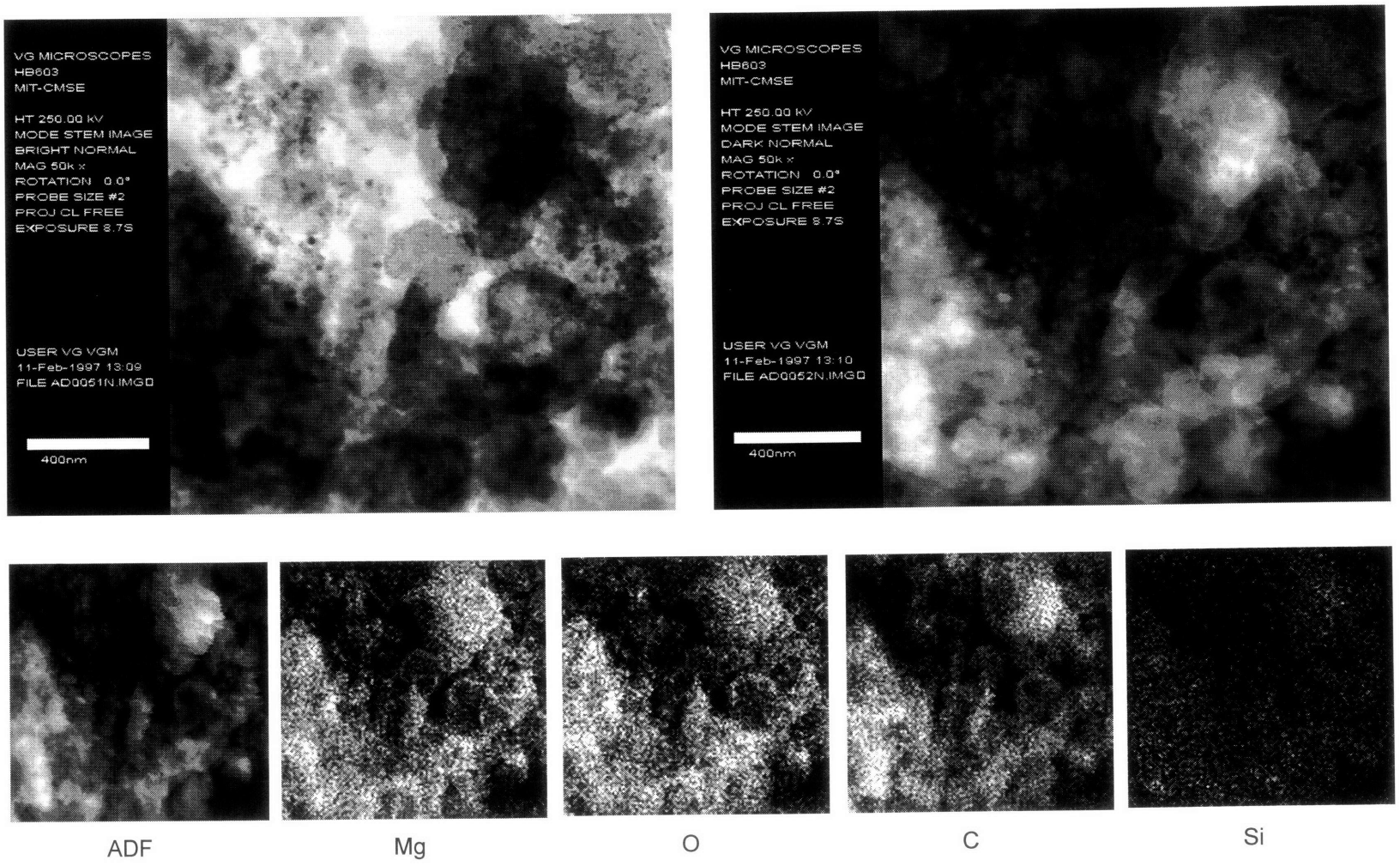

Figure 3-23A. STEM Images and Elemental Mapping of Sample from Run M7 (30 l/min CH_4; 5% MgO "Mg" Conversion to Mg_2C_3)

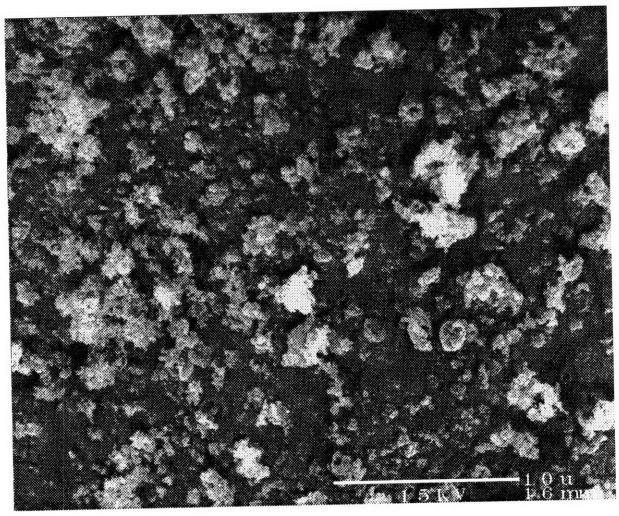

Figure 3-23B. SEM of Run M7 Sample, x3,500

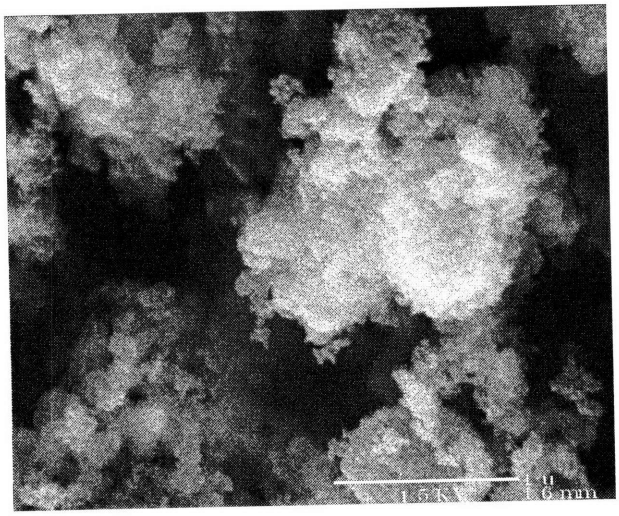

Figure 3-23C. SEM of Run M7 Sample, x35,000

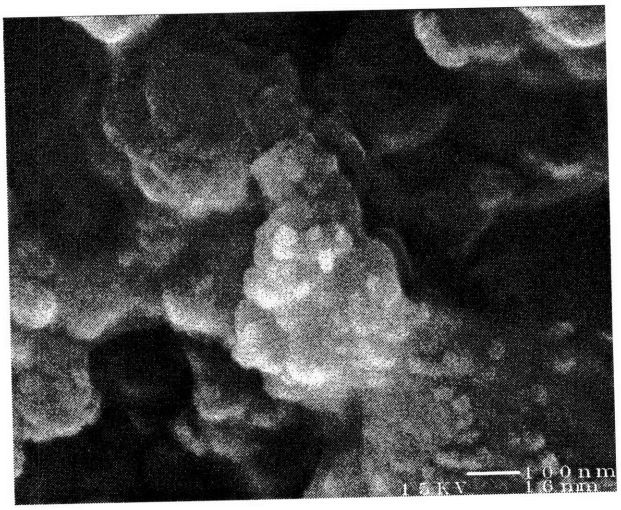

Figure 3-23D. SEM of Run M7 Sample, x100,000

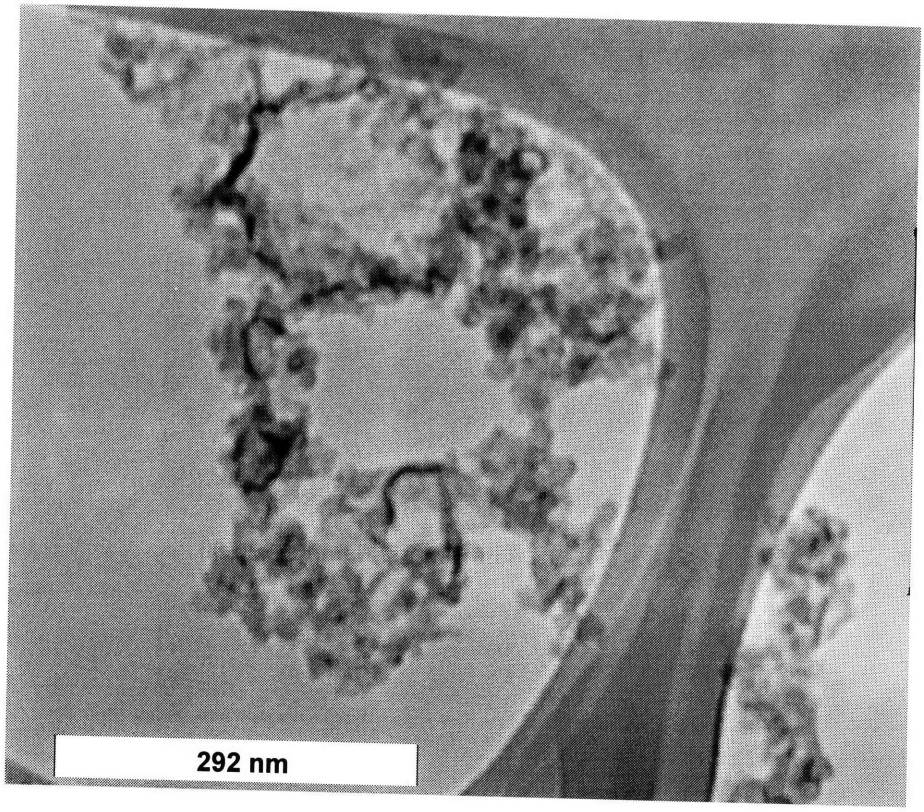

Figure 3-24A. TEM of Run M13 Sample, x120,000

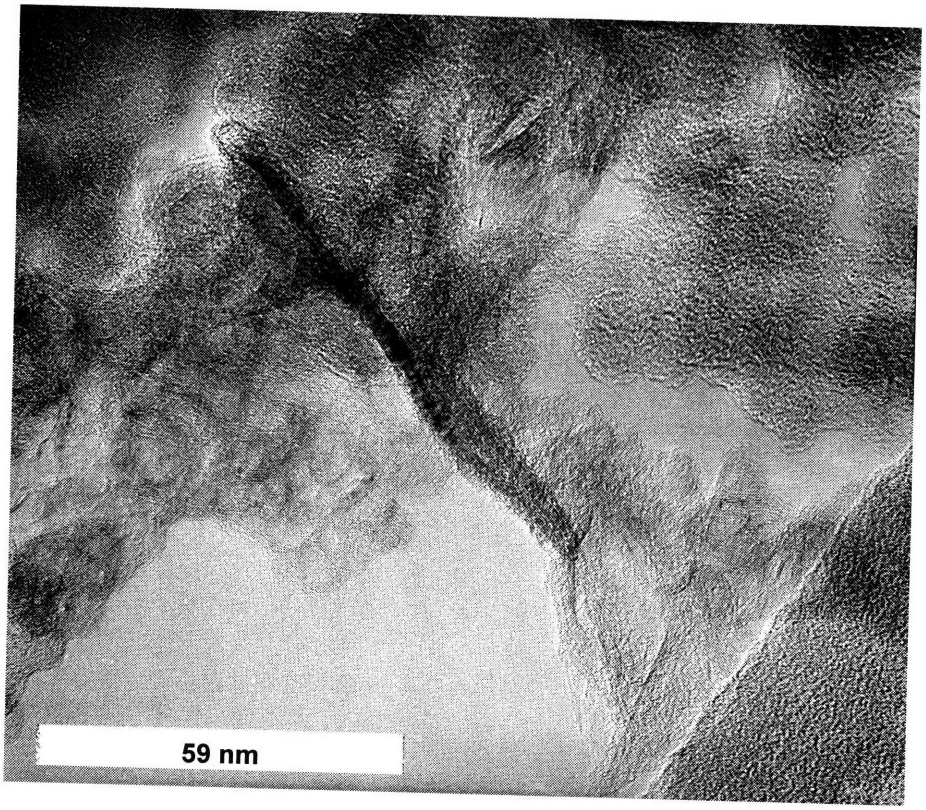

Figure 3-24B. TEM of Run M13 Sample, x590,000

3.3 MgO-Ar System

Blank runs with MgO but without CH_4 were conducted by passing MgO through an Argon plasma to gain an insight on how exposure to a plasma affected solids morphology. The effect of the magnetic field was studied by feeding MgO at low (6 g/min) and high (22 g/min) feed rates into a 100% 50 l/min Argon plasma with and without the 118 G magnetic field. Four such runs were performed: 1) Low MgO feed without magnetic field, Run LM; 2) Low MgO feed with magnetic field, Run LMM; 3) High MgO feed without magnetic field, Run HM; and 4) High MgO feed with magnetic field, Run HMM. The reactor conditions for these runs are summarized in Table 3-16.

Table 3-16. Summary of Reactor Conditions for MgO-Ar System [Ave ± 1 s.d.]

Run	LM	LMM	HM	HMM
Main Argon Flow, l/min	50	50	50	50
Carrier Argon Flow, l/min	4.2	4.2	4.2	4.2
MgO Feed, g/min	6.4	6.4	22.3	22.3
MgO Particle Size, μm	44 to 104	44 to 104	44 to 104	44 to 104
Chamber Pressure, mm Hg	680 ± 29	626 ± 67	666 ± 73	726 ± 59
Arc Voltage, V	25.6 ± 1.1	22.0 ± 3.7	25.2 ± 1.3	16.9 ± 0.6
Arc Current, A	583 ± 111	560 ± 103	607 ± 104	707 ± 94
Arc Power Input, kW	14.9 ± 2.8	12.2 ± 2.8	15.3 ± 2.5	12.0 ± 1.8
Quench Distance, in	5	5	5	5
Magnetic Field, G	0	118	0	118

The interaction of the magnetic field with the arc has the effect of lowering the arc voltage and thus, the arc power input (by about 20%). A significant difference is observed between the runs with and without the magnetic field. Figures 3-25 to 3-28 show SEM images of the solid samples collected through the sample collection probe from each run. Both runs with a magnetic field yielded darker gray samples in greater quantities. In addition, solidified deposits of MgO formed in the anode nozzle in Run HMM, suggesting melting or vaporization and condensation. For both low and high MgO feed runs, the application of a magnetic field results in solid products that are smaller, more rounded and, in the HMM case, even agglomerated. Thus, the magnetic field appears to enhance plasma-particle heat transfer rates.

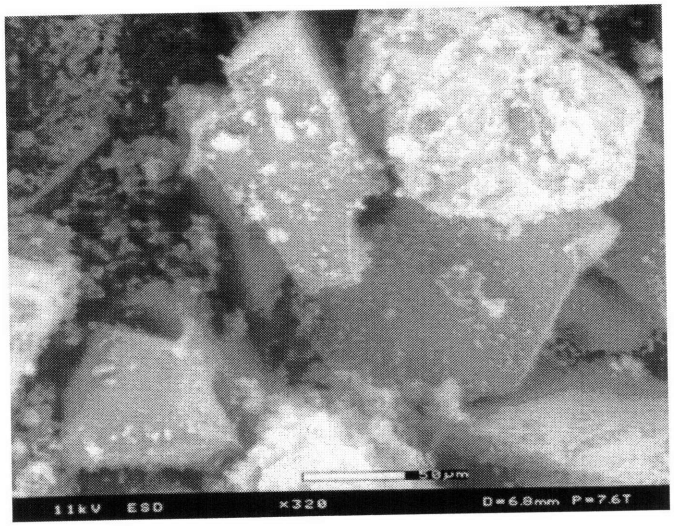

Figure 3-25. SEM of Run LM Sample, x320

Figure 3-26. SEM of Run LMM Sample, x750

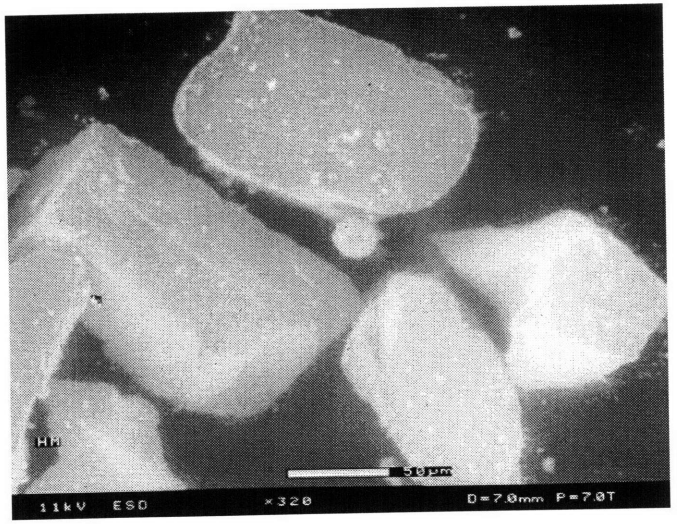

Figure 3-27. SEM of Run HM Sample, x320

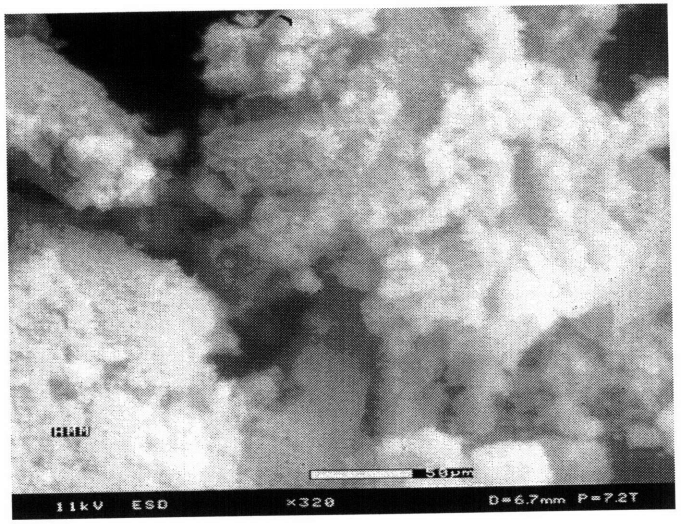

Figure 3-28. SEM of Run HMM Sample, x320

3.4 MgO-CH_4-C-Ar System

The addition of solid graphitic carbon to the MgO powder was studied in five runs, designated Runs MC1 to MC5, as a means of improving the magnesium and/or magnesium carbide yields from the reaction of MgO with carbon. The proposition is that doping the MgO with carbon can increase the plasma concentration of nascent carbon species, which can react with MgO to form the metal or the carbide. A mixture of MgO and graphite powder was entrained in 4.2 l/min Argon and fed with 10 l/min of CH_4 into the plasma reactor. The MgO was doped with enough carbon so that the molar ratio of graphite C to MgO in the feed is about 1:3. The inlet MgO:CH_4 molar ratio was 1.15:1 and the arc was operated in the 19-33 kW range. The reactor operating conditions are given in Table 3-17.

Table 3-17. Summary of Reactor Conditions for MgO-CH_4-C-Ar System [Ave (± 1 s.d.)]

Run	MC1	MC2	MC3	MC4	MC5
Main CH_4 Flow, l/min	10.0	10.0	10.0	10.0	10.1
Carrier Argon Flow, l/min	4.2	4.2	4.2	4.2	4.2
MgO+C Feed, g/min	21.3	21.3	21.3	21.3	21.3
MgO:C:CH_4 Molar Ratio	1.16:0.4:1	1.16:0.4:1	1.16:0.4:1	1.16:0.4:1	1.15:0.4:1
MgO Feed, g/min	19.3	19.3	19.3	19.3	19.3
MgO Particle Size, μm	44 to 104	44 to 104	44 to 104	44 to 104	44 to 104
Chamber Pressure, mm Hg	760 ± 6	754 ± 10	756 ± 9	759 ± 8	754 ± 14
Arc Voltage, V	65.4 ± 7.2	70.6±11.3	67.9±11.0	60.5±11.5	72.1±10.9
Arc Current, A	501 ± 48	390 ± 77	365 ± 87	512 ± 84	273 ± 52
Arc Power Input, kW	32.4 ± 1.8	26.8 ± 2.4	23.9 ± 2.1	30.0 ± 2.4	19.2 ± 1.6
Quench Distance, in	5	5	5	5	5
Magnetic Field, G	118	118	118	118	118

3.4.1 Reaction Products of MgO-CH_4-C-Ar System

The reaction products of the MgO-CH_4-C-Ar system are Mg, H_2, CO, Mg_2C_3, MgC_2 and non-carbide C. In addition to Reactions (1-2), (1-3), and (1-4), the additional carbon can react with magnesium oxide according to the global reactions:

$$5\,C + 2\,MgO \rightarrow Mg_2C_3 + 2\,CO \qquad \text{Reaction (3-3)}$$

$$3\,C + MgO \rightarrow MgC_2 + CO \qquad \text{Reaction (3-4)}$$

$$C + MgO \rightarrow Mg + CO \qquad \text{Reaction (1-15)}$$

The solid product is a finely divided dark gray powder and is composed of Mg, Mg_2C_3, MgC_2 and non-carbide C. Non-carbide C comprises less than 5% of the unhydrolyzed solids. When hydrolyzed, the solid evolves H_2, C_3H_4 and C_2H_2. In addition, small amounts of C_2H_6, C_2H_4, C_3H_8 and C_3H_6 have been detected in the headspace above the hydrolyzed solids, which probably desorbed from the solids upon hydrolysis. The gaseous product is comprised mainly of H_2 and CO, with less than 1% of C_2H_2, C_3H_4 and unreacted CH_4 and with trace amounts of C_2H_4 and C_3H_8.

Material balances on the constituent elements of the CH_4/C and MgO reactants for Runs MC1 to MC5 are given in Tables 3-18 and 3-19, respectively. The percent molar carbon conversion in Table 3-18 refers to conversion of the total carbon in the methane and graphite additive. This total carbon is converted to CO gas, solid C, solid Mg_2C_3 and MgC_2, and other gaseous HCs while the methane hydrogen is transformed to H_2 gas and other HCs. The magnesium in MgO is converted to Mg, Mg_2C_3 and MgC_2 in the solid products while the oxygen in MgO is converted to CO gas.

Table 3-18. Percent Methane and Graphite Molar Conversion to Products in MgO-CH_4-C-Ar System

Run	MC1		MC2		MC3		MC4		MC5	
Products	Total "C"	CH_4 "H"	Total "C"	CH_4 "H"	Total "C"	CH_4 "H"	Total "C"	CH_4 "H"	Total "C"	CH_4 "H"
Mg_2C_3	4.7		3.5		2.2		3.5		4.1	
MgC_2	0.8		0.6		0.4		0.8		0.6	
Non-carbide C	8.5		7.7		15.4		9.7		9.3	
CO	79.0		78.8		70.7		78.6		52.3	
C_2H_2	0.7	0.2	0.5	0.2	0.6	0.2	1.2	0.4	1.0	0.4
C_3H_4	0.2	0.1	0.2	0.1	0.3	0.1	0.1	0.1	0.5	0.2
Other C_2, C_3, C_4	0.1	0.1	0.1	0.1	0.1	0.1	0.3	0.3	0.5	0.5
Unreacted CH_4	0.1	0.2	0.2	0.2	0.1	0.2	0.2	0.2	0.2	0.3
H_2		101.4		115.2		120.4		124.8		103.6
Total	94.0	102.0	91.6	115.8	89.8	121.0	94.4	125.8	68.5	105.0

Table 3-19. Percent Magnesium Oxide Molar Conversion to Products in MgO-CH_4-C-Ar System

Run	MC1		MC2		MC3		MC4		MC5	
Products	MgO "Mg"	MgO "O"	MgO "Mg"	MgO "O"	MgO "Mg"	MgO "O"	MgO "Mg"	MgO "O"	MgO "Mg"	MgO "O"
Mg_2C_3	3.7		2.8		1.8		2.8		3.3	
MgC_2	0.5		0.4		0.3		0.5		0.4	
Mg	63.2		66.1		63.2		72.6		64.2	
CO		67.9		68.0		61.2		67.7		45.6
Total	67.4	67.9	69.3	68.0	65.3	61.2	75.9	67.7	67.9	45.6

3.4.2 Effect of Carbon Addition

The extents of reactant conversion to various products in the experimental runs with carbon addition were compared with the extents of conversion in runs under similar reaction conditions but without carbon addition. The results of the comparison of the two sets of runs are summarized in Table 3-20. The *p*-value is the probability of rejecting the null hypothesis that the mean values with carbon addition are less than or equal to the mean values without carbon addition when the null hypothesis is correct.

Table 3-20. Summary Statistics of Reactant Conversion to Products and H_2/CO Ratio with and without Carbon Addition

% Conversion	Carbon Addition	Mean	Standard Deviation	95% C.I.	Min.	Max.	*p*-value
$(Mg)\alpha_{MgO}^{Mg}$	Yes	65.9	3.9	[61.0,70.8]	63.2	72.6	0.00
	No	51.5	8.7	[40.8,62.3]	39.1	60.2	
$(Mg)\alpha_{MgO}^{Mg_2C_3}$	Yes	2.9	0.7	[2.0,3.8]	1.8	3.7	0.30
	No	2.6	1.1	[1.2,3.9]	1.2	3.4	
$(H)\alpha_{CH_4}^{H_2}$	Yes	113.1	10.3	[100.3,125.8]	101.4	124.8	0.00
	No	83.9	9.8	[71.7,96.1]	73.6	99.7	
$(C)\alpha_{CH_4+C}^{CO}$	Yes	71.9	11.5	[57.6,86.2]	52.3	79.0	0.44
	No	70.9	8.7	[60.2,81.6]	62.2	85.2	
$(C)\alpha_{CH_4+C}^{C}$	Yes	10.1	3.0	[6.3,13.9]	7.7	15.4	0.18
	No	15.6	12.1	[0.5,30.6]	3.2	32.0	
H_2/CO Ratio	Yes	2.3	0.4	[1.8,2.8]	1.8	2.8	0.33
	No	2.4	0.0	[2.3,2.4]	2.3	2.4	

The mean $(Mg)\alpha_{MgO}^{Mg}$ and $(H)\alpha_{CH_4}^{H_2}$ are found to be significantly higher with carbon addition than without carbon addition at the 0.05 significance level under the experimental conditions investigated. This can also be seen from plots of $(Mg)\alpha_{MgO}^{Mg}$ and $(H)\alpha_{CH_4}^{H_2}$ vs. power input with and without carbon addition under similar reaction conditions in Figures 3-29 and 3-30. The improvement in the mean $(Mg)\alpha_{MgO}^{Mg}$ from 51.5% to 65.9%, which can be attributed to Reaction (1-15), corresponds to a 28% increase, in reasonable agreement with the 40% increase in carbon feed. The greater than 100% CH_4 "H" conversion to H_2 indicates the high degree of uncertainty in the data but, assuming that the error is systematic, H_2 formation is enhanced from an average of 84% without carbon addition to virtually complete conversion with carbon addition. The foregoing observations are consistent with the hypothesis of magnesium formation via nascent carbon reaction with MgO and suggest that the extents of MgO "Mg" conversion to Mg and CH_4 "H" conversion to H_2 can be improved by doping the MgO feed with carbon.

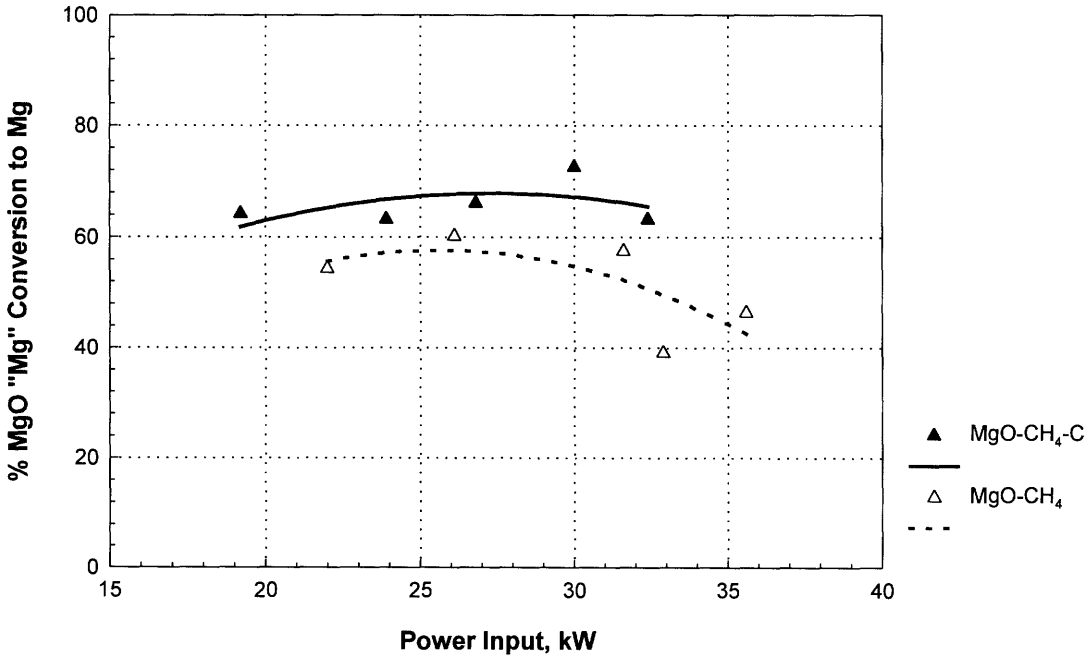

Figure 3-29. MgO "Mg" Conversion to Mg vs. Power Input at 10 l/min CH_4 and 1.15:1 MgO:CH_4 with and without Carbon Addition

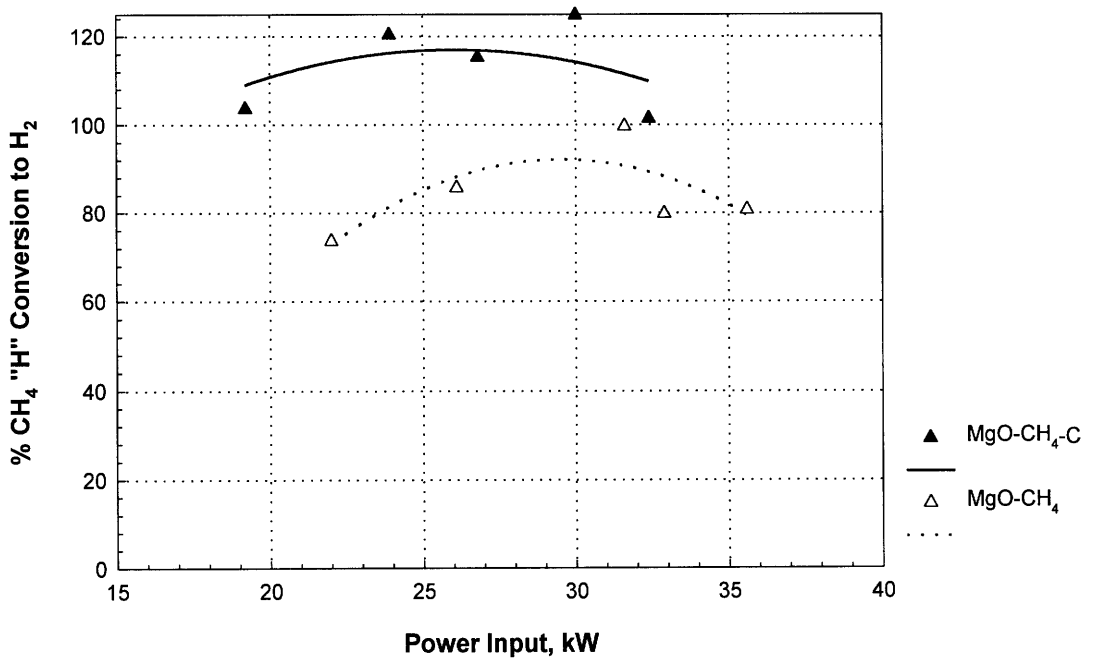

Figure 3-30. CH_4 "H" Conversion to H_2 vs. Power Input at 10 l/min CH_4 and 1.15:1 MgO:CH_4 with and without Carbon Addition

Whereas $(Mg)\alpha_{MgO}^{Mg}$ was enhanced by the inclusion of solid carbon, $(Mg)\alpha_{MgO}^{Mg_2C_3}$ remained below the 5% level. The absence of any noticeable effect on carbide formation suggests that Reactions (3-3) and (3-4) do not contribute significantly to the overall reaction.

The conversion of the total carbon (from CH_4 and graphite) to CO, $(C)\alpha_{CH_4+C}^{CO}$, is plotted as a function of power input for the MgO-CH_4-C-Ar system in Figure 3-31. A plot of CH_4 "C" conversion to CO for the MgO-CH_4-Ar system under similar reaction conditions is also shown in the figure. The agreement between the two cases is remarkable. This observation suggests that, if the additional CO is being formed from the carbon in the graphite, it is formed at the same extent as the CO formed from the carbon in methane. This would likewise support a mechanistic pathway for magnesium formation from MgO involving nascent carbon species. Thus, if nascent carbon is reacting with MgO in the

plasma to form CO and Mg, graphite powder can serve as an additional source of this nascent carbon species together with methane.

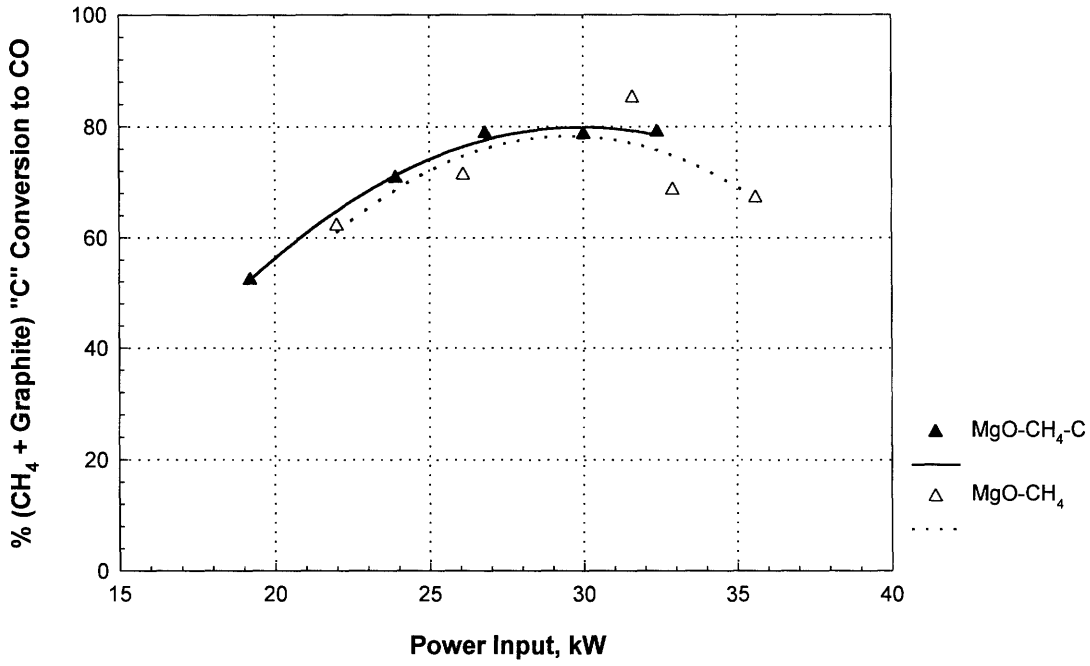

Figure 3-31. (CH_4 + Graphite) "C" Conversion to CO vs. Power Input at 10 l/min CH_4 and 1:15:1 MgO:CH_4 with and without Carbon Addition

3.4.3 Product Morphology and Elemental Distribution

The STEM/EDS analysis results of a solid sample from Run MC5 are shown in Figure 3-32A while SEM images of the same sample at increasing magnification levels are presented in Figures 3-32B to 3-32D. Figure 3-32A shows that the sample is composed primarily of magnesium metal. Since the oxygen signals observed are less intense than those of magnesium, except on the rightmost cluster, the oxygen again exists as an oxide layer on the magnesium. The strong oxygen signals on the rightmost agglomerate correspond to similarly intense signals from C and Si. Thus, this particular cluster is probably a mixture of magnesium oxide and silicon oxide with some carbon on them. The

less intense carbon signals suggest that a relatively small amount of carbon is dispersed throughout the sample. Mg_2C_3 and MgC_2 were not detected in this sample.

Similar to the products of the MgO-CH_4-Ar system, the solid products of the MgO-CH_4-C-Ar system are agglomerates of very fine particles in the 0.1 to 1 μm size range. Although some small hexagonal particles are seen in the sample, the particles are prominently spherical in shape. These spheres also exhibit rough surfaces with scale-like tiny particles depositing on or fusing with them. Figures 3-32C and 3-32D show this phenomenon clearly. This observation again suggests that the products heterogeneously condense and grow on previously formed solid particles during quenching.

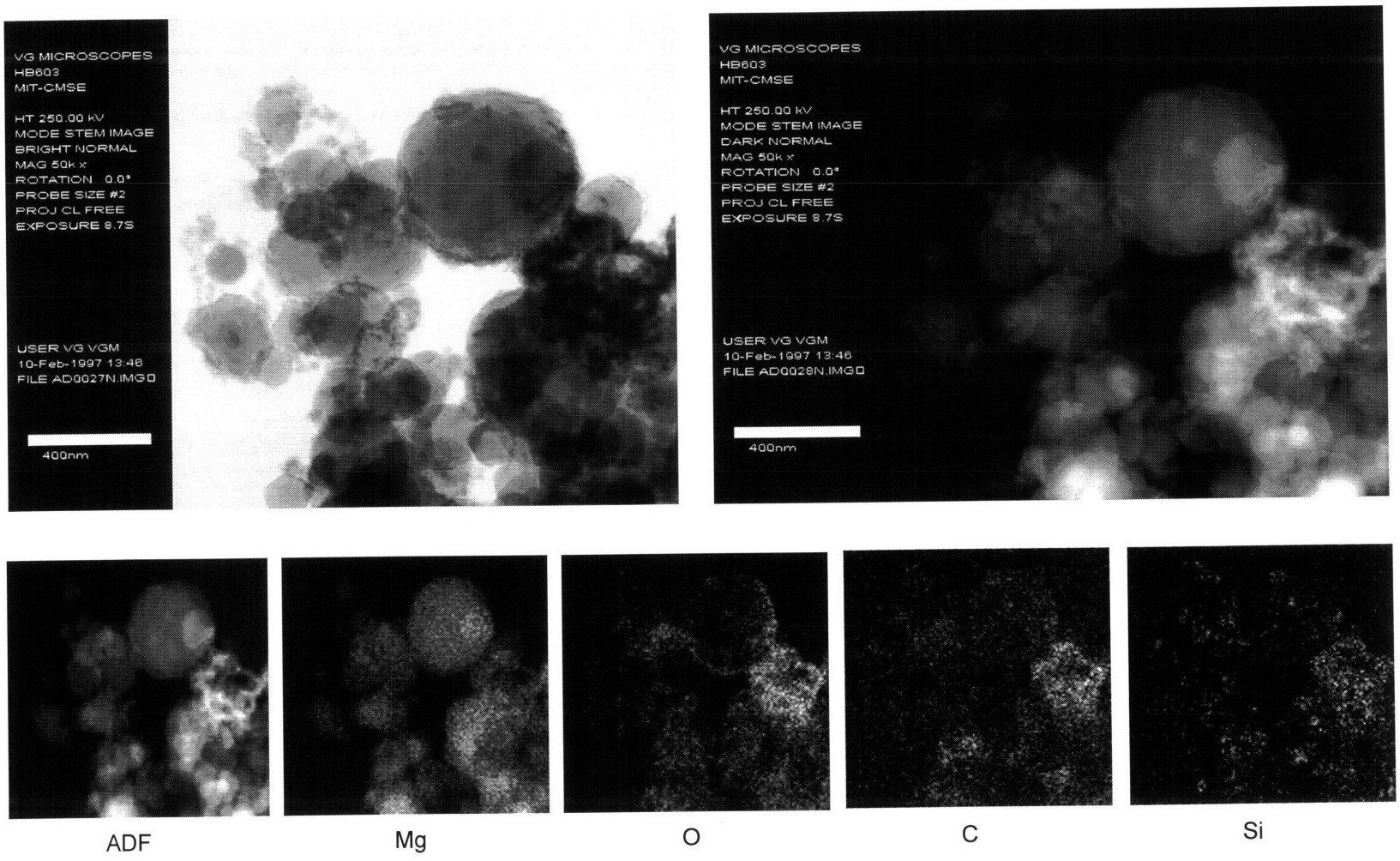

Figure 3-32A. STEM Images and Elemental Mapping of Sample from Run MC5 (10 l/min CH_4; 1.15:0.4:1 MgO:C:CH_4; 64% MgO "Mg"Conversion to Mg)

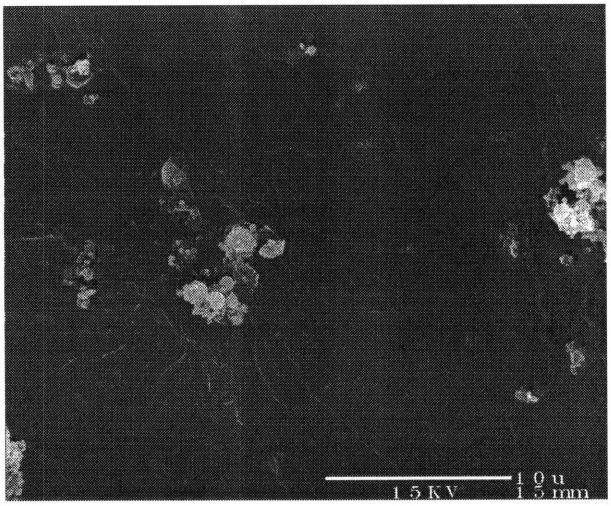

Figure 3-32B. SEM of Run MC5 Sample, x3,500

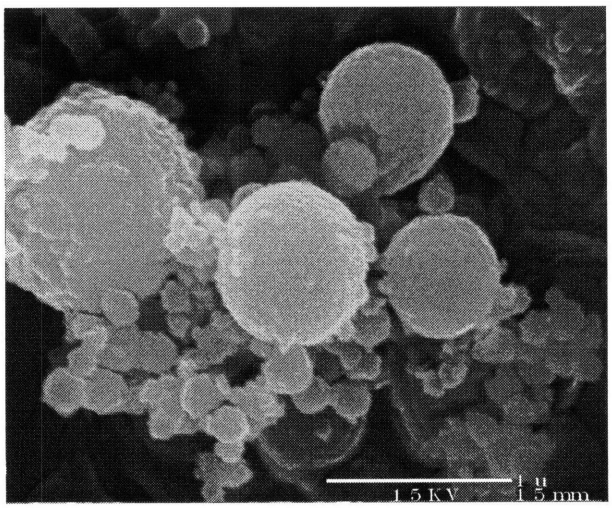

Figure 3-32C. SEM of Run MC5 Sample, x35,000

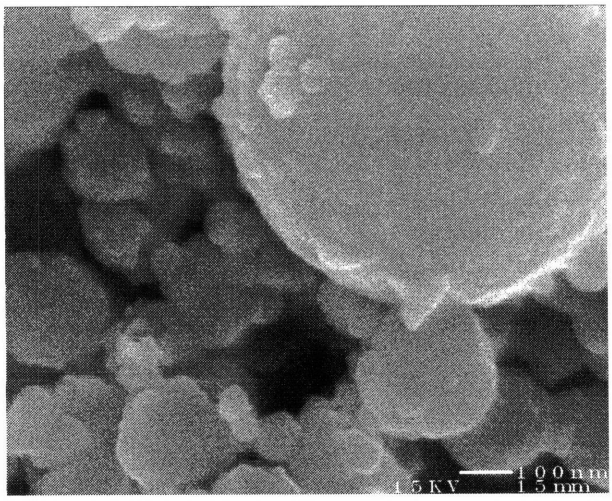

Figure 3-32D. SEM of Run MC5 Sample, x100,000

3.5 Mg-CH_4-Ar System

A study of the reaction of magnesium metal with CH_4 in the plasma reactor was conducted in order to assess the feasibility of synthesizing Mg_2C_3 according to Reaction (1-21). Mg powder entrained in 4.2 l/min Ar was introduced at a rate of 7 g/min with 10 l/min CH_4 into the plasma reactor in three experimental runs, designated Runs MG1 to MG3. A fourth run, Run MG4, was performed by feeding the Mg powder at 7 g/min into an 11 l/min Ar plasma with 10 l/min secondary CH_4 quench. The inlet Mg:CH_4 molar ratio in all four runs was set at 0.7:1 to match the stoichiometric ratio of Reaction (1-21). The reactor conditions for these runs are presented in Table 3-21.

Table 3-21. Summary of Reactor Conditions for Mg-CH_4-Ar System [Ave (± 1 s.d.)]

Run	MG1	MG2	MG3	MG4
Main CH_4 Flow, l/min	10.0	10.1	10.1	
Secondary CH_4 Flow, l/min				9.9
Main Argon Flow, l/min				10.9
Carrier Argon Flow, l/min	4.2	4.2	4.2	4.2
Mg Feedrate, g/min	7.0	7.0	7.0	7.0
Inlet Mg/CH_4 Molar Ratio	0.69	0.69	0.69	0.69
Mg Particle Size, μm	74 to 140	74 to 140	74 to 140	74 to 140
Chamber Pressure, mm Hg	760 ± 7	756 ± 8	761 ± 8	754 ± 5
Arc Voltage, V	51.9±14.0	63.6±14.5	59.0±15.3	14.9 ± 0.2
Arc Current, A	587 ± 108	416 ± 118	434 ± 114	706 ± 2
Arc Power Input, kW	29.0 ± 3.6	24.8 ± 2.9	23.9 ± 2.7	10.5 ± 0.2
Quench Distance, in	5	5	5	5
Magnetic Field, G	118	118	118	118

The solid product in this system is a finely divided gray powder and is found to be composed predominantly of Mg, with up to 25% by weight non-carbide C and small amounts of Mg_2C_3 and MgC_2. In addition to the H_2, C_3H_4 and C_2H_2 evolved upon hydrolysis, some C_2H_6, C_2H_4, C_3H_8 and C_3H_6 have also been detected in the headspace above the hydrolyzed solids, which probably desorbed from the solids upon hydrolysis. The gaseous product in Runs MG1 to MG3 is comprised mainly of H_2, with less than 2% of C_2H_2, C_3H_4 and unreacted CH_4 and with trace amounts of C_2H_4, C_2H_6 and C_3H_8. In

MG4, the gas sample was mostly unreacted CH_4, some H_2 and small amounts of C_2H_2, C_2H_4, C_2H_6, C_3H_4, C_3H_6 and C_3H_8.

Material balances on the constituent elements of CH_4 and Mg for Runs MG1 to MG4 are given in Tables 3-22 and 3-23, respectively. The carbon in CH_4 is converted to solid C, solid Mg_2C_3 and MgC_2, and other gaseous HCs while the hydrogen in CH_4 is transformed to H_2 gas and other HCs. The magnesium metal is recovered as Mg, Mg_2C_3 and MgC_2 in the solid products.

Table 3-22. Percent Methane Molar Conversion to Products in Mg-CH_4-Ar System

Run	MG1		MG2		MG3		MG4	
Products	CH_4 "C"	CH_4 "H"	CH_4 "C"	CH_4 "H"	CH_4 "C"	CH_4 "H"	CH_4 "C"	CH_4 "H"
Mg_2C_3	4.2		1.8		1.9		0.8	
MgC_2	0.3		0.1		0.1		0.1	
Non-carbide C	24.4		47.7		7.6		2.9	
C_2H_2	1.1	0.3	0.4	0.1	0.0	0.0	0.0	0.0
C_3H_4	0.8	0.3	0.8	0.3	2.3	0.8	0.1	0.0
Other C_2, C_3, C_4	2.6	2.0	2.7	2.0	6.4	4.8	0.3	0.3
Unreacted CH_4	0.4	0.4	0.5	0.5	2.1	2.1	88.5	88.5
H_2		84.1		98.0		82.2		1.3
Total	33.8	87.0	54.0	100.9	20.4	89.9	92.7	90.1

Table 3-23. Percent Magnesium Molar Conversion to Products in Mg-CH_4-Ar System

Run	MG1	MG2	MG3	MG4
Products				
Mg_2C_3	4.0	1.8	1.8	0.7
MgC_2	0.2	0.1	0.1	0.0
Unreacted Mg	75.7	75.7	76.4	88.9
Total	79.9	77.6	78.3	89.6

The conversion of Mg metal to Mg_2C_3 is observed to be less than 5% in all cases. Therefore, Mg_2C_3 is not formed in significant yields from CH_4 and Mg according to Reaction (1-21) under the conditions studied. Since Reaction (1-21) is known to occur at 973 K (Durrant and Durrant, 1970), the operating conditions of the plasma reactor are probably much more severe than those favorable for Mg_2C_3 formation. Furthermore, the reaction products are most likely quenched from a much higher temperature than 973 K. On the other hand, greater than 80% CH_4 "H" conversion to H_2 is achieved under the

plasma conditions studied. Thus, CH_4 is reduced to H_2 and solid C under these conditions. Statistics on the reactant conversion data are summarized in Table 3-24.

Table 3-24. Summary Statistics of Reactant Conversion to Products for Mg-CH_4-Ar System

% Conversion	Mean	Std. Dev.	95% C.I.	Minimum	Maximum
$(Mg)\alpha_{Mg}^{Mg_2C_3}$	2.5	1.3	[-0.6,5.7]	1.8	4.0
$(H)\alpha_{CH_4}^{H_2}$	88.1	8.6	[66.7,109.5]	82.2	98.0
$(C)\alpha_{CH_4}^{C}$	26.6	20.1	[-23.4,76.5]	7.6	47.7

Figure 3-33A shows the STEM/EDS analysis of a solid sample from Run MG1, which is composed mostly of magnesium metal. The large particle at the top exhibits the hexagonal feature characteristic of magnesium crystal. MgO is present in the sample as an oxide layer on the metal surface. Much smaller carbon particles in the 50-200 nm size range can also be seen in the sample but no evidence of magnesium carbide can be found. SEM images of the same sample are shown in Figures 3-33B to 3-33D. The solid particles range from 0.1 to 1 μm in size and are prominently spherical in shape, with the same rough surfaces seen in the products of the MgO-CH_4-C-Ar system.

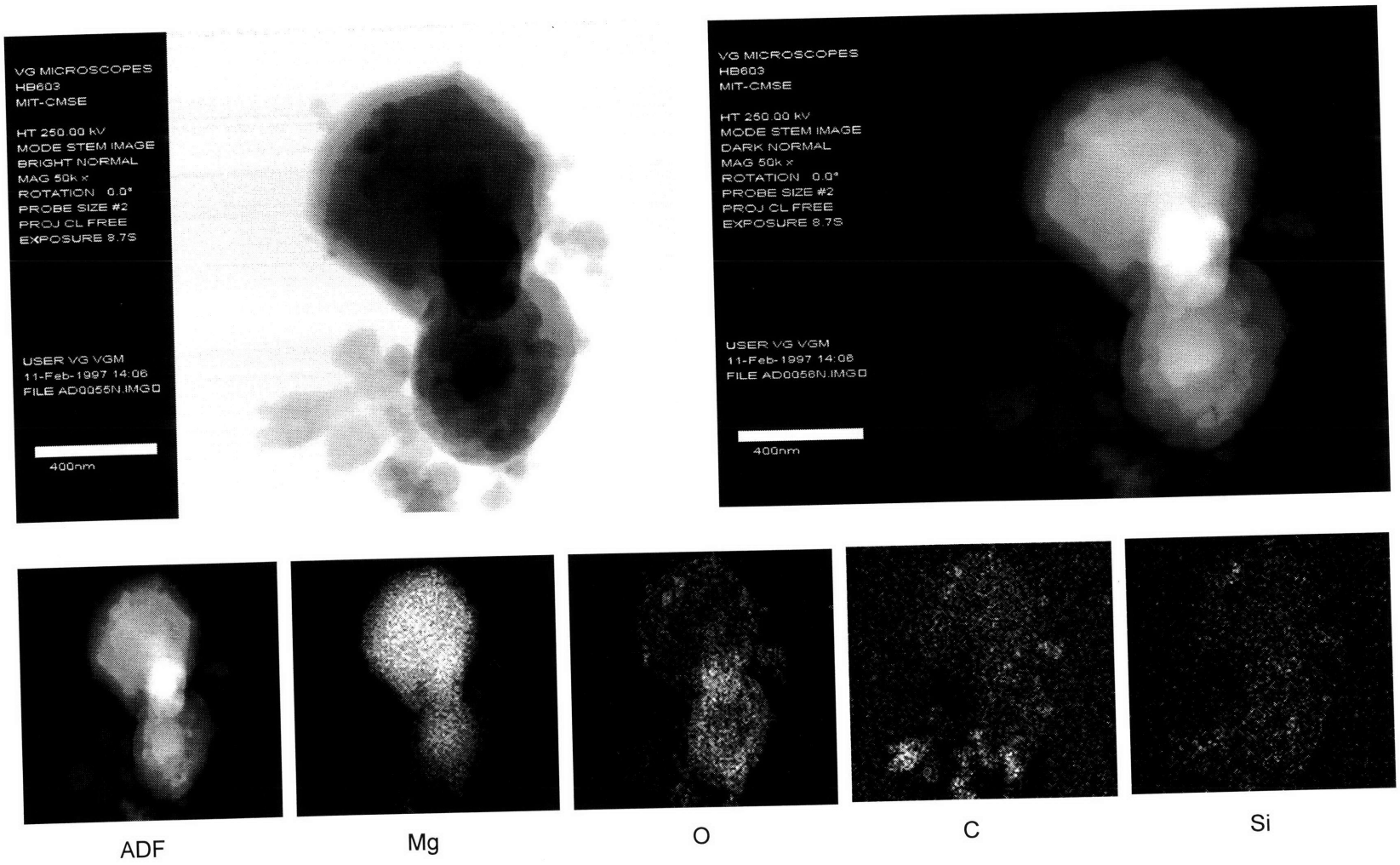

Figure 3-33A. STEM Images and Elemental Mapping of Sample from Run MG1 (10 l/min CH_4; 0.7:1 Mg:CH_4; 4% Mg Conversion to Mg_2C_3)

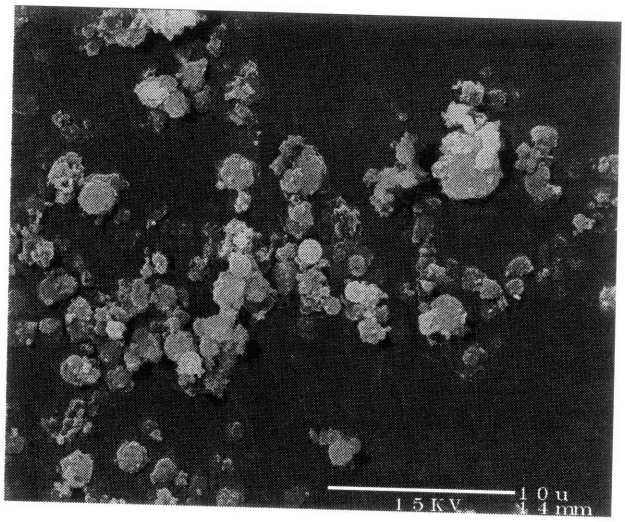

Figure 3-33B. SEM of Run MG1 Sample, x3,500

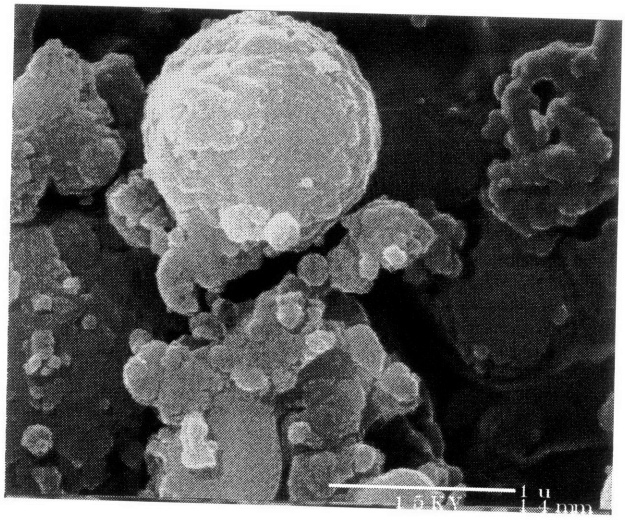

Figure 3-33C. SEM of Run MG1 Sample, x35,000

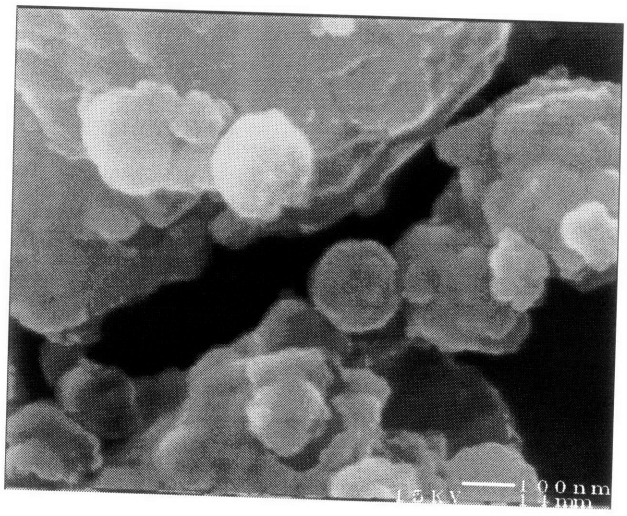

Figure 3-33D. SEM of Run MG1 Sample, x100,000

3.6 CaO-CH_4-Ar System

An exploratory plasma reactor study of the CaO-CH_4-Ar system was undertaken for comparison with the MgO-CH_4-Ar system. Four experimental runs, designated Runs C1 to C4, were conducted to gain an insight on the fundamental differences between the two systems. CaO powder entrained in 4.2 l/min Ar was introduced at a rate of 7.8 g/min with 10 l/min CH_4 into the plasma reactor in all the runs. The arc was operated in the 21-29 kW power input range and the inlet CaO:CH_4 molar ratio was set at 0.34:1 to match the stoichiometric ratio of Reaction (1-1). The reactor conditions for these runs are summarized in Table 3-25.

Table 3-25. Summary of Reactor Conditions for CaO-CH_4-Ar System [Ave (± 1 s.d.)]

Run	C1	C2	C3	C4
Main CH_4 Flow, l/min	10.1	10.0	10.0	10.1
Secondary CH_4 Flow, l/min				
Main Argon Flow, l/min				
Carrier Argon Flow, l/min	4.2	4.2	4.2	4.2
CaO Feed, g/min	7.8	7.8	7.8	7.8
Inlet CaO/CH_4 Molar Ratio	0.34	0.34	0.34	0.34
CaO Particle Size, μm	44 to 104	44 to 104	44 to 104	44 to 104
Chamber Pressure, mm Hg	760 ± 4	760 ± 4	757 ± 5	759 ± 4
Arc Voltage, V	36.5 ± 3.7	30.7 ± 2.5	31.0 ± 0.8	33.4 ± 2.8
Arc Current, A	585 ± 30	720 ± 17	434 ± 114	718 ± 49
Arc Power Input, kW	21.2 ± 1.1	22.1 ± 1.3	28.9 ± 0.3	23.9 ± 0.6
Quench Distance, in	5	5	5	5
Magnetic Field, G	118	118	118	118

Compared to the MgO-CH_4-Ar system, the CaO-CH_4-Ar system exhibits a higher degree of product selectivity. The major reaction products of this system are CaC_2, C_2H_2, H_2 and CO, which can be attributed globally to the carbide formation reaction, Reaction (1-1), and to the overall methane decomposition reaction to acetylene, Reaction (1-24). The solid product is a light gray powder composed of CaC_2 and non-carbide solid carbon. Upon hydrolysis, the solids evolve C_2H_2 and a trace amount of n-C_4H_{10} but no H_2. The gaseous product is mainly H_2 and CO, with some C_2H_2 and unreacted CH_4. Other C_2, C_3 and C_4 species observed in the MgO-CH_4-Ar system were not detected in this system.

Material balances on the constituent elements of the CH_4 and CaO reactants for Runs C1 to C4 are given in Tables 3-26 and 3-27, respectively. The carbon in methane is converted to CaC_2 and non-carbide C in the solid product and to CO and C_2H_2 in the gaseous product. The hydrogen in methane is recovered as H_2 and C_2H_2 gas. The calcium in CaO is converted to solid CaC_2 while the oxygen is transformed to CO gas.

Table 3-26. Percent Methane Molar Conversion to Products in CaO-CH_4-Ar System

Run	C1		C2		C3		C4	
Products	CH_4 "C"	CH_4 "H"	CH_4 "C"	CH_4 "H"	CH_4 "C"	CH_4 "H"	CH_4 "C"	CH_4 "H"
CaC_2	35.5		32.0		60.0		28.9	
Non-carbide C	27.2		15.9		8.2		15.0	
CO	34.5		34.6		47.6		34.4	
C_2H_2	11.6	2.9	9.0	2.3	9.5	2.4	12.4	3.1
Unreacted CH_4	0.2	0.2	0.0	0.0	0.0	0.0	0.1	0.1
H_2		64.8		65.7		87.2		66.2
Total	109.0	67.9	91.5	68.0	125.3	89.6	90.8	69.4

Table 3-27. Percent Calcium Oxide Molar Conversion to Products in CaO-CH_4-Ar System

Run	C1		C2		C3		C4	
Products	CaO "Ca"	CaO "O"	CaO "Ca"	CaO "O"	CaO "Ca"	CaO "O"	CaO "Ca"	CaO "O"
CaC_2	53.0		47.6		89.4		43.1	
CO		103.0		103.1		141.8		102.6
Total	53.0	103.0	47.6	103.1	89.4	141.8	43.1	102.6

The average CaO "Ca" conversion to CaC_2 is 58% while the mean CH_4 "H" conversion to H_2 is 80% for the four experimental runs. The extent of conversion of CH_4 "C" to CO ranges from 34 to 48%, in good agreement with the expected conversion of 33%. But the CH_4 "C" conversion to CaC_2 ranges only from 29 to 60%, which is below the expected 67% according to Reaction (1-1). The shortfall is accounted for by an 8-27% CH_4 "C" conversion to non-carbide C and an 11% CH_4 "C" conversion to C_2H_2. The formation of significant amounts of C_2H_2 is a noticeable difference in the CaO-CH_4-Ar system compared to the MgO-CH_4-Ar system. The H_2/CO ratio is fairly constant at

3.8, which is lower than the expected ratio of 6 according to Reaction (1-1), because of the methane carbon conversion to non-carbide C. Table 3-28 summarizes the statistics on the CaO and CH_4 conversion and H_2/CO ratio.

Table 3-28. Summary Statistics of Reactant Conversion to Products and H_2/CO Ratio for CaO-CH_4-Ar System

% Conversion	Mean	Std. Dev.	95% C.I.	Minimum	Maximum
$(Ca)\alpha_{CaO}^{CaC_2}$	58.3	21.1	[24.6,91.9]	43.1	89.4
$(H)\alpha_{CH_4}^{H_2}$	80.0	10.8	[53.7,88.2]	64.8	87.2
$(C)\alpha_{CH_4}^{CO}$	37.8	6.6	[27.4,48.2]	34.4	47.6
$(C)\alpha_{CH_4}^{CaC_2}$	39.1	14.2	[16.5,61.6]	28.9	60.0
$(C)\alpha_{CH_4}^{C_2H_2}$	10.6	1.6	[8.0,13.2]	9.0	12.4
$(C)\alpha_{CH_4}^{C}$	16.6	7.9	[4.0,29.1]	8.2	27.2
H_2/CO Ratio	3.8	0.1	[3.6,3.9]	3.7	3.9

The solid products from this system exhibit a different texture from that observed with the products of the MgO-CH_4-Ar system. The solids resemble ash in constituency, are lighter gray compared to the solids from the previous systems and are more easily removed from the chamber walls. STEM/EDS analysis results for a sample from Run C3 are presented in Figure 3-34A, which shows a cluster composed mostly of CaO. No CaC_2 particle was readily identified in the sample by STEM/EDS, apparently due to degradation and decomposition of the very fine carbide particles during the exposure to the atmosphere prior to mounting in the microscope. Carbon is present in the sample, although dispersed throughout the cluster. The corresponding SEM images of the same sample at three levels of magnification are shown in Figures 3-34B to 3-34D. The sample is observed to be composed of agglomerates of very fine particles in the 0.1 to 1 μm size range. The small particles have irregular geometry with rounded edges and seem to fuse with one another.

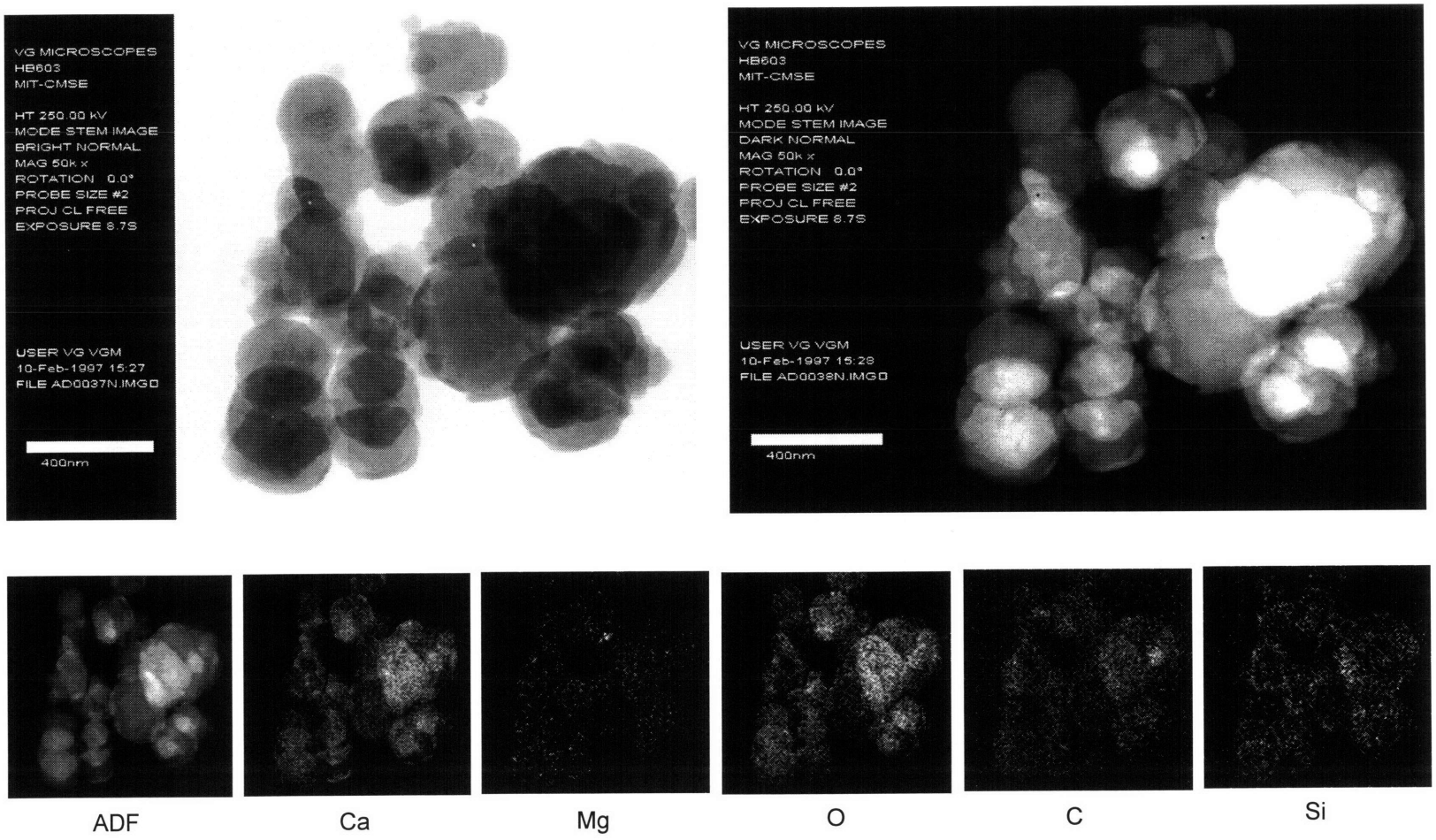

Figure 3-34A. STEM Images and Elemental Mapping of Sample from Run C3 (10 l/min CH_4; 0.34:1 CaO:CH_4; 89.4% CaO "Ca" Conversion to CaC_2)

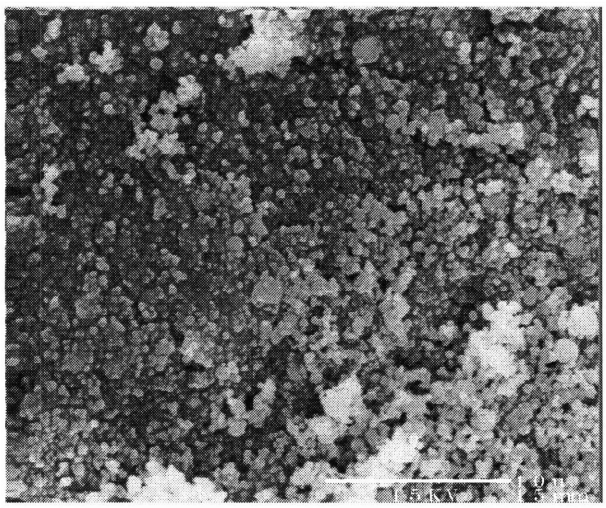

Figure 3-34B. SEM of Run C3 Sample, x3,500

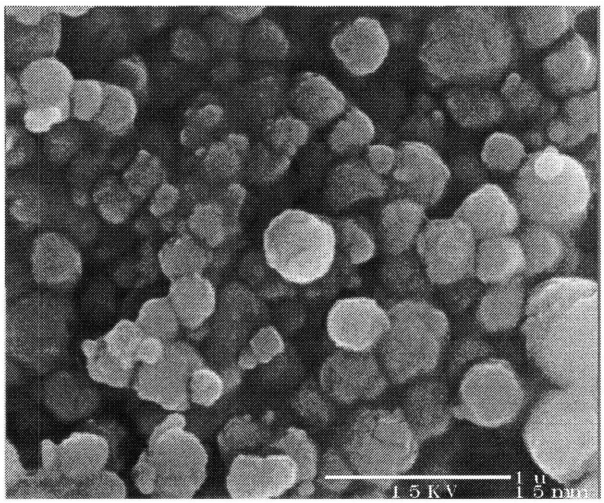

Figure 3-34C. SEM of Run C3 Sample, x35,000

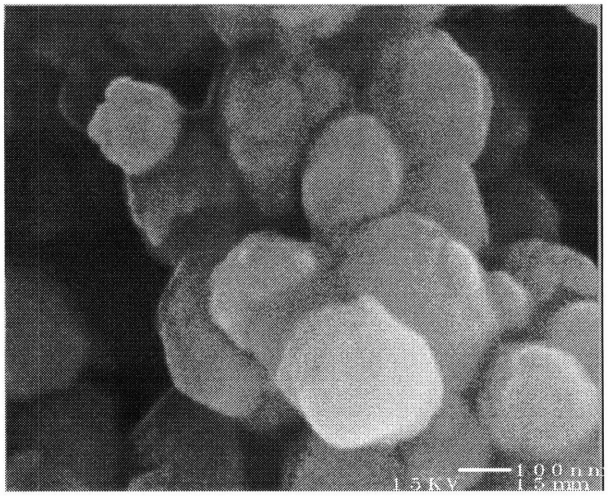

Figure 3-34D. SEM of Run C3 Sample, x100,000

3.7 MgO-CaO-CH_4-Ar System

An exploratory study of the MgO-CaO-CH_4-Ar system was also undertaken to determine the product selectivity and yields of a system with the two alkaline earth metal oxides combined, such as is found in calcined dolomite. Five experimental runs, designated Runs CM1 to CM5, were conducted with this system. A mixture of MgO and CaO powder at a 1:1 molar ratio entrained in 4.2 l/min Ar was introduced at a rate of 8.2 g/min with 10 l/min CH_4 into the plasma reactor. This corresponds to an inlet MgO:CaO:CH_4 molar ratio of 1:1:5. The arc was operated in the power input range of 19-32 kW. The reactor conditions for these runs are given in Table 3-29.

Table 3-29. Summary of Reactor Conditions for MgO-CaO-CH_4-Ar System [Ave (± 1 s.d.)]

Run	CM1	CM2	CM3	CM4	CM5
Main CH_4 Flow, l/min	10.0	10.0	10.0	10.0	10.0
Secondary CH_4 Flow, l/min					
Main Argon Flow, l/min					
Carrier Argon Flow, l/min	4.2	4.2	4.2	4.2	4.2
CaO/MgO Feed, g/min	8.2	8.2	8.2	8.2	8.2
CaO:MgO:CH_4 Molar Ratio	1:1:5	1:1:5	1:1:5	1:1:5	1:1:5
CaO/MgO Particle Size, μm	44 to 104	44 to 104	44 to 104	44 to 104	44 to 104
Chamber Pressure, mm Hg	759 ± 4	759 ± 5	760 ± 2	759 ± 8	757 ± 9
Arc Voltage, V	31.9 ± 1.4	35.1 ± 1.4	51.0 ± 2.2	38.5±13.3	32.9 ± 1.6
Arc Current, A	824 ± 24	688 ± 26	611 ± 14	539 ± 118	826 ± 11
Arc Power Input, kW	26.3 ± 0.4	24.1 ± 0.1	31.1 ± 0.8	19.2 ± 2.5	27.2 ± 1.0
Quench, in	5	5	5	5	5
Magnetic Field, G	118	118	118	118	118

The major reaction products of the combined system are CaC_2, Mg, H_2, CO and C_2H_2, which can be attributed globally to CaC_2 formation, Reaction (1-1), Mg metal formation, Reaction (1-4), and the overall methane decomposition reaction to acetylene, Reaction (1-24). The solid product is composed of CaC_2, Mg, Mg_2C_3 and non-carbide carbon. Upon hydrolysis, the solids evolve C_2H_2, H_2 and C_3H_4. Trace amounts of C_2H_4, C_2H_6, C_3H_6, C_3H_8 and n-C_4H_{10} are also detected in the headspace above the hydrolyzed solids. Since MgC_2 also yields C_2H_2 upon hydrolysis, MgC_2 is also probably present in

the solid product, although most likely in small quantities as in the MgO-CH_4-Ar system. The gaseous product is mainly H_2 and CO with some C_2H_2, unreacted CH_4 and trace amounts of C_2H_4.

Material balances on the constituent elements of the CH_4, MgO and CaO reactants for Runs CM1 to CM5 are presented in Tables 3-30 and 3-31, respectively. The carbon in methane is converted to solid CaC_2, Mg_2C_3 and non-carbide solid C, as well as to CO and C_2H_2 in the gaseous product. The hydrogen in methane is transformed to H_2 and C_2H_2 gas. The magnesium in MgO is converted to solid Mg and Mg_2C_3 while the calcium in CaO is converted to solid CaC_2. The oxygen in the two oxides cannot be readily identified separately in the final CO gas product; thus, the reported conversion is for the total oxygen of the two oxides.

Table 3-30. Percent Methane Molar Conversion to Products in MgO-CaO-CH_4-Ar System

Run	CM1		CM2		CM3		CM4		CM5	
Products	CH_4 "C"	CH_4 "H"	CH_4 "C"	CH_4 "H"	CH_4 "C"	CH_4 "H"	CH_4 "C"	CH_4 "H"	CH_4 "C"	CH_4 "H"
Mg_2C_3	0.7		0.8		0.7		0.7		0.8	
CaC_2	22.9		22.7		13.2		11.9		23.6	
Non-carbide C	10.9		10.4		7.0		17.2		4.6	
CO	46.4		42.5		46.3		43.9		56.7	
C_2H_2	6.8	1.7	4.8	1.2	2.8	0.7	10.0	2.5	6.6	1.7
C_3H_4	0.0	0.0	0.0	0.0	0.0	0.0	0.0	0.0	0.0	0.0
Other C_2, C_3, C_4	0.0	0.0	0.0	0.0	0.1	0.1	0.0	0.0	0.0	0.0
Unreacted CH_4	0.1	0.1	0.1	0.1	0.1	0.1	0.1	0.1	0.1	0.1
H_2		88.6		91.1		89.6		88.9		97.7
Total	87.9	90.4	81.3	92.4	70.2	90.5	83.8	91.5	92.4	99.5

Table 3-31. Percent Magnesium Oxide and Calcium Oxide Molar Conversion to Products in MgO-CaO-CH_4-Ar System

Run	CM1			CM2			CM3			CM4			CM5		
Products	CaO "Ca"	MgO "Mg"	CaO/ MgO "O"	CaO "Ca"	MgO "Mg"	CaO/ MgO "O"	CaO "Ca"	MgO "Mg"	CaO/ MgO "O"	CaO "Ca"	MgO "Mg"	CaO/ MgO "O"	CaO "Ca"	MgO "Mg"	CaO/ MgO "O"
CaC_2	56.5			56.0			32.5			29.4			58.2		
Mg_2C_3		2.2			2.4			2.2			2.1			2.5	
Mg		66.3			64.9			64.9			66.6			63.8	
CO			113.7			104.7			113.5			107.7			138.7
Total	56.5	68.5	113.7	56.0	67.3	104.7	32.5	67.1	113.5	29.4	68.7	107.7	58.2	66.3	138.7

Under the conditions investigated, the extent of MgO "Mg" conversion to Mg is relatively constant at 65% while the MgO "Mg" conversion to Mg_2C_3 is below 3% in all the runs. Thus, the extents of conversion of MgO "Mg" to Mg and to Mg_2C_3 do not seem to be affected by the presence of CaO feed in the system. The average CaO "Ca" conversion to CaC_2 is 47%. The hydrogen in CH_4 is almost completely converted to H_2 while the carbon is converted in decreasing levels to CO (43-57%), CaC_2 (12-24%), non-carbide C (5-17%), C_2H_2 (3-10%) and Mg_2C_3 (<1%). There is no readily apparent dependence of conversion on arc power input under the conditions studied. The mean H_2/CO ratio is 3.9 over the power range investigated, which is comparable to that of the CaO-CH_4-Ar system. The summary statistics of reactant conversion and H_2/CO ratio for the MgO-CaO-CH_4-Ar system is presented in Table 3-32.

Table 3-32. Summary Statistics of Reactant Conversion to Products and H_2/CO Ratio for MgO-CaO-CH_4-Ar System

% Conversion	Mean	Std. Dev.	95% C.I.	Minimum	Maximum
$(Ca)\alpha_{CaO}^{CaC_2}$	46.5	14.3	[28.8,64.2]	29.4	58.2
$(Mg)\alpha_{MgO}^{Mg}$	65.3	1.1	[63.9,66.7]	63.8	66.6
$(Mg)\alpha_{MgO}^{Mg_2C_3}$	2.3	0.2	[2.1,2.5]	2.1	2.5
$(H)\alpha_{CH_4}^{H_2}$	91.2	3.8	[86.5,95.9]	88.6	97.7
$(C)\alpha_{CH_4}^{CO}$	47.2	5.6	[40.2,54.1]	42.5	56.7
$(C)\alpha_{CH_4}^{CaC_2}$	18.9	5.8	[11.7,26.0]	11.9	23.6
$(C)\alpha_{CH_4}^{C_2H_2}$	6.3	2.6	[3.0,9.5]	2.9	10.0
$(C)\alpha_{CH_4}^{C}$	10.0	4.8	[4.1,15.9]	4.6	17.2
H_2/CO Ratio	3.9	0.3	[3.5,4.3]	3.5	4.3

The solid products from this system resemble those from the MgO-CH_4-Ar system in terms of color and texture. The STEM/EDS analysis of a sample from Run CM1, presented in Figure 3-35A, shows a cluster composed of CaO, Mg and CaC_2. The presence of CaC_2 can be deduced from the almost equally intense signals corresponding to the particle on upper right hand corner of the Ca and C images, without any similarly

intense oxygen signals in the same area. The associated SEM images of the sample at three levels of magnification are shown in Figures 3-35B to 3-35D. The sample is seen to be composed of agglomerates of very fine particles also in the 0.1 to 1 μm size range. Similar to the CaO-CH_4-Ar system, the small particles have irregular geometry with rounded edges and seem to fuse with one another.

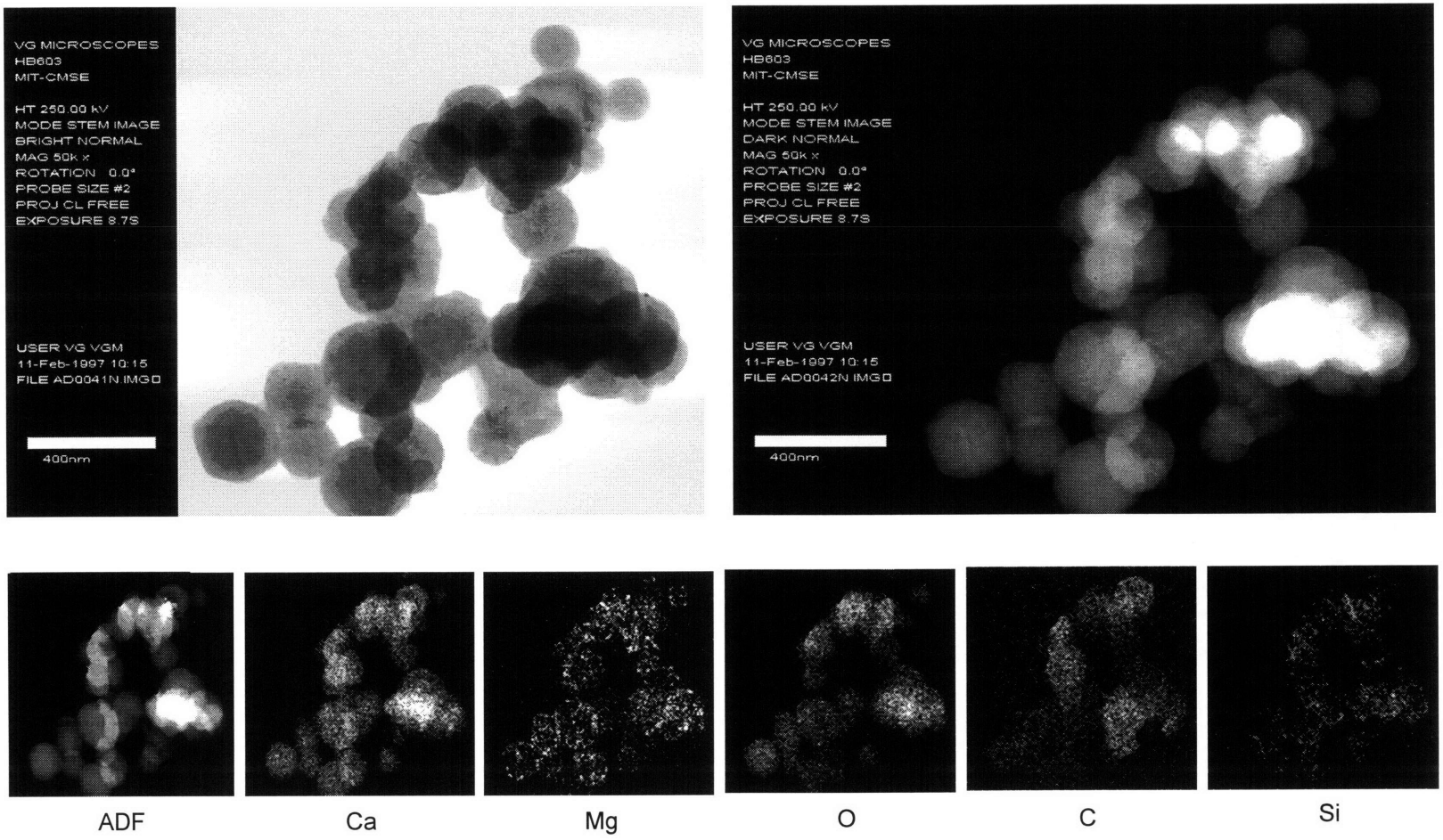

Figure 3-35A. STEM Images and Elemental Mapping of Sample from Run CM1
(10 l/min CH_4; 1:1:5 MgO:CaO:CH_4; 66% MgO "Mg" Conversion to Mg and 57% CaO "Ca" Conversion to CaC_2)

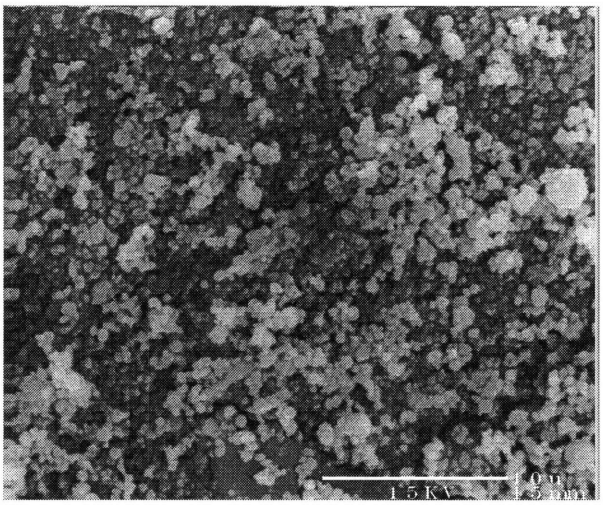

Figure 3-35B. SEM of Run CM1 Sample, x3,500

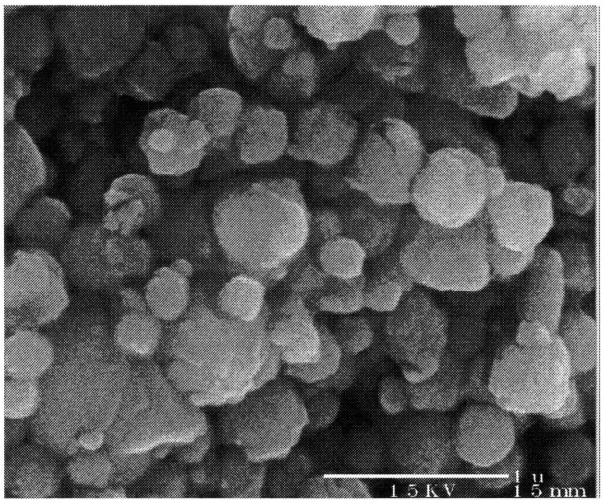

Figure 3-35C. SEM of Run CM1 Sample, x35,000

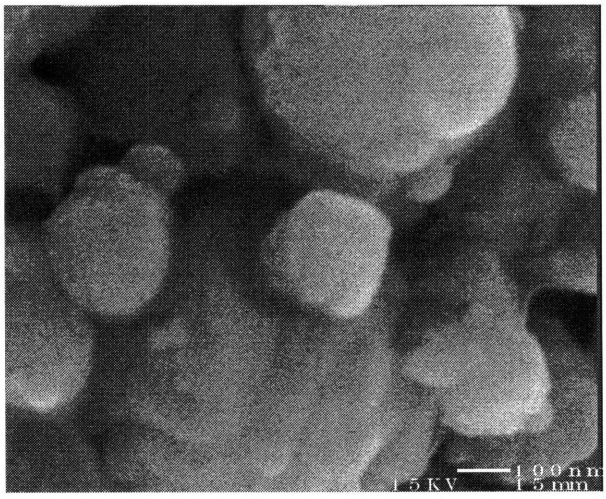

Figure 3-35D. SEM of Run CM1 Sample, x100,000

3.8 Operational Characteristics

The voltage-current curves of the CH_4 arc during MgO feeding, depicted in Figure 3-36, illustrate the falling voltage-rising current characteristic of a low to medium intensity arc. The effect of increasing the gas flow rate is to shift the curves upward. The higher voltage levels measured at the same current under the higher CH_4 flow rates are due to the increased convective cooling of the arc column as well as to the elongation of the column which is sustained in a cross flow of the gas.

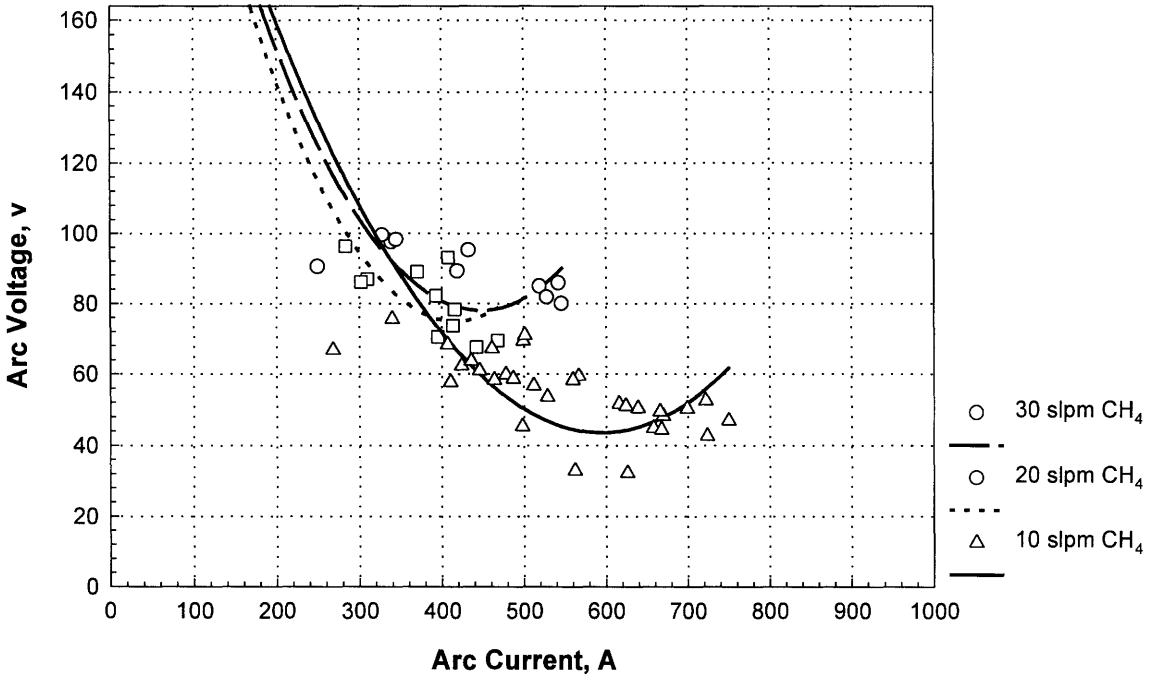

Figure 3-36. Voltage-Current Curves of CH_4 Arc with MgO Feeding

Setting the arc to operate at a particular power input level proved to be challenging as the voltage and current were continuously fluctuating. The arc was observed to be more stable in the runs at 10 and 20 l/min CH_4 flow rates. Although a discharge can be sustained at a flow rate of 30 l/min CH_4, this arc is very difficult to establish without MgO feeding. Initially, the MgO feeding was started after the switchover from Argon to methane, as was done by Kim (1977) with his CH_4-CaO arc. However, this practice usually resulted in the arc being extinguished before a complete transition is achieved. As methane displaces

Argon in the arc discharge, the arc voltage starts to increase and the arc current starts to decrease. If the current control is not adjusted rapidly enough to keep the arc current above 200 A, the arc is extinguished. In order to enable a smoother transition, the procedure was modified by initiating the MgO feeding before the switchover to methane. The commencement of MgO feeding results in a drop in the arc voltage due to ionization of the MgO, giving rise to a lower arc voltage during the transition period.

The wear and tear of the graphite electrodes was gauged by weighing the electrodes before and after each run. The erosion of the cathode tip was always less severe than that of the anode insert, despite the rotation of the arc over the larger annular surface of the anode insert. In fact, the graphite cathode tip gained 0.8 g on average over all the runs. This represents an average of only 2% of the carbon content of the CH_4 feed. The cathode tip was found to grow radially at the bottom from deposition and fusion of carbon from the CH_4. With the downward flow of gas restricting the cathodic end of the arc to the bottom of the cathode tip, a flared bottom with a crater-like center developed from carbon deposition after each run. The bottom section grew radially from the original diameter of 0.75 in. to a maximum of 0.87 in. and the cathode was elongated at the skirts of the bottom section from an overall length of 1.5 in. to as much as 1.6 in. in some runs. Hardly any axial recession of the cathode tip was observed in any of the runs. Thus, the cathode tip may not have been heated as intensely as the anode, with the current density at the cathode tip having reached a maximum of only 350 A/cm^2 under the most severe arc current of 1000 A.

The anode insert always had the inner surface of its bottom 1 in. section receding away in a spiral direction. The anode itself gained an average of 1 g while the anode insert lost an average of 0.5 g over all the runs which lasted for about five minutes each. Thus, there is a net gain (average of 1.3 g) on the graphite anode, anode insert and cathode tip, corresponding to about 1% of the carbon in the CH_4.

In most runs, a certain amount of solids is deposited on the inside walls of the anode insert, which spilled onto the inner surface of the graphite anode. These hard deposits amount to an average of 7.4 g per run over all the runs. Assuming the deposits are all MgO, this corresponds to about 7% of the solid feed. However, no correction is made in

the conversion calculations because the deposition is believed to occur mostly prior to methane switchover, when the plasma is still relatively cool.

The MgO-CH_4-C-Ar system is operationally similar to the MgO-CH_4-Ar system in terms of voltage-current arc characteristics and erosion rates of the graphite electrodes. Likewise, a plasma with Mg-CH_4-Ar was not difficult to sustain under the experimental conditions investigated. However, the post-operation procedures for this system proved to be extremely hazardous because of the large quantities of very finely divided pyrophoric magnesium powder produced and deposited on the chamber walls and lines. In the Mg-CH_4-Ar runs, the graphite anode inserts were eroded at their inner walls but the cathode tips grew radially from an original diameter of 0.75 in. to as much as 0.875 in. over the bottom 0.5 in. section. The deposition on the cylindrical surface of the cathode resembles solidified droplets. The graphite anode, anode insert and cathode tip gained an average of 2 g over 3 runs which lasted about 5 minutes each.

The operational characteristics of the plasma reactor with the CaO-CH_4-Ar system are very different from those of the other systems investigated. Although a stable arc can be sustained in this system, the anode nozzle always clogged up with brittle but abundant deposits. This clogging eventually led to the arc being extinguished in a few instances. Furthermore, solidified droplets of CaO have been found at the bottom of the chamber and even in the sampler after each run. Relative to the other systems, the anode insert and cathode tip were more severely eroded in this system. The inner surface of the insert always had a deep spiral groove and its wall thickness was reduced drastically. The sharp circular edge of the cylindrical cathode tip was always rounded after every run, although a radial growth developed on the bottom ½ in. section and the tip did not recede axially. The graphite anode, anode insert and cathode tip lost an average of 5.8 g over the four runs which lasted about 5 minutes each. The deposits collected from the electrodes weighed 9.5 g per run on average.

Unlike the CaO-CH_4-Ar system, operation of the MgO-CaO-CH_4-Ar system in the plasma reactor did not result in as much clogging of the anode nozzle. However, the anode insert and cathode tip were just as severely eroded. The wall thickness of the insert was reduced drastically and the sharp circular edge of the cylindrical cathode tip was always

rounded after every run. Although axial recession of the cathode tip was not significant in most runs, the tip receded in one run from 1.5 in. to 1.1 in. and widened from 0.75 in. to about an inch in diameter. The radial growth on the bottom ½ in. section increased the diameter of the tip to 0.87 in. in most of the runs. The graphite anode, anode insert and cathode tip lost an average of 11.6 g over the five runs which lasted about 5 minutes each while the deposits collected from the electrodes weighed 19.3 g per run on average.

Chapter 4

Thermodynamic Analysis

To obtain an assessment of the thermodynamic driving forces of possible chemical reactions within the plasma, multiphase equilibrium composition calculations based on the minimization of Gibbs free energy were performed for the Mg-C-H-O-Ar, Mg-C-H-Ar, Ca-C-H-O-Ar and Mg-Ca-C-H-O-Ar systems. The calculations were made with the GIBBS routine of HSC Chemistry for Windows version 2.03 from Outokumpu Research Oy (Talonen *et al.*, 1994).

The GIBBS program determines the most stable phase combination and individual phase compositions at which the Gibbs free energy, G, of the system reaches a minimum subject to mass balance, constant pressure and constant temperature constraints. The Gibbs free energy is determined from enthalpy H, entropy S and temperature T according to:

$$G = H - TS \qquad \text{Equation (5-1)}$$

The enthalpy, $H(T)$, and entropy, $S(T)$, at temperature T are calculated from the standard enthalpy, H_f^o, and standard entropy, S_f^o, of formation at 298.15 K and the constant pressure heat capacity c_p as

$$H(T) = H_f^o + \int_{298.15}^{T} c_p \mathrm{d}T + \sum H_t \qquad \text{Equation (5-2)}$$

$$S(T) = S_f^o + \int_{298.15}^{T} \frac{c_p}{T} dT + \sum \frac{H_t}{T_t} \qquad \text{Equation (5-3)}$$

where H_t is the enthalpy of transformation of the substance at temperature T_t. The temperature dependence of the heat capacity is accounted for by using a polynomial fit to experimental data. The Kelley equation is used in the program in the following form:

$$c_p = A + B \times 10^{-3} T + C \times 10^5 T^{-2} + D \times 10^{-6} T^2 \qquad \text{Equation (5-4)}$$

where A, B, C and D are coefficients fitted to the available data.

The available species in the HSC database from the elements specified in each system, divided into gas and condensed phases, have been included in the calculations. The gases are assumed to be ideal and to form ideal mixtures. Condensed phases are also assumed to be pure or to form ideal solutions, with the activity coefficient of each species in the mixture taken as 1.

The equilibrium composition calculations are for systems at atmospheric pressure (except where the pressure is stated otherwise) and have been performed at temperatures between 298 K and 6000 K in 50 K increments. With plasma temperatures likely to exceed 10,000 K, all reactants injected into the plasma are completely vaporized into atomic species provided that there is sufficient residence time. Since most elements are in the atomic gas state above 6000 K and chemical reactions with the atomic gas species begin as the reactants cool down from this temperature, the equilibrium calculations start from 6000 K all the way down to 298 K. Most atomic gases are not sufficiently ionized at T $\leq$ 6000 K, so there are no ionized atomic species considered in the calculations. These considerations are primarily based on the study of the thermochemistry of thermal plasma chemical reactions by Chang and Pfender (1987). Only species with equilibrium amounts greater than 10^{-4} mole have been included in the equilibrium diagrams.

The maximum possible temperature for the MgO-CH_4 reaction system as a function of the specific gas energy input is presented in Figure 4-1. For each specific gas energy, the maximum temperature that can be reached by a reacting system composed of

one mole of CH_4 and one mole of MgO, assuming that Reaction (1-4) goes to completion and that there is no heat loss from the system, has been calculated. Since the arc power input levels and methane flow rates investigated correspond to specific gas energies in the 1500-5500 kJ/g atom C range, the results of the calculations show that the reaction system is conceivably well over 6000 K even at the lower limit of the experimental specific gas energy range.

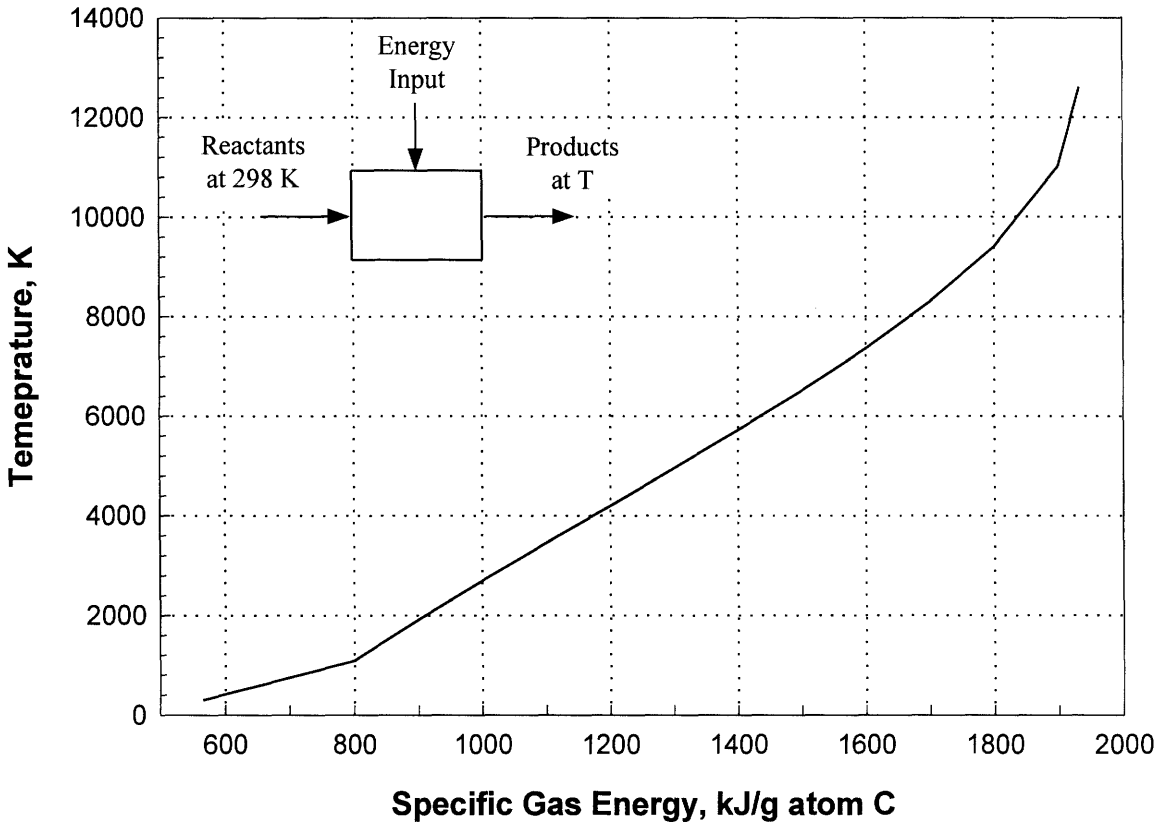

Figure 4-1. Maximum Reaction Temperature as a Function of Specific Gas Energy for 1 $CH_{4\,(g)}$ + 1 MgO → 1 $Mg_{(g)}$ + 1 $CO_{(g)}$ + 2 $H_{2\,(g)}$

4.1 Mg-C-H-O-Ar System

The thermodynamic equilibrium diagram for the 1.15 MgO + 1 CH_4 + 0.42 Ar reaction system at 1 atmosphere, which corresponds to 10 l/min CH_4 with 4.2 l/min Ar carrier gas, is shown in Figure 4-2. According to this analysis, MgO introduced above 6000 K

immediately dissociates into atomic Mg and O gases while CH_4 dissociates into atomic C and O. However, above 6000 K (not shown in Figure 4-2), C and O combine to form carbon monoxide as represented by:

$$C_{(g)} + O_{(g)} \rightarrow CO_{(g)} \qquad \text{Reaction (4-1)}$$

The CO is seen to be stable over a wide temperature range down to about 2000 K. Because the MgO reactant is in stoichiometric excess, there will still be free oxygen atoms when the carbon is fully consumed. Water is gradually formed from the reaction of atomic hydrogen and the excess atomic oxygen starting at around 5000 K:

$$2\,H_{(g)} + O_{(g)} \rightarrow H_2O_{(g)} \qquad \text{Reaction (4-2)}$$

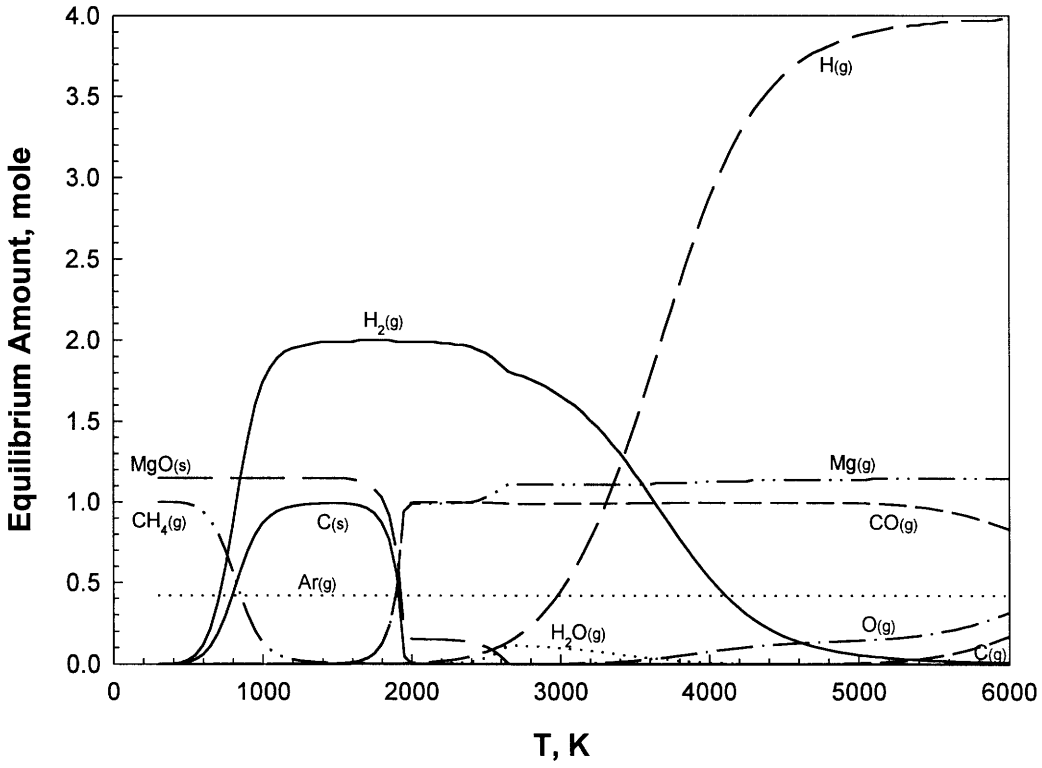

Figure 4-2. Thermodynamic Equilibrium Diagram for 1.15 MgO + 1 CH_4 + 0.42 Ar

At 2600 K, the following possible reactions can take place to form MgO and H_2:

$$Mg_{(g)} + H_2O_{(g)} \rightarrow H_{2\,(g)} + MgO_{(s)} \qquad \text{Reaction (4-3)}$$

$$H_2O_{(g)} \rightarrow 2\,H_{(g)} + O_{(g)} \qquad \text{Reaction (4-4)}$$

$$2\,H_{(g)} \rightarrow H_{2\,(g)} \qquad \text{Reaction (4-5)}$$

$$Mg_{(g)} + O_{(g)} \rightarrow MgO_{(g)} \qquad \text{Reaction (4-6)}$$

Just below 2000 K, magnesium starts to form MgO at the expense of carbon monoxide with the formation of solid carbon according to the reverse of Reaction (1-15) :

$$Mg_{(g)} + CO_{(g)} \rightarrow MgO_{(s)} + C_{(s)} \qquad \text{Reaction (4-7)}$$

At 1600 K, Reaction (4-7) is complete and all the magnesium has reverted back to MgO form. Neither Mg_2C_3 nor MgC_2 exists at equilibrium in significant amounts over the entire temperature range.

Experimentally, the major final products of the reaction system have been found to be Mg, H_2, CO and non-carbide C. In general, very little (<5%) magnesium carbides and only trace amounts of C_2, C_3 and C_4 hydrocarbons have been detected. Under equivalent experimental starting conditions, the average extents of conversion in the plasma reactor are 52% for MgO "Mg" to Mg, 3% for MgO "Mg" to Mg_2C_3, 84% for CH_4 "H" to H_2, 71% for CH_4 "C" to CO and 16% for CH_4 "C" to non-carbide solid C. The equilibrium composition that would match these observations corresponds to the temperature range from 2000 to 1800 K. Accordingly, the reaction rates may be fast enough to allow equilibrium to be maintained as the temperature decreases to 2000-1800 K, where the rates may be slow enough for the mixture composition to be frozen. The reaction products are therefore hypothesized to be quenched down to room temperature from somewhere in the 2000 to 1800 K temperature range. However, despite the agreement with experimental data, the detection of small amounts of Mg_2C_3, MgC_2 and C_2, C_3 and C_4 hydrocarbon species in the final products suggests that complete thermodynamic equilibrium is not attained in the plasma reaction.

In Section 3.2.5, the dilution of the MgO-CH_4 system with 15 l/min Argon has been shown to increase the conversion of MgO "Mg" to Mg from an average of 52 to 82%. CH_4 "H" conversion to H_2 is likewise observed to proceed to virtual completion from an average of 84% while CH_4 "C" conversion to CO is enhanced from 71 to 82%. These observations are consistent with Le Chatelier's Principle, the effect being similar to that of a system pressure reduction.

The equilibrium diagram for the 1.15 MgO + 1 CH_4 + 1.92 Ar system, corresponding to the 10 l/min CH_4 condition with 4.2 l/min Ar carrier gas plus 15 l/min Ar dilution, is presented in Figure 4-3. In comparison to Figure 4-2, Figure 4-3 shows that there is a slight reduction, from 2000 K to 1950 K, in the temperature at which Mg is favored to start to react to form MgO at the expense of CO according to Reaction (4-7).

To compare the effect of Argon dilution to one of reduced system pressure, the thermodynamic equilibrium composition diagram for 1.15 MgO + 1 CH_4 was also prepared on an Argon-free basis at the lower system pressure of 0.34 atm, equivalent to the original inlet conditions with inert gas dilution. The same effect, although more pronounced, is seen in the equilibrium diagram for this system at 0.34 atm, shown in Figure 4-4. The temperature at which Mg can start to reoxidize is decreased from around 2000 K at 1 atm system pressure to 1900 K in the Ar-free system at 0.34 atm. Similarly, the temperature at which MgO can first start to form by the reaction of Mg with H_2O according to Reaction (4-3) is reduced by about 100 K.

With a reduction in the temperature at which Reaction (4-7) begins, the product composition is then richer in Mg and CO at the temperature from which the products are quenched, assuming that the plasma effluent is quenched at the same rate from the same temperature range of 2000 to 1800 K. Thus, the thermodynamic analysis is consistent with the observation of higher Mg and CO yields upon addition of Argon.

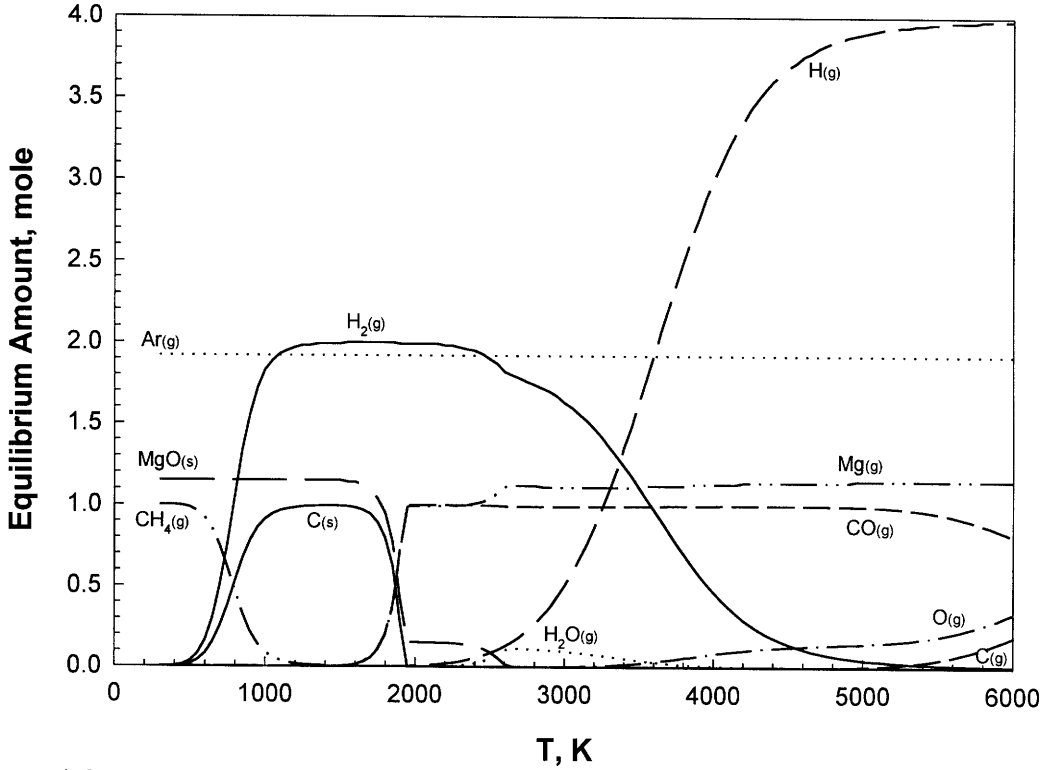

Figure 4-3. Thermodynamic Equilibrium Diagram for 1.15 MgO + 1 CH_4 + 1.92 Ar

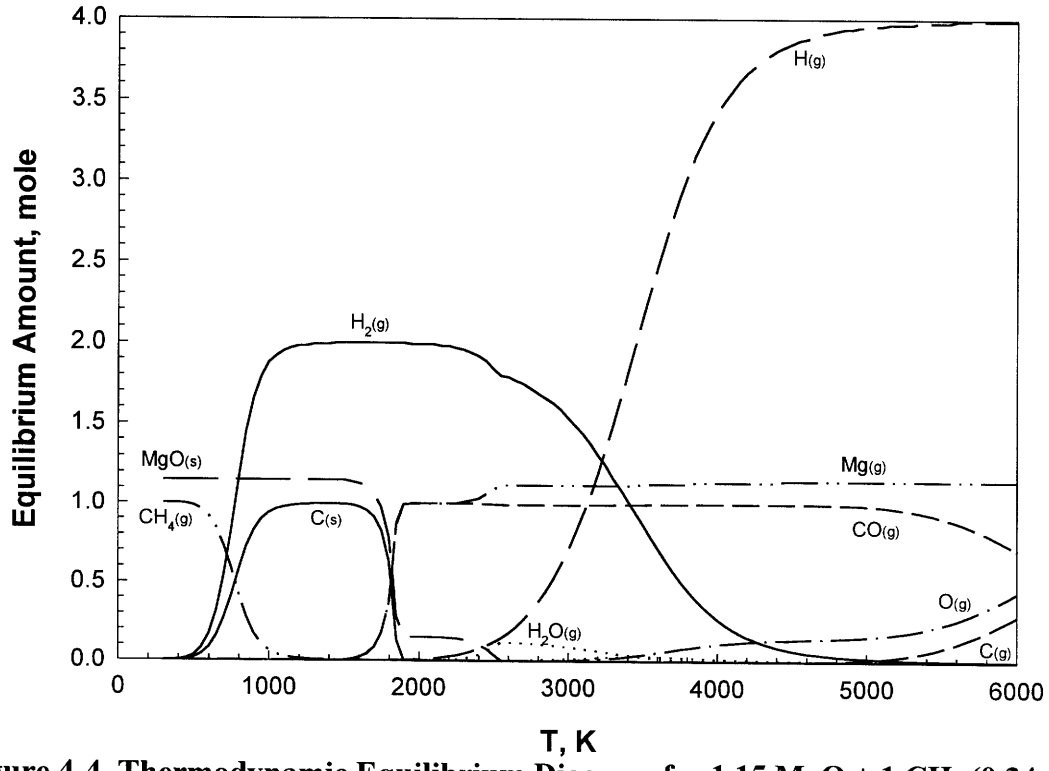

Figure 4-4. Thermodynamic Equilibrium Diagram for 1.15 MgO + 1 CH_4 (0.34 Atm)

Kim (1977) postulated that the formation of CaC_2 can be enhanced by H atoms which can directly reduce CaO to Ca and H_2O. With the large yields of H_2 resulting from the nearly complete conversion of CH_4, the recycling of H_2 as a potential source of H atoms to enhance the reduction of MgO to Mg may be of practical interest from a process point of view. The addition of H_2 to the MgO-CH_4 system can improve the formation of Mg, according to the reverse of Reaction (4-3). Thus, thermodynamic calculations were performed for the 1.15 MgO + 1 CH_4 + 0.42 Ar + 2 H_2 reaction system to simulate full recycling of H_2 back into the system. The results of these calculations are presented in the equilibrium diagram in Figure 4-5. Although the temperature at which MgO first forms is decreased from 2600 to 2500 K (also possibly due to a system pressure reduction effect), Mg depletion via Reaction (4-7) still dominates at 2000 to 1800 K. Therefore, the recycling of H_2 back into the process is not expected to increase Mg yields significantly given the same quenching rate.

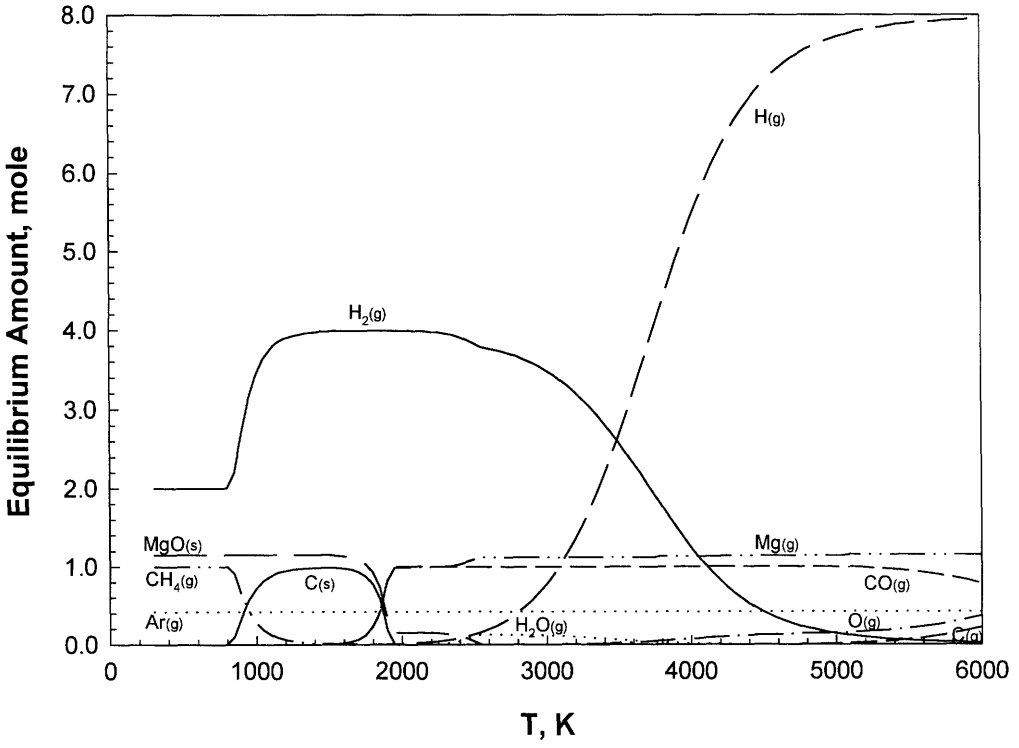

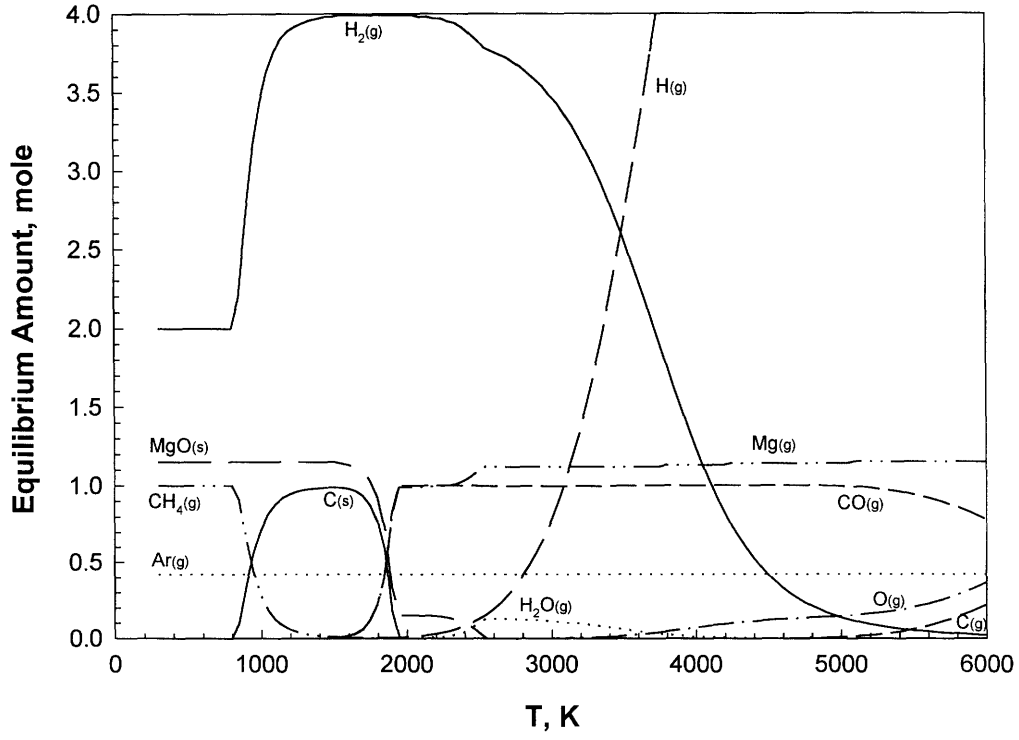

Figure 4-5. Thermodynamic Equilibrium Diagram for 1.15 MgO + 1 CH_4 + 0.42 Ar + 2 H_2

The equilibrium diagram for the 0.46 MgO + 1 CH_4 + 0.42 Ar reaction system is shown in Figure 4-6. With a substoichiometric initial amount of MgO in the system, there is still appreciable atomic gaseous C at 6000 K, after complete reaction with atomic O to form CO according to Reaction (4-1). The atomic C species is steadily depleted by the formation of C_2 starting at 5600 K, formation of C_2H beginning at 5000 K and formation of C_2H_2 starting at 4200 K:

$$2\,C_{(g)} \rightarrow C_{2\,(g)} \qquad \text{Reaction (4-8)}$$

$$2\,C_{(g)} + H_{(g)} \rightarrow C_2H_{(g)} \qquad \text{Reaction (4-9)}$$

$$2\,C_{(g)} + 2\,H_{(g)} \rightarrow C_2H_{2\,(g)} \qquad \text{Reaction (4-10)}$$

C_2 and C_2H can also be consumed by reaction with H via:

$$C_{2\,(g)} + H_{(g)} \rightarrow C_2H_{(g)} \qquad \text{Reaction (4-11)}$$

$$C_2H_{(g)} + H_{(g)} \rightarrow C_2H_{2\,(g)} \qquad \text{Reaction (4-12)}$$

and solid C is formed starting at 3150 K by:

$$\tfrac{1}{2}\,C_2H_{(g)} \rightarrow C_{(s)} + \tfrac{1}{4}\,H_{2\,(g)} \qquad \text{Reaction (4-13)}$$

$$\tfrac{1}{2}\,C_2H_{2\,(g)} \rightarrow C_{(s)} + \tfrac{1}{2}\,H_{2\,(g)} \qquad \text{Reaction (4-14)}$$

Magnesium exists completely as atomic gaseous Mg above 1850 K, in contrast to the 1.15 MgO + 1 CH_4 + 0.42 Ar reaction system at 1 atmosphere, where about 15% of the magnesium already exists as MgO from 2600 to 2000 K. The backward reaction of magnesium with carbon monoxide via Reaction (4-7) starts at a lower temperature of 1850 K and is complete at 1600 K. Neither Mg_2C_3 nor MgC_2 exists at equilibrium in significant amounts over the entire temperature range. With enough carbon to keep oxygen from reacting with Mg above 1850 K, the product composition is then richer in Mg at the temperature from which the products are possibly quenched. Again, the

thermodynamic analysis is consistent with the observation of higher Mg and lower CO yields when the MgO is stoichiometrically deficient.

Under similar initial experimental conditions, the average extents of conversion in the plasma reactor are 68% for MgO "Mg" to Mg, 3% for MgO "Mg" to Mg_2C_3, 83% for CH_4 "H" to H_2, 42% for CH_4 "C" to CO and 25% for CH_4 "C" to non-carbide solid C. The extents of conversion to Mg and CO would still roughly correspond to the same temperature of 2000 to 1800 K. The reaction products are thus proposed to be quenched down to room temperature from somewhere in the 2000 to 1800 K temperature range, although the detection of magnesium carbides and other hydrocarbons also suggests that full equilibrium at these temperatures is not reached.

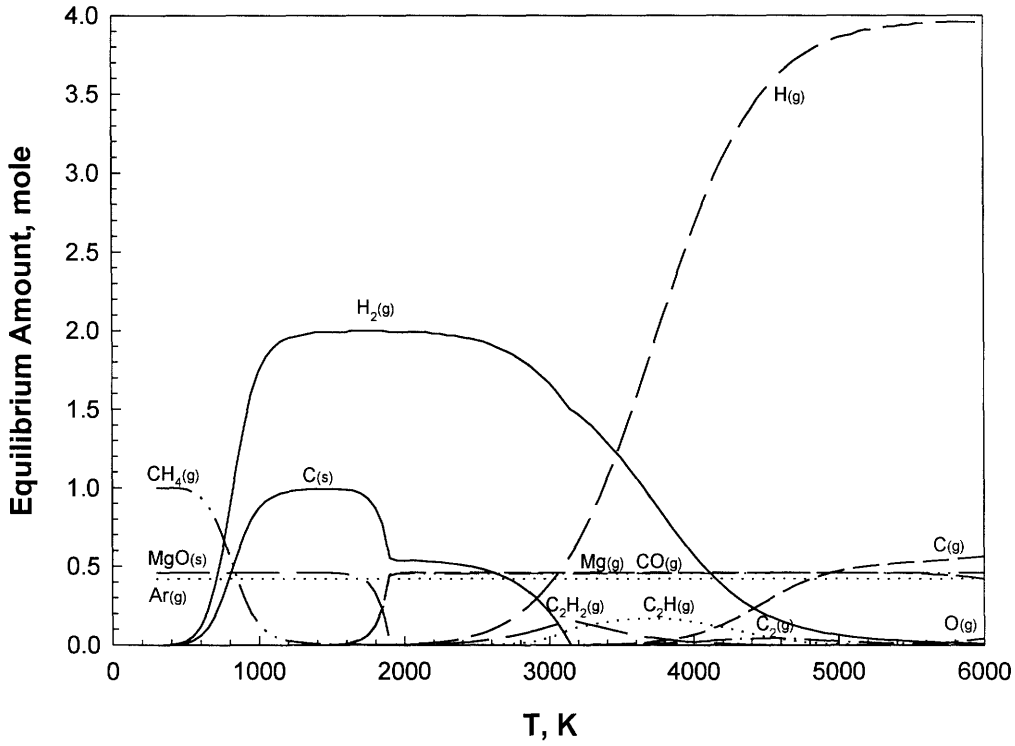

Figure 4-6. Thermodynamic Equilibrium Diagram for 0.46 MgO + 1 CH_4 + 0.42 Ar

Figure 4-7 shows the equilibrium diagram for the 1.15 MgO + 1 CH_4 + 0.4 C + 0.42 Ar reaction system, corresponding to the inlet conditions of the experiments with the MgO feed doped with graphite. With the addition of solid carbon in the reactants, MgO is no longer stoichiometrically deficient. All the magnesium exists as atomic gaseous Mg

above 2000 K, as there is sufficient carbon to keep the oxygen bound as CO above this temperature.

Under similar experimental conditions, the average extents of conversion in the plasma reactor are 66% for MgO "Mg" to Mg, 3% for MgO "Mg" to Mg_2C_3, virtually complete for CH_4 "H" to H_2, 72% for CH_4 "C" to CO and 10% for CH_4 "C" to non-carbide solid C, which would correspond to the product composition in the 2000 to 1800 K range. Consistent with analysis of the other experimental systems studied, the reaction products are presumed to quenched down from the 2000 to 1800 K temperature range.

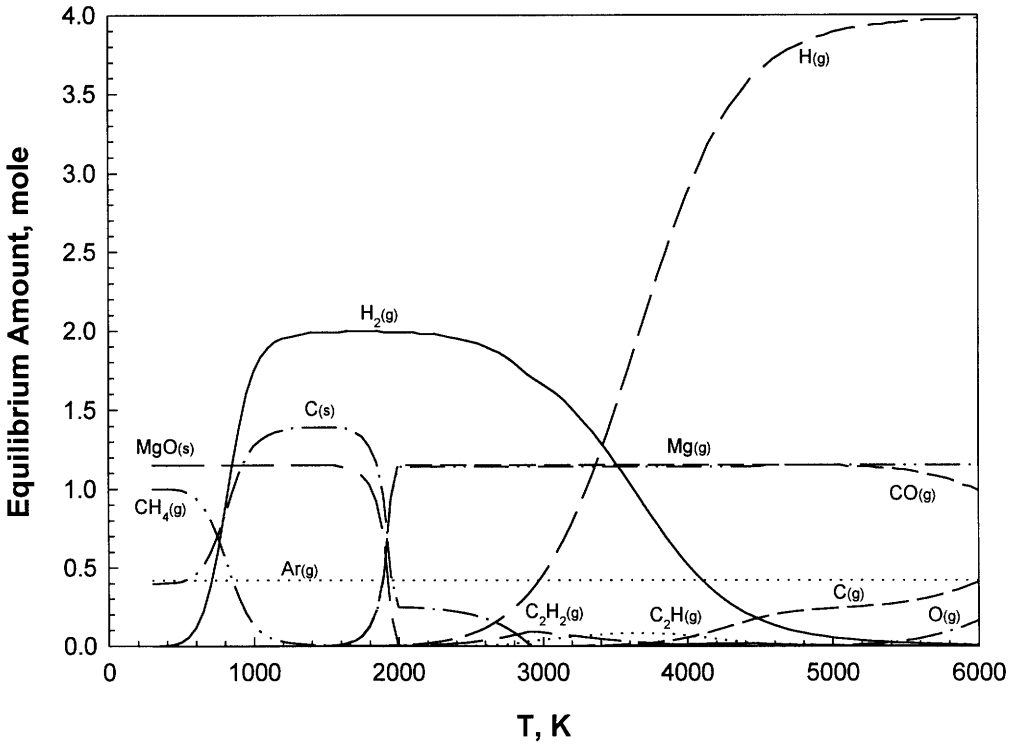

Figure 4-7. Thermodynamic Equilibrium Diagram for 1.15 MgO + 1 CH_4 + 0.4 C + 0.42 Ar

4.2 Mg-C-H-Ar System

The 0.7 Mg + 1 CH_4 + 0.42 Ar system was also investigated in the plasma reactor to test the feasibility of carbide formation in the absence of oxygen. The thermodynamic equilibrium diagram for this system is presented in Figure 4-8. As in the analysis of the

Mg-C-H-O-Ar system, the formation of Mg_2C_3 and MgC_2 is found not to be thermodynamically favored even in the absence of oxygen. Reactions (4-8) to (4-10) in the 0.46 MgO + 1 CH_4 + 0.42 Ar reaction system are also possible reactions pathways for atomic carbon depletion in this system. However, without oxygen, the C_2, C_2H and C_2H_2 species are more abundant. In addition, C_3 starts to form at around 5200 K according to:

$$C_{(g)} + C_{2\,(g)} \rightarrow C_{3\,(g)} \qquad \text{Reaction (4-15)}$$

and solid carbon formation begins at a higher temperature of 3350 K.

Based on the experimentally observed products composed of H_2, solid C and Mg, with small amounts of other hydrocarbon species, the probable quenching temperature window is a much wider. The equilibrium diagram shows that the product mix and composition are relatively invariant from 2400 K down to 1400K. Thus, the plasma effluent was presumably quenched somewhere in this temperature range.

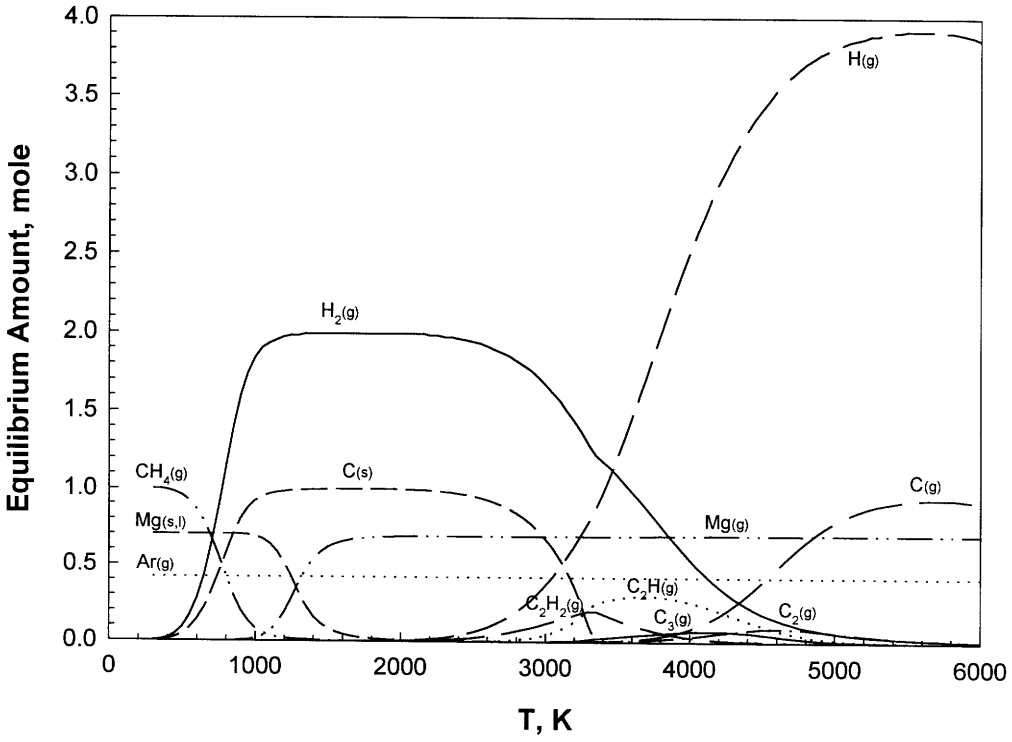

Figure 4-8. Thermodynamic Equilibrium Diagram for 0.7 Mg + 1 CH_4 + 0.42 Ar

4.3 Ca-C-H-O-Ar System

The equilibrium calculation results for the 0.34 CaO + 1 CH_4 + 0.42 Ar reaction system significantly differ from those of the previous MgO systems with the formation of a solid carbide phase. The thermodynamic equilibrium diagram for this system is shown in Figure 4-9. According to this diagram, solid calcium carbide starts to form at 2700 K via:

$$Ca_{(g)} + 2\,C_{(s)} \rightarrow CaC_{2\,(s)} \qquad \text{Reaction (4-16)}$$

But at 2000 K, the carbide starts to decompose according to:

$$CaC_{2\,(s)} + CO_{(g)} \rightarrow 3\,C_{(s)} + CaO_{(s)} \qquad \text{Reaction (4-17)}$$

which is complete at 1700 K.

Experimental results show that the products of this system are composed of CaC_2, CO, H_2, C_2H_2 and non-carbide C. Furthermore, compared to the Mg-C-H-O-Ar system, the product selectivity of this system is higher in that no other hydrocarbon species are detected even in minute quantities. The average extents of conversion are 39% for CH_4 "C" to CaC_2, 38% for CH_4 "C" to CO, 11% for CH_4 "C" to C_2H_2, 80% for CH_4 "H" to H_2, 17% for CH_4 "C" to non-carbide C and 58% for CaO "Ca" to CaC_2. These experimentally observed extents of conversion suggest a quenching temperature in the 2800 to 2200 K range.

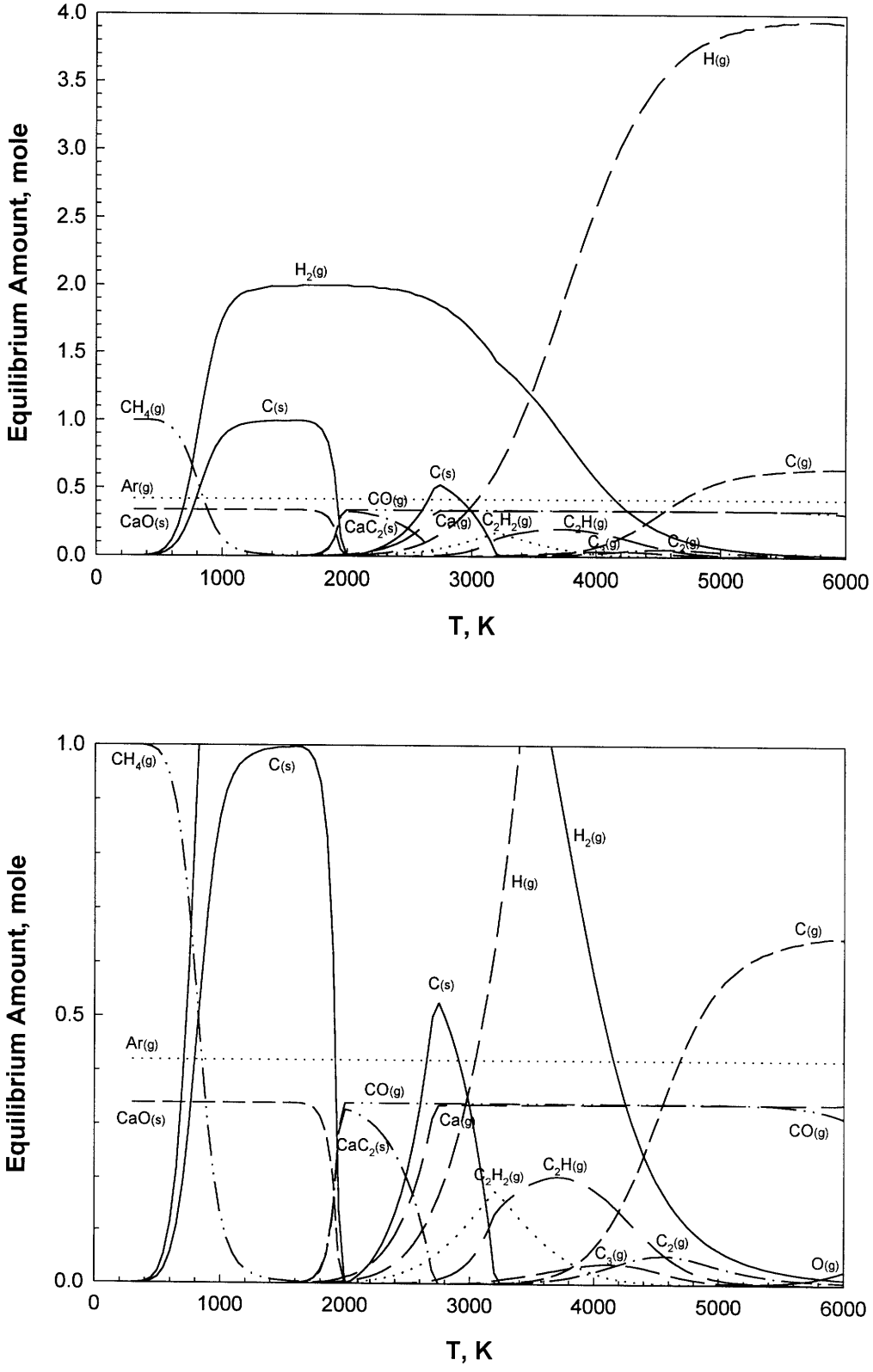

Figure 4-9. Thermodynamic Equilibrium Diagram for 0.34 CaO + 1 CH_4 + 0.42 Ar

That solid carbon is more thermodynamically favored to form starting at 3200 K before CaC_2 is noteworthy. The formation of carbon in the solid phase in this system is represented by Reactions (4-13) and (4-14). Pfender and Chang (1987) have postulated that solid carbon will not form from C_2H at temperatures down to 2000 K according to Reaction (4-13) and will not form at all from C_2H_2 according to Reaction (4-14). This is because the log K_p for Reaction (4-13) is only 1.17 at 2500 K and 2.8 at 2000 K while the log K_p for Reaction (4-14) is -5.48 at 2000 K and -8.28 at 1500 K (Chang and Pfender, 1987). Homogenous nucleation from the gas phase occurs appreciably only when the supersaturation ratio S exceeds a critical value. With S proportional to the equilibrium constant K_p for a deposition reaction, a higher log K_p would entail a higher S. Thus, they used log K_p for predicting precipitation at various temperatures.

Using classical nucleation theory, Chang and Pfender (1987) proposed a modification to the standard technique of Gibbs free energy minimization for predicting the composition of products from thermal plasma reactions to account for the dominating effect of nucleation kinetics which is a non-equilibrium effect. In their approach, species with low supersaturation pressures are considered unlikely to precipitate and are excluded from the calculations. The nucleation rate of liquid droplets from the supersaturated vapor is dependent on temperature and on surface energy. For inorganic solids with surface energies on the order of 10^3 ergs/cm^2, production of droplets requires a supersaturation ratio as high as 10^5 (Hecht *et al.*, 1980). Thus, they used a log K_p of 5 as a criterion for powder formation from deposition reactions.

Applying this technique to the Ca-C-H-O-Ar system, the formation of solid carbon is suppressed by eliminating this species altogether in the equilibrium calculations. Figure 4-10 shows the quasi-equilibrium diagram of the system without free carbon formation. Calcium carbide can start to form at 3000 K through:

$$Ca_{(g)} + C_2H_{2\,(g)} \rightarrow CaC_{2\,(s)} + H_{2\,(g)} \qquad \text{Reaction (4-18)}$$

$$Ca_{(g)} + C_2H_{(g)} \rightarrow CaC_{2\,(s)} + H_{(g)} \qquad \text{Reaction (4-19)}$$

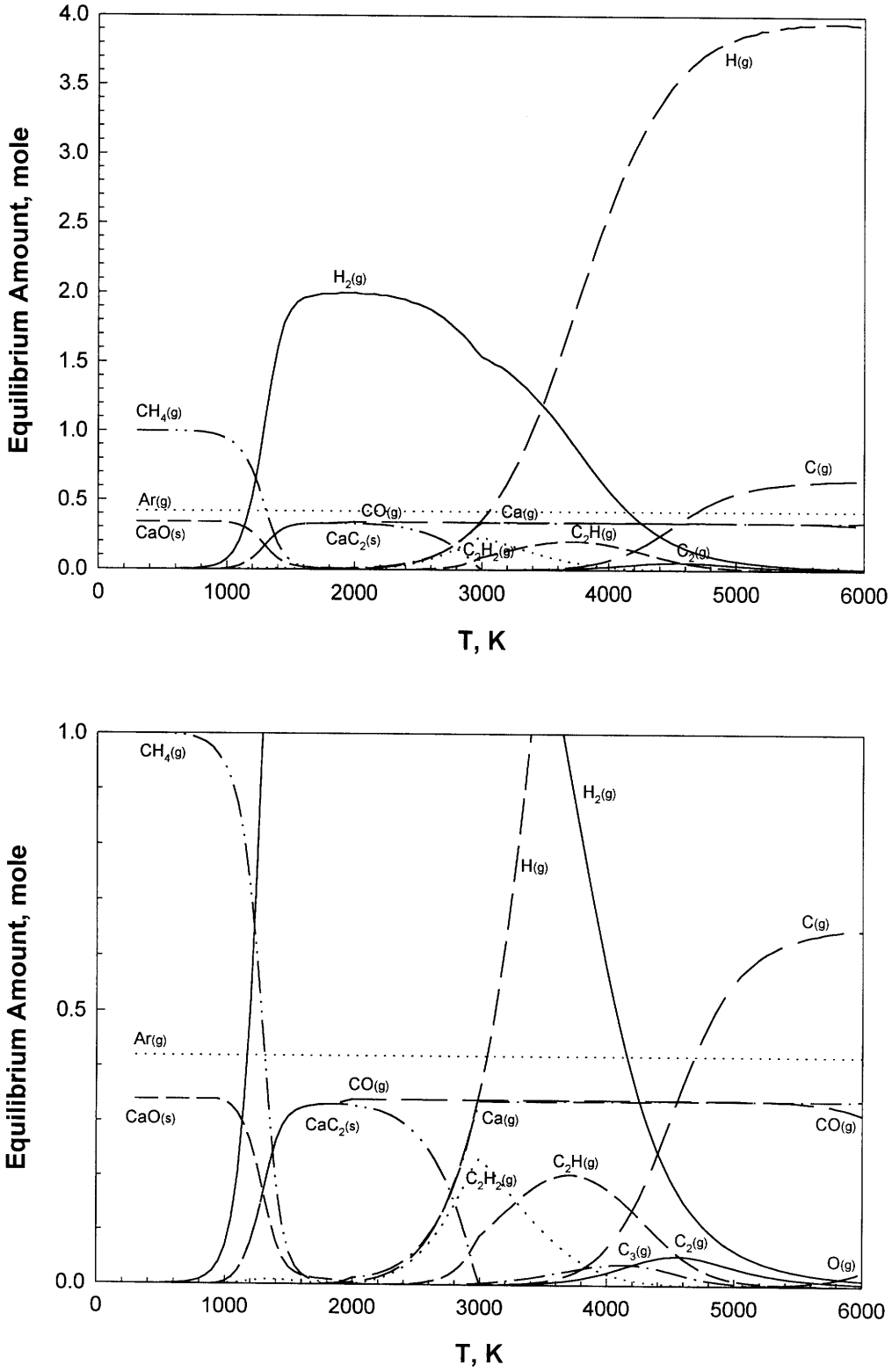

Figure 4-10. Thermodynamic Equilibrium Diagram for 0.34 CaO + 1 CH_4 + 0.42 Ar with Solid Carbon Formation Suppressed

The calculated log K_p values for Reaction (4-18) are 1.76 at 3000 K, 3.22 at 2500 K and 5.46 at 2000 K. Those for Reaction (4-19) are 1.54 at 3000 K, 3.05 at 2500 K and 5.38 at 2000 K. Therefore, CaC_2 should be able to form and nucleate via the above reactions at temperatures from 3000 K down to as low as 1500 K. In contrast to the conventional equilibrium calculations, the backward reaction of CaC_2 with CO through Reaction (4-17) does not occur until the temperature is down to about 1400 K. The proposed quenching temperature range is not significantly affected, as the yields of CaC_2, CO, H_2 and C_2H_2 would still match the quasi-equilibrium amounts in the 2800 to 2000 K temperature range.

4.4 Mg-Ca-C-H-O-Ar System

The thermodynamic equilibrium diagram for the 0.2 MgO + 0.2 CaO + 1 CH_4 + 0.42 Ar reaction system in Figure 4-11 shows that a combined MgO-CaO feed in a methane plasma reaction system will have a combined product stream of Mg, CaC_2, CO and H_2. Neither Mg_2C_3 nor MgC_2 is favored to form in this system. MgO can start to form at the expense of Mg and CO at 2000 K as represented by Reaction (4-7). Similarly, CaO can form at the expense of CaC_2 and CO at 2000 K as represented by Reaction (4-17). However, the formation of CaO occurs over a much narrower temperature range than the formation of MgO. The reaction of CaC_2 with CO is complete at 1900 K whereas Mg is fully converted to MgO only at 1500 K. Thus, Mg appears to be even more stable than CaC_2 in the presence of CO below 2000 K. A probable non-equilibrium explanation for the experimentally observed higher CaC_2 stability relative to Mg in the presence of CO is a possibly much slower rate of the heterogeneous reverse reaction of CaC_2 with CO according to Reaction (4-17) compared to the homogeneous backward reaction of Mg with CO via Reaction (4-7).

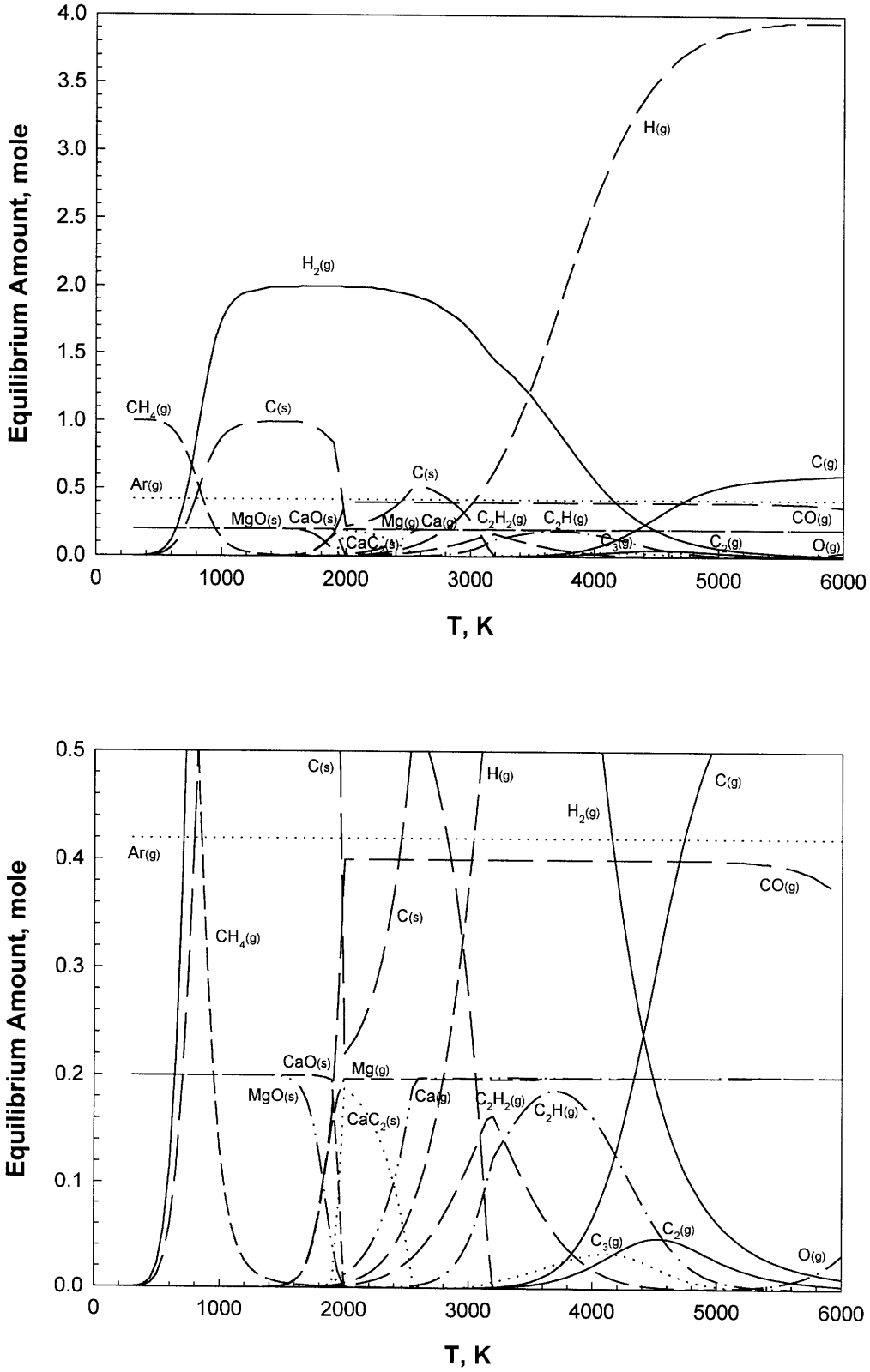

Figure 4-11. Thermodynamic Equilibrium Diagram for 0.2 MgO + 0.2 CaO + 1 CH_4 + 0.42 Ar

The formation of solid carbon at 3200 K from C_2H_2 and C_2H again precedes the formation of the solid calcium carbide phase, as in the previous system. Applying Chang and Pfender's approach, the quasi-equilibrium diagram of the same system with carbon formation suppressed is shown in Figure 4-12. The depletion of Mg by reaction with CO starts at a much lower temperature of 1800 K and is complete at 1500 K. On the other hand, the formation of CaC_2 commences at 2900 K and its backward reaction with CO begins only at 1500 K (when all the Mg has been converted to MgO), reaching completion at 1000 K.

Experimentally, the observed average extents of CH_4 "C" conversion are 47% to CO, 19% to CaC_2, 6% to C_2H_2, 10% to non-carbide C and 1% to Mg_2C_3. The mean CH_4 "H" conversion to H_2 is 91%. The CaO "Ca" conversion to CaC_2 is 47% and the MgO "Mg" conversion to Mg is 65%, on average. Based on Figure 4-12, this product composition would correspond to a temperature range of 2000 to 1600 K. The plasma effluent is therefore believed to be quenched down to room temperature from this temperature range.

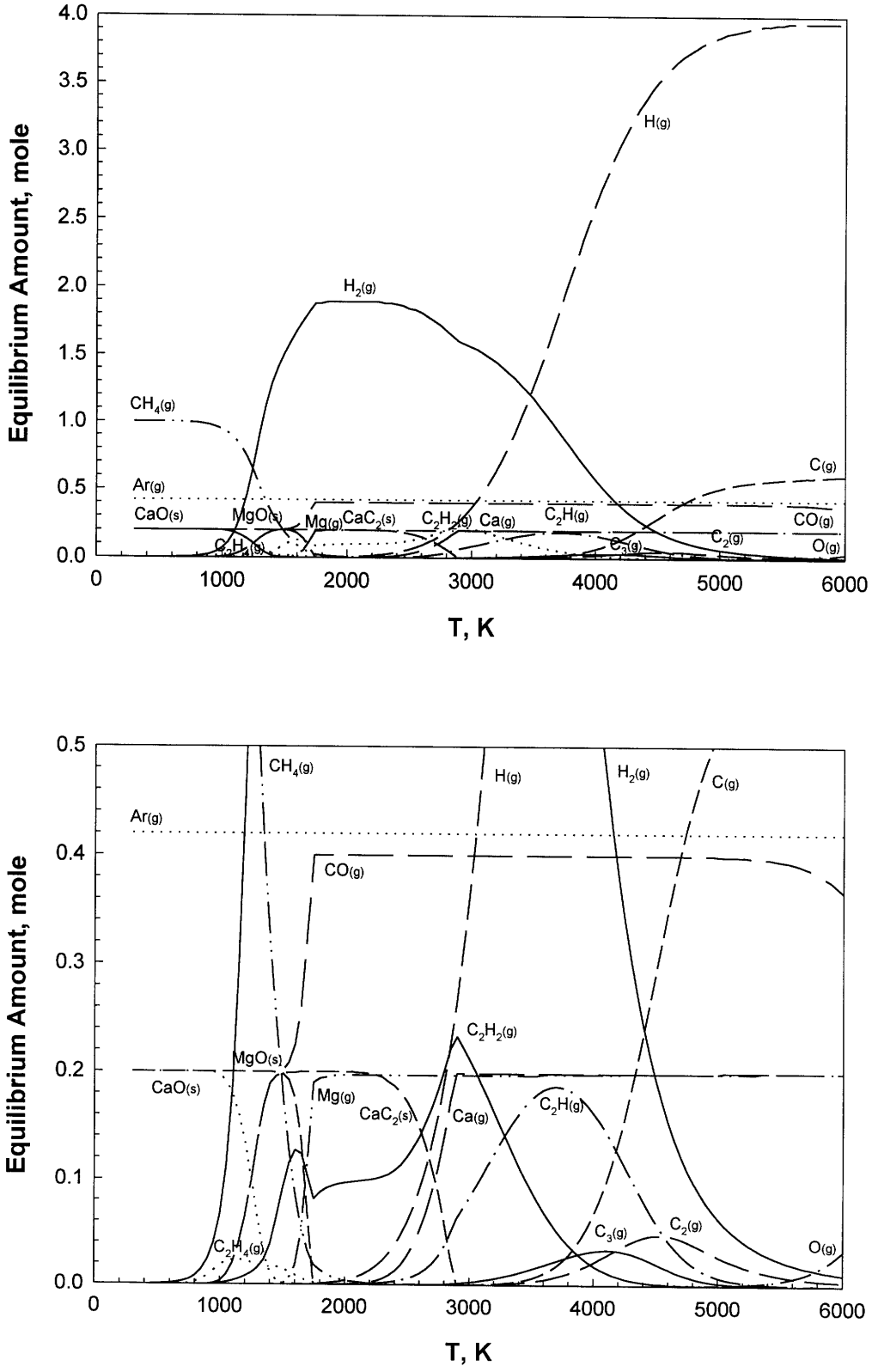

Figure 4-12. Thermodynamic Equilibrium Diagram for 0.2 MgO + 0.2 CaO + 1 CH_4 + 0.42 Ar with Solid Carbon Formation Suppressed

4.5 Accuracy and Sensitivity Analysis of Thermodynamic Calculations

The accuracy of the thermodynamic analysis was assessed by comparison with well-established equilibrium calculations. Equilibrium composition calculations using HSC Chemistry were benchmarked against the calculations of Chang and Pfender (1987) on the $2CH_4 \rightarrow C_2H_2 + 3H_2$ reaction system. Chang and Pfender used a modified program based on SOLGASMIX (Besmann, 1977). Quasi-equilibrium calculations for the case where solid carbon formation is suppressed were also performed. The results of these calculations using HSC Chemistry, shown in Figures 4-13 and 4-14, are found to be virtually identical to the results of Chang and Pfender (1987). The original plots of Chang and Pfender can be found in Ref. 9.

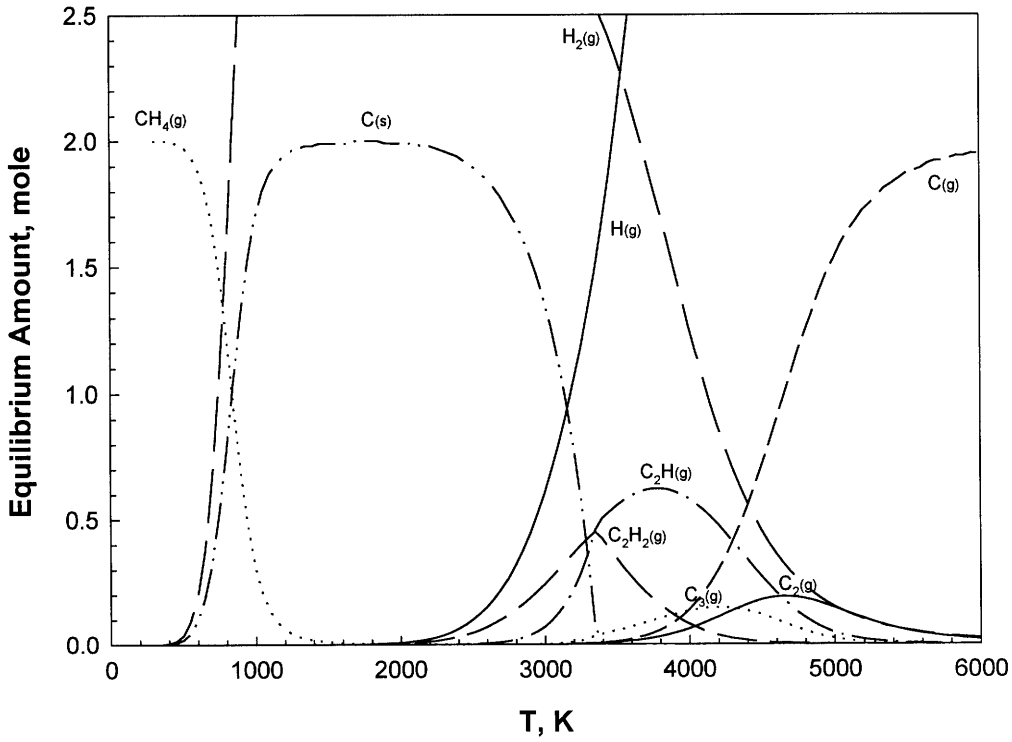

Figure 4-13. Thermodynamic Equilibrium Diagram for $2\ CH_4 \rightarrow C_2H_2 + 3\ H_2$

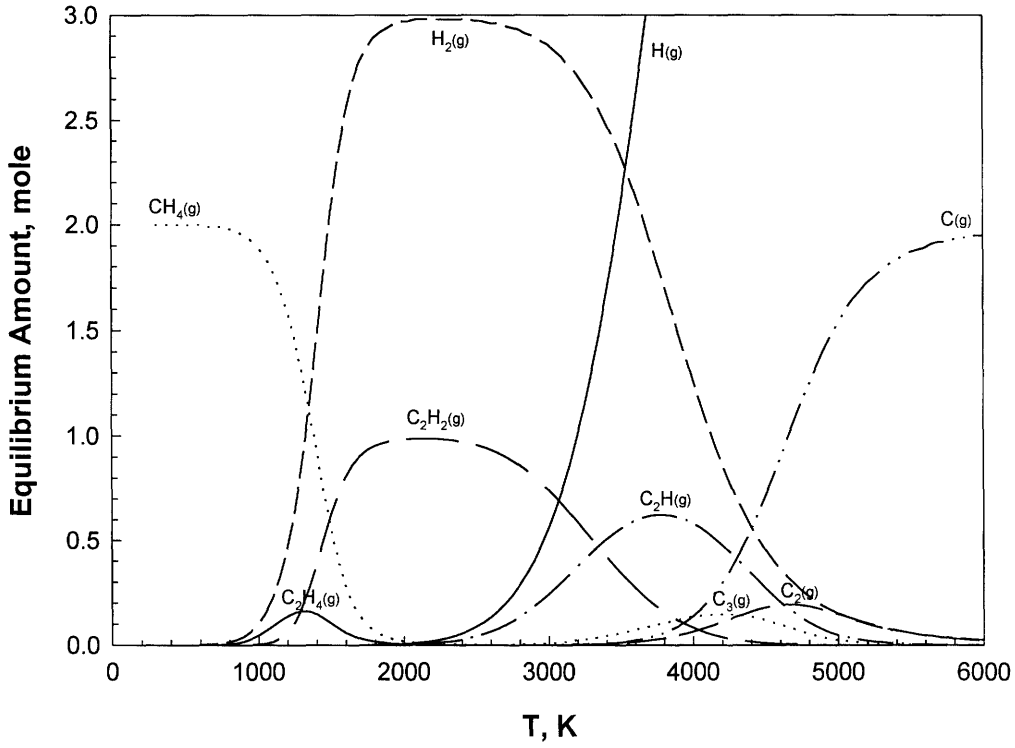

Figure 4-14. Thermodynamic Equilibrium Diagram for 2 $CH_4 \rightarrow C_2H_2 + 3\ H_2$ with Solid Carbon Formation Suppressed

To the extent that thermodynamic properties of the different species in the reaction systems of interest have uncertainties, a sensitivity analysis of the equilibrium calculations to these thermodynamic properties would help in establishing a level of confidence for interpretation of the results. A simple sensitivity analysis of the equilibrium calculations for the 0.46 MgO + 1 CH_4 + 0.42 Ar reaction system to the standard heat of formation of MgO, $\Delta H_{f,MgO}$, was performed to gain an insight on the robustness of these calculations. The standard heat of formation of MgO at 298.15 K, $\Delta H^{o}_{f,MgO}$ (298.15 K), is reported as -601.241 kJ/mol with an uncertainty of ± 0.63 kJ/mol or about 0.1% (JANAF Tables, 1985). Equilibrium calculations were carried out using heats of formation of MgO at 298.15 K that are 10% below and 10% above this standard value over the 6000 to 300 K temperature range. The resulting equilibrium diagrams are presented in Figures 4-15 and 4-16. The baseline diagram for comparison is Figure 4-6.

In Figure 4-6, the temperature window for the backward reaction of Mg with CO to form MgO and C is 1900-1600 K. In Figure 4-15 where $\Delta H_{f,MgO}(298.15K) = 0.9\Delta H^{o}_{f,MgO}(298.15K)$, this temperature window was shifted down to 1700-1400 K, whereas in Figure 4-16 where $\Delta H_{f,MgO}(298.15K) = 1.1\Delta H^{o}_{f,MgO}(298.15K)$, the window was shifted up to 2100-1800 K. Thus, the 10% change in standard heat of MgO formation resulted in shifts of the equilibrium composition in both directions by about 200 K. These shifts would entail significantly different postulated quenching temperatures. Thus, although the reported uncertainties in the standard heat of formation of MgO are actually two orders of magnitude smaller, the results of this sensitivity analysis should serve as a caution and should be kept in mind when interpreting any thermodynamic equilibrium calculation results.

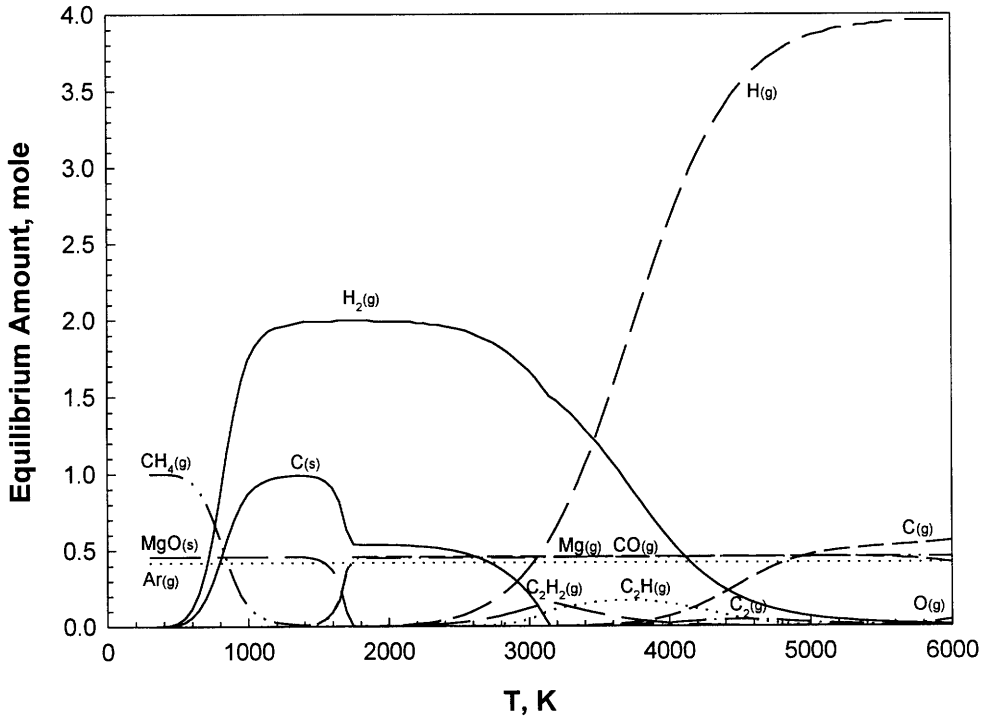

Figure 4-15. Thermodynamic Equilibrium Diagram for 0.46 MgO + 1 CH_4 + 0.42 Ar with $\Delta H_{f,MgO}(298.15K) = 0.9\,\Delta H^{o}_{f,MgO}(298.15K)$

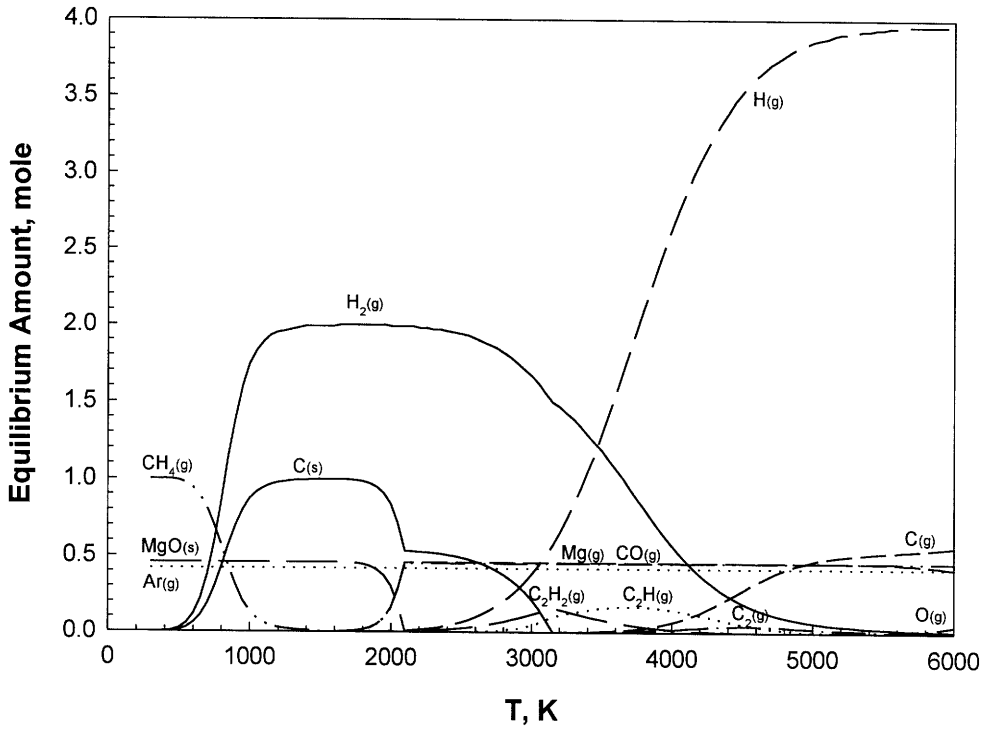

Figure 4-16. Thermodynamic Equilibrium Diagram for 0.46 MgO + 1 CH_4 + 0.42 Ar with $\Delta H_{f,MgO}$ (298.15K) = 1.1 $\Delta H^{o}_{f,MgO}$ (298.15K)

Chapter 5

Mechanistic Interpretation and Practical Implications

A mechanism for the formation of magnesium metal from the overall reaction of MgO with CH_4, depicted in Figure 5-1, is proposed in order to shed some light on the complex physico-chemical nature of the plasma reaction. The mechanism is deduced from experimental observations, thermodynamic analysis and mass transfer considerations. Since plasma temperatures may exceed 10^4 K, the assumption of full vaporization of reactants into atomic species is justified as long as the reactants have sufficient residence time in the plasma reactor (Chang and Pfender, 1987). For the present reactor system, residence times have been estimated to be on the order of 2 to 5 ms. These estimates are based on assumptions of an average gas temperature of 6000 K, complete conversion of the methane reactant to hydrogen and a reactor volume consisting of the 3-in. long, 1-in. diameter cylindrical volume from the base of the cathode tip to the anode nozzle exit.

Chemical reactions are considered to proceed as the reaction system cools down from 6000 K to below 1000 K. Although an electrical arc discharge generates free electrons and ions (in addition to neutral radicals) which have a higher chemical potential than the original reactants, the proposed mechanism does not explicitly include these species because most atomic gases are not sufficiently ionized below 6000 K.

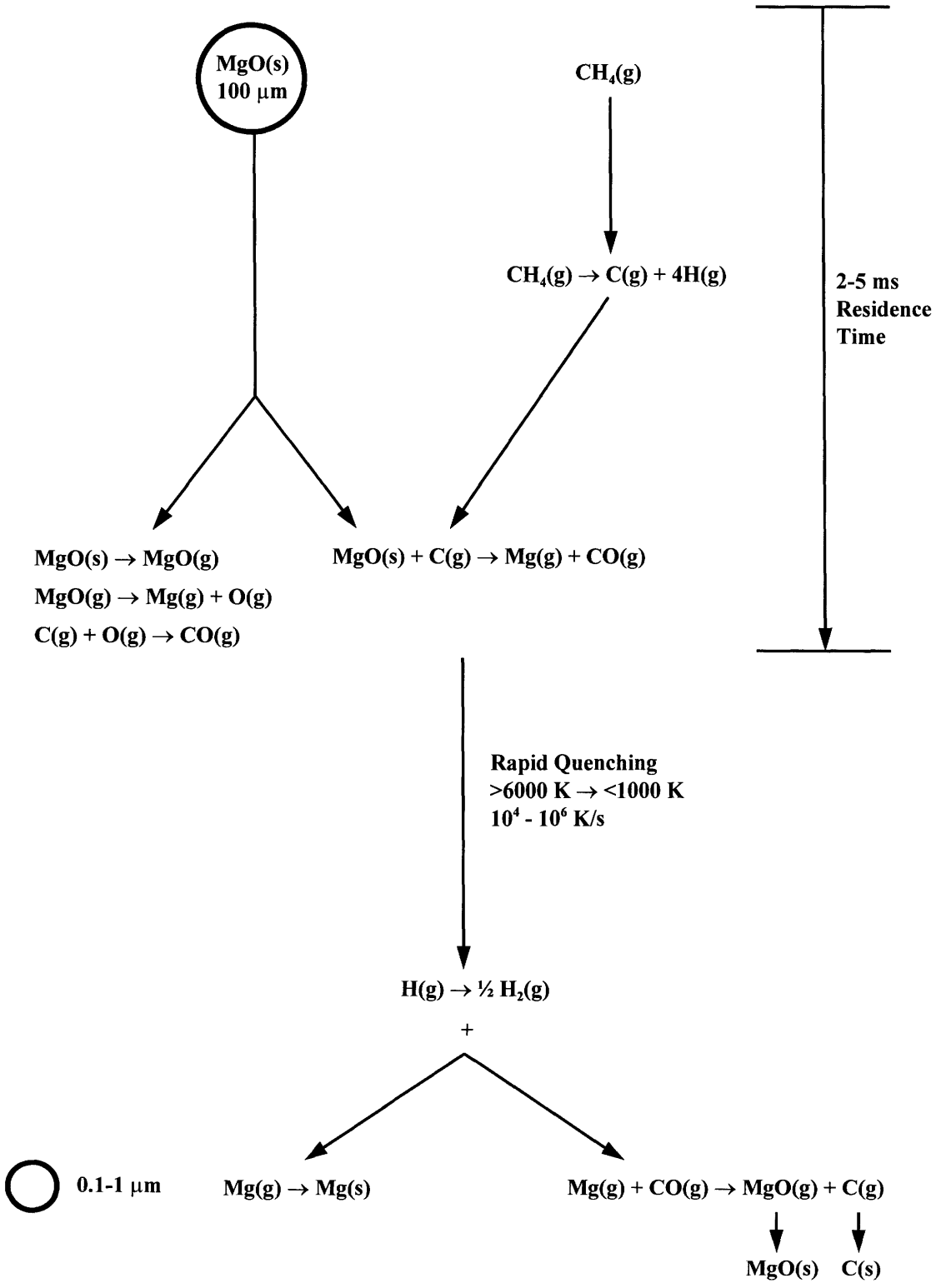

Figure 5-1. Proposed Overall Mechanism for Mg Formation

As the reaction system exits the anode nozzle, it is rapidly quenched from plasma temperatures by expansion into the cooling chamber and with the application of Argon quench gas at the tip of the sample collection probe. Quenching rates for this system have been estimated to be on the order of 10^4 to 10^6 K/s. The contribution of the Argon quench gas injected at the probe tip is not expected to be significant because solid products collected from the chamber walls and bottom show indications of magnesium metal content comparable to samples collected through the probe.

5.1 Reactant Evaporation and Decomposition

The gaseous methane reactant, upon introduction into the electric arc discharge, absorbs energy through inelastic collisions which is channeled into the instantaneous production of atomic, radical and ionic species. With plasma temperatures above 10^4 K, methane is dissociated into atomic C and H species, according to the following path:

$$2\,CH_4 \rightarrow C_2H_6 + H_2 \rightarrow C_2H_4 + H_2 \rightarrow C_2H_2 + H_2 \rightarrow 2\,C + H_2 \qquad \text{Reaction (1-24)}$$

which is very rapid at temperatures above 1500 K.

The initiation step of methane decomposition follows one or both of the following reactions (Chen *et al.*, 1975):

$$CH_4 \rightarrow CH_3 + H \qquad \Delta H_{298\,K} = 435\ \text{kJ} \qquad \text{Reaction (1-25)}$$

$$CH_4 \rightarrow CH_2 + H_2 \qquad \Delta H_{298\,K} = 464\ \text{kJ} \qquad \text{Reaction (1-26)}$$

The CH_3 and CH_2 radicals are transient species and do not exist in significant quantities in thermodynamic equilibrium even at temperatures substantially greater than 2000 K. When allowed to reach thermodynamic equilibrium, the reaction mixture ultimately decomposes to C and H_2. Chen *et al.* (1975) calculated the overall activation energy in the pressure-independent region based on Rice-Ramsperger-Kassel-Marcus (RRKM)

theory to be 448 kJ/mol assuming that the initiation step is Reaction (1-25). Kim (1977) postulated that the presence of a critical specific gas energy in his experiments corresponds to the activation energy of the initiation step of methane decomposition when an outburst of atoms and free radicals of carbon and hydrogen occurs. The high enthalpy but thermodynamically unstable species thus liberated then diffuse to the solid particles to form more stable species by recombination or decomposition or by direct reaction with CaO to form CaC_2.

Although no analogous critical specific gas energy for magnesium metal formation was observed in the present study, the calculated specific gas energies of more than 1500 kJ/g atom C nevertheless exceed the overall activation energy for methane decomposition. Thus, there is more than sufficient energy in the electric discharge for methane decomposition.

For the 100 μm MgO particles, two possible pathways for decomposition are considered. Upon introduction into the plasma, the oxide particles are heated very rapidly. MgO can vaporize in the plasma environment and then dissociate into its constituent atomic species, Mg and O:

$MgO_{(s)} \rightarrow MgO_{(g)}$			Reaction (5-1)
$MgO_{(g)} \rightarrow Mg_{(g)} + O_{(g)}$			Reaction (5-2)
$MgO_{(s)} \rightarrow Mg_{(g)} + O_{(g)}$		$\Delta H = 1{,}250$ kJ	Reaction (5-3)
298 K	6000 K		

The time scale for complete evaporation of a 100 μm MgO particle is evaluated assuming, for simplicity, that the particle is spherical and is at an average gas temperature of 6000 K. For vapor diffusion from an evaporating solid into the surrounding gas:

$$\frac{-1}{4\pi r^2}\frac{dN_{MgO}}{dt} = h\left(C_s - C_\infty\right) \qquad \text{Equation (5-1)}$$

where N_{MgO} is the number of moles of diffusing MgO vapor, r is the radius of the particle, t is time, h is the mass transfer coefficient and C is the concentration of the diffusing species. The subscripts s and ∞ refer to the surface of the particle and to infinite distance from the particle, respectively. The boundary conditions for this problem are $C_s = P_{MgO}/RT$ at $r = 50$ μm and $C_\infty = 0$ at $r = \infty$, where P_{MgO} is the partial pressure of MgO, taken to be 1 atm, R is the universal gas constant and T is the temperature.

Substituting $\rho(4\pi r^3/3)/M$ for N_{MgO}, where ρ is the density of MgO, $4\pi r^3/3$ is the volume of a spherical particle with radius r and M is the molecular weight of MgO, Equation (5-1) reduces to:

$$-\frac{\rho}{M}\frac{dr}{dt} = h\left(C_s - C_\infty\right) \qquad \text{Equation (5-2)}$$

For droplet evaporation, Ranz and Marshall (1952), whose experiments were confined to Reynolds numbers of 0-200, give the following correlation:

$$\frac{hd}{D} = 2.0 + 0.6N_{\mathrm{Re}}^{1/2}N_{Sc}^{1/3} \qquad \text{Equation (5-3)}$$

where d is the diameter of the droplet, D is the binary diffusion coefficient, N_{Re} is the Reynolds number and N_{Sc} is the Schmidt number. When particles are injected into a plasma jet, the particles are initially accelerated but, as the velocity of the plasma jet decays, the particle velocity will exceed the velocity of plasma flow due to inertia. Between these two regimes, the particle and the plasma have a relative velocity that approaches zero (Chen and Pfender, 1982). Thus, N_{Re} can be taken as zero and Equation (5-3) simplifies to:

$$\frac{hd}{D} = 2.0 \qquad \text{Equation (5-4)}$$

The binary diffusion coefficient, D, can be evaluated for a mixture of MgO and H_2 according to the equation developed by Fuller *et al.* (1966):

$$D_{A-B} = \frac{1.013x10^{-7}\, T^{1.75}\left(\frac{1}{M_A}+\frac{1}{M_B}\right)^{1/2}}{P\left[\left(\sum_A v_i\right)^{1/3}+\left(\sum_B v_i\right)^{1/3}\right]^2} \qquad \text{Equation (5-5)}$$

where D_{A-B} = binary diffusivity of a vapor mixture of species A and B, m^2/s

T = temperature, K

M_A, M_B = molecular weights of species A and B

P = total pressure, bar

$\sum_A v_i$, $\sum_B v_i$ = summation of the special diffusion volume coefficients for A and B

Substituting Equation (5-4) in Equation (5-2) gives

$$-\frac{\rho}{M}\frac{dr}{dt} = \frac{D}{r}\left(C_s\right) \qquad \text{Equation (5-6)}$$

which, when integrated from $r = r_p = 50$ μm at $t = 0$ to $r = 0$ at $t = \tau_e$, the time scale for complete evaporation, results in:

$$\tau_e = \frac{r_p^2 \rho RT}{2DMP_{MgO}} \qquad \text{Equation (5-7)}$$

When appropriate values are substituted in Equation (5-7), the time for complete evaporation of a 100 μm spherical MgO particle, τ_e, is determined to be 4.3 ms. This time scale does not include the time required for additional processes such as initial heating or melting. For comparison, Chen and Pfender (1982) considered the effect of evaporation on the heat flux to a particle exposed to steady-state plasma conditions. For a 50 μm diameter particle exposed to an Argon plasma at 12,000 K, they reported a time

scale for complete evaporation of 41.5 ms for an alumina particle and 50.2 ms for graphite. Kitamura *et al.* (1992) studied steady-state heat conduction of a spherical particle in a uniform 10,000 K plasma and calculated the time scales for complete evaporation of a 100 μm diameter Fe_2O_3 particle to be 17.4 ms in an Ar plasma, 1.4 ms in an H_2 plasma and 2.1 ms in an N_2 plasma.

Given residence times on the order of 2 to 5 ms, a time scale of 4.3 ms would seem to be insufficient for complete evaporation of 100 μm MgO particles. Thus, MgO depletion according to the proposed pathway of vaporization followed by decomposition into atomic species is not likely to be significant. Rather than accounting for the MgO disappearance by evaporation, an alternative pathway for MgO consumption is by the heterogeneous reaction of C vapor with the solid MgO particles according to a shrinking particle model:

$$MgO_{(s)} + C_{(g)} \rightarrow Mg_{(g)} + CO_{(g)} \qquad \Delta H_{298\,K} = -79\ kJ \qquad \text{Reaction (5-4)}$$

The observations of higher magnesium yields upon doping of the MgO with graphite and of the inverse trends in CO and non-carbide C yields support this mechanism for magnesium vapor formation. The higher CH_4 "C" conversion to non-carbide C at higher CH_4 flow rates also suggests that the carbon vapor may not have sufficient residence time for reaction with the MgO. Since experimental observations from SEM and STEM analyses of solid samples from lower CH_4 flow rate runs do not show indications of unreacted MgO particles in the solid products collected, Reaction (5-4) is believed to go to completion under these conditions.

5.2 Nucleation and Growth of Magnesium Particles

The magnesium vapor formed by dissociation of MgO (Reaction (5-3)) and by MgO reaction with carbon vapor (Reaction (5-4)) is rapidly quenched from plasma temperatures greater than or equal to 6000 K down to 1000 K or lower, together with atomic carbon and hydrogen in the gaseous state. Any carbon vapor that did not have

sufficient residence time to react with the MgO or that was in stoichiometric excess would be precipitated as solid carbon. Any remaining H atoms, on the other hand, once quenched, would rapidly react to form molecular hydrogen. CO is postulated to form primarily via Reaction (5-4), although some of it is also formed from its constituent atomic species above 6000 K, as suggested by the thermodynamic analysis. CO remains stable down to around 2000 K, when the backward reaction with Mg becomes favorable.

Rapid quenching of the plasma effluent is crucial to attaining the desired products particularly if the desired composition corresponds to equilibrium at high temperatures and is drastically different at low temperatures. The species which are stable at high temperatures may undergo undesirable transformations if cooled gradually to room temperature. The pyrolysis of methane for acetylene formation is a good example of how rapid quenching preserves the equilibrium composition corresponding to high temperatures. If the quenching rate is inadequate, the acetylene formed at high temperatures is transformed to carbon and hydrogen. Similarly, the magnesium metal vapor formed from the plasma reaction of MgO and CH_4 will be reoxidized by CO back to MgO and form C, if the reaction mixture were allowed to cool down gradually.

The rapid quenching of the plasma product species in the vapor state gives rise to a high supersaturation, which, in turn, leads to homogeneous nucleation (Granqvist *et al.*, 1976). Since nucleation rates increase very sharply with decreasing temperature, the particles produced will all solidify within a small temperature range (McPherson, 1973; Young and Pfender, 1985). The observation of high yields of magnesium in the solid products supports nucleation and condensation as the primary pathway for magnesium vapor depletion. Furthermore, STEM and SEM analyses which revealed submicron hexagonal magnesium crystals suggest that the magnesium particles were directly crystallized from the vapor phase. Crystallization in a cooling environment occurs at a temperature substantially below the solid melting point T_m (Young and Pfender, 1985). Turnbull (1950) experimentally found that the solidification temperature of a group of isolated particles is 0.82 T_m for a wide range of metals in the 10 to 1000 μm particle size range at slow cooling rates ($<10^3$ K/s). McPherson (1973) postulated a solidification temperature lower than 0.82 T_m for plasma-prepared particles which are subjected to

much higher quenching rates. This would suggest that the plasma effluent in the present study was quenched down to lower than 0.82(923 K) or 757 K.

For a decaying plasma containing only supersaturated vapor, homogeneous nucleation will occur. However, even in the presence of heterogeneous nuclei or remaining condensed material that can act as condensation sites, homogeneous nucleation is still the dominant mechanism for particle formation from vapor phase reactions, (Young and Pfender, 1985; Chang and Pfender, 1987). Heterogeneous nucleation would occur to some extent, as was observed by Kong *et al.* (1986) in the thermal cracking of methane in a free-burning Argon arc. With pure methane injection, the carbon product was amorphous but, with the addition of a small amount of graphite powder in the methane, only graphitic carbon was found.

In the case of homogeneous nucleation, Dahlin *et al.* (1981) and Chang and Pfender (1987) describe the particle formation process as a series of events. First, the gas-phase reaction proceeds until a critical supersaturation ratio is exceeded. Nucleation then occurs like a burst over a very short period of time (10^{-6} s). When nucleating species are depleted by diffusion to newly formed particles, the nucleation terminates and the particles continue to grow by physical condensation and particle coagulation.

Based on the STEM and SEM results, the magnesium particles are postulated to crystallize after nucleation from the supersaturated magnesium vapor. These particles then grow by condensation of vapor as well as of smaller particles on the surface of larger particles. The observations of tiny scale-like particles on the surface of larger hexagonal crystals are consistent with this proposed sequence.

The time scale for nucleation and growth of magnesium particles from the vapor, which represents the first of two pathways for metal vapor depletion presented in Figure 5-1, is considered here. The second path which involves reoxidation by CO will be discussed in the next section.

The rate of homogeneous nucleation depends on the net number of molecular clusters per unit time that grow beyond a critical nucleus size. At this critical size, the cluster's growth rate equals its decay rate. Clusters that grow larger than the critical nucleus are likely to grow to macroscopic size while those smaller than the critical size

tend to evaporate. The critical nucleus size, d_c, is given by the Kelvin relation (Friedlander, 1977):

$$d_c = \frac{4\sigma v}{RT \ln \frac{P_i}{P_v}} \qquad \text{Equation (5-8)}$$

where σ is the surface tension, v is the molar volume, R is the universal gas constant, T is temperature, P_i is the equilibrium vapor pressure of a drop of species i, taken to be equal to the partial pressure of i in the gas mixture, and P_v is the vapor pressure of i above a flat surface.

The critical nucleus size, d_c, is now determined for magnesium nucleating from a supersaturated gas that is rapidly quenched to the metal melting point of 923 K. The gas is assumed to be composed of 25% Mg, 25% CO and 50% H_2, corresponding to complete reaction of stoichiometric inputs of MgO and CH_4. Thus, at a system pressure of 1 atm, P_i is 0.25 atm or 190 mm Hg. At the melting point, the surface tension of magnesium is 559 mN/m and the liquid density is 1.59 g/cm^3 (Smithells and Brandes, 1976). The vapor pressure of magnesium at 923 K is 2.75 mm Hg (Emley, 1966). Substituting these values into Equation (5-8) gives a critical nucleus size of 10.5 Å.

The time scale for a nucleus to reach this critical size is governed by gas phase kinetics. For a nucleating particle, the molar flux is equal to the root-mean-square (rms) velocity of the gas, v_{rms}, times the concentration, C, of the species in the gas phase corrected by a factor of 1/3 for the directional component of velocity resulting in effective collisions:

$$\frac{1}{A}\frac{dN}{dt} = \frac{1}{3} v_{rms} C \qquad \text{Equation (5-9)}$$

where N is the number of moles of nucleating species over a surface area A. Assuming a spherical nucleus and substituting $\rho(4\pi r^3/3)/M$ for N, $4\pi r^2$ for A, $\sqrt{3RT/M}$ for v_{rms}, and P_{Mg}/RT for C, where ρ is the density of Mg, $4\pi r^3/3$ is the volume of a spherical particle

with radius r, M is the molecular weight of Mg and P_{Mg} is the partial pressure of magnesium in the gas mixture, Equation (5-9) can be written as:

$$\frac{\rho}{M}\frac{\mathrm{d}r}{\mathrm{d}t} = \frac{1}{3}\sqrt{\frac{3RT}{M}}\frac{P_{Mg}}{RT} \qquad \text{Equation (5-10)}$$

Integrating Equation (5-10) from $r = 0$ at $t = 0$ to $r = d_c/2 = r_c$ at $t = \tau_n$, the time scale for nucleation, gives

$$\tau_n = \sqrt{\frac{3RT}{M}}\frac{\rho}{P_{Mg}}r_c \qquad \text{Equation (5-11)}$$

Solving for τ_n at 923 K and at $P_{Mg} = 0.25$ atm results in a time scale for nucleation of 3.2 x 10^{-8} s.

The growth of the particle beyond the critical nucleus size by condensation is controlled by diffusion. Analogous to the evaporation of a droplet, the diffusion of magnesium vapor to the growing spherical particle assumed to be at the metal melting point is described by:

$$\frac{\rho}{M}\frac{\mathrm{d}r}{\mathrm{d}t} = h\left(C_\infty - C_s\right) \qquad \text{Equation (5-12)}$$

where ρ is the density of magnesium, r is the radius of the particle, t is time, h is the mass transfer coefficient and C is the concentration of magnesium vapor. The subscripts ∞ and s refer to infinite distance from the particle and to the surface of the particle, respectively. The boundary conditions for this problem are $C_\infty = P_{Mg}/RT$ at $r = \infty$ and $C_s = 0$ at $r = r_p$. Equation (5-4) is used to determine h, assuming a zero relative velocity between the particle and the gas. The binary diffusion coefficient, D, is evaluated for a mixture of Mg and H_2 according to Equation (5-5).

Substituting Equation (5-4) in Equation (5-12) gives

$$\frac{\rho}{M}\frac{\mathrm{d}r}{\mathrm{d}t} = \frac{D}{r}\left(C_\infty\right) \qquad \text{Equation (5-13)}$$

Integrating Equation (5-13) from $r = r_c = 5.25$ Å at $t = \tau_n = 3.2 \times 10^{-8}$ s to $r = r_p = 0.5$ μm at $t = \tau_g$, the time for a magnesium particle to grow to a conservatively large diameter of 1 μm,

$$\tau_g = \left(\frac{r_p^2 - r_c^2}{2}\right)\frac{\rho RT}{DMP_{Mg}} + \tau_n \qquad \text{Equation (5-14)}$$

gives a total time scale of 4.7×10^{-6} s.

5.3 Backward Reaction of Mg Vapor with CO

The second pathway for magnesium vapor depletion is by the backward reaction with CO which, according to the thermodynamic analysis, starts at around 2000 K. Mechanistically, this involves the homogeneous reaction:

$$Mg_{(g)} + CO_{(g)} \rightarrow MgO_{(g)} + C_{(g)} \qquad \Delta H_{2000\,K} = 763\ kJ \qquad \text{Reaction (5-5)}$$

followed by rapid precipitation of the supersaturated MgO and C vapor:

$$MgO_{(g)} \rightarrow MgO_{(s)} \qquad \Delta H_{2000\,K} = -654\ kJ \qquad \text{Reaction (5-6)}$$

$$C_{(g)} \rightarrow C_{(s)} \qquad \Delta H_{2000\,K} = -717\ kJ \qquad \text{Reaction (5-7)}$$

The overall combined reaction of Reactions (5-5) to (5-7) is Reaction (4-7)

$$Mg_{(g)} + CO_{(g)} \rightarrow MgO_{(s)} + C_{(s)} \qquad \Delta H_{2000\,K} = -608\ kJ \qquad \text{Reaction (4-7)}$$

which is highly exothermic.

The experimental results suggest that the dominant pathway for magnesium vapor consumption is by nucleation and condensation and that the loss of magnesium via Reaction (5-5) is not as significant. The relative rates of these two pathways are now assessed. Having estimated τ_g, the time needed for a magnesium particle to grow to a maximum diameter of 1 μm, the extent of Reaction (5-5) can be determined during this time scale. If the nucleation and condensation kinetics are indeed faster the kinetics of Reaction (5-5), the magnesium vapor concentration at the end of τ_g should not be significantly different from the initial concentration of the supersaturated vapor.

The rate of the bimolecular homogeneous reaction of Mg with CO, dC_{Mg}/dt, is given by

$$-\frac{dC_{Mg}}{dt} = kC_{Mg}C_{CO} \qquad \text{Equation (5-15)}$$

where k is the rate constant, C_{Mg} is the concentration of magnesium vapor and C_{CO} is the CO concentration. For equimolar initial concentrations of Mg and CO, which correspond to a complete reaction of stoichiometric inputs of MgO and CH_4, Equation (5-15) simplifies to

$$-\frac{dC_{Mg}}{dt} = kC_{Mg}^2 \qquad \text{Equation (5-16)}$$

Integrating Equation (5-16) from $t = 0$ to $t = \tau_g$ yields

$$\frac{1}{C_{Mg,f}} - \frac{1}{C_{Mg,i}} = k\tau_g \qquad \text{Equation (5-17)}$$

where the subscripts f and i on C_{Mg} refer to the final and initial values, respectively.

The final magnesium vapor concentration, $C_{Mg,f}$, can be calculated from Equation (5-17) given $C_{Mg,i}$ and τ_g, if the rate constant k is known at the temperature of interest. The temperature dependence of k is given by the Arrhenius equation

$$k = Ae^{-E_a/RT} \qquad \text{Equation (5-18)}$$

where E_a is the activation energy. Although a literature search uncovered the work on the oxidation of magnesium with a CO/CO_2 mixture by several workers (Shafirovich *et al.*, 1992; Yuasa and Fukuchi, 1994; Fukuchi *et al.*, 1996), no experimentally determined values of the rate constant k for homogeneous Reaction (5-5) or Reaction (4-7) was found.

In the absence of empirical data on the kinetics of Reaction (5-5) or Reaction (4-7), k can be estimated from the kinetic theory of collisions. According to collision theory, the pre-exponential factor, A, corresponds to the collision frequency factor, z, multiplied by the steric factor, p, which represents the fraction of properly energized collisions with the geometry effective for chemical reaction (Benson, 1976; Laidler, 1987):

$$k = pze^{-E_a/RT} \qquad \text{Equation (5-19)}$$

For bimolecular reactions, the collision frequency factor, z_{AB}, for two unlike molecules A and B is given by

$$z_{AB} = N\pi d_{AB}^2 \left(\frac{8RT}{\pi\bar{\mu}_{AB}}\right)^{1/2} \qquad \text{Equation (5-20)}$$

where d_{AB} is the distance between the centers of mass of A and B in the collision complex, N is Avogadro's number and $\bar{\mu}_{AB} = M_A M_B/(M_A + M_B)$ is the reduced molar mass of the colliding pair.

As a first approximation, k is estimated with z, assuming p to be one and E_a to approach zero. The high exothermicity of Reaction (4-7) would justify the latter assumption. Such approximation then gives an upper limit for k. For the bimolecular reaction of Mg and CO, $d_{Mg\text{-}CO} = r_{Mg} + r_{CO} = 3.33$ Å where r_{Mg} is the atomic (covalent) radius of Mg = 1.45 Å (Gillespie *et al.*, 1986) and r_{CO} is the collision radius of CO = 1.8815 Å (Hirschfelder *et al.*, 1954). r_{CO} is taken as half the separation distance, σ, at which the Lennard-Jones potential is zero at an effective temperature of $\varepsilon/k = 100$ K, where ε is the depth of the well and k is Boltzmann's constant. At T = 2000 K, $z_{Mg\text{-}CO}$ is determined to be 3.8×10^{14} cm^3/mol-s. Substituting this value for k in Equation (5-17), $P_{Mg}/RT = 0.25$ atm/[R(2000 K)] for $C_{Mg,i}$ and 4.7×10^{-6} s for τ_g, the final magnesium partial pressure is estimated to be 9.2×10^{-5} atm. However, such an estimate implies that virtually all the magnesium vapor would react with CO within the time scale τ_g, contrary to experimental observations. For a τ_g of 4.7×10^{-6} s and an MgO "Mg" conversion to Mg of 60%, k would need to take on a value of 9.3×10^{10} cm^3/mol-s, which is four orders of magnitude lower than that predicted by collision theory. Therefore, the use of $z_{Mg\text{-}CO}$ to approximate k does not appear to be valid.

A much slower rate of reaction between Mg and CO is conceivable if the reaction is taking place in its pressure-dependent region where k is in the fall-off region and thus takes on a lower value. Furthermore, the steric factor p, or the fraction of effective collisions, is very likely to be less than 1. The colliding Mg and CO could be so energetic that the atoms and molecules simply fly apart before any reaction can occur.

A modified Lindemann scheme has been postulated to describe the collisional mechanism underlying Reaction (5-5). When a magnesium atom collides with a CO molecule, an energized adduct, Mg-O-C*, is formed. This adduct can re-dissociate or collide with a third body M, which may be Mg, CO, H_2 or even the adduct Mg-O-C* itself, to form MgO and C.

$$Mg + CO \xrightarrow{k_1} Mg\text{-}O\text{-}C^* \qquad \text{Reaction (5-8)}$$

$$Mg\text{-}O\text{-}C^* \xrightarrow{k_{-1}} Mg + CO \qquad \text{Reaction (5-9)}$$

$$\text{Mg-O-C*} + \text{M} \xrightarrow{k_2} \text{MgO} + \text{C} + \text{M} \qquad \text{Reaction (5-10)}$$

where k_1, k_{-1} and k_2 are rate constants for Reaction (5-8) to (5-10), respectively. The essential step here is that both the energy of the adduct and the bond dissociation energy of CO has been transferred to M and to MgO in Reaction (5-10). Applying a pseudo-steady state treatment to this mechanism yields

$$\frac{dC_{Mg-O-C^*}}{dt} = k_1 C_{Mg} C_{CO} - k_{-1} C_{Mg-O-C^*} - k_2 C_{Mg-O-C^*} C_M = 0 \qquad \text{Equation (5-21)}$$

where $C_{Mg\text{-}O\text{-}C^*}$ is the concentration of the Mg-O-C* adduct and C_M is the concentration of species M. Solving Equation (5-21) for $C_{Mg\text{-}O\text{-}C^*}$ leads to

$$C_{Mg-O-C^*} = \frac{k_1 C_{Mg} C_{CO}}{k_{-1} + k_2 C_M} \qquad \text{Equation (5-22)}$$

The rate of disappearance of magnesium vapor is given by

$$-\frac{dC_{Mg}}{dt} = k_2 C_{Mg-O-C^*} C_M = \frac{k_1 k_2 C_{Mg} C_{CO} C_M}{k_{-1} + k_2 C_M} \qquad \text{Equation (5-23)}$$

With equimolar Mg and CO initial concentrations, Equation (5-23) simplifies to

$$-\frac{dC_{Mg}}{dt} = \frac{k_1 k_2 C_{Mg}^2 C_M}{k_{-1} + k_2 C_M} \qquad \text{Equation (5-24)}$$

When C_M is sufficiently large, $k_2 C_M \gg k_{-1}$, the overall rate is controlled by the rate of formation of the adduct which is rapidly de-energized and Equation (5-24) is reduced to Equation (5-16) for bimolecular collisions. On the other hand, when the pressure is sufficiently low, $k_{-1} \gg k_2 C_M$,

$$-\frac{dC_{Mg}}{dt} = \frac{k_1 k_2}{k_{-1}} C_{Mg}^2 C_M = K_1 k_2 C_{Mg}^2 C_M \qquad \text{Equation (5-25)}$$

with an apparent trimolecular rate constant, $k_r = K_1 k_2$ where K_1 is the equilibrium constant for the formation of Mg-O-C* from Mg and CO. Integrating Equation (5-25) from $t = 0$ to $t = \tau_g$ assuming C_M is constant yields

$$\frac{1}{C_{Mg,f}} - \frac{1}{C_{Mg,i}} = k_r C_M \tau_g \qquad \text{Equation (5-26)}$$

where the subscripts f and i on C_{Mg} refer to the final and initial values, respectively.

Analogous to the previous analysis with bimolecular collisions, the collision frequency factor, z_{ABC}, for molecules A, B and C can be used to estimate the trimolecular rate constant, k_r. Assuming a steric factor of unity and a zero activation energy would again give an upper limit for the rate constant. For most trimolecular reactions, very small, zero or even negative Arrhenius activation energies are found experimentally, validating the assumption of unit exponential term (Moore and Pearson, 1981). However, for a three-body collision, the hard sphere assumption has to be relaxed because the probability of having simultaneous contact of the spherical surfaces of three molecules is zero. For a finite number of trimolecular collisions, a collision may be assumed to consist of the approach of rigid spheres to within some arbitrary distance of each other. The collision number is then given by

$$z_{ABC} = 8N^2 \left(\pi d_{AB}^2\right)\left(\pi d_{BC}^2\right)\delta\left(\frac{2RT}{\pi}\right)^{1/2}\left[\left(\frac{1}{\bar{\mu}_{AB}}\right)^{1/2} + \left(\frac{1}{\bar{\mu}_{BC}}\right)^{1/2}\right] \qquad \text{Equation (5-27)}$$

for collision among A, B and C such that A and C are within a distance δ of B, where d_{AB} is the collision diameter of A and B, d_{BC} is the collision diameter of B and C, and $\bar{\mu}_{AB} = M_A M_B/(M_A + M_B)$ and $\bar{\mu}_{BC} = M_B M_B/(M_B + M_C)$ are the reduced molar masses of the

colliding pairs. Without much loss of accuracy, δ can be taken as 1 Å (Benson, 1976; Moore and Pearson, 1981).

For the trimolecular reaction of Mg, CO and H_2, assuming M to be H_2 and H_2 stays inert, $d_{Mg\text{-}CO}$ = 3.33 Å and $d_{CO-H_2} = r_{CO} + r_{H_2}$ = 3.37 Å. The collision radius of H_2, r_{H_2}, taken as $\sigma/2$ at an effective temperature of ε/k = 33.3 K, is 1.485 Å (Hirschfelder *et al.*, 1954). At T = 2000 K, $z_{Mg-CO-H_2}$ is calculated to be 1.2 x 10^{17} cm^6/mol^2-s. Substituting this value for k_r in Equation (5-26), 0.25 atm/[R(2000 K)] for $C_{Mg,i}$, 0.5atm/[R(2000 K)] for C_{H_2} and 4.7 x 10^{-6} s for τ_g, the final magnesium partial pressure is estimated at 0.07 atm. The final concentration is the amount of magnesium vapor remaining after reaction with CO during the time scale for crystallization and growth of the particles to 1 μm. Thus, the remaining magnesium vapor can be assumed to precipitate and condense to the solid phase. This implies an MgO "Mg" conversion to Mg of 28%, which is of the same order of magnitude as the observed conversion. Again, the predicted rate constant is an upper limit with the collision efficiency assumed to be 100%. Although slightly lower than the experimental average value, the implied conversion is conceivably consistent with experimental observations considering the approximate nature of the calculations and the conservative assumptions used in this analysis.

Estimation of the rate constant for the reaction of Mg with CO in the presence of H_2 according to a modified Lindemann mechanism supports the hypothesis that the depletion of magnesium vapor via Reaction (4-7) or (5-5) is less significant than consumption by nucleation and condensation. The preceding analysis, though approximate at best, has provided a theoretical basis for postulating that the reverse reaction of Mg with CO to form MgO and C can be sufficiently slow relative to the nucleation and condensation kinetics of supersaturated magnesium vapor. The dramatic change in the environment of the high-temperature plasma effluent brought on by rapid quenching provides the majority of the magnesium vapor with enough driving force to condense and form agglomerates of submicron particles before consumption via Reaction (4-7) or (5-5) becomes dominant.

5.4 Process Economics

The formation of magnesium by the reduction of its oxide is a high-temperature, energy intensive process. The energy required is the enthalpy change of the reaction, ΔH, which is composed of ΔG, the change in Gibbs free energy, and $T\Delta S$, the absolute temperature times the change in entropy. While the $T\Delta S$ requirement can be supplied with low quality process heat, the ΔG component may have to be supplied as high quality energy in the form of electrical work, for example. Alternatively, the use of a reducing agent such as carbon can lower the ΔG requirement (Murray *et al.*, 1995). The use of methane as reductant is noteworthy because methane is reformed into hydrogen and carbon monoxide using the metal oxide as oxidant without the need for catalysts. The integration of the two high-temperature reactions, metal oxide reduction and methane reforming, can therefore give rise to improved energy efficiencies.

Figure 5-2 shows that the endothermic requirement of Reaction (1-4) is relatively constant over a wide temperature range except at the metal boiling point of 1383 K. But with the increasing $T\Delta S$ component, the ratio of work to thermal energy needed, $\Delta G/T\Delta S$, decreases with temperature. Such characteristic makes the implementation of Reaction (1-4) favorable at high temperatures and therefore suitable for a plasma extractive metallurgy process.

In the present study, the lowest Specific Energy Requirement (SER) achieved on the laboratory-scale plasma reactor is 30.4 kWh/kg Mg. However, the experimental results suggest that the energy efficiency can be enhanced at higher gas flow rates. Kim (1977) observed a similar trend in his experiments. Gold *et al.* (1975) at Bethlehem Steel demonstrated that a favorable energy efficiency for an endothermic heterogeneous reaction in a thermal plasma reactor can be achieved when they reduced iron oxide in an arc-heated mixture of hydrogen and natural gas at 100 kW and 1 MW at an SER of 1.2 times the thermodynamic minimum energy requirement.

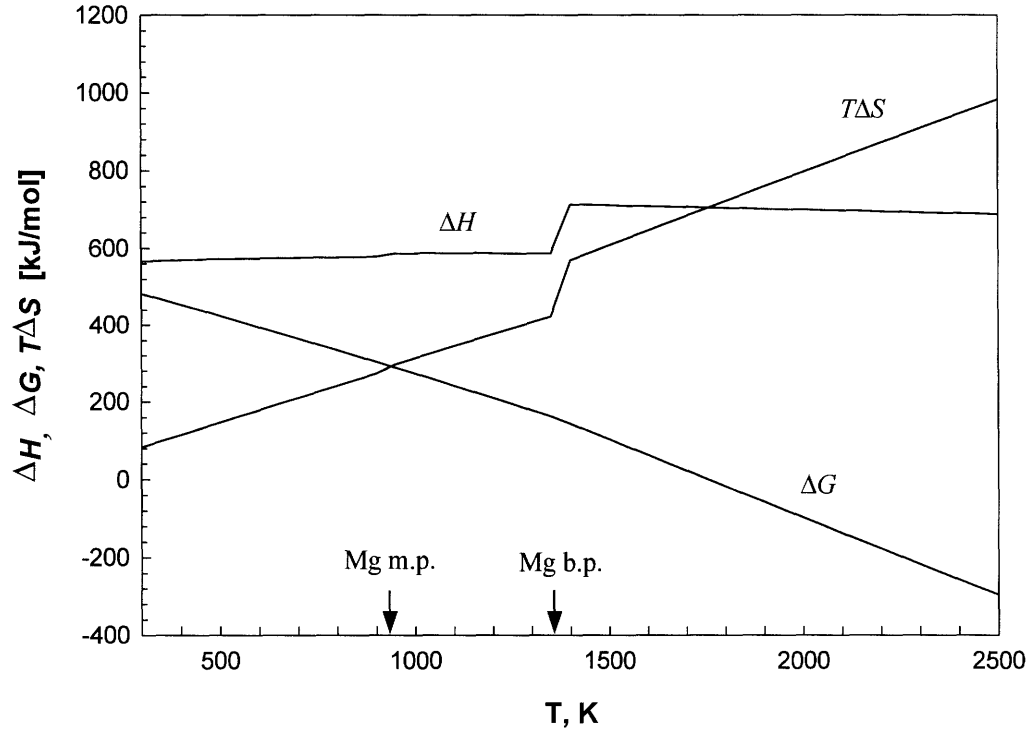

Figure 5-2. ΔH, ΔG and $T\Delta S$ as a Function of Temperature for $CH_4 + MgO \rightarrow Mg + 2H_2 + CO$

The theoretical energy requirement to produce a kilogram of magnesium as a function of temperature is shown in Figure 5-3 for the conventional magnesium production technologies, including carbothermic reduction, and for the contemplated approach according to Reaction (1-4). The reduction of MgO with CH_4 is seen to be on par, at least on a theoretical basis, with electrolysis which is the most commonly used industrial process. The energy requirement of Reaction (1-4) is higher than that for the purely carbothermic reaction because of the additional energy needed to decompose methane into C and H_2. However, no energy credit is taken for the H_2 and CO by-products, which can be utilized to significantly reduce the energy requirements in actual operations.

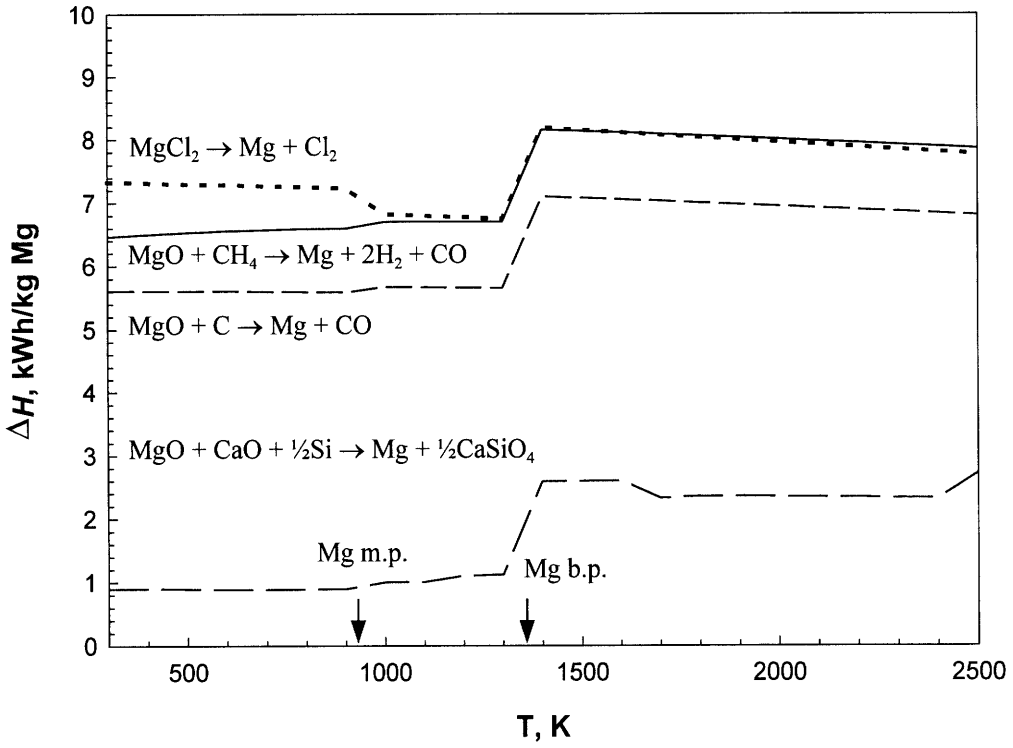

Figure 5-3. Theoretical Energy Requirement, ΔH, as a Function of Temperature for Different Magnesium Production Processes

The actual energy consumption for the different approaches to magnesium production are presented in Table 5-1. An upper limit of 30 kWh/kg Mg has been estimated for the actual energy of Reaction (1-4), corresponding to the best laboratory scale SER. The additional energy requirements for commercial scale operation of Reaction (1-4) have been taken to be of the same magnitude as the energy needed for sublimation and remelting, since the products are similar to those from the carbothermic route. These energy requirements would, of course, be different if the magnesium can be condensed in relatively pure form from the vapor phase, such as in a liquid metal condenser. Even without accounting for the energy and/or chemical value of the H_2 and CO by-products, a commercial implementation of Reaction (1-4) appears to have competitive potential from an energy standpoint.

Table 5-1. Comparison of Theoretical and Actual Energy Requirement for Magnesium Production by Various Processes[a]

Process	Global Chemical Reaction	Theoretical ΔH_{Rxn} (kWh/kg Mg)	Actual Energy for Reaction (kWh/kg Mg)	Additional Energy Requirements (kWh/kg Mg)
Electrolysis	$MgCl_{2\,(l)} \xrightarrow{1073\ K} Mg_{(l)} + Cl_{2\,(g)}$	6.8	12 -18	~15[b]
Silicothermic Reduction	$2\ MgO_{(s)} + 3\ CaO_{(s)} + 1.5\ Al_2O_{3\,(s)} + Si_{(s)} + Fe_{(s)} \xrightarrow[298\ K]{} 2\ Mg_{(g)} + 3\ CaO{\cdot}SiO_2{\cdot}1.5\ Al_2O_3 + Fe_{(l)}$	~5.3	17.2	11.7[c]
Carbothermic Reduction	$MgO_{(s)} + C_{(s)} \xrightarrow[298\ K]{2100\ K} Mg_{(g)} + CO_{(g)}$	8.4	14.4	≥5.6[d]
Present Study	$MgO_{(s)} + CH_{4\,(g)} \xrightarrow{\geq 2000\ K} Mg_{(g)} + CO_{(g)} + H_{2\,(g)}$	8.0	≥8 - 30	≥8[d,e]

[a]Adapted from Cameron *et al.* (1987) and Flemings *et al.* (1981).
[b]For preparing anhydrous feed for electrolytic cell.
[c]For preparation of ferrosilicon reductant.
[d]For Mg recovery by sublimation and remelting.
[e]Includes estimated 1.3 kWh/kg Mg for calcining magnesite and dolomite ores.

In assessing the feasibility of implementing Reaction (1-4) on a commercial scale, one has to consider the overall process economics relative to the conventional magnesium production technologies. Although it is a good starting point, the comparison of the energy requirements for the various processes does not give a complete picture because the total production costs would depend on both capital and operating requirements, energy being but a component of the operating cost. Nonetheless, the potential energy parity with the conventional routes is encouraging.

Several features of an approach to magnesium production based on Reaction (1-4) provide distinct advantages over existing processes. First, the proposed approach can be operated continuously and thus can overcome the limitations of batch operation associated with the metallothermic route. Second, it can directly utilize MgO and MgO precursors (dolomite) as feed material which can lead to a chlorine-free process. MgO and MgO precursors are in abundant supply worldwide, making them attractive as feedstock material. Likewise, the abundance of potentially cheap methane or natural gas can contribute to an economically competitive process. Third, the process can be operated at atmospheric or even higher pressures which would reduce the product losses from air influx experienced in vacuum thermal reduction processes. Atmospheric pressure operation can also increase the production throughput significantly. Fourth, there is potential for significant capital (and operating) cost reduction relative to the electrolytic approach because the upstream process for feed preparation may not be as capital-intensive. Cell feed preparation can account for a significant (~50% or more) portion of the total capital requirements for electrolytic processes. In addition to this potentially lower capital need for front-end operation, the simplicity of the rotating arc reactor may also lead to even lower capital investment. Fifth, H_2 and CO, which have premium energy and chemical values, are co-products of magnesium.

5.5 Process Design and Development

Commercialization of a thermal plasma implementation of Reaction (1-4) would entail scale-up of the laboratory scale reactor to successively larger prototypes, in addition to

developing the upstream and downstream operations of the process. Alternatively, a multijet reactor design composed of small-scale plasma torches can be used to increase total processing capacity. Although no experimental work was performed to identify and test scaling parameters, a brief introduction to the subject is given here. Gannon and Krukonis (1972) gave specifications for a 1 MW rotating DC arc reactor to process 10 tons/day of coal with 500 scfm of H_2 which was scaled up from their laboratory scale reactor by a factor of 10. They based their design on the coal mass flux and the current density at the cathode tip. These two parameters were maintained at levels representative of stable operations.

Similarity theory can also be used to describe the interaction between an arc discharge and its surrounding environment and to extrapolate experimental data to different conditions as a way to circumvent expensive experimental testing. Zhukov (1994) provides five similarity criteria that can be used in scaling DC plasma torches, in addition to the widely used similarity criteria in classical hydrodynamics such as the Mach number, N_M, and the Prandtl number, N_{Pr}. The first similarity criterion is for electrical field strength, S_E, which is derived from Ohm's Law:

$$S_E = \frac{\sigma E d^2}{I} \qquad \text{Equation (5-28)}$$

where σ is the conductivity, defined as the ratio of current density, $J \sim I/d^2$, to the electric field strength E, d is the characteristic linear size (diameter of anode nozzle) and I is the arc current. S_E may be replaced by an equivalent criterion based on the voltage drop across the arc, S_V:

$$S_V = \frac{\sigma V d}{I} \qquad \text{Equation (5-29)}$$

where V is the arc voltage drop. The second criterion applies to energy and is based on the energy equation:

$$S_i = \frac{I^2}{\sigma \rho u h d^3}$$ Equation (5-30)

where S_i is the energy criterion, ρ is the density of the medium, u is the characteristic mean mass flow velocity and h is the characteristic flow enthalpy. With the dependence of arc voltage drop on current and mass flow rate, $G \sim \rho u d^2$, of the plasma-forming gas, i.e. $V(I,G)$, S_i can more conveniently be expressed as:

$$S_i = \frac{I^2}{\sigma h G d}$$ Equation (5-31)

A third criterion characterizes the contribution of radiant energy to the process of plasma heat transfer, S_r, and follows from the energy equation as well:

$$S_r = \frac{4\pi\varepsilon d^2}{\mu h}$$ Equation (5-32)

where ε is the emissivity and μ is the medium viscosity. The combination criterion, S_r/N_{Re}, gives the ratio of radiation energy to gas flow energy. The fourth similarity criterion applies to the case of an external magnetic field. The magnetic interaction criterion, S_B, is based on the momentum equation and shows the correlation between magnetic and inertial forces:

$$S_B = \frac{IB}{\rho u^2 d}$$ Equation (5-33)

where B is the magnetic field induction. The fifth criterion is the Reynolds number, which is more conveniently expressed as:

$$N_{\mathrm{Re}} = \frac{4G}{\pi d\mu}$$ Equation (5-34)

Furthermore, the breakdown voltage is a function of the Knudsen number, $N_{\mathrm{Kn}} = l_e/d$, where l_e is the mean free path of the electron in a given gas. The arc length depends on the Knudsen number ($N_{\mathrm{Kn}}^{-1} \sim Pd$) where P is the characteristic pressure at the end of the discharge nozzle. These similarity criteria can be used to develop semi-empirical methods to calculate the electric and thermal properties of thermal plasma reactors for different conditions and sizes based on available experimental data.

Chapter 6

Conclusions

The reaction of methane with magnesium oxide in a rotating DC arc discharge (thermal plasma) reactor was investigated in the present thesis. Originally proposed as an alternative method for methane conversion to solid magnesium carbide intermediates to overcome transportation limitations associated with remote natural gas, this approach has developed into a novel plasma extractive metallurgy method for the formation of magnesium metal. The key findings of this study are:

1. The extents of conversion of CH_4 and MgO to Mg_2C_3 and MgC_2 according to

$$5\ CH_4 + 2\ MgO \rightarrow Mg_2C_3 + 10\ H_2 + 2\ CO \qquad \text{Reaction (1-2)}$$

$$3\ CH_4 + \ MgO \rightarrow MgC_2 + 6\ H_2 + \ CO \qquad \text{Reaction (1-3)}$$

are not significantly appreciable under the thermal plasma conditions investigated. The highest molar conversion of the magnesium in MgO to Mg_2C_3 achieved is 9%. The reaction of CH_4 with Mg metal in the thermal plasma reactor according to:

$$3\ CH_4 + 2\ Mg \rightarrow Mg_2C_3 + 6\ H_2 \qquad \text{Reaction (1-21)}$$

likewise does not proceed to appreciable extents, although CH_4 is converted to carbon and hydrogen;

2. Rather, the global chemistry of the reaction of CH_4 and MgO under the thermal plasma conditions studied is attributed to:

$$CH_4 + MgO \rightarrow Mg + 2\ H_2 + CO \qquad \text{Reaction (1-4)}$$

The magnesium formed is recovered as agglomerated, hexagonal crystalline particles in the 0.1 to 1 μm size range. The molar conversion of the magnesium in MgO to elemental Mg over the range of experimental conditions investigated has a mean of 64% and a standard deviation of 16%, with extents as high as 95% achieved. The mean molar conversion of the hydrogen in CH_4 to H_2 is 91%, with a standard deviation of 16%;

3. A systematic study of preferred ranges of plasma operating conditions for magnesium formation indicates that MgO conversion to Mg can be enhanced by:

a) feeding CH_4 in stoichiometric excess;
b) doping the MgO feed with solid carbon as an additional reducing agent; and
c) diluting the system with an inert gas which has an effect analogous to the reduction of system pressure.

Similarly, the conversion of the carbon in CH_4 to CO and of the hydrogen in CH_4 to H_2 can be enhanced by:

a) feeding MgO in stoichiometric excess;
b) doping the MgO feed with solid carbon as an additional reducing agent (only for hydrogen conversion to H_2);
c) diluting the system with an inert gas; and
d) increasing the residence time in the thermal plasma by lowering the methane flow rate (only for carbon conversion to CO).

Operation at higher methane flow rates suggests that the energy efficiency of the conversion process can be improved at higher throughputs. The formation of Mg has also been found to be feasible even with a mixed feed of CaO and MgO. The CaO is converted to CaC_2 according to:

$$3\,CH_4 + \quad CaO \rightarrow CaC_2 \quad + \quad 6\,H_2 + \quad CO \qquad \text{Reaction (1-1)}$$

4. The CH_4 and MgO reactants are completely vaporized to their constituent atomic species at plasma temperatures estimated to be well over 6000 K, provided there is sufficient residence time. However, the estimated residence times in the thermal plasma reactor are not likely to be long enough for complete evaporation of the 100 μm MgO particles. Thus, the formation of magnesium is postulated to occur mainly by the alternative pathway of nascent carbon species reaction with the MgO particles. The observation of higher magnesium yields upon doping of the MgO reactant with graphite supports this mechanistic pathway for magnesium formation; and

5. Thermodynamic considerations indicate that magnesium vapor and carbon monoxide exist above 2000 K in equilibrium but that the reoxidation of Mg by CO back to MgO would be favored below 2000 K. Rapid quenching of the plasma effluent to below the metal melting point is postulated to freeze the equilibrium at the 2000 to 1800 K temperature range. Such rapid cooling provides the magnesium vapor with enough driving force to nucleate, crystallize, condense and form agglomerates of submicron particles before consumption by reoxidation with CO becomes dominant. Estimated reaction and condensation rates support the high experimental yields of Mg obtained and suggest that the backward reaction of Mg with CO to form MgO and C can be sufficiently slow relative to the nucleation and condensation kinetics of supersaturated magnesium vapor.

A novel approach to magnesium metal formation based on the reaction of MgO with CH_4 in a rotating DC arc discharge reactor has been developed. Relative to the conventional processes, a technology based on this chemistry potentially offers a chlorine-free, continuous and atmospheric pressure process for magnesium production from low-cost and abundant raw materials, such as natural gas and dolomite, at competitive energy, environmental and capital costs.

Chapter 7

Recommendations

Further research is needed to provide sound scientific and engineering foundations for the assessment of the technical and economic promise of a magnesium metal production process based on the reaction of CH_4 and MgO under thermal plasma conditions. Future work is recommended to gain a better understanding of the chemical and physical mechanisms for forming and preserving magnesium with the goal of developing a full-scale commercial process as follows:

1. Investigate the role of impurities, MgO particle size and MgO preparation history on the yields and generation rates of magnesium and its co-products in the interest of understanding the issues needed to develop the upstream section of the process;

2. Study the relative kinetics of the backward reaction of magnesium vapor with CO and of the nucleation and growth kinetics of magnesium from the vapor phase in the presence of CO with the goal of minimizing Mg loss from reoxidation;

3. Elucidate the role of H_2 in inhibiting the reverse reaction of magnesium vapor with CO at low temperatures. Experiments with MgO and C with and without H_2 as well as with He instead of H_2 can shed light on this issue. Experiments with CO and Mg in the plasma reactor, if feasible, can likewise be used to assess the importance of the presence of H_2 in the system;

4. Investigate various options for magnesium separation, recovery and purification with their associated energy implications, including the use of in-line and downstream separation devices, various quenching techniques and liquid metal condensers in the interest of developing the downstream section of the process;

5. Undertake a process development and economic feasibility study;

6. Determine the role of the plasma in the implementation of the reaction of CH_4 and MgO to form Mg, H_2 and CO. Perform experiments designed to assess the viability of the reaction scheme without an electrical arc discharge using a purely thermal approach; and

7. Investigate the feasibility of using a three-phase alternating current (AC) arc discharge reactor to implement the reaction of CH_4 and MgO to form Mg, H_2 and CO.

The present scheme also presents opportunities for applications to other systems. Research aimed to study the feasibility of producing various metals, metal carbides and even metal nitrides from their parent metals, metal oxides, hydroxides or halides, which are inherently high-temperature, energy intensive processes is recommended.

Appendix A

Propagation of Errors Analysis Sample Calculation

Two basic rules for the propagation of errors are presented by Day and Underwood (1980) and are applied to the conversion computations in this study. First, where addition or subtraction is performed, the absolute determinate errors are transmitted directly into the result. Therefore, for a computed result, R, based on the measured quantities A, B, and C, where $R = A + B - C$

$$R + \rho = (A + \sigma) + (B + \beta) - (C - \gamma) \qquad \text{Equation (A-1)}$$

where ρ is the maximum resulting error in R, and σ, β and γ represent the determinate errors in A, B and C. The maximum error is given by

$$\rho = \sigma + \beta + \gamma \qquad \text{Equation (A-2)}$$

Second, where multiplication or division is performed, the relative determinate errors are transmitted directly into the result. For example, if $R = AB/C$,

$$R+\rho=\frac{(A+\sigma)(B+\beta)}{(C-\gamma)}$$ Equation (A-3)

it can be shown, with simplifying assumptions that the errors are small compared to the measured values, that

$$\frac{\rho}{R}=\frac{\sigma}{A}+\frac{\beta}{B}+\frac{\gamma}{C}$$ Equation (A-4)

In computing the conversion of the magnesium in MgO to Mg, $(Mg)\alpha_{MgO}^{Mg}$, according to:

$$(Mg)\alpha_{MgO}^{Mg}=\frac{\left[\frac{A_{H_2}^{HS}}{A_{H_2}^{std}}\times V_{H_2}^{std}\times f_{H_2}^{std}\right]}{\left[\frac{A_{Ne}^{HS}}{A_{Ne}^{std}}\times V_{Ne}^{std}\times f_{Ne}^{std}\right]}\times V_{IS}\times f_{IS}}{[Mg]_f\times V_f\times 22{,}412}\times 100\%$$ Equation (2-14)

the relative error of $(Mg)\alpha_{MgO}^{Mg}$, $e\left[(Mg)\alpha_{MgO}^{Mg}\right]$ is given by:

$$\begin{aligned}e\left[(Mg)\alpha_{MgO}^{Mg}\right]=&\,e\left[A_{H_2}^{HS}\right]+e\left[A_{H_2}^{std}\right]+e\left[V_{H_2}^{std}\right]+e\left[f_{H_2}^{std}\right]+e\left[A_{Ne}^{HS}\right]\\&+e\left[A_{Ne}^{std}\right]+e\left[V_{Ne}^{std}\right]+e\left[f_{Ne}^{std}\right]+e\left[V_{IS}\right]+e\left[f_{IS}\right]\\&+e\left[[Mg]_f\right]+e\left[V_f\right]\end{aligned}$$ Equation (A-5)

Substituting

$$e\left[A_{H_2}^{HS}\right]=1\%,\ e\left[A_{H_2}^{std}\right]=1\%,\ e\left[V_{H_2}^{std}\right]=1\%,\ e\left[f_{H_2}^{std}\right]=2\%,\ e\left[A_{Ne}^{HS}\right]=1\%,\ e\left[A_{Ne}^{std}\right]=1\%$$

$$e\left[V_{Ne}^{std}\right]=0.5\%,\ e\left[f_{Ne}^{std}\right]=2\%,\ e\left[V_{IS}\right]=0.5\%,\ e\left[f_{H_2}^{std}\right]=2\%,\ e\left[[Mg]_f\right]=5\%,\ e\left[V_f\right]=0.1\%$$

into Equation (A-5) gives $e\left[(Mg)\alpha_{MgO}^{Mg}\right]=17.1\%$.

Bibliography

1. Air Reduction, AIRCO, "Singe-Range DC Bumblebee," Installation, Operation, Maintenance Manual, 13, New York.
2. Baddour, R.F. and R.S. Timmins, eds., *The Application of Plasmas to Chemical Processing*, MIT Press, Cambridge, MA, (1967).
3. Barin, I. and O. Knacke, *Thermochemical Properties of Inorganic Substance*, Springer-Verlag, Berlin, Germany, (1973).
4. Benson, S.W., *Thermochemical Kinetics*, John Wiley & Sons, New York, (1976).
5. Besmann, T.M., "SOLGASMIX-PV, A Computer Program to Calculate Equilibrium Relationships in Complex Chemical Systems," Oak Ridge National Laboratory, ORNL/TM-5775, April (1977).
6. Blanchet, J.L., "Reactions of Carbon Vapor with Hydrogen and Methane in a High Intensity Arc," Sc.D. Thesis, Department of Chemical Engineering, MIT, Cambridge, MA, (1963).
7. Byrns, A.C., "Carbothermic Process for Magnesium at Permanente," *Trans. Section, Chemical Engineering Progress* **43**(4), 172-173, (1947).
8. Cameron, A.M., A. van Hattem and V.G. Aurich, "Extractive Metallurgy of Magnesium," *Magnesium Technology*, 7-17, Metals Technology, Metal Science, and Materials Engineering Committees of The Institute of Metals, Nov. 3-4, 1986 at The Royal Society, London, Book 396, The Institute of Metals, Brookfield, VT (1987).
9. Chang, Y. and E. Pfender, "Thermochemistry of Thermal Plasma Chemical Reactions. Part I. General Rules for the Prediction of Products," *Plasma Chemistry and Plasma Processing*, **7**(3), 275-297, (1987).

10. Chase, Jr., M.W., C.A. Davies, J.R. Downey, Jr., D.J. Frurip, R.A. McDonald, and A.N. Syverud, JANAF Thermochemical Tables, Third Edition, *Journal of Physical and Chemical Reference Data* **14**, *Supplement No. 1,* published by American Chemical Society and American Institute of Physics for National Bureau of Standards, (1985).
11. Chen, C.-J., M.H. Back, and R.A. Back, "The Thermal Decomposition of Methane. I. Kinetics of the Primary Decomposition to C_2H_6 + H_2; Rate Constant for the Homogeneous Unimolecular Dissociation of Methane and its Pressure Dependence," *Can. J. Chem.* **53**, 3580-3590, (1975).
12. Chen, X. and E. Pfender, "Heat Transfer to a Single Particle Exposed to a Thermal Plasma," *Plasma Chemistry and Plasma Processing*, **2**(2), 185-212, (1982).
13. Clarke, J.T. in Baddour, R.F. and R.S. Timmins, *The Application of Plasmas to Chemical Processing*, MIT Press, Cambridge, MA, (1967).
14. Copp, A.N. and R. Wardle, *Kirk-Othmer: Encyclopedia of Chemical Technology* **14**, 615-646, 3rd Ed., John Wiley & Sons, (1980).
15. Dahlin, R.S., J. Su, and L.K. Peters, *AIChE J.* **27**(3), 404, (1981).
16. Day, R.A. Jr. And A.L. Underwood, *Quantitative Analysis*, Prentice-Hall, New Jersey, (1980).
17. Detering, B.A., J.A. Batdorf and C.M. Wai, "Reduction of Selected Metal Oxides in a Thermal Plasma Produced by a Nontransferred Arc Torch," *Materials Research Symposium Proceedings* **98**, Material Research Society, (1987).
18. Detz, C.M. and H.B. Sargent, *Kirk-Othmer: Encyclopedia of Chemical Technology* **1**, 193-203, 3rd Ed., John Wiley & Sons, (1980).
19. Driscoll, D.J., W.M. Martin, J. Wang, J.H. Lunsford, *Am. Chem. Soc.*, **107**, 58-63, (1985).
20. Duncan, D.A., *Kirk-Othmer: Encyclopedia of Chemical Technology* **1**, 211-237, 3rd Ed., John Wiley & Sons, (1980).
21. Durrant, J.P. and B. Durrant, *Introduction to Advanced Inorganic Chemistry*, 2nd Ed., 478, 611, Longman, London, (1970).

22. El-Naas, M.H., R.J. Munz and F. Ajersch, "Production of Calcium Carbide in a Plasma-Jet Fluidized Bed Reactor," *12th International Symposium on Plasma Chemistry Proceedings Volume II*, 613 - 618, The International Union of Pure and Applied Chemistry and The American Physical Society, Minneapolis, MN, August (1995).

23. Emley, E.F., *Principles of Magnesium Technology*, Pergamon Press, Oxford (1966).

24. Erekson, E.J. and F.Q. Miao, "Gasoline from Natural Gas by Sulfur Processing," *Coal Liquefaction and Gas Conversion Contractors Review Conference*, 553-561, U.S. DOE, Pittsburgh Energy Technology Center, Pittsburgh, PA, August (1995).

25. Fjellvåg, H. and P. Karen, "Crystal Structure of Magnesium Sesquicarbide," *Inorganic Chemistry* **31**, 3260-3263, (1992).

26. Flemings, M.C., chairman, Commission on Engineering and Technical Systems, NRC, "Plasma Processing of Materials," Report of the Committee on Plasma Processing of Materials, National Materials Advisory Board, Commission on Engineering and Technical Systems, National Research Council, National Academy Press, Washington D.C., (1985), available from the Defense Technical Information Center, Cameron Station, Alexandria, VA 22312.

27. Flemings, M.C., G.B. Kenney, D.R. Sadoway, J.P. Clark and J. Szekely, "An Assessment of Magnesium Primary Technology," A Report of the Materials Processing Center, MIT, Cambridge, MA; A Final Report on Contract No. EX-76-A-01-2295, submitted to the U.S. DOE, Office of Industrial Programs, Washington, D.C., Feb. 1 (1981).

28. Fox, J.M., T-P Chen, B.D. Degen, A.H. Koenig, M.C. Weekes and T. Yambao, "Direct Methane Conversion Process Evaluations," Report to the U.S. DOE, by Bechtel National Inc., San Francisco, CA, July (1988).

29. Fox, J.M., R.F. Geosits, A.H. Koenig and P.R. Danforth, "Remote Gas Processing and Marketing," *Energy Progress* **8**(1), 39-47, (1988).

30. Friedlander, S.K., *Smoke, Dust and Haze*, John Wiley & Sons, New York (1977).

31. Fukuchi, A., M. Kawashima and S. Yuasa, "Combustion Characteristics of Mg-CO_2 Counterflow Diffusion Flames," *Proceedings of Twenty-Sixth Symposium*

(International) on Combustion, The Combustion Institute, Pittsburgh, 1945-1951, (1996).

32. Fuller, E.N., P.D. Schettler and J.C. Giddings, "A New Method for the Prediction of Gas-Phase Diffusion Coefficients," *Ind. Eng. Chem.* **58**, (1966).
33. Gannon R.E. and V. Krukonis, "Arc-Coal Process Development," OCR Contract No. 14-01-0001-493, NTIS PB-235 300, Springfield, VA, (1972).
34. Gary, J.H. and G.E. Handwerk, *Petroleum Refining Technology and Economics*, Second Edition, 207, Marcel Dekker, New York, (1984).
35. Gesser, H.D., N.R. Hunter and C.B. Prakash, "Direct Conversion of Methane to Methanol by Controlled Oxidation," *Chem. Rev.*, **85**, 235-244, (1985).
36. Gillespie, R.J., D.A. Humphreys, N.C. Baird and E.A. Robinson, *Chemistry*, Allyn and Bacon, Massachusetts, (1986).
37. Gold, R.G., W.R. Sandall, P.G. Cheplick and D.R. Mac Rae, "Plasma Reduction of Iron Oxide with Hydrogen and Natural Gas at 100 kW and One Megawatt," *Proceedings 1975 International Round Table on Study and Applications of Transport Phenomena in Thermal Plasmas*, C. Bonet, ed., International Union of Pure and Applied Chemistry, France (1975).
38. Granqvist, C.G. and R.A. Buhrman, *J. Appl. Phys.* **47**, 2200, (1976).
39. Gross, B., B. Grycz and K. Miklossy, *Plasma Technology*, American Elsevier Publishing Company, Inc., New York (1969).
40. Guthrie, H.D., G.J. Stiegel and R.D. Malone, "Gas-to-Liquids Program Overview," presentation at 1995 Coal Liquefaction and Gas Conversion Contractors Review Conference, Pittsburgh, PA, August 29-31 (1995).
41. Halliday, D. and R. Resnick, *Physics*, Part II, 3rd Edition, John Wiley & Sons, Inc., New York (1978).
42. Hecht, J., W.P. West and M.A. Norton, *Suf. Sci.* **106**, 131, (1980).
43. Hirschfelder, J.O., C.F. Curtis and R.B. Bird, *Molecular Theory of Gases and Liquids*, John Wiley & Sons, New York (1954).

44. Huff, Jr., G.A. and A.D. Eastman, *Symposium on Methane Upgrading*, Am. Chem. Soc. Div. of Petrol. Chem., Spring National Meeting, 141-182, Atlanta, GA, April (1991).

45. Kim, C.S., "Formation of CaC_2 from CaO and 'Nascent' Carbon Species in a Rotating-Arc Reactor," Sc.D. Thesis, Department of Chemical Engineering, MIT, Cambridge, MA, (1977).

46. Kim, C.S., R.F. Baddour, J.B. Howard and H.P. Meissner, "CaC_2 Production from CaO and Coal or Hydrocarbons in a Rotating-Arc Reactor," *Ind. Eng. Chem. Process Des. Dev.* **18**, 323-328, (1979).

47. Kitamura, T., K. Shibata and K. Takeda, "In-Flight Reduction of Fe_2O_3, Cr_2O_3, TiO_2 and Al_2O_3 by Ar-H_2 Plasma," in El-Kaddah, N., ed., *Thermal Plasma Applications in Materials and Metallurgical Processing*, Proceedings of an International Symposium Sponsored by TMS Process Fundamentals Committee, The Minerals, Metals & Materials Society, Pennsylvania, (1992).

48. Knight, R., M.J. Murawa, N.M. Girgis and K.J. Reid, "Arc Characteristics in Small-Scale DC Plasma Arc Furnaces Using Graphite Cathodes," *Plasma Chemistry and Plasma Processing* **10**(2), 359-373, (1990).

49. Kong, P., R.M. Young, T.T. Huang and E. Pfender, "Beta-SiC Synthesis in an Atmospheric Pressure Convection-Stabilized Arc," Proceedings of International Symposium of Plasma Chemistry, Eindhoven, (1985).

50. Kosolapova, T. Ya., translated from Russian by N.B. Vaughan, *Carbides: Properties, Production, and Applications*, Plenum Press, New York-London, (1971).

51. Krukonis, V.J., R.E. Gannon and M. Modell, "Deuterium and Carbon-13 Tagging Studies of the Plasma Pyrolysis of Coal," in Massey, L.G., ed., *Coal Gasification*, 29-41, American Chemical Society, Washington, D.C., (1974).

52. Kusch, H.J., *Chem. Ing. Techn.*, **65**, 448 (1963).

53. Kuo, J.C.W. and A.B. Ketkar, "Evaluation of Direct Methane Conversion to Higher Hydrocarbons and Oxygenates," Report No. DOE/PC/90009-3 to the U.S. DOE, by Mobil Research and Development Corporation, Paulsboro, NJ, August (1987).

54. Laidler, K.J., *Chemical Kinetics*, HarperCollins *Publishers*, New York, (1987).

55. Lockwood, L.F., G. Ansel and P.O. Haddad, *Kirk-Othmer: Encyclopedia of Chemical Technology* **14**, 570-615, 3rd Ed., John Wiley & Sons, (1981).

56. Longwell, J.P., "Diversification of Raw Materials for Domestically Produced Transportation Fuels," *Energy & Fuels* **7**, 23-26, (1993).

57. Malone, R.D. and C.A. Komar, eds., "Natural Gas to Liquids Technology Status Report," Report No. DOE/METC-89/0265, U.S. DOE, Morgantown Energy Technology Center, Morgantown, WV, January (1989).

58. Malone, R.D., H.D. Shoemaker and C.W. Byrer, eds., "Proceedings of the Natural Gas Research and Development Contractors Meeting," Report No. DOE/METC-91/6117, U.S. DOE, Morgantown Energy Technology Center, Morgantown, WV, 241-295, 308-315, and 324, November 14-15 (1990).

59. McPherson, R., "Formation of Metastable Phases in Flame- and Plasma-Prepared Alumina," *Journal of Materials Science* **8**, 851-858, (1973).

60. Merriam, E.S., "Reduction of Metal Ores," United States Patent No. 2,364,742; Assigned to Marietta Manufacturing Company, Point Peasant, WV, December 12 (1944).

61. Miller, S.A., *Acetylene - Its Properties, Manufacture and Uses, Vol. I*, Ernest Benn Limited, London, (1965).

62. Moore, J.W. and R.G. Pearson, *Kinetics and Mechanism*, John Wiley & Sons, New York, (1981).

63. Murray, J.P., A. Steinfeld and E.A. Fletcher, "Metals, Nitrides, and Carbides via Solar Carbothermal Reduction of Metal Oxides," *Energy* **20**(7), 695-704, (1995).

64. National Bureau of Standards (U.S.) Monogram, 25, 21 82 (1984).

65. Perry, R.H., D.W. Green and J.O. Maloney, eds., *Perry's Chemical Engineers' Handbook*, 6th Ed., McGraw-Hill, New York, (1984).

66. Peters, W.A. and J.B. Howard, "Methane Conversion Illustrated by Examples of Applications to Conversion of Remote Natural Gas to Hydrogen and to Transportable Solids and Liquids with Preliminary Cost Estimates, Technical

Assessments, and Critical Research Needs," MIT Energy Laboratory Report, MIT, Cambridge, MA, April (1989).

67. Peters, W.A. and J.B. Howard, "Method for Methane Conversion," United States Patent No. 4,921,685; 15 Claims, Assigned to MIT, May 1 (1990).
68. Peters, W.A. and J.B. Howard, "Method for Methane Conversion," United States Patent No. 5,246,550, 10 Claims, Assigned to MIT, September 21 (1993).
69. Ranz, W.E., and W.R. Marshall, Jr., *Chem. Eng. Prog.* **48**, 141, 173 (1952).
70. Ridgeway, J.M., "Magnesium," *The Mining Annual Review, The Mining Journal, Ltd.*, 65, July, (1995).
71. Saito, H., Department of Chemical Engineering, MIT, Cambridge, MA, personal communications, (1991, 1992).
72. Shafirovich, E. Ya. and U.I. Goldshleger, "Combustion of Magnesium Particles in CO_2/CO Mixtures," *Combustion Science and Technology* **84**, 33-43, (1992).
73. Shine, N.B., *Kirk-Othmer: Encyclopedia of Chemical Technology* **4**, 505-519, 3rd Ed., John Wiley & Sons, (1980).
74. Shreve, R.N. and J.A. Brink, Jr., *Chemical Process Industries,* 4th Ed., 167, McGraw-Hill, New York, (1977).
75. Smithells, C.J. and E.A. Brandes, *Metals Reference Book*, Buttersworth, London, (1976).
76. Spitz, P.H., *Petrochemicals: The Rise of an Industry*, John Wiley & Sons, New York, (1988).
77. Steinfeld, A., A. Frei, P. Kuhn and D. Wuillemin, "Solar Thermal Production of Zinc and Syngas via Combined ZnO-Reduction and CH_4-Reforming Processes," *Int. J. Hydrogen Energy* **20**(10), 793-804, (1995).
78. Stephen, R.L., M.K. Wu, B.J. Welch, J.S. McFeaters and J.J. Moore, "A Thermodynamic Analysis of Titanium Carbide Synthesis in a Thermal Plasma Reactor," in Upadhya, K., ed., *Plasma Synthesis and Processing of Materials*, The Minerals, Metals & Materials Society, Pennsylvania, (1993).
79. Stokes, C.S. in Venugopalan, M., ed., *Reactions Under Plasma Conditions, Vol. II*, 259-298, Wiley-Interscience, New York, (1971).

80. Tagawa, H. and H. Sugawara, "The Kinetics of the Formation of Calcium Carbide in a Solid-Solid Reaction," *Bull. Chem. Soc. Japan*, **35**(8), 1276-1279, (1962).

81. Talonen, T., J. Eskelinen, T. Syväjärvi and A. Roine, "Calculation of Equilibrium Composition," in Roine, A., *Outokumpu HSC Chemistry for Windows ver. 2.03*, Chemical Reaction and Equilibrium Software with extensive Thermochemical Database, Outokumpu Research Oy, Pori, Finland, (1994).

82. Tedeschi, R.J., *Acetylene-Based Chemicals from Coal and Other Natural Resources*, Marcel Dekker, New York, (1982).

83. Turnbull, D., *J. Appl. Phys.* **21**, 1022, (1950).

84. Venugopalan, M. in Venugopalan, M., ed., *Reactions Under Plasma Conditions, Vol. I*, 1-28, Wiley-Interscience, New York, (1971).

85. Venugopalan, M. in Venugopalan, M., ed., *Reactions Under Plasma Conditions, Vol. II*, 1-34, Wiley-Interscience, New York, (1971).

86. Vursel, F. and L. Polak in Venugopalan, M., ed., *Reactions Under Plasma Conditions, Vol. II*, 299-326, Wiley-Interscience, New York, (1971).

87. Weast, R.C. and M.J. Astle, eds., *CRC Handbook of Chemistry and Physics*, 62nd Ed., B-88, B-116, CRC Press, Florida, (1982).

88. Yarlagadda, P.S., L.A. Morton, N.R. Hunter and H.D. Gesser, "Direct Catalytic Conversion of Methane to Higher Hydrocarbons," *Fuel Sci. & Tech. Int'l.*, **5**(2), 169-183, (1987).

89. Young, R.M. and E. Pfender, "Generation and Behavior of Fine Particles in Thermal Plasmas - A Review," *Plasma Chemistry and Plasma Processing* **5**(1), 1-37, (1985).

90. Yuasa, S. and A. Fukuchi, "Ignition and Combustion of Magnesium in Carbon Dioxide Streams," *Proceedings of Twenty-Fifth Symposium (International) on Combustion*, The Combustion Institute, Pittsburgh, 1587-1594, (1994).

91. Zhukov,, M.F., "Linear Direct Current Plasma Torches," in Solonenko, O.P. and M.F. Zhukov, eds., *Thermal Plasma and New Materials Technology, Vol 1: Investigations and Design of thermal Plasma Generators*, Cambridge Interscience Publishing, Cambridge, England (1994).